THE UNIVERSITY *of* EDINBURGH

This thesis has been submitted in fulfilment of the requirements for a postgraduate degree (e.g. PhD, MPhil, DClinPsychol) at the University of Edinburgh. Please note the following terms and conditions of use:

- This work is protected by copyright and other intellectual property rights, which are retained by the thesis author, unless otherwise stated.
- A copy can be downloaded for personal non-commercial research or study, without prior permission or charge.
- This thesis cannot be reproduced or quoted extensively from without first obtaining permission in writing from the author.
- The content must not be changed in any way or sold commercially in any format or medium without the formal permission of the author.
- When referring to this work, full bibliographic details including the author, title, awarding institution and date of the thesis must be given.

Role of Periaxin Dimerization in Peripheral Myelination

Lai Man (Natalie) Wu

Ph.D.
University of Edinburgh

Centre for Neuroregeneration
2011

DECLARATION

I declare that this thesis and the work described in it are my own except where indicated and have not been submitted for any other degree.

Lai Man (Natalie) Wu
November 2011

ACKNOWLEDGEMENTS

I would like to thank my supervisors, Professor Peter J. Brophy and Dr. Diane L. Sherman for their support and excellent supervision over the course of this work. I am very grateful for all past and current members of the Brophy lab for helpful discussions, outstanding advice and technical assistance. I specifically express my gratitude to Stewart Gillespie, Matthew Grove, Qiushi Li, Barbara Zonta, Anne Desmazieres, Shona Melrose, Stuart Flemming and Heather Anderson for help and encouragement.

Special thanks also go to Professor Richard Ribchester for teaching me the basic electrophysiological techniques for determining nerve conduction velocity and for all the thorough discussions. I would also like to acknowledge Steven Mitchell at the EM facility for technical help, and members of staff at the Centre for Neuroregeneration for assistance.

I thank the Wellcome Trust, College of Medicine & Veterinary Medicine MTEM scholarships and the Scottish Overseas Research Student Awards Scheme (SORSAS) for funding my PhD work. Finally, I want to thank my family for giving me much freedom and support to pursue my dreams in life.

CONTENTS

LIST OF FIGURES

LIST OF TABLES

ABBREVIATIONS

3D	Three-dimensional
aa	Amino acid
ADAM	A disintegrin and metalloprotease
BDNF	Brain-derived neurotrophic factor
BrdU	Bromodeoxyuridine
BSA	Bovine serum albumin
CMT	Charcot-Marie-Tooth neuropathy
CNS	Central nervous system
DEPC	Diethyl pyrocarbonate
DGC	Dystrophin glycoprotein complex
Dlg	Disc large
DRG	Dorsal root ganglia
DRP2	Dystrophin-related protein 2
DTT	Dithiothreitol
E	Embryonic day
EDTA	Ethylene diaminetetra-acetic acid
EM	Electron microscopy
FAK	Focal adhesion kinase
FITC	Fluorescein isothiocyanate
GDNF	Glial cell line-derived neurotrophic factor
GRIP1	Glutamate receptor interacting protein 1
h	hour
HRP	Horseradish peroxidase
Ig	Immunoglobulin
IL	Internodal length
kDa	KiloDalton
KO	Knockout
L1	L1 cell adhesion molecule
MAG	Myelin associated glycoprotein
MBP	Myelin basic protein
min	minute
mRNA	Messenger RNA
mTOR	Mammalian Target of Rapamycin
NCAM	Neural cell adhesion molecule
nNOS	Neuronal nitric oxide synthase
NRG1	Neuregulin 1
nt	Nucleotide
P_0	Myelin protein zero
PBS	Phosphate-buffered saline

PCR	Polymerase chain reaction
PDG	Periaxin-DRP2-Dytroglycan
PDZ	PSD-95/disc large/zonula occludens-1
PLP	Proteolipid protein
PMSF	p-methane-sulfonic acid
PNS	Peripheral nervous system
POMT	Protein O-Mannosyltransferase
Prx	Periaxin
Prx	*periaxin* gene
PSD-95	Postsynaptic density protein 95
RNA	Ribonucleic acid
RNase	Ribonuclease
ROCK	Rho kinase
rpm	Revolutions per minute
RT-PCR	Reverse-transcription polymerase chain reaction
s	Second
SAP97	Synapse-associated protein 97
SDS	Sodium dodecyl sulfate
SDS-PAGE	Sodium dodecyl sulphate-polyacrylamide gel electrophoresis
TAE	10 mM Tris, 1 mM EDTA, pH8.0
TBS	Tris-buffered saline
TE	10 mM Tris, 1 mM EDTA, pH8.0
TLCK	Tosyl-L-lysyl-chloromethylketone
TRITC	Tetramethylrhodamine isothiocyanate
UV	Ultraviolet
WT	Wild-type
ZO	Zonula occludens

ABSTRACT

In the peripheral nervous system (PNS), Schwann cells ensheathe and myelinate axons to promote saltatory conduction of nerve impulses. Close interactions between Schwann cells and axons, and Schwann cells and the basal lamina are essential for the regulation of Schwann cell development and function. Myelinating Schwann cells are highly polarized radially and longitudinally for specifying distinct domains in the axon, which is required for fast action potential propagation. In addition, the Schwann cell cytoplasm is organized into discrete compartments, called Cajal bands, which contain different dystrophin-glycoprotein complexes that are believed to segregate the Schwann cell plasma membrane into appositions between the outer surface of the myelin sheath and the cytoplasmic face of the Schwann cell plasma membrane.

Periaxin is expressed in myelinating Schwann cells, and homodimerizes at its PDZ domain to form a transmembrane complex with dystrophin-related protein 2 (DRP2) and dystroglycan. This PDG complex is concentrated at the appositions, and is essential for myelin sheath maintenance and stability in the mature PNS. In mice lacking Periaxin, an intact myelin sheath is formed but subsequently becomes unstable. Periaxin-null Schwann cells are also shorter, which has been proposed to result in a reduction in nerve conduction velocity.

This thesis is a study of how Periaxin PDZ domain dimerization contributes to the regulation of PDG complex stability, apposition maintenance, Schwann cell internodal distance and myelin stability. I have studied the function of Periaxin by generating a conditional mutant mouse that lacks the PDZ domain, which is predicted to abrogate dimerization. In these mutants, DRP2 is severely depleted and appositions containing DRP2 fail to form. Mutant Schwann cells also have disrupted Cajal bands and shorter internodal lengths. In the mature peripheral nerves, mutant mice display a peripheral neuropathy characterized by hypermyelination with focally folded myelin. Nerve conduction velocity, motor coordination and sensory function were also studied in these mutant mice. Taken together, these data suggest that dimerization of the Periaxin PDZ domain is required for the stabilization of the PDG and appositions, and regulation of Schwann cell elongation and myelin maintenance.

By analyzing a tamoxifen-inducible conditional mouse lacking Periaxin's PDZ domain in mature myelinating Schwann cells, this work also shows that Periaxin dimerization is essential for maintaining Schwann cell compartmentalization and myelin stability in adult nerves.

Finally, studies of single amino acid mutations of the Periaxin PDZ reveal that subtle changes in the structure of the PDZ domain can abrogate dimerization, and a possible mechanism for PDZ-PDZ homodimerization of Periaxin is proposed.

1- INTRODUCTION

OVERVIEW

A fundamentally important step in the evolution of the vertebrate nervous system was the acquisition of the myelin sheath, which has allowed the development of a complex system for rapid impulse propagation resulting in, among other things, more rapid and sustained responses in a predator-and-prey environment (Hartline and Colman, 2007; Nave, 2010). Myelin-forming glial cells ensheathe and form a multilamellar structure with a high lipid-to-protein ratio (70-80% lipids and 20-30% proteins) around axons in order to facilitate rapid saltatory conduction of action potentials (Garbay et al., 2000). Myelination involves close interactions between the neuron and the myelin-forming glia (Sherman and Brophy, 2005). In the vertebrate peripheral nervous system (PNS), Schwann cells, named after the German physiologist Theodor Schwann, are the major glial cells that are responsible for forming and maintaining the myelin sheath around axons (Schwann, 1839). Their counterparts in the central nervous system (CNS) are oligodendrocytes, first described as mesoglia by William Ford Robertson (Robertson, 1899). Though they perform a similar function in the nervous system, the origins of these two myelinating cell types differ. Schwann cells are generated from the neural crest (Jessen and Mirsky, 2005), and most oligodendrocytes are derived in the subventricular germinal zone in the forebrain, and in the ventral ventricular zone in the spinal cord in the CNS (Richardson et al., 2006).

The close association between neurons and glia has offered mutual benefits for both cell types. In the PNS, Schwann cells depend on axonal signals such as Neuregulin-1 (NRG1) throughout development for survival, migration, proliferation, differentiation and myelination (Jessen and Mirsky, 2005). Neurons benefit from myelination of their axons by glia for fast propagation of action potentials. The non-conductive lipid-rich myelin sheath coats and thus provides insulation for the most part of the axonal surface, increasing electrical resistance and decreasing capacitance between the inside and outside of a nerve fiber. This prevents internodal current leakage and restricts ion currents to gaps not covered by myelin that occupies less than 0.5% of the axonal surface, namely the nodes of Ranvier (Hartline and Colman, 2007). This arrangement allows action potential regeneration exclusively at the nodes followed by rapid electrotonic conduction along the internode. Consequently,

energy consumption from restoring the ion gradients between the interior and exterior surfaces of the nerve fiber is highly reduced (Nave, 2010). The speed of action potential conduction, therefore, is increased up to 100-fold. Moreover, myelinating glia continue to support axons by ensuring the long-term integrity and survival of axons throughout life, although the mechanisms underlying this trophic support are still not clear (Nave, 2010).

In addition to the close communication with axons, all Schwann cells in the endoneurium are surrounded by a basal lamina, which is composed of extracellular matrix molecules that regulate crucial aspects of Schwann cell development including proliferation, formation and function of myelin, and formation of Remak bundles (Feltri and Wrabetz, 2005; Yu et al., 2009b). In the following three main parts, I will review the development of a myelinating Schwann cell, how its interactions with the axon and the basal lamina impact its function, with special emphasis on the role of an important myelinating Schwann cell membrane-associated protein Periaxin.

1.1 SCHWANN CELL LINEAGE DEVELOPMENT

During vertebrate development, the neural crest comprises a population of cells originating from the dorsal-most surface of the neural tube. Following neurulation, the crest cells segregate from the dorsal regions of the neural folds, extensively migrate within the developing embryo and differentiate into diverse cell types, including neurons and glia of the sensory, autonomic and enteric nervous systems, smooth muscle cells, melanocytes in the skin, and cells of the cranio-facial skeleton (Le Douarin and Dupin, 2003). In the PNS, generation of myelinating and non-myelinating Schwann cells from migrating neural crest cells involves three main transitional stages. First, neural crest cells are specified to form Schwann cell precursors (SCPs), which are present at around embryonic day (E) 14-15 in rat nerves (E12-13 in mouse). They give rise to immature Schwann cells, which occupy nerves from E17-18 in the rat (E15-16 in mouse). At birth, immature Schwann cells transform into either myelinating or non-myelinating Schwann cells, depending on the axons they randomly associate with (Fig. 1) (Jessen and Mirsky, 2005). Schwann cells in the dorsal and ventral spinal roots are believed to be derived from a distinct population of neural crest derivatives, namely the boundary cap cells that are in small clusters where dorsal and ventral roots enter and exit the spinal cord (Maro et al., 2004).

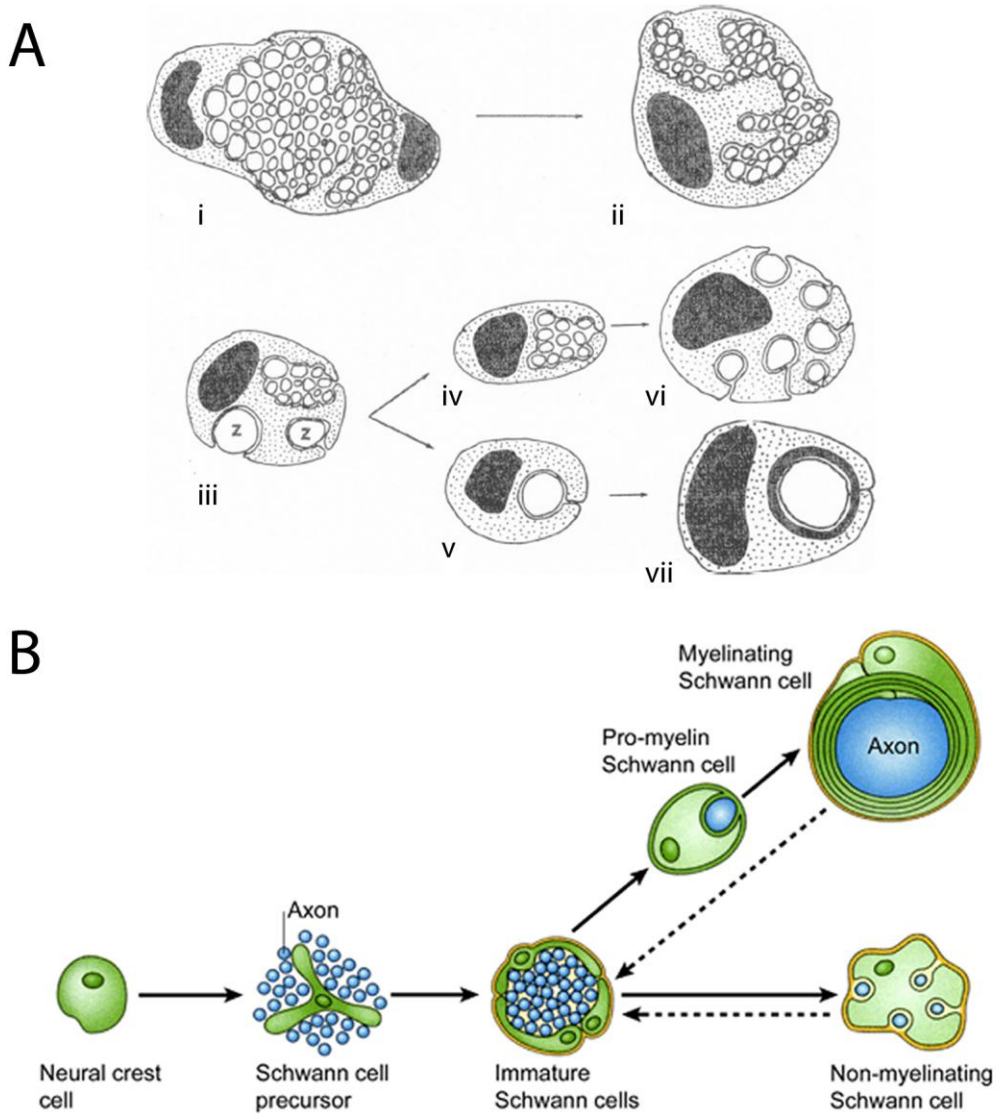

Figure 1. The Schwann cell lineage.

A. The successive stages in the relationship between Schwann cells and axons during development. (i-ii) Schwann cells extend cytoplasmic processes into the nerves dividing axons into bundles. (iii) Schwann cells segregate large diameter axons (Z), (v) form a 1:1 relationship with the axon, and (vii) later myelinate it. (iv) Schwann cells that ensheathe small diameter axons progress to become mature non-myelinating Schwann cells, (vi) forming Remak bundles. This is the first demonstration of radial axonal sorting and two mature Schwann cell populations in the rat (Peters and Muir, 1959).

B. The diagram depicts the development of mature Schwann cells from neural crest cells. Lineage progression of Schwann cells involves two intermediate stages, Schwann cell precursors and immature Schwann cells. Dashed arrows represent the reversibility of the final, mainly postnatal transition that generates mature myelinating and non-myelinating Schwann cells (Jessen and Mirsky, 2005).

1.1.1 THE MOLECULAR PROFILE OF THE SCHWANN CELL LINEAGE IN DEVELOPMENT

Each transitional stage of the Schwann cell lineage is characterized by a distinct set of molecular markers. A number of molecules including the NRG1 receptor ErbB2/3, the transcription factor Sox10, p75 neurotrophin receptor ($p75^{NTR}$) and L1 cell adhesion molecule, are universally expressed at all developmental stages of the Schwann cell. Transition from neural crest cells to SCPs can be identified by the appearance of stage specific markers such as brain fatty acid-binding protein (BFABP), desert hedgehog (DHH), growth-associated protein-43 (GAP43), myelin protein zero (P_0), cadherin19 and connexin 29 (Mirsky et al., 2008). With the exception of cadherin19, which is specific to SCPs (Takahashi and Osumi, 2005), these markers also persist in the progeny of SCPs, i.e. immature Schwann cells. In addition, the transcription factor AP2α and N-cadherin are strongly downregulated in the transition to immature Schwann cells. Immature Schwann cells display some of the same molecular markers as SCPs, and can be distinguished from SCPs by the expression of glial fibrillary acidic protein (GFAP), S100, the transcription factor Oct-6 and lipid antigen O4 (Mirsky et al., 2008).

During myelination at birth, maturation of immature Schwann cells into myelinating Schwann cells is accompanied by an upregulation of myelin-associated markers including Krox-20, P_0, myelin basic protein (MBP), Periaxin and myelin-associated glycoprotein (MAG), peripheral myelin protein 22 (PMP22), connexin32 and galactocerebroside (GalC). Expression of immature Schwann cell molecules, which still persist in mature non-myelin forming Schwann cells, such as NCAM, L1, GAP-43 and $p75^{NTR}$, are downregulated in myelinating Schwann cells. Non-myelinating Schwann cells are distinct from immature Schwann cells in that they also express $\alpha1\beta1$ integrin, and GalC (Fig. 2) (Mirsky et al., 2008).

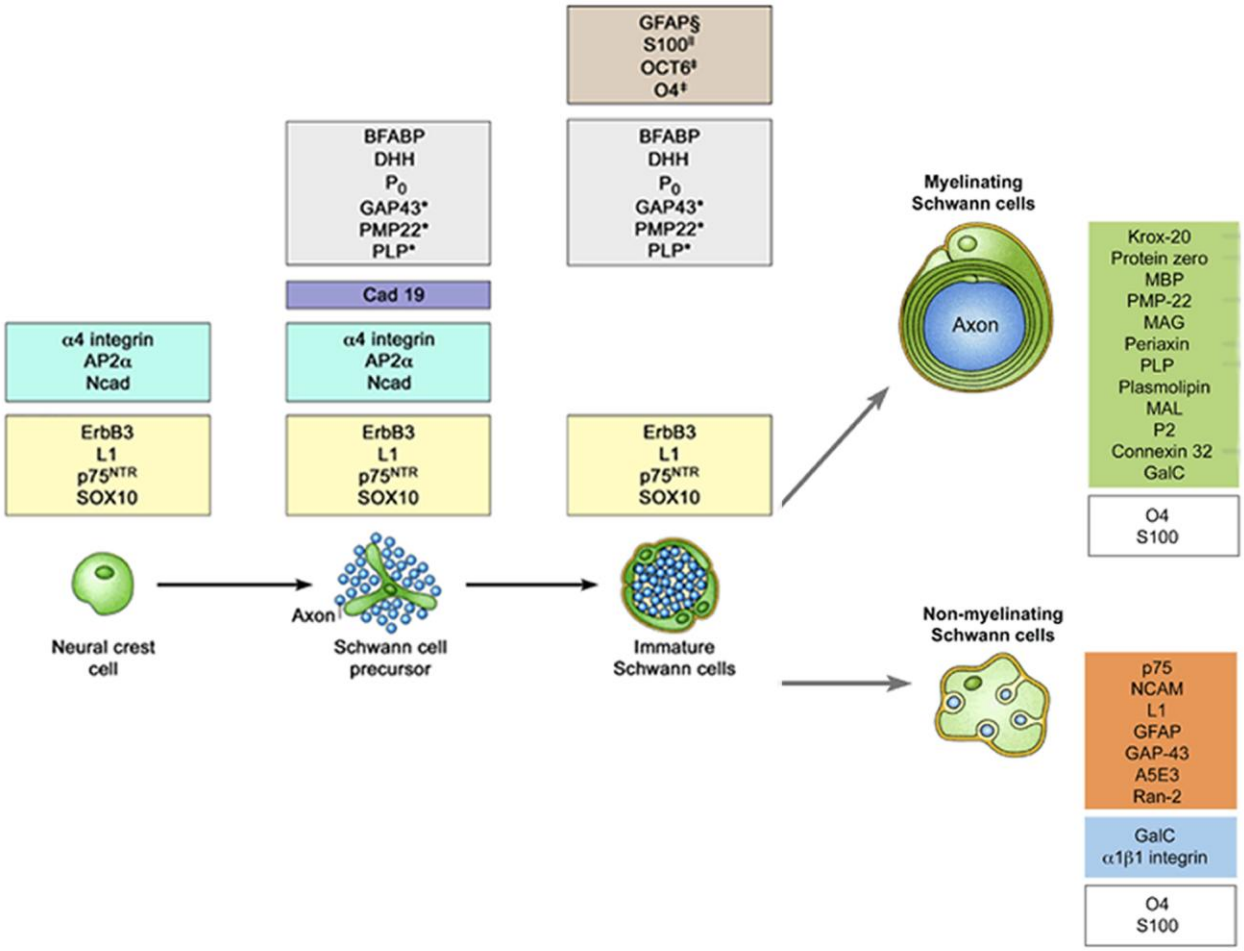

Figure 2. The phenotypic profile of each of the developmental stages of the Schwann cell lineage.

The boxes above the lineage drawing during embryonic development (from neural crest cells to immature Schwann cells), and those on the right of the drawing of the mature phenotypes show the molecular profile of each step. Yellow boxes show molecules expressed by all three embryonic cell types, while the other boxes show stage-restricted markers. Mature myelinating Schwann cells express myelin-specific proteins. AP2α, activator protein 2α; BFABP, brain fatty acid–binding protein; DHH, desert hedgehog; ErbB3, neuregulin receptor; GAP43, growth-associated protein 43; L1, L1 cell adhesion molecule; Ncad, N-cadherin; Oct6, octamer-binding transcription factor 6; O4, lipid antigen; PLP, proteolipid protein; PMP22, peripheral myelin protein 22 kDa; P_0, protein zero; $p75^{NTR}$, p75 neurotrophin receptor; Sox10, SRY (sex-determining region Y) box 10. Figure adapted and modified from (Jessen and Mirsky, 2005; Mirsky et al., 2008).

1.1.2 ORIGIN OF SCHWANN CELLS: NEURAL CREST CELLS

The extracellular signals that instruct neural crest cells to adopt a glial cell fate are currently not well defined. The commitment of neural crest cells to the Schwann cell lineage has been proposed to be enabled by a default pathway when neurogenesis or other cell fates are suppressed (Jessen and Mirsky, 2005). A key transcription factor Sox10 that regulates glial cell differentiation is expressed in all developmental stages of Schwann cells, including neural crest cells (Kuhlbrodt et al., 1998). Initial generation of neurons in dorsal root ganglia in mice mutant for Sox10 is normal, but SCPs and satellite cells are not present (Britsch et al., 2001). Later in development, the absence of SCPs leads to severe death of sensory and motor neurons. However, the observation that Sox10 is not confined to the glial lineage but is expressed by all neural crest cells and other lineages such as melanocytes renders it unlikely that Sox10 alone is sufficient to activate glial cell acquisition (Britsch et al., 2001).

Sox10 may function through maintaining the ability of neural crest cells to respond to the axonal signal NRG1, which is required for different stages of Schwann cell development, since expression of the NRG1 receptor ErbB3 in neural crest cells is downregulated when Sox10 is inactivated (Britsch et al., 2001). In neural crest cell cultures, NRG1 promotes the glial cell fate by inhibition of neurogenesis (Shah et al., 1994). However, mice deficient for NRG1 or NRG1 receptors, ErbB2 or ErbB3, show a dramatic loss of SCPs along peripheral nerves, but satellite glia form normally in the DRGs (Garratt et al., 2000a; Riethmacher et al., 1997), suggesting that NRG1 is not essential for determination of glial differentiation from neural crest cells.

Similar to NRG1 activity, Notch promotes glial specification of neural crest cells (Kubu et al., 2002; Morrison et al., 2000). Constitutive activation of the Notch pathway in chick embryos has been demonstrated to suppress neuronal differentiation and enhance gliogenesis by neural crest cells. In the same study, addition of the Notch ligand Delta to neural crest cell cultures, irreversibly inhibited neurogenesis, and instructed and accelerated glial differentiation (Morrison et al., 2000). Interestingly, conditional deletion of RBPJ, an effector of the canonical Notch signaling from neural crest cells suppresses gliogenesis in the peripheral ganglia of the developing PNS, but glial differentiation in the peripheral nerve remains normal

(Taylor et al., 2007). This suggests that Notch may be required for gliogenesis in the ganglia by neural crest cells, but perhaps not for glial fate acquisition in general in the PNS.

1.1.3 SCHWANN CELL PRECURSORS

1.1.3.1 Survival of Schwann cell precursors

Around E12-13 in mouse, Schwann cell precursors (SCPs) are in close contact with axons. Unlike neural crest cells, which need to maintain contact with the extracellular matrix for NRG1-dependent survival, survival of SCPs is ECM-independent (Woodhoo et al., 2004), but relies on axonal-derived signals. Transition from neural crest cells also increases the responsiveness of SCPs to survival factors, such as fibroblast growth factor (FGF2) and insulin-like growth factor (IGF1) (Jessen and Mirsky, 2005).

SCPs are the intermediates in the generation of Schwann cells from neural crest cells, thus constituting the source of Schwann cells in peripheral nerves (Jessen and Mirsky, 2005). They provide essential trophic support for survival of sensory and motor neurons in developing nerves and are important for nerve fasciculation (Morris et al., 1999; Woldeyesus et al., 1999). Inactivation of ErbB2 in mice, with a genetic rescue of cardiac development, results in the absence of SCPs in peripheral nerves due to their dependence on NRG1 for survival. Sensory and motor neurons are initially generated. However, loss of SCPs leads to defects in fasciculation of nerves and aberrant axonal projections to final target tissues, and eventually to neuronal cell death by E18 (Morris et al., 1999; Woldeyesus et al., 1999). Similarly, initial formation of sensory and motor neurons in the DRG is normal in mice mutant for ErbB3 or Sox10. However, the absence of SCPs and Schwann cells leads to neuronal degeneration at later stages (Britsch et al., 2001; Riethmacher et al., 1997).

Selective ablation of membrane-bound NRG1 type III isoform, the major NRG1 in sensory and motor neurons, in mice results in a depletion of SCPs that populate spinal nerves by E14 (Wolpowitz et al., 2000). Isoform specific *Nrg1* mutations in mice show that the presence of Type III isoform is sufficient to drive early development of Schwann cells (Meyer et al., 1997). Recently, it has been shown that stage-dependent release of soluble Type I/II isoforms mediated by BDNF/TrkB signaling plays a critical role in SCP differentiation and survival in

chick (Ma et al., 2011), although mice lacking Type I and II isoforms display normal peripheral glia development (Meyer et al., 1997; Wolpowitz et al., 2000).

1.3.1.2 Transition of SCPs to Schwann cells

Differentiation of SCPs into immature Schwann cells is also dependent upon close axo-glial relationships. Several axonal signals and growth factors have been shown to promote the conversion of SCPs into Schwann cells. In culture, FGF-2 supports the generation of Schwann cells from SCPs (Jessen et al., 1994), and accelerates the Schwann cell maturation mediated by NRG1 (Dong et al., 1999).

NRG1 signaling is important for the transition of SCPs into Schwann cells. Isolated E14 SCPs from rat, when cultured in the presence of NRG1 for 2-4 days show characteristics of Schwann cells removed from nerves at the equivalent ages *in vivo*, i.e. E16-18, including the development of autocrine survival mechanisms, S100 expression and mitogenic response to FGF-2. The phenotypic change *in vivo* can be reproduced on schedule in a NRG1-mediated manner *in vitro* (Dong et al., 1995; Dong et al., 1999).

Recently, Notch signaling has also been demonstrated to drive the differentiation of SCPs to Schwann cells. SCPs express Notch receptors on their cell surface. Inactivation of Notch signaling in SCPs results in a delay in the generation of immature Schwann cells. On the contrary, constitutive overexpression of the active Notch intracellular domain (NICD) accelerates the transition of SCPs to Schwann cells (Woodhoo et al., 2009).

Negative regulation of SCP differentiation involves endothelin signaling. *In vitro,* endothelin promotes the survival of SCPs but retards their progression into Schwann cells. Endothelin also opposes the effects of NRG1 on SCP maturation (Brennan et al., 2000). Transcription factor AP2α expressed in SCPs also negatively regulates their transition to Schwann cells. *In vitro,* the rate of SCP-Schwann cell transition is slowed down by enforced expression of AP2α in SCPs (Stewart et al., 2001). In summary, SCP progression is controlled by positive and negative regulators that direct the timing of Schwann cell generation.

1.1.4 IMMATURE SCHWANN CELLS

By E17-18 in rat nerves (E15-16 in mouse), immature Schwann cells ensheathe groups of axons in clusters forming irregular Schwann cell-axon bundles. These Schwann cell-axon units, alongside blood vessels, endoneurial fibroblasts and extracellular matrix are enclosed by the developing perineurium. Apart from the distinct molecular profile, immature Schwann cells differ from SCPs in that they have a basal lamina and develop autocrine survival mechanisms, which are absent in SCPs. When removed from axonal contacts, unlike SCPs, immature Schwann cells do not undergo cell death, but are able to survive by secreting a combination of survival growth factors, such as FGF plus IGF, and neurotrophin 3 (NT3) (Woodhoo and Sommer, 2008). The autocrine survival circuits ensure axon-independent survival of Schwann cells, which may provide trophic support for axons in injured postnatal nerves (Jessen and Mirsky, 2005).

1.1.4.1 Radial axonal sorting

Immature Schwann cells continuously associate with axons in peripheral nerves during embryonic stages. The postnatal fate of immature Schwann cells depends on the axons they associate with, and may become either myelinating or non-myelinating Schwann cells. Schwann cells associating with larger caliber axons (Nave and Salzer, 2006), typically with a diameter of at least 1 μm, will segregate them to the periphery of an axon bundle and then into a 1:1 relationship, and subsequently myelinate them. Non-myelinating Schwann cells remain associated with multiple small diameter axons that are unmyelinated in Remak bundles (Jessen and Mirsky, 2005). The establishment of the characteristic 1:1 ratio between myelinating Schwann cells and large diameter axons is referred to as radial sorting, which involves several distinct but concerted steps: Schwann cell proliferation, bipolar shape formation and process extension (Martin and Webster, 1973). Extensive Schwann cell proliferation ensures a precise match of Schwann cell number with axon number for individual axon ensheathment by the end of radial sorting. The change to spindle-shaped morphology of Schwann cells followed by process extension is necessary for interdigitation and ensheathment of axons. The process of radial axonal sorting involves the following steps (Berti et al., 2011):

(1) Schwann cell families are formed and surrounded by a common basal lamina,
(2) Schwann cells extend and insert processes within axons,
(3) Schwann cells recognize and segregate large axons at the periphery,
(4) Schwann cells extensively proliferate to match axons and SC number,
(5) Axons are defasciculated with formation of an independent basal lamina.

A growing spectrum of signals that regulate radial sorting, and more specifically proliferation and/or process extension associated with sorting has been identified. These include focal adhesion kinase (FAK), laminins (laminin-2, laminin-8 and laminin-γ1), laminin receptors, β1-integrin and dystroglycan, the Rho GTPases Rac1 and cdc42 and leucine-rich, glioma-inactivated 4 (LGI4). (Benninger et al., 2007; Bermingham et al., 2006; Berti et al., 2011; Grove et al., 2007; Nodari et al., 2007; Yang et al., 2005; Yu et al., 2005; Yu et al., 2009b). Schwann cell-specific deletion of these molecules in mouse mutants profoundly impairs radial axonal sorting, which will be discussed in detail in the following subsections.

1.1.4.1a- Process extension and stabilization in radial sorting

Prior to myelination at birth, immature Schwann cells insert cytoplasmic processes into axon bundles, progressively defasciculating them into smaller bundles, and establish a 1:1 relationship with single large caliber axons (Jessen and Mirsky, 2005). The deposition of basal lamina, or at least the major basal lamina component laminin, is required for axonal sorting by Schwann cells (Bunge et al., 1986; Podratz et al., 2001). Schwann cells lacking laminin-γ1 lose all laminin expression and display severe sorting defects. The impairment of radial sorting in laminin-γ1 mutants is contributed by a dramatic decrease in proliferation, increased postnatal apoptosis, and reduced ErbB2 phosphorylation (Yu et al., 2005), as well as defective process extension (Yu et al., 2009b). It is widely accepted that laminin signals through α6β1 integrin on Schwann cells for proper radial sorting of axons (Bradley and Jenkison, 1973; Chen and Strickland, 2003; Feltri et al., 2002; Previtali et al., 2003b; Yang et al., 2005; Yu et al., 2005). Genetic deletion of β1-integrin in Schwann cells impairs process extension in the interdigitation and sorting of axons (Feltri et al., 2002) (see section 1.2).

Laminin signaling, originating from the basal lamina on the outside of the Schwann cell surface, controls axon sorting that dynamically rearranges the inner Schwann cell membrane through the activation of the Rho family GTPase Rac1 in Schwann cells. This has been demonstrated by the inactivation of the downstream effector of β1-integrin, Rho GTPase Rac1 in Schwann cells, which impairs extension of radial lamellae of cytoplasm without affecting proliferation during radial sorting (Benninger et al., 2007; Nodari et al., 2007). In addition, integrin linked kinase (ILK), an important regulator of integrin and growth factor–mediated signaling, is also required for extension and stabilization of Schwann cell processes by negatively regulating Rho/Rho kinase signaling (Pereira et al., 2009). Interestingly, ErbB signaling, in addition to promoting Schwann cell proliferation, also plays a direct role in process extension in the sorting process in zebrafish (Raphael et al., 2011).

1.1.4.1b- Schwann cell proliferation during radial sorting

Preceding myelination, establishment of the 1:1 relationship between Schwann cells and axons is associated with extensive Schwann cell proliferation (Martin and Webster, 1973; Stewart et al., 1993). Interaction with axons stimulates Schwann cell proliferation. NRG1 is a major mitogenic factor, as has been shown in Schwann cell-DRG co-cultures *in vitro* (Morrissey et al., 1995). Transforming growth factor-β (TGF-β) also induces Schwann cell proliferation both *in vitro* and *in vivo*. Specific ablation of type II TGF-β receptor in Schwann cells compromises Schwann cell proliferation (D'Antonio et al., 2006). In addition, Notch drives Schwann cell proliferation. Conditional deletion of Notch signaling components in immature Schwann cells reduces Schwann cell proliferation. In contrast, enforced expression of active Notch intracellular domain upregulates cell cycle markers and induces a mitogenic effect on Schwann cells (Woodhoo et al., 2009).

1.1.5-6 SCHWANN CELL MYELINATION

Following radial sorting, a Schwann cell in a 1:1 association with an axon, is described as the promyelinating Schwann cell, which will exit the cell cycle and initiate myelination. The progressive changes in the morphology and molecular profiles of promyelinating Schwann cells at the onset of myelination are governed by multiple signaling pathways activated by Schwann cell-axon and Schwann cell-basal lamina interactions. These pathways converge onto the nucleus to regulate the transcriptional programs directing myelination. Myelination is controlled by a balance between positive and negative transcriptional programs (Svaren and Meijer, 2008). In the next sections, recent understanding of the regulation of myelination by Schwann cell-axon communication (section 1.1.5) and the transcriptional control of myelination (section 1.1.6) will be reviewed. Schwann cell-basal lamina interactions will be reviewed in section 1.2.

1.1.5 Regulation of Schwann cell function by axonal signals

As described already, throughout development, Schwann cells are in close association with axons and communication between neuron and glia is necessary for regulating different steps of Schwann cell development and myelination.

1.1.5.1 Neuregulin-1/ErbB signaling

Neuregulins (NRGs) are a family of structurally related proteins that share an extracellular epidermal growth factor (EGF)-like signaling domain for activation of their receptors, ErbB receptor tyrosine kinases (Birchmeier and Nave, 2008). These proteins act as survival, growth and differentiation factors in various tissues. Four distinct neuregulin genes (*Nrg1-4*) are present in mammals, with *Nrg1* being the best-characterized member of the family in mice (Nave and Salzer, 2006).

NRG1 generates six types of protein (I–VI) and comprises at least 31 isoforms due to multiple transcription start sites and alternative mRNA splicing of the *nrg1* gene (Mei and Xiong, 2008). The NRG1 isoforms are classified into different subtypes based on their distinct N-terminal domains. NRG1 type I (initially identified as neu differentiation factor, heregulin or acetylcholine receptor-inducing activity (ARIA)) and type II, also known as glial growth factor (GGF) are generated as single pass transmembrane proteins and harbor N-terminal immunoglobulin-like

domains. Type I differs from Type II in that Type I has a glycosylation domain, whereas Type II contains a kringle-like domain. NRG1 type III (sensory and motor neuron-derived factor) has a unique cysteine-rich domain (CRD), which acts as the second transmembrane domain (Fig. 3). Other isoforms include NRG1 Type IV-VI, which contain shorter amino termini, but they have not been well-studied (Nave and Salzer, 2006).

NRG1 isoforms transduce cellular signals by binding to transmembrane receptor tyrosine kinases, ErbB proteins, which are members of the EGF receptor superfamily. In the PNS, the ErbB2/ErbB3 heterodimer is the major NRG1 receptor expressed by Schwann cells (Morrissey et al., 1995; Nave and Salzer, 2006).

1.1.5.1a- Proteolytic processing of NRG1

Most NRG1 isoforms are anchored in the membrane. Proteolytic cleavage of these membrane-bound NRG1 isoforms at the juxtamembrane region C-terminal to the EGF-like domain is required for the binding of the secreted NRG1 fragment to ErbB receptors. NRG1 Types I-III that share stalk, transmembrane and C-terminal sequences undergo proteolytic cleavage by proteases at the stalk region (Fig. 3). Upon proteolytic processing, soluble forms of NRG1 (Type I and II) are shed from the axonal surface and able to diffuse or adhere with heparan sulfate-rich cell surfaces in the extracellular matrix via the N-terminal heparan-binding domains. NRG1 Type III, however, remains bound to the axonal membrane after cleavage through the N-terminal cysteine rich domain (Birchmeier and Nave, 2008; Mei and Xiong, 2008).

The proteases involved in proteolytic processing of NRG1 subtypes have been partly characterized, which include membrane-anchored metalloproteases known as ‘a disintegrin and metalloprotease’ ADAM proteins, and type I transmembrane aspartyl protease BACE1.

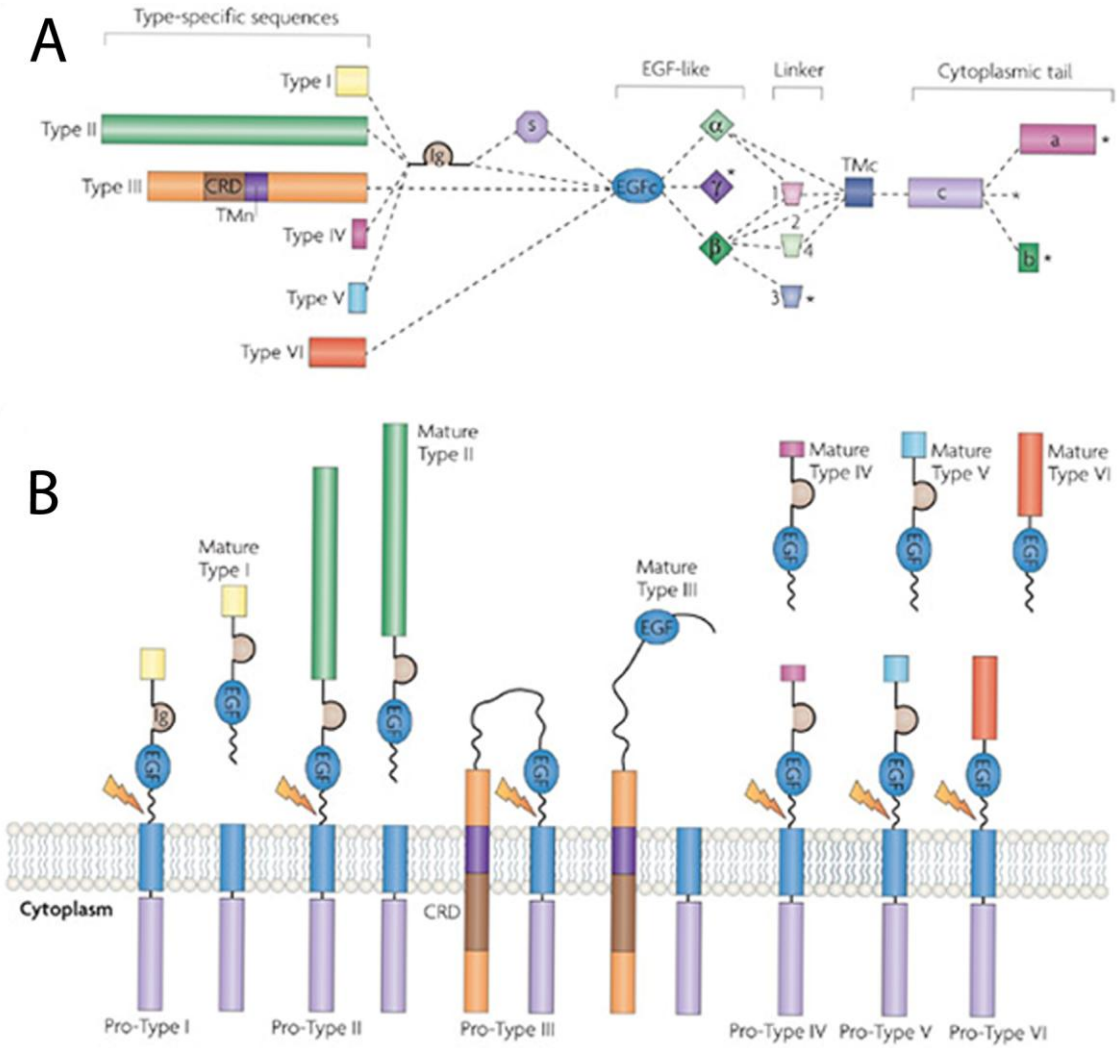

Figure 3. Schematic representation of the six types of neuregulin-1 (NRG1) isoforms (Mei and Xiong, 2008).

A. NRG1 isoforms are classified according to their distinct N-terminal sequences. An EGF-like domain is present in all isoforms. Types I, II, IV and V have an Ig-like domain between the N-terminal sequence and the EGF domain, whereas the N-terminal region of Types III and VI is directly connected to the EGF domain. A signal peptide and a kringle-like domain are present in Type II isoform. In Type III isoform, the specific N-terminal sequence contains a unique cysteine-rich domain (CRD) that has a transmembrane domain (TMn).

B. Proteolytic cleavage generates mature NRG1s as paracrine signals that are soluble, with the exception of Type III NRG1, which remains tethered through its CRD and functions in a manner that requires cell contact. The processing of Type IV, Type V and Type VI pro-NRG1s is less well characterized.

The ADAMs family

Metalloproteases ADAM10, ADAM17 (also known as TACE) and ADAM19 (meltrin-β) function as α-secretases for NRG1 processing (Blobel, 2005; La Marca et al., 2011; Luo et al., 2011; Shirakabe et al., 2001). Mouse mutants deficient for these ADAM proteins have been studied. Despite active participation in NRG1 cleavage, altered expression of ADAM10 in mice does not influence myelination (Freese et al., 2009). Consistently, myelination is unaffected by inhibition or knockdown of ADAM10 expression *in vitro* (Jangouk et al., 2009; Luo et al., 2011). Mice deficient for ADAM19 also myelinate normally, but exhibit a delay in remyelination due to delayed activation of myelin-inducing transcription factor Krox20 and myelin-related proteins (Wakatsuki et al., 2009). Interestingly, conditional deletion of neuronal TACE (ADAM17) in mice results in hypermyelination and aberrant myelination of Remak fibers (La Marca et al., 2011). TACE regulates myelination by controlling the amount of active membrane-bound NRG1 type III, and is a negative regulator of peripheral myelination.

Another important member of the ADAM family implicated in myelination is ADAM22, which is expressed on the axon surface. Neuronal ADAM22 acts as a receptor and binds leucine-rich glioma-inactivated 4, Lgi4 expressed and secreted by Schwann cells in developing nerves to promote Schwann cell differentiation (Ozkaynak et al., 2010). Mutation of Lgi4 in claw paw mice leads to retention of Lgi4 mutant protein within Schwann cells, which contributes to delayed axonal sorting and the hypomyelinating phenotype of claw paw mice (Bermingham et al., 2006). Similarly, mice lacking ADAM22 also display hypomyelinated nerves (Sagane et al., 2005). However, since ADAM22 does not have a catalytic-site consensus sequence, and thus lacks metalloprotease activity, it is not likely to participate in NRG1 Type III processing (Yang et al., 2006). Recently, Ozkaynak et al. showed that NRG1 expressed on axonal membranes of ADAM22-deficient neurons normally activate downstream PI3K and ERK signaling pathways in Schwann cells *in vitro,* suggesting that ADAM22-Lgi4 is not required for NRG1 Type III activity (Ozkaynak et al., 2010).

BACE1

BACE1 is a type I transmembrane aspartyl protease, known for processing amyloid precursor protein for the generation of amyloid-β peptide in Alzheimer's disease and its expression is preferentially enriched in neurons. Mice lacking BACE1 accumulate unprocessed NRG1 in the brain. These animals display hypomyelination of peripheral nerves and abnormal axonal segregation of sensory axons (Hu et al., 2008; Willem et al., 2006), reminiscent of defects in mice haploinsufficent for NRG1 Type III or lacking Schwann cell-specific ErbB2 receptor (Michailov et al., 2004; Woldeyesus et al., 1999). Moreover, *in vitro* inhibition of BACE1 activity reduces or delays myelination in Schwann cell-DRG co-cultures (Luo et al., 2011). Nevertheless, BACE1 processing is not required for NRG1 Type III-stimulated myelination since overexpression of neuronal full-length NRG1 type III in BACE1-null mutants causes hypermyelination, suggesting that NRG1 type III can function normally even in the absence of BACE1 (Velanac et al., 2011).

Recently, the cleavage sites of NRG1 Type I and III by ADAM10 and BACE1 have been identified. ADAM10 processes NRG1 at a distinct but adjacent site to that of BACE1. Cleavage of NRG1 by BACE1 and ADAMs mediate differential effects on myelination (Luo et al., 2011).

1.1.5.1b- Regulation of Schwann cell myelination by NRG1 signaling

NRG1 levels determine whether axons are ensheathed or myelinated

Studies on the function of NRG1 on the ensheathment fate of axons by Taveggia et al. suggest that the amount of NRG1 type III on the axon surface, rather than axon size, instructs whether the axon is to be myelinated. Small caliber axons such as sympathetic neurons of the superior cervical ganglia (SCG) are not myelinated due to low expression levels of NRG1. Conversely, large caliber axons such as BDNF- and NT3-dependent neurons from the DRG, express high levels of NRG1 and are heavily myelinated (Taveggia et al., 2005). Mouse DRG neurons lacking NRG1 Type III co-cultured with Schwann cells are poorly ensheathed, incompletely sorted, and fail to be myelinated. Myelin proteins, P_0 and MBP or myelin-related transcription factors, such as Oct-6 are not expressed in the co-cultures. In addition, mice haploinsufficient for NRG1 Type III have a higher proportion of unmyelinated fibers. Forced

expression of NRG1 Type III in normally unmyelinated SCG neurons promotes myelination of these small caliber axons. These findings suggest that whether Schwann cells myelinate is dependent upon the threshold levels of NRG1 Type III on the axon surface (Fig. 4) (Taveggia et al., 2005).

NRG1 regulates myelin sheath thickness

The optimal myelin sheath thickness determined by the *g*-ratio (the ratio of axon diameter to fiber diameter of a myelinated axon) is approximately 0.68 in peripheral axons in most vertebrates. In general, the thickness of myelin changes according to the diameter of the axon: larger axons have thicker myelin sheath and vice versa (Nave and Salzer, 2006). Achieving optimal myelin thickness is essential for rapid action potential propagation. The correct number of myelin wraps produced by Schwann cells is quantitatively controlled by the amount of membrane-bound NRG1 Type III on the axon surface. Axons from NRG1 Type III heterozygous mouse mutants, which contain about half of the normal levels of NRG1, are hypomyelinated and conduct considerably more slowly than normal mice (Michailov et al., 2004; Taveggia et al., 2005).

Similarly, mice mutant for Schwann cell-specific ErbB2 or ErbB3, and mice that express a dominant-negative ErbB receptor in Schwann cells suffer from hypomyelination (Chen et al., 2006; Garratt et al., 2000b). However, NRG1 appears to be the limiting factor in determining myelin thickness. The amounts of ErbB receptors on Schwann cells appear saturated since mice heterozygous for the ErbB2 receptor make normal myelin (Michailov et al., 2004). On the contrary, transgenic overexpression of NRG1 Type III, but not Type I, in postnatal motor neurons and DRG neurons in mice results in hypermyelination with a striking increase in the number of myelin wraps in axons, suggesting that NRG1 Type III is a critical regulator of myelin thickness (Fig. 4) (Michailov et al., 2004).

The NRG1-ErbB receptor system may regulate myelin thickness by stimulating Schwann cell cholesterol biosynthesis. *In vitro*, cholesterol depletion activates ErbB receptors, which may function as a sensing mechanism for plasma membrane cholesterol levels. Expression of recombinant NRG1 in cultured Schwann cells enhances the transcription of the 3-hydroxy-3-methylglutarylcoenzyme A reductase, the rate-limiting enzyme for cholesterol biosynthesis (Pertusa et al., 2007).

Addition of exogenous cholesterol into Schwann cell-DRG cocultures accelerates myelination. Moreover, mice lacking cholesterol biosynthesis in Schwann cells show severe hypomyelination in peripheral nerves (Saher et al., 2009).

The extent of myelin production may also be determined by other signaling mechanisms, for example BDNF and receptor $P75^{NTR}$. Axon size and myelin thickness in transgenic mice overexpressing BDNF are both increased but the level of enhanced myelination exceeds the overall increase in axon caliber, resulting in a reduction in the *g*-ratio of myelinated fibers (Tolwani et al., 2004).

NRG1 signaling in myelin sheath maintenance

Although NRG1 is crucial in many stages of Schwann cell development and myelination, it appears that NRG1/ErbB signaling is dispensable for myelin sheath maintenance. This is supported by *in vivo* analysis of mice deficient of Nrg1/ErbB signaling in adult myelinating glia. When the ErbB2 receptor gene is ablated in adult myelinating Schwann cells, the myelin sheath remains normal (Atanasoski et al., 2006). Similarly, tamoxifen-inducible conditional inactivation of NRG1 in the adult nerve also does not alter the myelin sheath (Fricker et al., 2011). However, NRG1 signaling may be important for remyelination in injury. NRG1 deletion in the adult nerves results in hypomyelination or lack of remyelination of axons after sciatic nerve crush, and hence a slow regeneration rate of axons (Fricker et al., 2011).

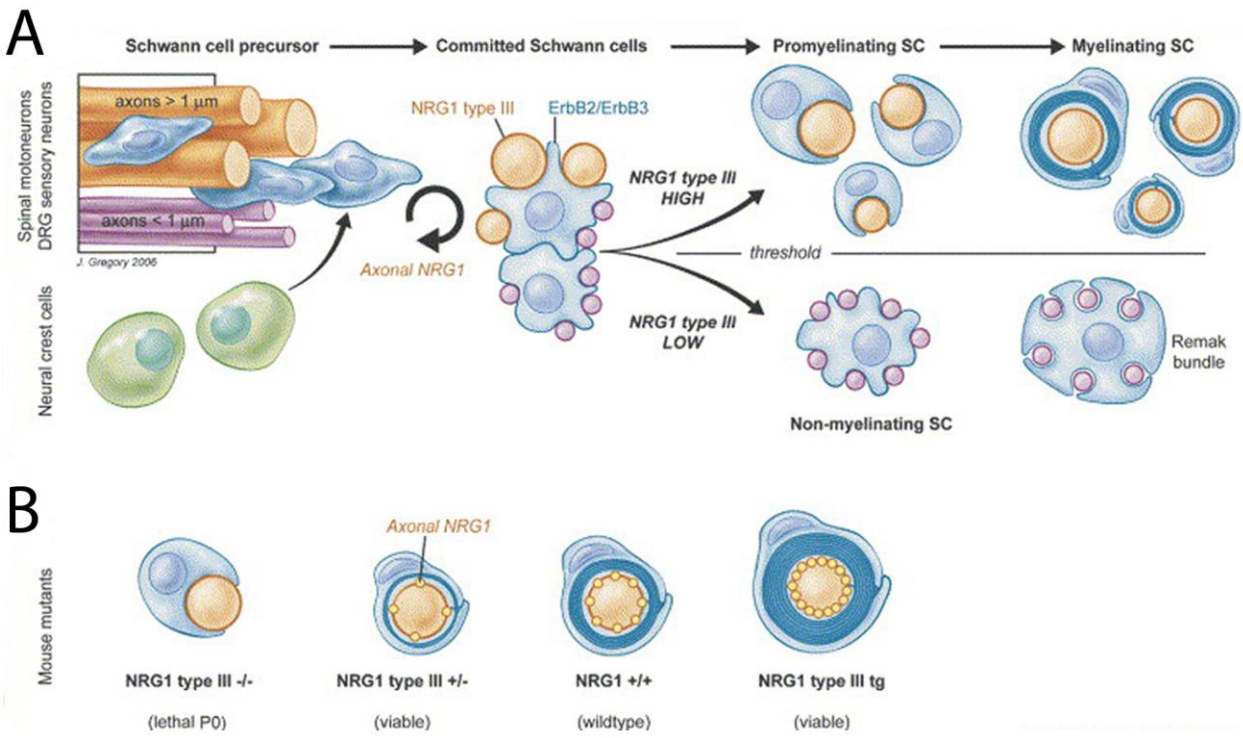

Figure 4. Regulation of Schwann cell development and myelination by axonal NRG1.

A. Schwann cells (in blue) are derived from neural crest precursor cells (in green) and interact with both large and small diameter axons of spinal motor and sensory neurons. NRG1 on the axon regulates Schwann cell development by interacting with ErbB2/3 receptors on the Schwann cell and activating downstream signaling cascades. The amount of NRG1 type III on the axon detected by Schwann cells, which is a function of axon size and NRG1 levels, then instructs them either into segregating single axons and myelination (top), or into a non-myelinating phenotype and formation of a Remak bundle (bottom). NRG1 type III signals axon size to myelinating Schwann cells to regulate the thickness of the myelin sheath.

B. In NRG1-null mice, in heterozygous NRG1 (+/−) mice, and in transgenic NRG1 overexpressing mice, instead of varying according to axon size, the amount of myelin made by Schwann cells changes directly as a function of axonal NRG1 type III levels (indicated by yellow dots). Modified from (Nave and Salzer, 2006).

1.1.5.1c- NRG1/ErbB signal transduction in Schwann cells

NRG1/ErbB signaling promotes survival, proliferation and differentiation of Schwann cell precursors, as well as their migration along the axon. At later developmental stages, NRG1/ErbB2/3 signaling also regulates myelination (Newbern and Birchmeier, 2010) One important question is how can the same receptor heterodimer and ligand (NRG1 via ErbB2/3) regulate specific cellular processes at distinct stages of Schwann cell development in a temporal and spatial manner.

Following NRG1 binding, heteromeric ErbB2/3 receptors mediate their effects on Schwann cell development through activation of multiple downstream signaling cascades, including Phosphatidylinositol-3-Kinase (PI3K)/AKT, Ras/Extracellular Signal Regulated Kinase 1/2 (ERK 1/2), FAK and Rac1/cdc42, and the regulation of calcium-dependent Protein Kinase C (PKC) for calcineurin/NFAT activation (Newbern and Birchmeier, 2010).

The PI3K/ AKT signaling pathway

Binding of NRG1 Type III to ErbB receptors activates the PI3K/AKT signaling pathway (Taveggia et al., 2005) that is indispensable for cellular responses including survival, proliferation and differentiation. Inhibition of PI3K/AKT signaling components pharmacologically in Schwann cells prevents NRG1-evoked Schwann cell survival and proliferation, and subsequently myelination induced by axonal NRG1 (GGF) and neurites (Maurel and Salzer, 2000). Selective activation of the PI3K pathway *in vitro* enhances Schwann cell differentiation and promotes myelin sheath formation (Ogata et al., 2004). Surprisingly, constitutive activation of AKT in Schwann cells *in vivo* does not alter peripheral myelination (Flores et al., 2008).

Enforced PI3K signaling in Schwann cells by conditional ablation of the negative regulator, PTEN (phosphatase and tensin homolog deleted on chromosome 10) results in increased myelin thickness for small caliber axons and focal hypermyelination in the form of myelin foldings and tomacula (Goebbels et al., 2010). Interaction of mammalian disc-large Dlg1 and PTEN has been suggested to act as a myelination brake to prevent peripheral nerve overmyelination via the PI3K/AKT signaling pathway (Cotter et al., 2010).

The calcineurin-NFAT signaling pathway

Another way in which NRG1/ErbB2/3 signaling is likely to regulate myelination independently of PI3K is by increasing Ca^{2+} levels in Schwann cells, which activates calcineurin/NFAT signaling. Specific deletion of calcineurin B1 subunit in the neural crest leads to severe defects in myelination but does not affect Schwann cell development (Kao et al., 2009). Exposure of NRG1 to Schwann cell precursors *in vitro* increases cytoplasmic Ca^{2+} for activation of phosphatase calcineurin, which dephosphorylates and activates the transcription factors NFATc3 and c4, promoting their nuclear translocation. Kao et al. showed that NFAT complexes with the transcription factor Sox10 in the nucleus to activate Krox-20, which globally regulates genes essential for myelination.

The Ras/ERK1/2 signaling pathway

Previous studies have shown that activation of the ERK1/2 pathway in Schwann cells *in vitro* suppresses Schwann cell differentiation by opposing PI3K/AKT activity (Maurel and Salzer, 2000; Ogata et al., 2004). Some evidence also shows that high doses of exogenously added soluble NRG1 Type II or III to Schwann cells suppresses myelination mediated via MEK/ERK activation (Syed et al., 2010), rendering ERK1/2 signaling as a negative regulator of Schwann cell myelination (Harrisingh et al., 2004; Maurel and Salzer, 2000; Ogata et al., 2004). However, recent genetic evidence based on conditional inactivation of ERK1/2 in the neural crest has revealed important functions of ERK1/2 in Schwann cell development and myelination. Specific ablation of ERK1/2 in the neural crest results in peripheral nerves lacking SCPs and subsequently axon defasciculation, loss of peripheral projections and sensory neuron death. SCP-specific inactivation of ERK1/2 inhibits differentiation and myelination, leading to hypomyelination (Newbern et al., 2011). Moreover, absence of ERK1/2 in glial progenitors blocks NRG1-induced survival *in vitro*. These data highlight the importance of ERK1/2 in transducing NRG1/ErbB signals.

A key activator and regulator of NRG1/ErbB-mediated signaling of Ras/ERK1/2 pathway is protein tyrosine phosphatase Shp2 (Grossmann et al., 2009). A Schwann cell-specific Shp2 mutation inhibits sustained ERK1/2 activation, but not PI3K/AKT activity. Conditional deletion of Shp2 in neural crest cells and in

myelinating Schwann cells results in severe perturbations in Schwann cell development, including peripheral nerves devoid of SCPs and marked hypomyelination of axons, respectively. The deficits in myelination are similar to the phenotypic changes seen in NRG1 or ErbB2/3 mutant mice (Grossmann et al., 2009). Therefore, the ERK1/2 pathway acts downstream of NRG1 signaling and can positively regulate myelination.

The FAK signaling

Focal adhesion kinase (FAK) acts downstream of NRG1/ErbB signaling. It has been shown that FAK is rapidly induced to bind to the Schwann cell ErbB2/ErbB3 complex upon NRG1 stimulation *in vitro* (Vartanian et al., 2000). In cultured Shp2-mutant Schwann cells, activity of FAK and Src, which phosphorylates FAK, is dramatically reduced in response to NRG1. Similar to decreased FAK activity seen in Schwann cell-specific ErbB2 mutants, activated FAK is also reduced in mice with a specific Shp2 mutation in myelinating Schwann cells (Grossmann et al., 2009). Specific ablation of FAK in Schwann cells severely impairs myelination, which is essentially caused by decreased proliferation, but not reduced process extension associated with radial sorting (Grove et al., 2007).

1.1.5.2 Notch signaling

The recent discovery of several neuronal signals has provided insights on other signaling cascades that may modulate the outcome of NRG1/ErbB signaling in Schwann cells. Other mechanisms involved in cooperatively regulating Schwann cell development and myelination with NRG1 signaling include Notch, Gpr126 and laminin/integrin (reviewed in section 1.2) signaling cascades (Fig. 5).

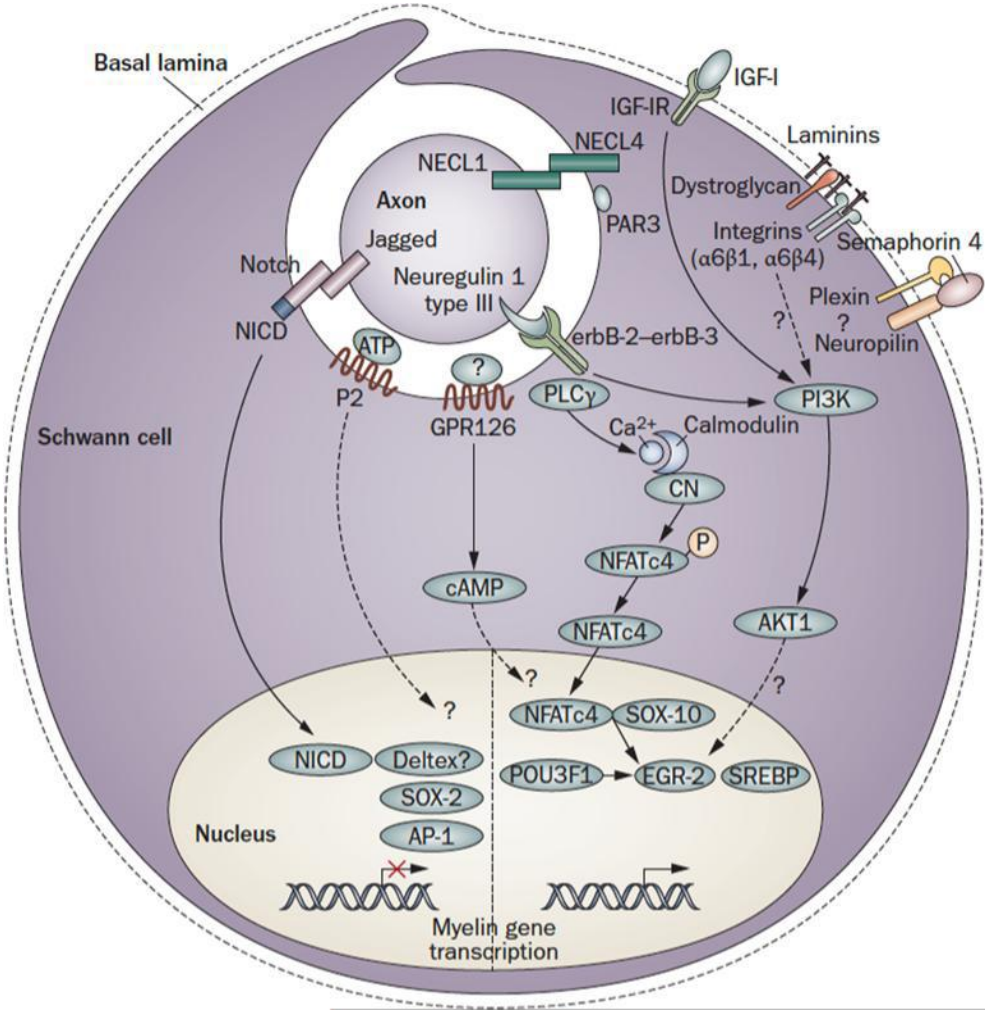

Figure 5. Diagram showing the main signaling pathways that regulate Schwann cell myelination.

The figure shows a promyelinating Schwann cell. The pathways illustrated are not comprehensive, but focus on signaling that converges on the nucleus. Dashed lines indicate signals with uncertain targets. Major signaling pathways regulating PNS myelination are described in sections 1.1.5.1-3. Figure from (Taveggia et al., 2010).

The Notch signaling is known for mediating cell-cell signaling between neighboring cells. Single-pass transmembrane Notch receptors interact with ligands that belong to the Delta and Jagged gene families. Upon ligand binding, cleavage of Notch releases from the plasma membrane the active intracellular domain of Notch (NICD), which translocates to the nucleus and complexes with other proteins to promote transcription of target genes. In addition, active NICD may also act through cytoplasmic Deltex but pathways are yet to be identified (D'Souza et al., 2008). In the PNS, Notch has been shown to suppress the neuronal lineage and hence promote glial differentiation from neural crest cells but its role in gliogenesis is still unclear (Kubu et al., 2002; Morrison et al., 2000).

Recently, Woodhoo et. al showed that Notch signaling regulates multiple stages of Schwann cell progression during development (Woodhoo et al., 2009). In the study, the authors demonstrated that Notch promotes SCP differentiation to immature Schwann cells via canonical signaling by maintaining elevated levels of ErbB2 receptors in SCPs. As a consequence, NRG1 signaling is enhanced, which promotes SCP survival and likely stimulates differentiation. In addition, Notch also accelerates Schwann cell formation and proliferation. In contrast to the stimulating effects of myelination by NRG1 signaling in perinatal nerves, Notch inhibits myelination by opposing the positive myelination regulator Krox-20 through non-canonical pathways independent of RBPJ effects. In adult injured nerves, it also induces demyelination and dedifferentiation of myelinating Schwann cells (Woodhoo et al., 2009).

1.1.5.3 Gpr126-cAMP signaling

Myelination is initiated by Schwann cell-axon contact. NRG1 and cyclic adenosine monophosphate (cAMP) are both essential myelin-related signals. Elevation of cAMP in Schwann cells drives myelin sheath formation (Morgan et al., 1991). *In vitro*, cAMP can mimic the effects of axonal contact in regulating the expression of transcription factors such as Oct-6 and Krox-20 necessary for induction of myelination (Monuki et al., 1989; Scherer et al., 1994). Monk et al. have recently identified a major role of an orphan G-protein coupled receptor Gpr126 in regulating cAMP levels required for initiation of myelination in zebrafish. In the absence of Gpr126 in zebrafish, axons are sorted normally but Schwann cell development is

arrested at the promyelinating state. Interestingly, this Schwann cell surface receptor induces the elevation of cAMP levels at the onset of myelination, and hence activates Oct-6 and Krox-20 expression. Treatment with forskolin that raises cAMP levels restores myelin protein MBP expression and myelination in Gpr126 fish mutants. Gpr126 expression and function does not depend on NRG1/ErbB signaling since NRG1 Type III and ErbB3 expression in Gpr126 mutants is not altered (Monk et al., 2009).

Mice lacking Gpr126 display severe hypomyelination and reduced expression of myelin markers. In addition to the myelin phenotype, Gpr126-null nerves also show delayed radial axonal sorting by Schwann cells and absence of Remak bundles. Failure of $Gpr126^{-/-}$ Schwann cells in providing trophic support to associated axons leads to a reduction in axon number in postnatal sciatic nerves. Moreover, absence of Gpr126 causes abnormal organization of the perineurium and ectopic fibroblast formation in the endoneurium (Monk et al., 2011).

Interestingly, NRG1 signaling synergizes with the cAMP pathway to drive myelination in cultured mouse Schwann cells (Arthur-Farraj et al., 2011). Elevated cAMP levels and the presence of NRG1 are required to synergistically trigger the expression of myelin-associated markers Krox-20 and P_0. Neither cAMP nor NRG1 alone is sufficient to induce myelin protein expression in mouse Schwann cells. NRG1 promotes cAMP-dependent myelin differentiation. cAMP levels determine the outcome of NRG1 signaling, whether it is to induce proliferation or differentiation of Schwann cells (Arthur-Farraj et al., 2011).

1.1.6 TRANSCRIPTIONAL CONTROL OF MYELINATION

1.1.6.1 Positive transcriptional regulators of myelination

A number of cell-intrinsic factors in Schwann cells that drive myelination have been identified, which include transcription factors Tst-1/SCIP/Oct-6 and Brn2, Krox-20/Egr2, Sox10, NFκB, YY1 and NFAT (He et al., 2010; Jessen and Mirsky, 2008; Kao et al., 2009; Svaren and Meijer, 2008).

1.1.6.1a- Oct-6

The POU homeo-domain transcription factors Tst-1/SCIP/Oct-6 and, to a lesser extent, Brn2 are important regulators for the transition of Schwann cells from the promyelinating stage to the myelinating stage (Bermingham et al., 1996; Jaegle et al., 2003; Jaegle et al., 1996). In the absence of Tst-1/SCIP/Oct-6, Schwann cell differentiation is transiently retarded at the promyelinating stage. By P8, more than 80% of wild-type Schwann cells have started elaborating a myelin sheath around axons. However it takes nearly 4 weeks for the same number of Schwann cells lacking Oct-6 to enter the myelinating phase, although once this stage is achieved, myelination appears to proceed as normal (Jaegle et al., 1996). The levels of P_0 and MBP mRNAs in mice deficient of Oct-6 remain normal (Bermingham et al., 1996), indicating that Oct-6 is not required to regulate these genes. Mice lacking both Brn2 and Oct-6 exhibit a more severe hypomyelinating phenotype. In these mice, promyelinating Schwann cells are still detected in adult nerves up to 4 months old. These data suggest that Oct-6 and Brn2 are essential for the correct timing of myelination (Jaegle et al., 2003).

In vitro, Oct-6 is strongly induced by the elevation of cAMP in Schwann cells, via the activation of protein kinase A (PKA). PKA phosphorylates immediate downstream targets including cAMP response element binding protein, Crebp and nuclear factor-kappaB, NFκB (Svaren and Meijer, 2008).

1.1.6.1b- Sox10

SRY-related HMG box (SOX) family member Sox10, expressed in multiple consecutive stages of the Schwann cell lineage, plays a key role in Schwann cell fate specification and is crucial throughout the myelination process. Mutations in the transcription factor Sox10 cause Waardenburg syndrome, Hirschsprung disease and

peripheral neuropathies in humans (Inoue et al., 2004). This is partly due to the essential role of Sox10 in neural crest cells for survival and cell lineage specification. Recently, the role of Sox10 in immature Schwann cells and in adult nerves has been deciphered. Immature Schwann cells lacking Sox10 fail to transform into non-myelinating and myelinating cells, and results in thinned and unsorted peripheral nerve axon bundles (Finzsch et al., 2010). Furthermore, the persistent expression of Sox10 in adult nerves is important for myelin sheath maintenance. Tamoxifen-inducible conditional ablation of Sox10 in adult Schwann cells results in demyelination, axon degeneration and neuroinflammation (Bremer et al., 2011).

Early embryonic expression of the *Mpz/P_0* gene requires binding of Sox10 to multiple response elements in its promoter (Peirano et al., 2000). Subsequent induction of *P_0* expression in myelinating cells also depends on Sox10 binding (Schreiner et al., 2007). Sox10 is required for activating Oct-6 expression in immature Schwann cells. Dimeric binding of Sox10 to the Oct-6 Schwann cell enhancer element drives Oct-6 expression in Schwann cells (Jagalur et al., 2011). As a result of Oct-6 activation, Sox10 and Oct-6 synergistically activate the expression of an immediate target, zinc finger transcription factor Krox-20/Egr2 (Svaren and Meijer, 2008).

1.1.6.1c- Krox-20

Krox-20, activated by both Sox10 and Oct-6, is required for normal development of myelinating Schwann cells. Unlike the transient arrest of Schwann cells at the promyelinating stage in Oct-6-deficient mutants, Schwann cell-specific inactivation of Krox-20 causes a differentiation block arresting Schwann cells permanently at a promyelinating phase. Krox-20-null Schwann cells normally form a 1:1 relationship with axons, but wrap only one and a half turns of myelin around the axon. Krox20-null Schwann cells also fail to express mature myelin proteins such as P_0 and MBP, although they express the early myelin marker, myelin-associated glycoprotein (MAG) (Topilko et al., 1994). The temporal profiles of the expression of Oct-6 and Krox-20 are different. Expression of Oct-6, induced by axonal contact, peaks in promyelinating Schwann cells around birth when myelination is initiated, and is downregulated as myelination progresses in the sciatic nerve; whereas Krox-20 expression is evident approximately 24-36 hours after Oct-6 appearance, parallels

other myelin-related genes and persists in mature myelinating Schwann cells (Blanchard et al., 1996; Jaegle and Meijer, 1998; Monuki et al., 1989; Zorick et al., 1996b). Krox-20 may repress Oct-6 expression since Oct-6 expression is sustained in Krox20-null mice (Zorick et al., 1999).

Sustained expression of Krox-20 in adult nerves is required for maintaining the peripheral myelin sheath. Demyelination and Schwann cell dedifferentiation results when Krox-20 is removed from adult Schwann cells (Decker et al., 2006). In humans, mutations in the *Krox-20/Egr2* gene lead to various human hereditary peripheral neuropathies including Charcot Marie Tooth disease and Dejerine-Sottas Syndrome (Suter and Scherer, 2003).

An upstream regulator of Krox-20 expression in response to NRG1 signaling is the zinc finger protein Yin Yang 1 (YY1). Schwann cell-specific YY1-null mice display severe hypomyelination. Schwann cells lacking YY1 express reduced levels of Krox-20 and myelin markers, and fail to activate Krox-20 upon exposure to NRG1 *in vitro*. YY1 activation upregulates Krox-20 expression, which initiates expression of myelin-related genes (He et al., 2010).

Analyses of myelin gene expression regulated by Krox-20 in primary Schwann cells and in mice with a hypomorphic Krox-20/Egr2 allele (Egr2Lo) have identified myelin genes including *Mpz/P_0, Pmp22, Periaxin (Prx), Connexin 32* and *Mag* (Le et al., 2005; Nagarajan et al., 2001). Importantly, convergent regulation by both Sox10 and Krox-20 is essential for activation of the myelination program in Schwann cells. The promoters of these myelin-related genes contain binding sites for both Krox-20 and Sox10, and myelin gene expression depends on activation by both Krox-20 and Sox10 (Svaren and Meijer, 2008). Regulatory elements in regions other than the promoter that control myelin gene expression have also been described. For example, Krox-20 and Sox10 act synergistically to activate a conserved composite module within the first intron of the *Mpz/P_0* gene comprising binding sites for both Sox10 and Krox-20 to regulate *Mpz/P_0* expression. This conserved element has also been identified in other major myelin genes (Jones et al., 2007; LeBlanc et al., 2006; LeBlanc et al., 2007).

1.1.6.1d- Nuclear factor κB (NFκB)

Transcription factor nuclear factor κB (NFκB), which functions as a downstream mediator of cAMP signaling, is crucial for activation of Oct-6 and myelination. Specifically, phosphorylation of the p65 subunit of NFκB by cAMP-dependent PKA activates NFκB during myelin formation. Inhibition of PKA-mediated NFκB transcriptional activation attenuates Schwann cell differentiation and myelin formation in response to elevated cAMP or in DRG cocultures (Yoon et al., 2008). The same group also identified that axonal NRG1 Type III, signalled through its cognate receptor ErbB2/3, regulates NFκB transcriptional activation during myelination in addition to cAMP. Furthermore, co-stimulation by both NRG1 Type III and cAMP considerably augments NFκB activation in Schwann cells (Limpert and Carter, 2010).

1.1.6.2 Negative transcriptional regulators of myelination

Myelinating Schwann cells display remarkable plasticity throughout life. In injured nerves or in demyelinating neuropathies, Schwann cells dedifferentiate into the immature-like phenotype and proliferate. Myelin protein expression is downregulated and expression of non-myelin markers is induced. Various signaling pathways that inhibit myelin differentiation must be suppressed to allow myelination. These pathways are activated in injury conditions. Among these negative regulatory pathways are transcription factors that act to oppose myelin formation (Jessen and Mirsky, 2008).

1.1.6.2a- c-jun

c-Jun is a basic leucine zipper transcription factor and a key component of the AP-1 transcription factor complex. c-Jun is constitutively expressed in cultured Schwann cells from perinatal nerves and promotes proliferation prior to the onset of myelination (Monuki et al., 1989; Parkinson et al., 2004). Its expression is suppressed by Krox-20 at the start of myelination. In hypomyelinating Krox-20-deficient mice, c-Jun expression is sustained (Parkinson et al., 2004). Persistent expression of c-Jun has been shown to abolish Krox-20 expression in response to cAMP elevation, and to inhibit Krox-20-mediated induction of myelin proteins P_0 and Periaxin expression in cultured Schwann cells. Conversely, conditional

inactivation of c-Jun in Schwann cells promotes myelin gene expression (Parkinson et al., 2008).

After injury c-Jun is potently induced and antagonizes Krox-20 expression in Schwann cells to promote conversion of a myelinating to promyelinating phenotype (Parkinson et al., 2008). Since Krox-20 downregulation in adult nerves results in myelin degradation (Decker et al., 2006), c-Jun may promote dedifferentiation and trigger myelin sheath breakdown by suppressing Krox-20 activity. In the absence of c-Jun, Schwann cell dedifferentiation and myelin breakdown is considerably delayed after nerve transection, suggesting that c-Jun actively drives Schwann cell dedifferentiation during injury (Parkinson et al., 2008). Interestingly, c-Jun acts in conjunction with the transcription factor Sox2, which inhibits myelination (Le et al., 2005). Sox2 is co-expressed with c-Jun in immature Schwann cells, suppressed in myelination and reexpressed during injury. *In vitro,* enforced Krox20 expression or upregulation of cAMP inhibits Sox2 (Parkinson et al., 2008).

1.1.6.2b- Other negative myelin transcription factors

Other negative transcription factors of myelination include Pax-3, Id2, Krox-24 and Egr3. Their expression resembles that of major negative myelination regulators such as c-Jun. They are expressed in immature Schwann cells and/or mature non-myelinating Schwann cells, but are downregulated in the myelinating phenotype. Upon injury, their expression is rapidly upregulated (Jessen and Mirsky, 2008).

1.1.6.3 Epigenetic regulation of myelination

Schwann cell myelination is also dependent on epigenetic regulation of myelin gene transcription by histone deacetylases HDAC1 and 2 (Chen et al., 2011; Jacob et al., 2011). Recent studies suggest that HDACs may orchestrate concerted expression of myelin-specific transcription factors, and hence myelin gene expression. Selective ablation of HDAC1 or HDAC2 in Schwann cell precursors does not affect Schwann cell development or myelination, indicating compensatory mechanisms between the functions of the two HDACs. However, deletion of both HDAC1 and HDAC2 results in defects in radial axonal sorting. Large caliber axons that are segregated fail to be myelinated. Disruption of myelination induction is correlated with a remarkable loss of Schwann cells after birth. Expression of Sox10 and Krox-20 is reduced, but Oct-6 is markedly increased. There is also a reduction in the expression of the myelin

proteins, MAG, MBP and P_0. Interestingly, overexpression of HDAC2, but not HDAC1, upregulates expression of myelin genes (Chen et al., 2011; Jacob et al., 2011). HDACs associate with Wnt signaling mediator β-catenin to regulate Schwann cell survival (Jacob et al., 2011). HDACs also interact with the Sox10 promotor region, and NFκB is a crucial intermediate in Sox10 activity regulation. In the absence of HDAC1 and HDAC2 in Schwann cells, the p65 subunit of NF-κB is heavily acetylated, resulting in suppression of mRNA expression of positive myelin regulators and induction of differentiation inhibitors such as Id2 and Id4 (Chen et al., 2011).

1.2 REGULATION OF SCHWANN CELL FUNCTION BY THE EXTRACELLULAR MATRIX

The importance of interactions between Schwann cells and axons for correct myelination in the developing PNS has been described in the previous section. Across the compact myelin sheath, the communication between the abaxonal Schwann cell plasma membrane with the extracellular matrix is equally essential for controlling the process of ensheathment and radial sorting, and modulating myelination. These secreted extracellular molecules may regulate Schwann cell myelination independently of, or in conjunction with axon-derived signals, such as NRG1 (Mirsky et al., 2008).

1.2.1 SCHWANN CELL POLARIZATION

The myelin sheath must achieve the optimal thickness and length for maximal nerve conduction efficiency. Up until now, how the radial and longitudinal extension of the myelin sheath is controlled is only partially understood.

An important feature of differentiated cells is cell polarization, which is a process of organizing membrane components and cytoskeletal structures in different parts of the cell, establishing distinct membrane domains. A simple system for cell polarization is seen in epithelial cells, which are polarized along an apical-basal axis. Epithelial polarization involves formation of cell-cell contact followed by establishment of cellular junctions and segregation of apico-basolateral membrane domains (Drubin and Nelson, 1996).

The Bunge group proposed that Schwann cells resemble epithelia in that they separate Schwann cell-axon units from mesenchymal tissues by forming a basal lamina (Bunge and Bunge, 1983). Schwann cells are highly polarized, with the outer abaxonal membrane domain apposing the basal lamina characterized as a basolateral-like domain, and the inner adaxonal surface contacting the axon and Schmidt-Lanterman incisures as an apical-like domain (Ozcelik et al., 2010). Moreover, myelin-forming Schwann cells develop a more complex geometric organization than epithelia with distinct subcellular domains asymmetrically organized on the radial and longitudinal axes (Salzer, 2003).

Radial polarity in a myelinating Schwann cell includes the adaxonal membrane of the Schwann cell adjacent to the axon, which harbors adhesion

molecules that may mediate axo-glial interactions, such as MAG. Across the compact myelin sheath is the abaxonal surface of the Schwann cell surrounded by the basal lamina. This domain harbors ECM receptors including integrins and dystroglycan (Fig. 6A).

Longitudinal polarization of the Schwann cell involves the internodal elongation of the myelin sheath, which extends from one node to another (Salzer, 2003). Longitudinally, a Schwann cell-axon unit is organized into distinct domains each containing a specific subset of junctional proteins. The node of Ranvier is contacted by cytoplasmic extensions formed by the Schwann cell called microvilli. Immediately adjacent to the node are the paranodal loops, which form septate junctions with the axon. The juxtaparanodes separate the paranode from the internode (Fig. 6B) (Salzer et al., 2008). Compact myelin is composed of alternating apposed layers and contains myelin proteins such as P_0 and MBP. Junctional proteins that form adherens, tight and gap junctions are found in non-compact myelin. Connecting the Schwann cell cytoplasm at the outer and inner margins of the myelin internode are cytoplasmic channels known as Schmidt-Lanterman incisures (Salzer, 2003).

In addition, along the abaxonal surface of the myelinating Schwann cell internode, the Schwann cell cytoplasm is compartmentalized into specialized domains, called Cajal bands, which harbor different dystrophin-glycoprotein complexes (DGCs) that are believed to segregate the Schwann cell plasma membrane into appositions between the outer surface of the myelin sheath and the cytoplasmic face of the Schwann cell plasma membrane (Albrecht et al., 2008; Court et al., 2004). Cajal bands, named after their initial description by the Spanish neuroanatomist Santiago Ramon y Cajal are cytoplasmic channels traversing the internode (Court et al., 2004). Compartmentalization of the Schwann cell cytoplasm has been associated with internodal length regulation, although this still remains unclear (Fig. 7) (Court et al., 2009; Court et al., 2004; Court et al., 2011).

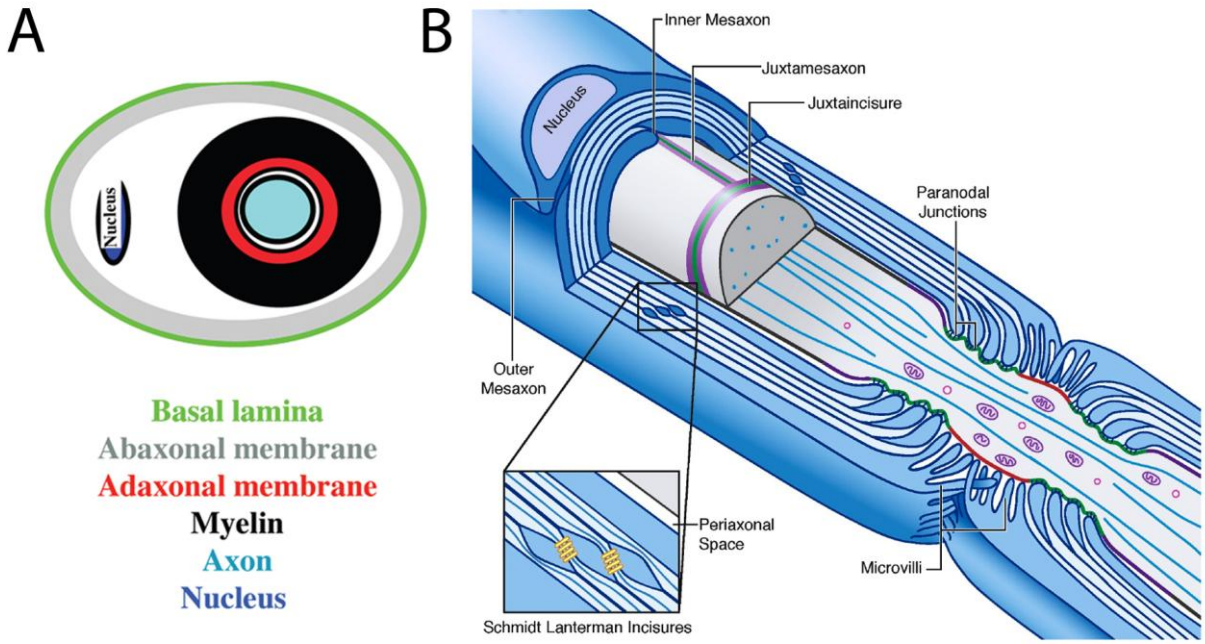

Figure 6. Polarized domains of a myelinated fiber.

A. Schematic representation of Schwann cell polarization on a radial axis. The adaxonal Schwann cell membrane contacts the axon, where the outer abaxonal membrane apposes the basal lamina. Between the abaxonal and adaxonal membranes of the Schwann cell is the compact myelin sheath. From (Berti et al., 2006).

B. The diagram depicts the longitudinal polarity of the Schwann cell. It illustrates a cross-section through a myelinated axon (gray) wrapped by myelin (blue). The node of Ranvier is shown in (red), to which Schwann cell microvilli project. The paranodal loops and junctions are in green. The juxtaparanodal region (purple) is separated from the node by the paranode. Schmidt-Lanterman incisures, which form tight junctions, are cytoplasmic channels that connect the outer and inner margins of the myelin internode. Modified from (Salzer, 2003).

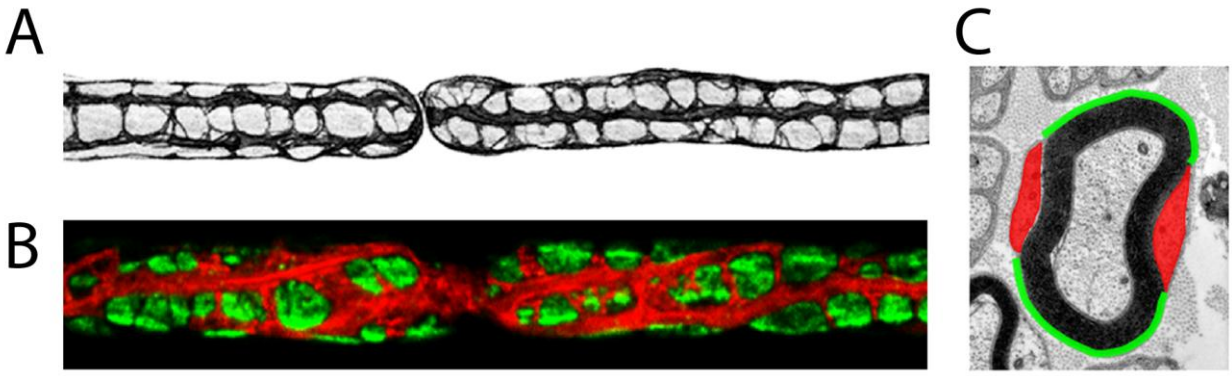

Figure 7. Compartmentalization of cytoplasm in the abaxonal region of the Schwann cell

A. Silver staining of a nerve fiber by Spanish neuroanatomist Santiago Ramón y Cajal (Ramón y Cajal, 1933) reveals Schwann cell cytoplasm as longitudinal bands (now known as Cajal bands) along the Schwann cell. These longitudinal domains are connected by transverse trabeculae.

B. Immunostaining of a teased fiber with an antibody against DRP2 (green) and fluorescent-conjugated phalloidin (red). DRP2-labeled regions denote appositions that are sites between the abaxonal Schwann cell membrane and the outermost layer of the myelin sheath, whereas phalloidin labeling reveals Schwann cell cytoplasmic domains termed Cajal bands. Note that Cajal bands are excluded from DRP2+ patches.

C. An electron micrograph of the transverse section of a myelinated fiber with appositions outlined in green and Cajal bands colored in red.

1.2.2 POLARITY PROTEINS REGULATE SCHWANN CELL MYELINATION

Epithelial-like cell polarity may allow proper establishment of the myelin sheath. Indeed, Par-3, a component of the Par polarity complex, accumulates at the adaxonal Schwann cell membrane contacting the axon, and plays a crucial role in initiation of myelination (Chan et al., 2006). Myelination is impaired when Par-3 localization is disrupted. Par-3, which complexes with Par-6 and atypical protein kinase C (aPKC), regulates myelination by interacting via its first PDZ domain with the neurotrophin receptor $p75^{NTR}$ that binds axonal BDNF, and recruiting the receptor to the axo-glial interface at the onset of myelination. Consequently, the targeting of $p75^{NTR}$ by the Par polarity complex ensures that Schwann cells efficiently respond to BDNF for activating signaling events that lead to myelin formation.

Par-3 is deacetylated by NAD+-dependent deacetylase Sir-two-homolog 2 (Sirt2), which in turn blocks aPKC activation. Par-3 deacetylation by Sirt2 temporally regulates the availability of the Par polarity complex for normal peripheral myelination (Beirowski et al., 2011). Similarly, adhesion molecules that mediate axo-glial interactions, such as nectin-like protein Necl-4 are found at the adaxonal membrane of the Schwann cell along the internode. Necl-4 is highly upregulated in premyelinating Schwann cells, and interacts with Necl-1 on the axonal surface to mediate axo-glial adhesion in the early stages of myelination (Maurel et al., 2007; Spiegel et al., 2007). *In vitro* knockdown of Necl-4 inhibits myelin formation. Disruption of the interaction between Necl-4 and Necl-1 also impairs myelination. Moreover, submembranous cytoskeletal proteins, spectrins (αII and βII) that are polarized at axon-glia contact sites in premyelinating Schwann cells, modulate myelination via regulation of actin cytoskeleton organization and Necl-mediated axon-glial interaction. *In vitro* silencing of spectrin reduces Necl-4 levels and disrupts the polarized localization of Necl-4 on the Schwann cell surface (Susuki et al., 2011).

Additionally, recent reports have identified the importance of other polarity proteins such as Pals1 and Dlg1 on the regulation of myelin assembly and production (Cotter et al., 2010; Ozcelik et al., 2010). Importantly, manipulation of these proteins affects the assembly of the myelin sheath, but does not result in Schwann cell

dysfunction. *In vivo* silencing of Pals1 in myelinating Schwann cells results in thinner myelin sheaths and formation of myelin infoldings in the sciatic nerve. The authors have also reported a defect in the longitudinal extension of the myelin sheath (Ozcelik et al., 2010). Dlg1 silencing affects the radial growth of myelin, resulting in overmyelination (Cotter et al., 2010).

1.2.3 INTERACTIONS BETWEEN SCHWANN CELLS AND THE EXTRACELLULAR MATRIX

The extracellular matrix (ECM) is composed of the basal lamina surrounding Schwann cells and endoneurial collagen. Basal lamina components typically include collagens, heparan sulfate proteoglycan, and non-collagenous glycoproteins, namely laminin, fibronectin, entactin (Bunge, 1993). It is a thin sheet of organized ECM as a three-layered structure, consisting of lamina fibroreticularis closest to the cell membrane, lamina lucida and lamina densa (Bunge and Bunge, 1983). Both non-myelinating and myelinating Schwann cells are enveloped by a basal lamina, which is in close association with the abaxonal Schwann cell membrane. Components of the ECM, such as laminins interact with their receptors, integrin and dystroglycan in the Schwann cell membrane (Feltri and Wrabetz, 2005). The interactions of Schwann cells with these extracellular modulators translate into intracellular signaling events that regulate many cellular responses including migration, proliferation and survival, differentiation and polarization. Schwann cell development and myelination depends on the interactions with ECM molecules such as laminins and collagens (Chernousov et al., 2008). Schwann cells require axonal contact for basal lamina assembly (Clark and Bunge, 1989), and a basal lamina, at least laminin signals, is necessary for Schwann cells to properly ensheathe and myelinate axons (Feltri and Wrabetz, 2005; Podratz et al., 2001).

1.2.3.1 Laminins and their functions

Laminins are heterotrimeric proteins formed by α-, β-, and γ-subunits. Five α-subunits, four β-subunits, and three γ-subunits have been identified so far, and 15 isoforms have been reported (Chernousov et al., 2008). Laminins are expressed in the CNS, PNS and the neuromuscular junction. In mature peripheral nerves, laminin-2 (α2β1γ1), the major isoform, and low levels of laminin-8 (α4β1γ1) are present in the endoneurium, whereas laminin-1 (α1β1γ1), -9 (α4β2γ1), and -11 (α5β2γ1) are

found in the basal lamina of perineurial cells (Feltri and Wrabetz, 2005). Both laminin-2 and laminin-10 (α5β1γ1) are abundant in the Schwann cell basal lamina surrounding nodes of Ranvier and paranodes (Occhi et al., 2005).

1.2.3.1a- Laminin-α2 chain

In humans and mice, mutations in the *Laminin-α2* gene, coding for the α2-laminin chain, cause congenital muscular dystrophy 1A, MDC1A, and the phenotype of the dystrophic (dy/dy and dy2J/dy2J) mouse. In the absence of laminin-α2 chain expression, mutant mice show hypomyelinated axons and defects in radial sorting in peripheral nerves characterized by the presence of naked axon bundles lacking ensheathment and remaining unmyelinated, most notable in spinal roots and proximal region of the nerve, but to a lesser extent in distal peripheral nerves (Bradley and Jenkison, 1973; Stirling, 1975). Schwann cells lacking laminin-α2 form patchy, discontinuous basal laminas both in roots and peripheral nerves (Madrid et al., 1975). Interestingly, in laminin-α2 mutant sciatic nerves, laminin-α1 is upregulated in the endoneurium (Previtali et al., 2003b). Schwann cells defective for laminin-α2 have shorter internodal lengths (Bradley and Jenkison, 1973; Court et al., 2009). These mutant mice have poorly formed microvilli, widened nodes of Ranvier and reduced sodium channel density (Occhi et al., 2005). Nerve conduction velocity is also reduced in mutant peripheral nerves (Rasminsky et al., 1978).

1.2.3.1b- Laminin-α4 chain

Mice lacking laminin-α4 chain, which forms laminin-8 in peripheral nerves, display a similar hypomyelinating phenotype as described in dy and dy2J mice (Wallquist et al., 2005; Yang et al., 2005). However, whereas laminin-α2 mutant nerves show more severe hypomyelination in spinal roots than distal nerves, laminin-α4 deficient nerves have normally myelinated roots, but more affected distal region of peripheral nerve (Yang et al., 2005). In addition, most small bundles of unsorted axons in laminin-α4 mutant nerves are 'myelinated' forming polyaxonal myelinated bundles, which are rarely seen in laminin-α2 dystrophic mice. Interestingly, unlike in laminin-α2 mutants, the composition and integrity of endoneurial basal lamina is not affected in the absence of laminin-α4. These differences may be attributed to compensatory mechanisms of other laminin isoforms. In the absence of both laminin-α2 and α4, mutant mice exhibit a more severe neuropathy with virtually complete amyelination

in distal nerves and a lack of basal lamina in both premyelinating and promyelinating Schwann cells, but paradoxically improved radial sorting in the spinal root (Yang et al., 2005). Laminin-α2 (laminin 2) and laminin-α4 (laminin 8) are required for Schwann cell proliferation during radial sorting. Moreover, transgenic expression of laminin-α5 chain of laminin-10 in the double knockouts rescues the sorting defect and promotes myelination (Yang et al., 2005). These results may indicate distinct roles of different laminin isoforms in various regions of the PNS during development.

1.2.3.1c- Laminin-γ1 chain

Schwann cells with specific disruption of laminin-γ1 subunit lack all laminin expression. Laminin-γ1 mutant mice have severely hypomyelinated axons, and mutant Schwann cells fail to extend processes to interdigitate axons resulting in impaired radial sorting (Yu et al., 2009a). Furthermore, proliferation of mutant Schwann cells required for radial axonal sorting is also severely compromised, leading to a remarkable reduction in Schwann cell number (Yu et al., 2005). The transcription factor Oct-6 is not downregulated and Krox-20 levels remain low in Schwann cells with complete ablation of laminin expression, arresting mutant Schwann cells at the premyelinating stage. Elevated Schwann cell apoptosis is also seen in postnatal mutant nerves due to decreased PI3K activity and activation of caspase cascades (Yu et al., 2005).

Schwann cells integrate signals from axons and the basal lamina for myelination. Laminins may influence Schwann cell proliferation during sorting through regulation of NRG1/ErbB signaling. Impaired axon-Schwann cell interactions due to impaired axonal sorting in laminin-deficient nerves result in a reduction in ErbB2 and ErbB3 receptor phosphorylation that is usually stimulated by NRG1, hence a reduction in proliferation (Yu et al., 2005). Laminins positively regulate proliferation and survival of Schwann cells via activation of PI3K, FAK and the Rho GTPase cdc42 (Benninger et al., 2007; Grove et al., 2007; Yang et al., 2005; Yu et al., 2005). Moreover, mice lacking all laminin expression display severe abnormalities in sodium channel clustering at the nodes (Occhi et al., 2005).

1.2.3.2 Laminin receptors

In the PNS, laminin receptors consist of integrins, dystroglycan and members of the collagen superfamily. During distinct stages of development, Schwann cells differentially express laminin receptors. Before birth, SCPs and immature Schwann cells express α6β1 integrin and low levels of α2β1 and α3β1. At the promyelinating stage, Schwann cells abundantly express α6β1 and α6β4 integrins, as well as non-integrin laminin receptor dystroglycan (Feltri et al., 1994; Feltri and Wrabetz, 2005). In addition to these laminin receptors, myelinating Schwann cells also express α7β1 integrin (Previtali et al., 2003a).

1.2.3.2a- Integrins and their functions

Integrins are type I transmembrane dimeric proteins made up of non-covalently bound α- and β-subunits (Feltri and Wrabetz, 2005). Schwann cell-specific ablation of β1-integrin in mice results in impaired radial axonal sorting, which recapitulates the phenotype described in laminin-γ1 mutants (Feltri et al., 2002). Cytoplasmic process formation during axonal sorting is defective in β1-integrin null Schwann cells, suggestive of β1-integrin's function in regulating actin cytoskeletal dynamics. Indeed, activation of the Rho GTPase Rac1 by β1-integrin receptor is essential for Schwann cell process formation and stabilization (Benninger et al., 2007; Nodari et al., 2007). However, in contrast to the reduced proliferation and increased apoptosis of laminin-lacking Schwann cells, the absence of β1integrin results in variable effects on proliferation and survival in different mouse strain backgrounds (Berti et al., 2011; Feltri et al., 2002). Normal Schwann cell proliferation and survival has been reported in β1-integrin mutants in a mixed 129/C57BL6 background (Feltri et al., 2002), but reduced proliferation and survival in β1-integrin mutants in congenic C57BL6 background (Berti et al., 2011), which underscores the importance of reporting results from a defined strain background.

α6β4-integrin is distinct from other integrins in that β4 has a long cytoplasmic tail for binding to intermediate filaments (Feltri and Wrabetz, 2005). Whereas integrins are expressed by both neurons and Schwann cells in the PNS, α6β4 integrin is only expressed by Schwann cells at the onset of myelination (Feltri and Wrabetz, 2005). Genetic inactivation of α6β4 integrin does not affect Schwann

cell function, and is dispensable for peripheral nerve development, myelin formation and regeneration. However, the authors suggest that α6β4 integrin may play a role in myelin sheath maintenance since α6β4 integrin-deficient nerves display mild abnormal myelin folding (Nodari et al., 2008). Ablation of both α6β4 integrin and dystroglycan increases myelin folding, accompanied by acute demyelination particularly in the ventral roots, suggesting that they may co-operate to maintain myelin sheath stability (Nodari et al., 2008). Similarly, Schwann cell specific inactivation of α7β1 integrin, the last laminin receptor expressed by differentiating Schwann cells, also does not affect peripheral nerve development, basal lamina formation or myelination (Previtali et al., 2003a).

1.2.3.2b- Dystroglycan and its function

Dystroglycan, originally isolated from skeletal muscle, is a key component of the dystrophin-glycoprotein complex (DGC) that links the extracellular matrix with the cytoskeleton in various tissues (Masaki and Matsumura, 2010). Dystroglycan is expressed in the abaxonal membrane of both non-myelin forming and myelin-forming Schwann cells and in perineurial cells and satellite cells of DRG (Saito et al., 1999; Yamada et al., 1996b). Dystroglycan consists of two subunits: extracellular α-subunit and transmembrane β-subunit (Ervasti and Campbell, 1993). Both subunits are encoded by a single mRNA as a propeptide, which is proteolytically processed into two proteins associated by noncovalent bonds. In Schwann cells, extracellular α-dystroglycan can bind laminin-2 and agrin, and the cytoplasmic tail of transmembrane β-dystroglycan is associated with cytoskeletal proteins that are members of various DGCs including dystrobrevins, syntrophins, β-, δ-, ε, and ζ-sarcoglycans and the dystrophin family members: Dp116, dystrophin-related protein 2 (DRP-2) and utrophin (Albrecht et al., 2008; Imamura et al., 2000; Saito et al., 1999; Sherman et al., 2001).

The molecular composition of DGC varies in spatially distinct compartments of the abaxonal Schwann cell membrane. Cajal bands harbor the DGC containing utrophin, Dp116, α-dystrobrevin1 and syntrophins, and separate the abaxonal membrane and the myelin layers (Albrecht et al., 2008). In appositions/patches, β-dystroglycan forms a complex with DRP-2 and Periaxin (Fig. 8) (Sherman et al.,

2001). The DGC found at the node of Ranvier comprises Dp116 and utrophin (Occhi et al., 2005).

In Schwann cells, β-dystroglycan can be cleaved by matrix metalloproteases MMP-2 and MMP-9 that yield a 30 kDa fragment unable to bind α-dystroglycan (Yamada et al., 2001; Zhong et al., 2006). Recently, it has been proposed that the cleaved 30 kDa β-dystroglycan is present in Cajal bands lacking α-dystroglycan, and that both subunits (α-, and uncleaved 43 kDa β-dystroglycans) are localized in appositions. Excessive dystroglycan cleavage by MMP-2 and -9 may alter the size of cytoplasmic compartments (Cajal bands/appositions). Formation of defective Schwann cell cytoplasmic compartments due to increased dystroglycan cleavage is associated with reduced internodal lengths in laminin-α2-null dy2J/dy2J mouse (Court et al., 2011).

When dystroglycan in Schwann cells is genetically disrupted, mutant mice exhibit a late onset neuropathy characterized by an aberrantly folded myelin sheath, redundant myelin loops and polyaxonal myelination in mature nerves (Saito et al., 2003). These morphological changes in the myelin sheath are due to disruption of the linkage between the ECM and Schwann cell cytoskeleton contributed by reduced laminin binding capacity of dystroglycan-null peripheral nerve membranes (Saito et al., 2003). Schwann cells lacking dystroglycan also have shorter internodes (Court et al., 2009). During development, the absence of Schwann cell-specific dystroglycan arrests sorting predominantly in spinal roots, but not in peripheral nerves (Berti et al., 2011; Saito et al., 2003). Dystroglycan in Schwann cells functions as a receptor for laminin-2, and their interaction is important for axon defasciculation into a 1:1 relationship during radial axonal sorting (Berti et al., 2011).

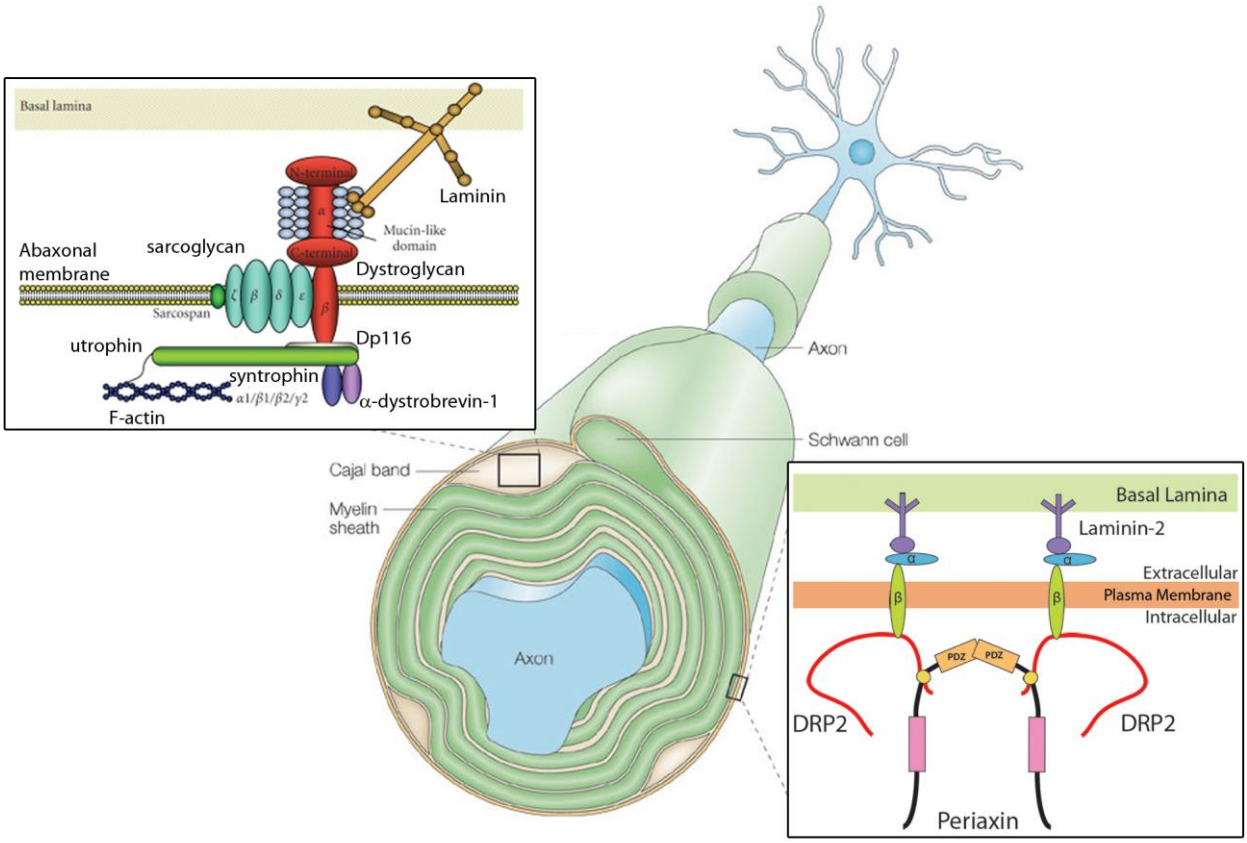

Figure 8. Molecular components of dystrophin-glycoprotein complexes (DGCs) present in Cajal bands and appositions of myelinated Schwann cells.

DGC complex containing utrophin, Dp116, dystrobrevins and syntrophins are formed in cytoplasm-filled channels, termed Cajal bands that lie underneath the plasma membrane of the Schwann cell. Utrophin interacts with F-actin at the N-terminus (top, left).

While its PDZ domain homodimerizes, Periaxin interacts via its basic domain with DRP2, which also associates with β-dystroglycan. This forms a transmembrane complex located at appositions between the outer membrane of myelin sheath and the cytoplasmic face of the Schwann cell plasma membrane (bottom, right). Image modified from (Masaki and Matsumura, 2010; Sherman and Brophy, 2005).

In the absence of dystroglycan, mutant mice also show nodal abnormalities such as reduced sodium channel expression and disorganized microvilli, which lead to a reduction in conduction velocity of mature peripheral nerves (Saito et al., 2003). Dystroglycan may link the basal lamina to the cytoskeleton of microvilli, forming a specific molecular scaffold that operates by limiting the lateral movement of sodium channels toward the nodes during Schwann cell elongation, and hence clustering sodium channels at the nodes (Occhi et al., 2005).

α-dystroglycan in the peripheral nerve is glycosylated, and glycosylation is important for dystroglycan functions. Mutations of genes encoding fukutin, POMT or LARGE glycosyltransferases, which have α-dystroglycan as a substrate, impair α-dystroglycan glycosylation and thereby attenuate the binding capacity to laminin and agrin (Kim et al., 2004; Michele et al., 2002). Glycosylation defects in dystroglycan cause human disorders, such as congenital muscular dystrophy 1D and Fukuyama-type congenital muscular dystrophy. Mice with mutations of fukutin or LARGE show sorting defects as revealed by the presence of clusters of naked axons in peripheral nerves and spinal roots (Levedakou et al., 2005; Saito et al., 2007). Moreover, fukutin-chimeric mutant mice show defective clustering of acetylcholine receptor and fragmented neuromuscular junctions (NMJs) (Saito et al., 2007). Collectively, these data indicate that regulation of the sugar chain structure of α-dystroglycan is important for binding with laminin or agrin, and that the linkage between α-dystroglycan and its ligands is essential for myelination of the peripheral nerve and establishing the architecture of the NMJ.

1.3 PERIAXIN

1.3.1 PERIAXIN AND CHARCOT-MARIE-TOOTH (CMT) 4F

Defects in PNS myelination can cause Charcot-Marie-Tooth disease (CMT), also known as hereditary sensory and motor neuropathy (HSMN). CMT is the most frequently inherited peripheral neuropathy, with a prevalence of 1 in 2500 people (Skre, 1974). The disease is classified into two major groups, namely a demyelinating form (CMT1, CMT3 and CMT4) when myelinating Schwann cells are primarily affected, and an axonal form (CMT2) when axons are the principal disease target (Dyck and Lambert, 1968; Maier et al., 2002). The demyelinating form of CMT is characterized by segmental demyelination followed by remyelination and onion bulb formations in patient nerves, with a reduction in nerve conduction velocities (NCVs). Patients with the axonal form CMT2 often display normal or near-normal NCVs, and nerve biopsies show myelinated axonal loss (Young and Suter, 2003).

The major demyelinating CMT disease characteristics include slowly progressive muscular atrophy and weakness, with sensory loss in the distal extremities of the limbs and absence of deep tendon reflexes (Guilbot et al., 2001). Deformed feet and claw toes are common features of the disease, leading to gait impairment (Young and Suter, 2003). Modes of inheritance can be autosomal dominant or recessive, or X-linked (Guilbot et al., 2001). The underlying gene defects affect myelinating Schwann cells thus triggering secondary axonal degeneration. Genes mutated in CMT encode proteins that are involved in 1) the regulation of myelin sheath development and maintenance of the myelin structure; 2) protein biosynthesis, sorting and degradation; 3) vesicular transport, endocytosis and mitochondrial morphology and dynamics (Berger et al., 2006). Mutations in genes of myelin components including PMP22, P_0/MPZ, connexin 32 and Periaxin are responsible for various subtypes of CMT. Some subtypes of CMT are caused by mutations in genes encoding myelin gene transcription factors such as EGR2/Krox-20 (Berger et al., 2006; Scherer and Wrabetz, 2008).

Autosomal recessive CMT, which is characterized by a severe, demyelinating early onset peripheral neuropathy, is defined as CMT4. To date, eight loci and seven genes have been implicated in CMT4 (Parman et al., 2004). Subtypes of CMT4 are

classified based on the mutations in the following genes (Berger et al., 2006; Parman et al., 2004):

CMT4A	Ganglioside-induced differentiation-associated gene 1 (*GDAP1*)
CMT4B1	Myotubularin-related protein 2 gene (*MTMR2*)
CMT4B2	*MTMR13/SBF2*
CMT4C	SH3 domain and tetratricopeptide repeats 2 gene (*SH3TC2*)
CMT4D	N-myc downstream-regulated gene 1 (*NDRG1*)
CMT4E	Early growth response gene 2 (*EGR2*)
CMT4F	Periaxin (*PRX*)

CMT type 4F neuropathy is caused by mutations in the human *Periaxin* gene (*PRX*) mapped on chromosome 19q13, which is syntenic with a region of chromosome 7 in the murine *Prx* gene (Delague et al., 2000; Gillespie et al., 1997; Guilbot et al., 2001). Amino acid sequence comparison of human, rat and mouse L-Periaxin reveals that human L-Periaxin shares ~73% and ~78% sequence identity with the rat and murine proteins (Boerkoel et al., 2001). Various nonsense or frameshift mutations in the *PRX* gene have been described in patients showing autosomal recessive, demyelinating CMT4F and Dejerine-Sottas neuropathy (DSN or CMT3) (Boerkoel et al., 2001; Guilbot et al., 2001; Kabzinska et al., 2006; Kijima et al., 2004; Marchesi et al., 2010; Otagiri et al., 2006; Parman et al., 2004; Takashima et al., 2002).

CMT4F patients carrying *PRX* mutations have early onset but in general slow disease progression (Marchesi et al., 2010). Delayed motor development with gait problems since childhood has been reported in a majority of CMT4F patients. Most patients show severe muscle weakness in distal limbs. Pes cavus (deformed feet and claw toes) and scoliosis is present in many CMT4F patients. A number of patients also show and severe sensory loss, often associated with sensory ataxia. A moderate- to dramatic reduction of motor NCVs, undetectable sensory nerve action potentials, and demyelination with onion bulb formation are common electrophysiological and pathological features of the disease (Barankova et al., 2008; Guilbot et al., 2001; Kabzinska et al., 2006; Kijima et al., 2004; Marchesi et al., 2010; Otagiri et al., 2006; Parman et al., 2004; Takashima et al., 2002).

In CMT 4F, all but one of the 16 human *PRX* mutations identified so far occur in the final exon (exon 7), which encodes 91% of the larger Periaxin isoform, L-Periaxin (Marchesi et al., 2010). In this case, the mRNA is predicted to be exempt from nonsense-mediated mRNA decay. Indeed, interestingly three of the *PRX* mutations identified (S399fsX410, C715X and R1070X) have been reported to generate truncated mutant Periaxin proteins revealed by immunofluorescence labeling and/or Western blotting of nerve biopsies (Kabzinska et al., 2006; Parman et al., 2004; Takashima et al., 2002).

A notable mutation at R1070X introduces a stop codon at 28 aa upstream of the Periaxin acidic domain. This mutation generates a large truncated protein of Periaxin lacking the acidic domain and the rest of the C-terminus. Patients display severe demyelination and axonal loss contributing to distal muscle weakness and sensory ataxia (Parman et al., 2004), confirming the importance of the C-terminus in the function of Periaxin. The most downstream mutation reported so far is the K1095fsX18 mutation, which causes a frameshift following amino acid lysine at codon 1095 and terminates the protein at amino acid 1113. The patient with this mutation developed an early-onset but slowly progressive demyelinating CMT (Barankova et al., 2008).

1.3.2 PERIAXIN ISOFORMS

The murine *Periaxin (Prx)* gene, which spans 20.6 kilobases, generates two mRNAs, of 4.6 and 5.2 kilobases. These two mRNAs encode two protein isoforms, L-Periaxin of 147 kDa and S-Periaxin of 16 kDa, respectively. The smaller isoform S-Periaxin is generated as a truncated protein bearing a unique 21 amino acid C-terminus due to alternative splicing involving the retention of an intron (intron 6) of the pre-mRNA (Dytrych et al., 1998). Interestingly, *Prx* shares a common genetic structure as *AHNAK*, characterized by a large exon flanked by multiple small exons. The L-Periaxin protein sequence also has a high degree of sequence similarity as AHNAK. *AHNAK* encodes a giant protein (700 kDa) and a small isoform (17 kDa) expressed in muscle. In peripheral nerves, AHNAK is localized to Cajal bands in Schwann cells (Salim et al., 2009).

Up until now, the major research focus has been placed on the function of L-Periaxin in myelinating Schwann cells, but little is known about S-Periaxin. S-

Periaxin is diffusely distributed in the cytoplasm with a punctated staining in the nucleus of Schwann cells (de Morree et al., 2011; Dytrych et al., 1998), and its functions have yet to be identified. Studies of the function of the small isoform of AHNAK (S-AHNAK) have shown that S-AHNAK traffics between the cytoplasm and the nucleus, and localize to the spliceosome to regulate mRNA splicing of its own locus. In the same study, recombinant S-Periaxin was also capable of regulating AHNAK splicing in the nucleus (de Morree et al., 2011). Whether S-Periaxin also regulates mRNA splicing of its own locus remains to be studied.

Both L-and S-Periaxin contain a protein interacting PDZ domain at the N-terminal region (PDZ: post-synaptic density protein **P**SD-95, *Drosophila discs large* (***d****lg*) tumor suppressor gene, tight junction-associated protein **Z**O-1) (Dytrych et al., 1998). Proteins with this protein binding domain are often membrane-associated and interact with the cytoplasmic tail of plasma membrane proteins and with the cortical cytoskeleton; they can also homo- or heterodimerize (Kim and Sheng, 2004). PDZ domains have four possible binding modes, including interaction with the carboxyl-terminal motif of binding partners, recognition of internal motifs in peptides, PDZ-PDZ dimerization and lipid recognition (Nourry et al., 2003).

In addition to functioning as scaffolding proteins that assemble signal transducing proteins into functional signaling complexes at the plasma membrane, PDZ domain proteins can act as adaptors for tyrosine kinase receptors. For example, the PDZ domain protein Erbin plays a role in stabilization and internalization of the ErbB2 protein. In the PNS, Erbin-null mice show hypomyelination and aberrant axonal ensheathment of unmyelinated small diameter C fibers. More specifically, mice lacking the PDZ domain of Erbin reproduce the phenotype seen in Erbin-/- mutants (Tao et al., 2009). Proteins containing PDZ domains, such as Dlg1, Par3 and Pals1 (see section 1.2.2) have also been implicated in tight junction assembly and the development of epithelial-like polarity. Indeed, many PDZ domain proteins are found at the synaptic junction between neurons that contain highly polarized subcellular compartments. They interact with neurotransmitter receptors for synapse signal transduction, examples of which are PSD-95, GRIP and Dlg1/SAP97 (Nourry et al., 2003). As for L-Periaxin, its PDZ domain is known to homodimerize (Sherman et al., 2001).

Downstream of L-Periaxin's PDZ domain is a highly basic region, which contains a nuclear localization signal (NLS) (Sherman and Brophy, 2000). The middle part of the protein consists of a series of repeats (432-725 aa), followed by a highly acidic domain towards the C-terminus (1036-1163 aa) of the protein (Fig. 9) (Dytrych et al., 1998; Gillespie et al., 1994). L-Periaxin is a protein of non-compact myelin, first identified at the periaxonal membranes of early postnatal myelin-forming Schwann cells in the PNS (Gillespie et al., 1994; Scherer et al., 1995). In this work L-Periaxin will be described simply as Periaxin.

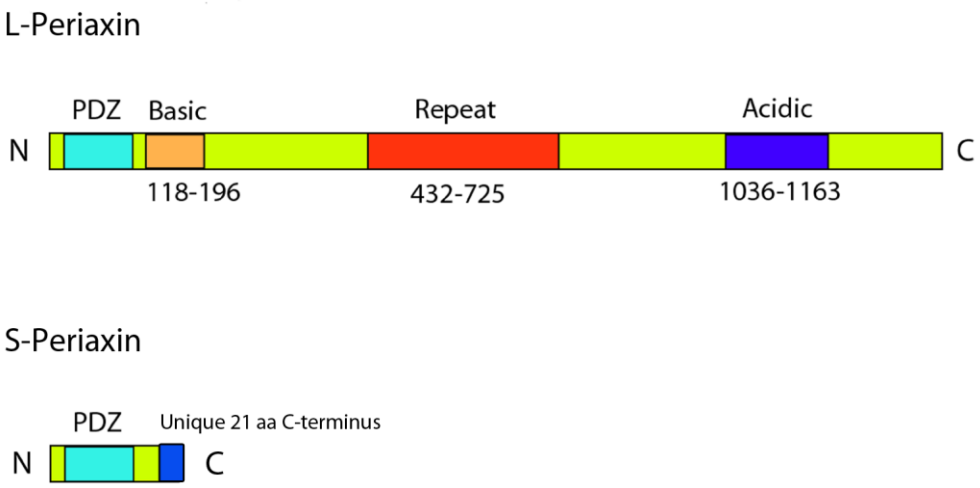

Figure 9. Domain structure of mouse L- and S- Periaxin.

Both isoforms contain a PDZ domain at their N-termini. S-Periaxin (16kDa) has a unique 21 aa C-terminus. Downstream of the PDZ domain of L-Periaxin is a highly basic domain. The middle of the protein is occupied by a series of repeats. Close to the C-terminus is an acidic domain. (Amino acid residues are shown).

1.3.3 PERIAXIN EXPRESSION IN SCHWANN CELLS

Proteomic analysis of PNS myelin protein content has revealed that Periaxin is the second most abundant myelin-related protein, constituting ~16% of all PNS myelin proteins (Patzig et al., 2011). Periaxin expression is not specific to the PNS. It is also present in cytoskeletal complexes of lens fibers (Straub et al., 2003), and is important for hexagonal geometry and membrane stability of lens fibers (Maddala et al., 2011).

In mature Schwann cells, Periaxin is expressed in the abaxonal membrane and the Schmidt-Lanterman incisures, but is absent from compact myelin and paranodal loops (Gillespie et al., 1994). During development, Periaxin is localized in the nuclei of murine embryonic Schwann cells as early as embryonic age 14.5 days

(E14.5) *in vivo*, in agreement with the presence of a nuclear localization signal in the protein. It is initially expressed in the nucleus until E16.5, and is then localized to the Schwann cell plasma membrane at E17.5 (Sherman and Brophy, 2000). However, as the myelin sheath matures and the spiralization process completes, Periaxin is predominantly localized to the abaxonal Schwann cell membrane (Gillespie et al., 1994; Scherer et al., 1995).

1.3.4 TRANSCRIPTIONAL REGULATION OF PERIAXIN EXPRESSION

Periaxin mRNA and protein are highly upregulated in early stages of myelination and peak between postnatal days 8 and 20 in peripheral nerves. The time course of Periaxin expression is similar to that of the major myelin protein P_0 (Gillespie et al., 1994). Like P_0, regulation of Periaxin expression requires axonal contact since levels of Periaxin mRNA and protein in myelinating Schwann cells are progressively lost from Schwann cell membranes and become associated with myelin debris following nerve transection or crush (Scherer et al., 1995).

The zinc finger transcription factor Krox-20 is an important regulator of the myelin program. *In vitro*, ectopic expression of Krox-20 in Schwann cells induces expression of a number of myelin genes, including *Mpz, Pmp22, Mbp, Mag, Connexin32* and *Prx* (Nagarajan et al., 2001). Interestingly, during normal nerve development, Periaxin expression in Schwann cells detected by immunofluorescence precedes that of Krox-20 induction by at least 2 days. Characterization of Periaxin expression in peripheral nerves and cultured Schwann cells lacking Krox-20 has revealed detectable Periaxin expression, albeit at reduced levels. In addition, in cultured Schwann cells lacking Krox-20, Periaxin expression can be elevated by the myelin differentiation signal cAMP. These data indicate that initiation of Periaxin expression is independent of Krox-20 regulation. Krox-20, however, may function as an amplifier of *Prx* gene expression since forced expression of Krox-20 in Schwann cells induces expression of Periaxin mRNA and protein in the absence of cAMP (Parkinson et al., 2003).

A conserved enhancer element in the first intron of the *Mpz* gene that consists of inverted dimeric Sox10 binding sites and at least one Krox-20/Egr2 binding site has been described as a myelin regulatory module (LeBlanc et al., 2006). This potential site of Krox20/Sox10 interaction was also identified in the first intron of the

Prx gene (Jones et al., 2007). The authors demonstrated binding of Krox20 and Sox10 to the conserved composite module in the *Prx* gene using chromatin immunoprecipitation (ChIP) assays, indicating that similar to P_0 expression regulation, synergistic interactions of Krox-20 and Sox10 to the first intron of the *Prx* gene may mediate an elevation of Periaxin expression in myelinating Schwann cells.

1.3.5 PERIAXIN FORMS A MEMBRANE COMPLEX WITH DRP2 AND DYSTROGLYCAN

In skeletal muscle and the PNS, dystrophin complexes with dystroglycan. The dystrophin glycoprotein complex (DGC) plays a significant role in linking extracellular matrix proteins such as laminins to the actin cytoskeleton (Ahn and Kunkel, 1993; Gee et al., 1993; Yamada et al., 1996a). Periaxin homodimerizes at its PDZ domain and associates via its basic domain with DRP2, which interacts with β-dystroglycan, forming a transmembrane complex (PDG complex) (Fig. 8) (Sherman et al., 2001). The complex is localized and clustered at appositions/patches (Court et al., 2004; Sherman and Brophy, 2005). As mentioned in the previous section, cytoplasmic-rich Cajal bands between appositions contain a specific DGC containing utrophin, Dp116, dystrobrevins and syntrophins, and ABC1 cholesterol transporter (Albrecht et al., 2008). Cajal bands may have an important role in microtubule-based mRNA transport (Court et al., 2004).

Periaxin is essential for clustering and stabilizing the PDG complex. In mice lacking Periaxin, DRP2 is severely depleted and fails to form at the clusters but is found diffusely in the cytoplasm (Sherman et al., 2001). In addition, the PDG complex is disrupted in Periaxin-null mice, leading to absence of appositions and disruption of Cajal bands (Court et al., 2004). Periaxin-deficient Schwann cells also have reduced internodal lengths. However, myelin thickness is not affected at 3 weeks old. A decrease in internodal length of Schwann cells has been proposed to result in a reduction in nerve conduction velocity in *Prx*-null mice (Court et al., 2004).

1.3.6 PERIAXIN-NULL MICE DISPLAY PERIPHERAL NERVE DEMYELINATION AND NEUROPATHIC PAIN

Periaxin-null Schwann cells are capable of ensheathing peripheral nerve axons and forming a functionally intact myelin sheath. 3-week-old *Prx*-null mutant mice exhibit a normal behavioral phenotype when tested for neuropathic pain behavior (Court et al., 2004). However, by 4-6 weeks of age they start to display a slight tremor and later a neuropathic pain behavior phenotype (Gillespie et al., 2000). There is no difference in the number of myelinated axons in wild-type and *Prx*-deficient sciatic nerves up to 12 weeks of age, indicating that mice lacking Periaxin have the ability to generate normal numbers of myelinated axons. The density of myelinated axons in older mice is reduced, and this is reflected in an increase in extracellular matrix (Williams and Brophy, 2002). After sciatic nerve crushes in 6-week-old Periaxin-null mice, peripheral nerve remyelination takes place in these mice, and the number of myelinated axons returns to normal. However, the axon calibers of myelinated fibers in the crushed nerve remain smaller than the contralateral uncrushed nerve. Axons are also hypermyelinated in regenerated nerves in the absence of Periaxin (Williams and Brophy, 2002), suggesting a role of Periaxin in myelin sheath maintenance.

Older mutant mice (6-9 months old) display hypermyelination with focal thickenings of myelin called tomacula, as well as extensive peripheral demyelination. This infolding of myelin leads to axon compression. Schmidt-Lanterman incisures, which are cytoplasm-filled structures along the length of the internodes, are also deranged. Peripheral nerves from these mice display onion bulb formation, a pathology indicative of supernumerary Schwann cells attempting to remyelinate following demyelination of nerve fibers. This is often associated with the human Charcot-Marie-Tooth disease and Dejerine-Sottas disease (Gillespie et al., 2000). In the absence of Periaxin in peripheral nerves, mutant animals displayed severe behavioral deficits due to instability of the myelin sheath, resulting in the development of a late-onset demyelinating neuropathy associated with mechanical allodynia and thermal hyperalgesia (Gillespie et al., 2000). Conduction velocities of sensory myelinated afferent fibers in *Prx*-null nerves are severely reduced, which is associated with the sensory deficits displayed by the mutant mice. Mutant sciatic and saphenous nerves also have significantly reduced conduction velocities by 6 months of age. Motor coordination deficits in Periaxin-deficient mice may be contributed by

the morphological abnormalities in the preterminal region of motor axons at the NMJs associated with demyelination (Court et al., 2008). This indicates that the Periaxin-DRP2-dystroglycan complex is essential for the maintenance and stabilization of the myelin sheath. Hence, the Periaxin-knockout mouse should be an excellent model for studying the development of demyelinating neuropathies.

1.4 AIMS OF THE PROJECT

Complete deletion of Periaxin in mouse peripheral nerves perturbs Schwann cell elongation and causes a severe demyelinating phenotype. However, the functions of the different domain regions of Periaxin remain unclear. In particular, Periaxin homodimerizes at its PDZ domain in the Periaxin-DRP2-dystroglycan complex at appositions of the Schwann cell membrane (Sherman et al., 2001). Is Periaxin PDZ homodimerization essential for stabilization of the Periaxin-DRP2 complex and Schwann cell cytoplasmic compartments, and hence Schwann cell function? In order to address these questions, this work aims to gain insight into the role of the PDZ domain of Periaxin in the following ways:

1. The first aim of the project was to characterize a mouse mutant containing a version of Periaxin lacking the PDZ domain in myelinating Schwann cells.

2. Before homodimerization during formation of the PDG complex, it is unknown whether the Periaxin PDZ domain has other functions. The second objective was to understand the consequences of disrupting the PDZ domain dimerization of Periaxin after compartmentalization of the Schwann cell cytoplasm is accomplished in adult nerves.

3. Since eliminating the N-terminal PDZ domain (about 10% of the protein) from Periaxin might induce changes in the protein folding mechanism; I aimed to study whether minimal disruption in the Periaxin PDZ domain structure by single amino acid mutations may also result in abrogation of PDZ dimerization.

2- MATERIALS AND METHODS

2.1 ANIMALS

All animal work conformed to UK legislation (Scientific Procedures) Act 1986 and the Edinburgh University Ethical Review policy. All mouse lines used in this work were of congenic C57Bl6 background. C57Bl6 strain was chosen due to its robustness, easy breeding and availability of knowledge in its physiology and genetics. Most importantly, many neurobiological mutations have been generated and studied in this strain.

Generation of *P_0CreERT* mice, which carries a transgene containing the P_0 promoter (specifying Schwann cell specific expression) together with an improved variant of the tamoxifen-inducible Cre recombinase CreERT2 (Leone et al., 2003), as well as that of *Cnp-Cre* mice, in which *Cre* is inserted into the *Cnp* locus has been previously described (Lappe-Siefke et al., 2003).

Generation of *Prx$^{fl/fl}$* transgenic mice: Homozygous *Prx$^{fl/fl}$* mouse line was generated by Dr. Diane Sherman. The *Prx* gene contains 7 exons, of which exons 4-7 are coding exons. 91 % of Periaxin is encoded by exon 7, whereas the PDZ domain is encoded by both exons 5 and 6. Two *loxP* sites were inserted to flank exon 5 of the *Prx* gene (A. Williams, unpublished). Upon Cre-mediated recombination of the *lox*P sites, exon 5 is predicted to be excised and this is predicted to introduce a frameshift leading to an in-frame stop codon in exon 6, thus arresting protein translation, or more likely causing nonsense-mediated RNA decay (Fig. 10).

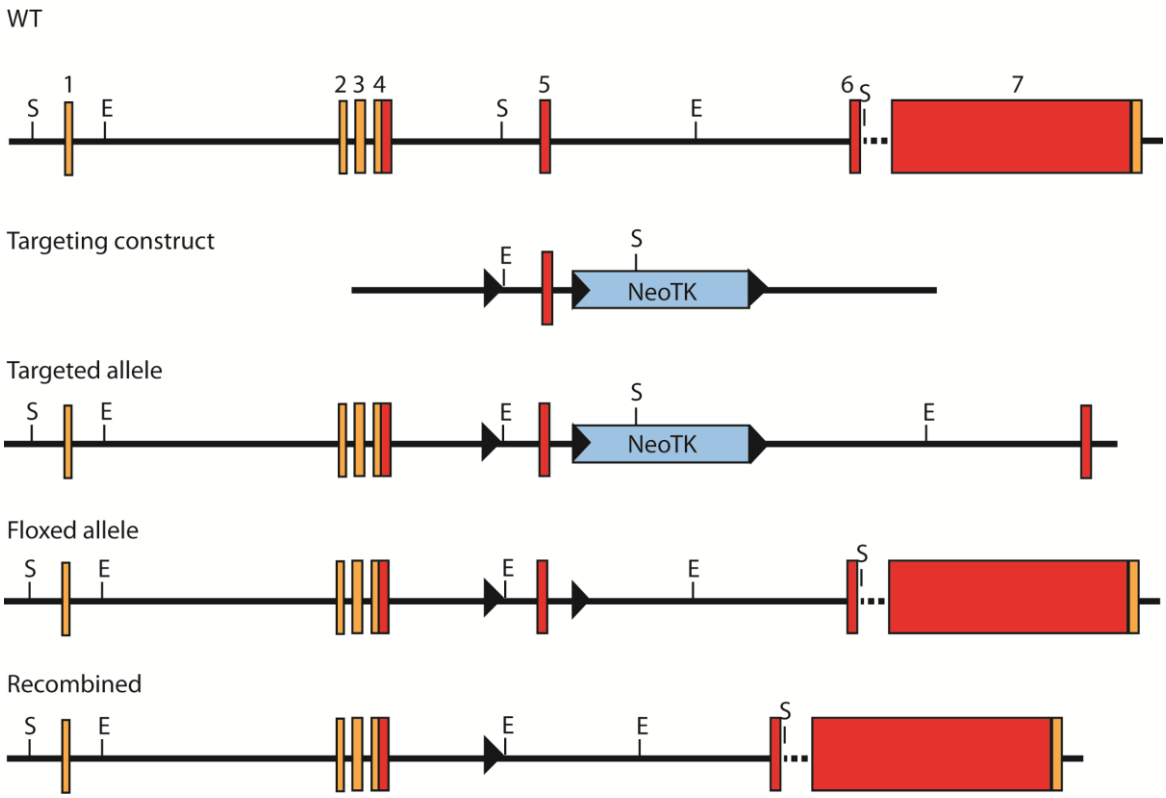

Figure 10. Targeting strategy for generating a *"floxed"* Periaxin mutant mouse.

Schematic representation of the genomic Periaxin (WT, wild type), floxed, and mutant recombined loci. Two *lox*P sites were positioned to flank exon 5. Upon Cre-mediated recombination of the loxP sites, a frameshift stop codon is introduced in exon 6, which is predicted to arrest protein translation, or more likely cause nonsense-mediated RNA decay. The location of the exons (1-7) and *loxP* sites (black triangles) are indicated. Orange rectangles denote non-coding exons, whereas red rectangles protein coding exons. E stands for EcoRI sites.

Generation of *Prx$^{fl/fl}$/Cnp-Cre* mice: Targeted ablation of Periaxin in myelinating Schwann cells was achieved by crossing homozygous *Prx$^{fl/fl}$* mice with mice homozygous for the *'floxed'* allele and heterozygous for *Cnp-Cre*. In the present study, *Prx$^{fl/fl}$* mice were defined as wild-type (WT), whereas *Prx$^{fl/fl}$/Cnp-Cre* mice as Δ*PDZ-Prx* mice.

Generation of *Prx$^{fl/fl}$/P$_0$CreERT* mice: homozygous *Prx$^{fl/fl}$* mice were crossed with mice homozygous for the *'floxed'* allele and heterozygous for *P$_0$CreERT* to produce *Prx$^{fl/fl}$/P$_0$CreERT*.

2.1.1 Peripheral nerve dissection

Trigeminal nerves were used for mRNA and protein level analysis because in our hands, they provide abundant amounts of proteins and RNA during extraction. Following euthanizing with CO_2 inhalation, the animal was beheaded, the skull was opened and brain removed to expose the trigeminal nerves. The trigeminal ganglion and the ophthalmic, maxillary, and mandibular branches of the trigeminal nerve were dissected, snap-frozen in liquid N_2 and stored at -80^{o}C until use.

Sciatic nerves were used for protein level analysis and cryostat sectioning. Sciatic nerves from the proximal region to the sciatic notch were dissected, snap-frozen in liquid N_2 and stored at -80^{o}C until use.

Quadriceps nerves, which are distal and consist mainly of motor nerve fibers, were used for all morphometric and electrophysiological analysis because distal motor nerves are often affected in CMT4F patients (see section 1.3.1). The nerve was dissected from the quadriceps branch of the femoral nerve, from where the saphenous and quadriceps branches separate to the distal end where it innervates the muscle. Nerves were either fixed for immunofluorescence staining and electron microscopy processing, or used fresh for electrophysiology.

2.2 PCR

PCR in this study was performed with Go Taq DNA polymerase (1U, Promega), unless otherwise stated, in a 25 µl reaction containing 1× Go Taq buffer, 1.5 mM $MgCl_2$, 0.2 mM dNTPs and 0.5 µM of primers. PCR conditions were: 1 cycle of a 1 min 30 s denaturation at 94^{o}C, a 30 s annealing at 57^{o}C and a 1min/kb extension at 72^{o}C depending on the product size, followed by 34 cycles of 94^{o}C for 40 s, 55^{o}C for 30 s and 72^{o}C for 1min/kb. PCR products were resolved on agarose gels, visualized by ethidium bromide under UV light in a Uvitec gel documentation system (Uvitec, Cambridge).

2.2.1 Genotyping PCR

Each ear clip was incubated in 50 µl of lysis buffer containing 50 mM Tris pH 8.0, 50 mM EDTA, 0.25% SDS (w/v) and 0.5 mg/ml Proteinase K (Roche) overnight at 55^{o}C. Next day, genomic DNA from lysed ear biopsies was diluted 1:10 in sterile

MiliQ water. 1 µl of the diluted genomic DNA was used as PCR template. PCR was performed with Go Taq polymerase.

To identify homozygous *Prx*$^{fl/fl}$ mice, primers (Peri 27 and Peri 28) were designed to flank exon 5. The PCR amplification protocol was: 1 cycle of 94^{o}C denaturation for 1 min 30 s, 55.6^{o}C annealing for 30 s, and 72^{o}C extension for 1 min, followed by 45 cycles of 94^{o}C for 40 s, 55.6^{o}C for 30 s and 72^{o}C for 1 min. The last cycle consisted of 94^{o}C for 40 s, 56^{o}C for 30 s and 72^{o}C for 2 min. PCR products were digested overnight at 37^{o}C with EcoRI and analyzed by agarose gel electrophoresis. Mice homozygous for floxed *Prx* (*Prx*$^{fl/fl}$) showed a single band of 0.5 kb, mice that were heterozygous for floxed *Prx* (*Prx*$^{fl/+}$) exhibited two major bands at 1.0 and 0.5 kb. Wild-type mice showed a PCR product of 1.0 kb (Fig. 11). Sequences of oligonucleotide primers used in this study were specified in Table 1.

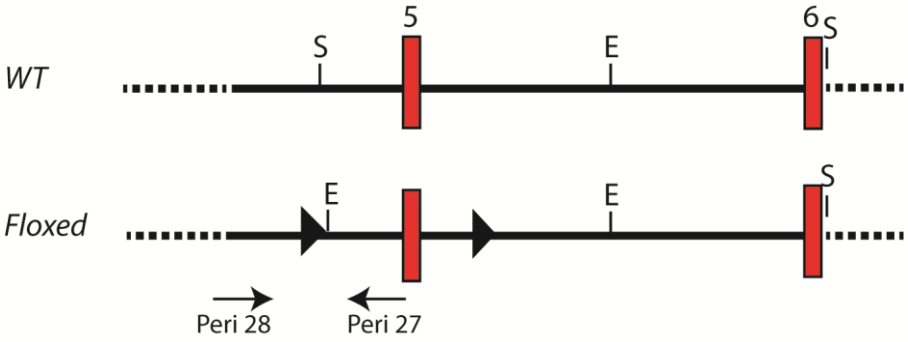

Figure 11. Genotyping for homozygous *Prx*$^{fl/fl}$ mice.

Schematic representation of exons 5-6 (red rectangles) of the genomic Periaxin (WT, wild type) and floxed loci. *loxP* sites (black triangles) and primers used for genotyping (Peri 27 and Peri 28) are indicated. E stands for EcoRI sites. An EcoRI site is introduced adjacent to the first *loxP* site (5'-end) in the floxed *Periaxin* gene. Primers Peri 27 and Peri 28 encode a PCR fragment containing the inserted EcoRI site in the floxed gene, which can be distinguished from WT by restriction digestion.

To identify *Prx*$^{fl/fl}$*/P*$_0$*CreERT* mice, transgene was identified by PCR amplification using primers P0 CXF and P0 CAR for *P*$_0$*CreERT*. The PCR conditions included 1 cycle of 94^{o}C denaturation for 2 min, 55^{o}C annealing for 1 min, and 72^{o}C extension for 1 min, 4 cycles of 94^{o}C for 1 min 30 s, 55^{o}C for 40 s and 72^{o}C for 1 min, followed by 28 cycles of 94^{o}C for 40 s, 55^{o}C for 30 s and 72^{o}C for 1 min. The last step consisted of 94^{o}C for 30 s, 55^{o}C for 30 s and 72^{o}C for 2 min. *Cre*-positive mice showed a 750 bp PCR product.

To identify *Prx*$^{fl/fl}$*/Cnp-Cre* mice, PCR analysis was performed with primers Cre F4 and Cre R6, which yielded a 941 bp product for *Cre*-positive animals. PCR conditions were: 1 cycle of denaturation at 94^{o}C for 1 min 30 s, annealing at 55^{o}C for 30 s, and extension at 72^{o}C for 1 min, followed by 39 cycles of 94^{o}C for 40 s, 55^{o}C for 30 s and 72^{o}C for 1 min. The final step consisted of 94^{o}C for 40 s, 55^{o}C for 30 s and 72^{o}C for 2 min. Positive and no template controls were always included.

Table 1. Oligonucleotide primer sequences

Primer		5’ to 3’	Restriction sites
BDF	F	TCATCGGAAGAGAGTAGTAACAAAG	
Cre F4	F	ACGAGTGATGAGGTTCGCAA	
Cre R6	R	GTTTCACTATCCAGGTTACGG	
CSG 3	R	AGCTTGGTGGCTCGCCCAGG	
CSG 26	F	TGACTCTCTGCAGAGCTAT	
DLS 29	F	GGGATTCGAGGCCAGGAGCCGCAGCGCT	EcoRI
GADPH F1	F	ATCACCATCTTCCAGGAGCG	
GAPDH R1	R	AGGCCATGCCAGTGAGCTTC	
LMD 7	R	AGTTCTCTTTTCCCAAGTTCTCCCGACT	
LMD12	F	CAGATTTGCTCTGCCCAAGT	
P0 CAR	R	TCCGATCCGCCGCATAACC	
P0 CXF	F	CTGCACAGACATGAGACCATAGG	
Peri 15R	R	CACCTGGGGCAAAAGAGATAC	
Peri 27	R	AAGAAGAGGGGATGAGTAGGCG	
Peri 28	F	CCTGTGACTTCCCAAAAAAAC	
Peri 89	F	CGAAGATCTGAGATGAAGGGCCCGCGAGC	BglII
Peri 96	F	CGGAATTCGCACAGACCGGGGTCAGC	EcoRI
Peri 97	R	CGGGATCCTCACCCGGTGGGCACAGTGCGCTTC	Stop, BamHI
Peri 98	R	CGGGATCCTCACTCTGCGCATTGCAGCAGGC	Stop, BamHI
Peri 101	F	GAGCGGAGTTGGTGGCCATTATCGTGGAGACAG	
Peri 102	R	CTGTCTCCACGATAATGGCCACCAACTCCGCTC	
Peri 103	F	GAGATTATCGTGGAGGCAGAGGCGCAGACCG	
Peri 104	R	CGGTCTGCGCCTCTGCCTCCACGATAATCTC	
Peri 105	F	GTTTGCAGGAAGGGGCCCAACTTCTGAGCGC	
Peri 106	R	GCGCTCAGAAGTTGGGCCCCTTCCTGCAAAC	
Peri 115	F	5’-ACCGGGGTCAGCGCCTTCAATGTAGCA -3’	
Peri 116	R	5’-CTGCTACATTGAAGGCGCTGACCCCGGT-3’	

2.3 REVERSE-TRANSCRIPTION PCR (RT-PCR)

2.3.1 RT-PCR

RNA was isolated from trigeminal nerves of 3- or 4-week-old wild-type and Δ*PDZ-Prx* mice by guanidinium-thiocyanate-phenol-chloroform extraction (Chomczynski and Sacchi, 1987; Chomczynski and Sacchi, 2006) with Trizol (TRI-reagent, Ambion), precipitated by isopropanol and purified. Briefly, 4-6 nerves were homogenized in 400 µl Trizol. 80 µl chloroform (200 µl/ ml Trizol) was added and homogenate was incubated for 5 min at room temperature. Following centrifugation for 15 min at 13000 rpm at 4^{o}C, the aqueous phase containing RNA was transferred to a fresh microcentrifuge tube. The phenol/choroform extraction step was repeated followed by extraction with chloroform for removal of phenol. Total RNA was precipitated from the aqueous phase with an equal volume of isopropanol, purified with 70% cold ethanol, and resuspended in RNase-free water. RNA concentration was determined by measuring absorbance at 260 nm. RNA was stored at -80^{o}C.

5 µg total RNA in a 20 µl reaction was transcribed into first strand cDNA at 42^{o}C for 1 h using Moloney Murine Leukemia Virus (M-MLV) reverse transcriptase (200 units, Promega) with random hexanucleotide primers (Gibco). The reverse transcription reaction was terminated by increasing the temperature to 80^{o}C for 20 min. cDNA was amplified by PCR using Go Taq polymerase with forward primer CSG 26 encoding exon 4 and reverse primer LMD 7 encoding exon 7 of the *Prx* gene, at an annealing temperature of 57^{o}C and a 35 s extension at 72^{o}C. Reverse transcription efficiency was evaluated by amplifying a 400 bp fragment of housekeeping gene GAPDH using primers GAPDH F1 and GAPDH R1 at an annealing temperature of 57^{o}C and a 20 s extension at 72^{o}C. PCR products were resolved on 1.5% agarose gels.

Predicted DNA fragment sizes:

PCR amplification of wild-type *Prx* cDNA would yield a DNA fragment of 513 bp, recombined *Prx* sequence due to Cre-mediated excision of exon 5 (157 bp) would give rise to a 356 bp PCR product. If exon skipping of exon 6 (194 bp) in the recombined gene occurs, a 162 bp fragment would result.

The 356 bp DNA fragment was extracted from an agarose gel, Qiaex-purified, subcloned into pGEM T-easy (Promega) and sequenced (DNA Sequencing & Services, Dundee University).

2.3.2 Semi-quantitative RT-PCR

Total RNA was prepared and cDNA synthesized from trigeminal nerves of 3-week-old WT and Δ*PDZ-Prx* mice as described. To compare wild-type and mutant Periaxin mRNA expression, semi-quantitative RT-PCR was performed by co-amplification of Periaxin cDNA for a ~400 bp fragment of exon 7 of the *Prx* gene using primers LMD 12 and Peri 15R, and of GAPDH cDNA using primers GAPDH F1 and GAPDH R1 as an endogenous control sequence. The relative amount of cDNA synthesized from each sample was evaluated by PCR amplification of GAPDH using the same primers. Equal quantity of cDNA was used for each genotype according to uniform expression of the reference gene. PCR was performed using Go Taq polymerase with annealing at 57^{o}C and extension at 72^{o}C for 20 s. To ensure that quantitation was done in the exponential phase of the amplification process for both sequences, PCR was performed at 20, 25 and 29 cycles for GAPDH and 27, 29 and 32 cycles for Periaxin. 25 cycles for GAPDH and 29 cycles for Periaxin were determined for quantitation of mRNA expression levels. PCR products were resolved on 1.5% agarose gels, visualized by ethidium bromide under UV light and photographed.

2.4 GST FUSION PROTEIN PULLDOWN ASSAYS

2.4.1 GST Fusion Protein Production

GST-DRP2 containing the Periaxin binding domain and GST-fusion protein containing the third fibronectin III domain of β4-integrin were generated by Dr. Diane Sherman. Briefly, DRP2 (aa 110-390) and β4-integrin 3rd fibronectin III were amplified by PCR and subcloned in frame into pGEX-KG for generation of GST fusion proteins. GST fusion constructs were transformed into *E.coli* BL21 CodonPlus-RIL (DE3) (Stratagene). Recombinant proteins were overexpressed by induction of transformed cells at log phase with 1 mM isopropyl-1-thio-D-galactopyranoside (IPTG) for 3 h at 28^{o}C. The bacterial pellet was lysed with 50 mM Tris, pH 8.0 and 2 mM DTT containing protease inhibitor cocktail (Roche) by

sonication (Branson Digital Sonifier), and the supernatant from a 13000 rpm centrifugation (SS34 rotor, Sorvall) was purified on a Glutathione-Sepharose 4B (Amersham Pharmacia Biotech) column at room temperature. Recombinant proteins were eluted from the column with 10 mM reduced glutathione in 50 mM Tris, pH 8.0. To remove glutathione, purified fusion proteins were dialyzed against 50 mM Tris, pH 8.0 and 100 mM NaCl at 4^{o}C. Protein concentration was estimated by comparing band intensity with known concentrations of bovine albumin (BSA) on an SDS polyacrylamide gel.

2.4.2 GST Pulldown Assays

Purified GST fusion proteins were used in GST pulldown assays to be analyzed by Western blotting or Coomassie blue stain/proteomics.

For Western blotting, GST alone or GST-DRP2 (6 μg) were coupled to Glutathione-Sepharose 4B beads (25 μl, Amersham Pharmacia Biotech) by incubation for 1 h at room temperature followed by 1 h at 4^{o}C in binding buffer (50 mM Tris, pH 7.5, 200 mM NaCl, 0.5% CHAPS, 1 mM EDTA) containing phosphatase (5 mM NaF, 1 mM Na_3VO_4, 2 mM $Na_4P_2O_7$) and proteinase inhibitors (0.5 mM TLCK, 1 mM benzamidine, 1 mM PMSF, 10 μg/ml leupeptin, 10 μg/ml antipain). Beads were washed three times with binding buffer to remove ethanol in the storage buffer prior to incubation with GST-fusion proteins. Following binding with GST-fusion proteins, beads were washed four times with binding buffer. Sciatic nerves of 6-week-old WT and Δ*PDZ-Prx* mice were homogenized in binding buffer, lysed on ice for 20 min, and centrifuged for 20 min at 13000 rpm at 4^{o}C. 1/10 volume of the cleared lysate was removed and used as input for Western blotting. The washed beads were incubated with the homogenate in binding buffer for 3 h at 4^{o}C with rotation on a rotating wheel. The beads were washed 6-10 times in binding buffer, followed by once with binding buffer lacking detergent. Proteins were eluted with SDS-PAGE sample buffer (50 mM Tris pH 6.8, 2% SDS, 0.1% bromophenol blue, 10% glycerol) containing 100 mM dithiothreitol (DTT), resolved on 5.5% SDS polyacrylamide gels, transferred to nitrocellulose and analyzed by Western blotting using anti-Periaxin repeat region (1:30,000).

For the purpose of N-terminal protein sequencing of mutant Periaxin, GST alone or GST-β4-integrin 3rd fibronectin III (6 μg) were coupled to Glutathione-

Sepharose 4B beads as described. This pulldown assay was performed by Dr. Diane Sherman. Trigeminal and sciatic nerves from 6-week-old Δ*PDZ-Prx* mice were homogenized in binding buffer. The washed beads were incubated with the homogenate in binding buffer for 3 h at 4^{o}C with rotation. The beads were washed extensively in binding buffer, and proteins were eluted with SDS-PAGE sample buffer and resolved in 6% SDS polyacrylamide gels. Proteins on SDS gels were stained with 0.1% Coomassie Blue G, 45% methanol and 10% glacial acetic acid for 1 h at room temperature, followed by destaining with 10% glacial acetic acid and 20% methanol to visualize the mutant Periaxin band. The eluted sample was sent for N-terminal Edman degradation sequencing (Aberdeen Proteomics, University of Aberdeen).

2.5 YEAST TWO-HYBRID INTERACTIONS

2.5.1 Generation of Periaxin PDZ mutant constructs as the bait plasmid

2.5.1a- Periaxin PDZ domain deletion mutants

PDZΔβ1 (nt 345-581; aa 25-103) and PDZΔβ6 (nt 276-536; aa 2-88) (Fig. 12) were amplified by PCR with introduction of an EcoRI restriction site at the 5' end and a termination codon and BamHI site at the 3' end. The PCR template was rat L-Periaxin cDNA in pSPORT (Gibco BRL). PCR reaction was performed using Phusion High-Fidelity DNA Polymerase (Finnzymes) with primers Peri 96 and 97 for PDZΔβ1, and DLS 29 and Peri 98 for PDZΔβ6. PCR conditions were: initial enzyme activation at 98^{o}C for 30 s; followed by 35 cycles consisting of denaturation at 98^{o}C for 10 s, annealing at 58^{o}C for 30 s and extension at 72^{o}C for 8 s. PCR products were purified and restriction digested with EcoRI and BamHI, and subsequently subcloned in frame into pAS2-1 and pGBKT7 yeast GAL4 DNA binding domain vectors (Clontech) to produce GAL-4 binding domain fusion proteins. 1U of T4 DNA ligase (Fermentas) with Quick Ligation buffer (New England BioLabs) was used for a 15 min ligation at room temperature. Competent DH5α cells were transformed (Sambrook and Russell, 2001), and plated on LB agar containing 0.1 mg/ml carbenicilin for pAS2-1 constructs or 25 μg/ml kanamycin for pGBKT7 constructs. Randomly selected colonies were checked for inserts by colony PCR using Go Taq polymerase with forward primer BDF in the vector and reverse

primer Peri 97. Colony PCR cycling parameters were: 1 cycle of denaturation at 94°C for 1 min 30 s, annealing at 55°C for 30 s and extension at 72°C for 20 s for a 400 bp product, followed by 35 cycles of 94°C for 40 s, 55°C for 30 s and 72°C for 20 s. The final cycle consisted of 94°C for 40 s, 55°C for 30 s and 72°C for 2 min.

Plasmid DNA containing the insert was purified using Nucleospin Plasmid DNA purification kit (MACHEREY-NAGEL) and sequenced (DNA Sequencing & Services, Dundee University).

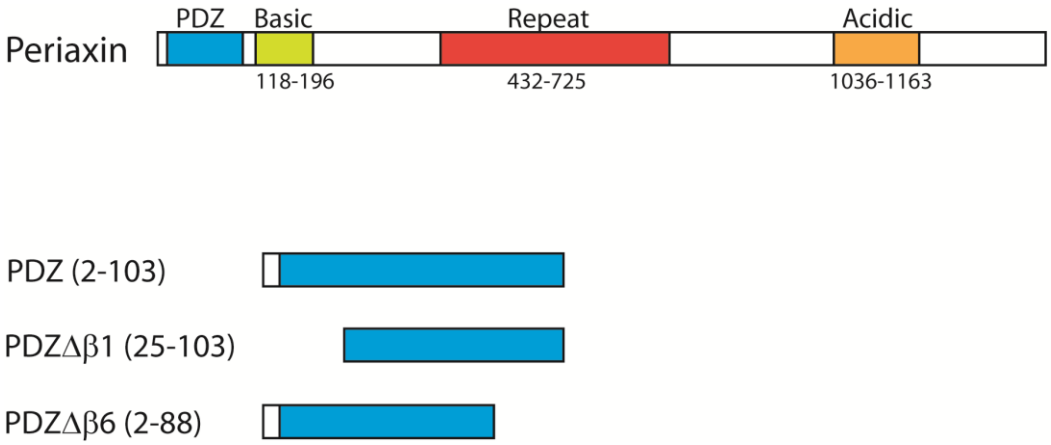

Figure 12. Periaxin PDZ domain deletion mutant constructs PDZΔβ1 and PDZΔβ6 in yeast.

2.5.1b- Periaxin PDZ domain single amino acid mutations

Single amino acid changes in Periaxin PDZ domain were introduced by PCR site-directed mutagenesis using a Quikchange site-directed mutagenesis kit (Strategene). Aspartate 63, glutamate 18, threonine 23 and glycine 31 were substituted by an alanine to generate the following PDZ domain mutants (nt 276-581; aa 2-103): PDZ-D63A, PDZ-E18A, PDZ-T23A and PDZ-G31A. In brief, site-directed mutagenesis was performed using PfuUltra II polymerase (1.25 U, Strategene) on rat L-Periaxin cDNA in pCB6 (10 kb, from Dr. Diane Sherman) with primers containing the desired mutation (see below). The PCR conditions were: 1 cycle of 95°C denaturation for 30 s, 16 cycles of denaturation at 95°C for 30 s, annealing at 55°C for 1 min and extension at 68°C for 10 min. The PCR product was treated with DpnI for 1 h at 37°C to digest methylated, non-mutated parental DNA template. The mutated plasmid was transformed into DH5α competent cells. Mutations were later confirmed by sequencing. Periaxin PDZ domain region (aa 2-103) harboring the

desired mutations was amplified by PCR using Phusion polymerase at an annealing temperature of 58^{o}C and a 9 s extension at 72^{o}C, with 5' EcoRI and 3' BamHI sites introduced. The primers were DLS 29 and Peri 97. Following restriction digestion and Qiaex-purification, PCR products were subcloned as described. Plasmid DNA was purified using Nucleospin columns and sequenced. All constructs generated by PCR were confirmed by DNA sequencing. Positive control PDZ (nt 276-581; aa 2-103) in pAS2-1 was provided by Dr. Diane Sherman.

Primer sequences:

PDZΔβ1 (nt 345-581; aa 25-103)

Peri 96	F	5'-CGGAATTCGCACAGACCGGGGTCAGC-3'	EcoRI
Peri 97	R	5'-CGGGATCCTCACCCGGTGGGCACAGTGCGCTTC-3'	Stop, BamHI

PDZΔβ6 (nt 276-536; aa 2-88)

DLS 29	F	5'-GGGATTCGAGGCCAGGAGCCGCAGCGCT-3'	EcoRI
Peri 98	R	5'-CGGGATCCTCACTCTGCGCATTGCAGCAGGC-3'	Stop, BamHI

PDZ-E18A (nt 276-581; aa 2-103)

Peri 101	F	5'-GAGCGGAGTTGGTGGCCATTATCGTGGAGACAG-3'
Peri 102	R	5'-CTGTCTCCACGATAATGGCCACCAACTCCGCTC-3'

PDZ-T23A (nt 276-581; aa 2-103)

Peri 103	F	5'-GAGATTATCGTGGAGGCAGAGGCGCAGACCG-3'
Peri 104	R	5'-CGGTCTGCGCCTCTGCCTCCACGATAATCTC-3'

PDZ-D63A (nt 276-581; aa 2-103)

Peri 105	F	5'-GTTTGCAGGAAGGGGCCCAACTTCTGAGCGC-3'
Peri 106	R	5'-GCGCTCAGAAGTTGGGCCCCTTCCTGCAAAC-3'

PDZ-G31A (nt 276-581; aa 2-103)

Peri 115	F	5'-ACCGGGGTCAGCGCCTTCAATGTAGCA -3'
Peri 116	R	5'-CTGCTACATTGAAGGCGCTGACCCCGGT-3'

2.5.2 Yeast-two-hybrid interaction assays

Yeast strain Y190 (Clontech) containing *lacZ* as a reporter gene was used for yeast two-hybrid interactions. Interactions were performed by co-transformation of the bait plasmid and the prey plasmid in Y190 or by yeast mating. PDZ (nt 276-764; aa 2-164) in GAL4 activation domain vector pACT2 (Sherman et al., 2001) was used as the prey plasmid in the interaction assays. For yeast mating, the bait in yeast strain Y190 was mated with the prey in strain Y187 (Clontech) according to the manufacturers' instructions (Clontech).

2.5.2a- Yeast transformation

Yeast transformation was based on the lithium acetate (LiAc)-mediated TRAFO method (Gietz and Schiestl., 1995). Frozen glycerol stock of Y190 strain was recovered on a YPAD agar plate at 30^{o}C for 72 h. 5 ml liquid YPAD was inoculated with a 2-3 mm yeast colony and incubated with shaking overnight at 30^{o}C. The following day, 50 ml liquid YPAD was inoculated with the overnight culture to a cell density of 5×10^{6}/ml and incubated at 30^{o}C with shaking at 200 rpm until a cell density of 2×10^{7}/ml was reached. The yeast culture was centrifuged at 3000 × g for 4 min and cells were resuspended in sterile MiliQ water. After centrifugation, yeast cells were resuspended in 1 ml 100 mM LiAc (Sigma) and pelleted again at 13000 rpm for 15 s. LiAc was removed and cells were resuspended to a final density of 2×10^{9}/ml in 100mM LiAc. 50 µl of resuspended cells was used for one transformation. The transformation mix was prepared by adding in sequence:

240 µl polyethylene glycol (PEG, MW 3350, 50 % w/v, Sigma)

36 µl 1M LiAc

25 µl sheared salmon sperm DNA (2 mg/ml, Eppendorf)

50 µl sterile MiliQ water and 1 µg plasmid DNA

The mix was vortexed vigorously for 1 min prior to incubation at 30^{o}C for 30 min, followed by a 22 min heat shock at 42^{o}C. Cells were pelleted at 7000 rpm for 15 sec, gently resuspended in sterile water and plated on synthetic minimal (SD) agar lacking tryptophan for selection of transformants. The omission of tryptophan from SD medium selects for the GAL4-binding domain vectors, pAS2-1 and pGBKT7, which contain the *TRP1* gene, whereas excluding leucine from SD medium selects

for activation domain vector pACT2, which contains the *LEU2* gene. Leaving out both amino acids from SD medium selects for both vectors.

Co-transformation of both the bait and prey plasmid was performed as described, and co-transformants were selected on SD agar plates lacking both tryptophan and leucine. Plates were incubated at 30^{o}C for 72 h, and transformant colonies were tested for β-galactosidase activity by filter-lift assay thereafter.

2.5.2b- Preparation of yeast protein extracts

After incubating for 72 h at 30^{o}C, a single colony of each transformed yeast strain was streaked out and incubated in SD medium without tryptophan at 30^{o}C with shaking at 200 rpm for 48 h. The culture was vortexed and pelleted at 2500 rpm for 5 min at 4^{o}C. The supernatant was removed and pellet was snap-frozen in liquid nitrogen. Subsequently, the pellet was thawed and resuspended in 60^{o}C pre-warmed cracking buffer consisting of 8M urea, 5% (w/v) SDS, 40 mM Tris-HCl, pH 6.8, 0.1 mM EDTA, 0.4 mg/ml bromophenol blue, 10 μl/ml β-mercaptoethanol, 0.1 mg/ml pepstatin A, 0.03 mM leupeptin, 145 mM benzamidine, 0.5 mg/ml antipain and 5 mM PMSF. The cell suspension was transferred to a microcentrifuge tube containing glass beads (Sigma), incubated at 70^{o}C for 10 min, and vortexed vigorously for 1 min for yeast cell wall disruption. Following centrifugation at 13000 rpm for 5 min, the supernatant was boiled for 5 min and proteins were resolved by SDS-PAGE on 14% gels. Protein expression of PDZ domain mutants was analyzed by Western blotting using anti-Periaxin N-terminus and anti-c-myc antibodies.

2.5.2c- Yeast mating

The bait in yeast strain Y190 was mated with the prey in strain Y187 (Clontech) in a 96-well plate. A single transformant colony of each type was resuspended in YPAD medium. Aliquots of cell suspensions containing the bait and prey plasmids were incubated in the same well at 30^{o}C overnight with shaking at 200 rpm. Next day, the mating culture was plated on SD agar without tryptophan and leucine, and tested for interaction by filter-lift assay 48 h later.

2.5.2d- Filter-lift assays

Interactions were tested for β-galactosidase activity by filter-lift assay, which was semi-quantitatively assessed by the amount of time taken for the development of blue

colonies: +++, <30 min; ++, 30-60 min; +, 60-180 min. In brief, for each plate of transformants to be assayed, a sterile filter paper (Whatman No. 5, 70 mm) was pre-soaked in 1 ml Z buffer (16.1 g/L Na_2HPO_4, 5.5 g/L NaH_2PO_4, 0.75 g/L KCl, 0.246 g/L $MgSO_4$, pH 7.0) containing 1.5 mg X-gal and 2.7 μl β-mercaptoethanol in a clean petri dish. A sterile, dry filter was placed over the surface of the plate of transformants and rubbed gently to collect colonies. The filter was snap-frozen for 15 s in liquid nitrogen, and then thawed at room temperature. This step was repeated. The filter containing transformant colonies was placed on the pre-soaked filter, and incubated at 37^{o}C for development of blue colonies.

2.6 CELL CULTURE

2.6.1 General cell culture

HEK 293 cell line was used for all transfection experiments in this work due to high efficiency of transfection and recombinant protein production (Thomas and Smart, 2005). Most importantly, the cell line, from human embryonic kidney origin, does not contain endogenous Periaxin. Therefore, any Periaxin levels detected are solely attributed to the exression of recombinant Periaxin. HEK 293 cell line was maintained in complete Dulbecco's Modified Eagle's medium (DMEM) containing 10% fetal calf serum (FCS, Sigma), 2 mM L-glutamine (Sigma), 100 U/ml penicillin and 100 μg/ml streptomycin (Sigma) at 37^{o}C in a humidified CO_2-enriched incubator. When ~90% confluent, cells were passaged by washing once with sterile PBS followed by incubating for 1-3 min in 0.25% (w/v) Trypsin/EDTA. After adding complete DMEM medium, the cells were pelleted by centrifugation at 1000 × g for 3 min. Cells were gently resuspended in 1 ml complete medium and plated either on glass coverslips or tissue culture Petri dishes (Greiner Bio-one) at the appropriate densities for transient transfection experiments. Alternatively, cells were frozen in 20% FCS, 10% DMSO in DMEM at -80^{o}C overnight, and then transferred to liquid nitrogen for long-term storage.

2.7 CELL TRANSFECTION

2.7.1 Generation of constructs for transfection

2.7.1a- FLAG-tagged and myc-tagged full length Periaxin

Generation of rat full length L-Periaxin cDNA (nt 268-4421; aa 1-1384) in mammalian expression vectors pFLAG-CMV5a (Sigma) with an introduced XbaI site and pCB6myc (gift of D.Russell, University of Texas) was performed by Dr. Diane Sherman, as previously described (Sherman et al., 2001). The constructs were expressed as full length Periaxin with a C-terminal myc-epitope tag and a C-terminal FLAG tag, respectively, and were used as positive controls.

2.7.1b- FLAG-tagged mutant Periaxin ΔPDZ-Prx lacking the PDZ domain

To generate ΔPDZ-Prx (nt 618-4421; aa 116-1384) in pFLAG-CMV5a, KpnI site (nt 1323) in L-Periaxin cDNA and XbaI site upstream of the triple c-myc epitope tag in pCB6 were digested and inserted into cloning vector pSP72 to generate Peri-pSP72. The 5'end of ΔPDZ-Prx up to downstream of the KpnI site was amplified by PCR using Phusion polymerase, with a BglII site introduced at the 5' end, at an annealing temperature of 57^{o}C and extension at 72^{o}C for 1.5 min. The template was rat L-Periaxin cDNA in pSPORT using primers Peri 89 and CSG 3. The PCR product was purified, restriction digested with BglII and KpnI, and cloned into BglII/KpnI digested Peri-pSP72. Correct sequence of the PCR generated region in the construct was confirmed by DNA sequencing. ΔPDZ-Prx cDNA was excised from pSP72 by BglII and XbaI, and cloned into BglII/XbaI digested pFLAG-CMV5a. This indirect strategy was used due to the presence of a KpnI site in pFLAG-CMV5a. The orientation of the insert was confirmed by restriction digestion. Plasmid DNA was sequenced to check for in frame insertion, and subsequently prepared for transfection using the Qiagen midiprep kit with endotoxins removed.

2.7.1c- myc-tagged full length Periaxin with single amino acid changes in PDZ domain

Single amino acid mutations (T23A, G31A and D63A) in the PDZ domain of full length Periaxin in pCB6 were introduced by site-directed mutagenesis as described. The 5'end up to the KpnI site in L-Periaxin cDNA containing the desired mutation was excised with BglII and KpnI, and subsequently subcloned into BglII/KpnI

digested non-mutated L-Periaxin in pCB6. The resulting mutant constructs were purified for transfection using Nucleospin columns, and sequenced to check for orientation and fidelity of the subcloned region.

2.7.2 *In vitro* transient transfection

HEK 293 cells were either seeded at 2×10^5 cells/ 35 mm Petri dish containing poly-D-lysine-coated (80 µg/ml, Sigma) acid-washed 13 mm glass coverslips or 6×10^5 cells/60 mm Petri dish 1 day before transfection. FuGENE 6 Transfection Reagent (Roche): DNA ratio of 3:1 was used for all transfections. For a 60 mm dish, 9 µl FuGENE 6 Reagent was incubated in 191 µl Opti-MEM I (Gibco) for 5 min at room temperature. Plasmid DNA of interest in total of 3 µg was added to the diluted FuGENE solution and incubated for 20 min at room temperature before adding to the cells. For a 35 mm dish, cells on coverslips were transiently transfected with 100 µl Opti-MEM I containing 1 µg DNA and 3 µl FuGENE 6 Reagent. Cells were harvested 24 h and 48 h later for immunostaining and co-immunoprecipitation, respectively.

2.8 CO-IMMUNOPRECIPITATION

2.8.1 Preparation of cell lysates and co-immunoprecipitation

48 h following transfection, cells were washed once with cold PBS, scraped off the dish and lysed with IP buffer (50 mM Tris pH 7.5, 150 mM NaCl, 1% Triton X-100, 1 mM EDTA, and phosphatase and proteinase inhibitors: 5 mM NaF, 1 mM Na_3VO_4, 2 mM $Na_4P_2O_7$, 0.5 mM TLCK, 1 mM benzamidine, 1 mM PMSF, 10 µg/ml leupeptin, 10 µg/ml antipain) for 30 min at 4^{o}C on wheel. Following centrifugation at 13000 rpm for 20 min at 4^{o}C, 1/10 of the lysate was set aside as input and the rest was incubated with 16 µl washed anti-FLAG M2 affinity gel (Sigma) at 4^{o}C overnight on wheel. Next day, the coupled FLAG M2 beads were pelleted by centrifugation at 6000 rpm, and washed 6-10 times with IP buffer and once with the same buffer without detergent. Immunoprecipitated proteins were eluted with SDS-PAGE sample buffer and resolved on 5.5% SDS polyacrylamide gels. Protein interaction was analysed by Western blotting using anti-FLAG M2 monoclonal antibody (1:8000, Sigma) and anti-c-myc (9E10), 1:10. The experiment was performed at least three times, including transient transfections.

2.9 SDS-PAGE AND WESTERN BLOTTING

2.9.1 Protein extraction from peripheral nerves

For general immunoblotting (for Periaxin, DRP2, γ-actin), trigeminal or sciatic nerves from 3-week and 4-month-old mice were dissected and homogenized in pre-warmed 2% SDS by boiling for 5 min. Following centrifugation at 13000 rpm for 5 min at room temperature, the cleared supernatant was recovered and stored at -80^{o}C until use. Protein concentration of the homogenate was determined by BCA assay (Pierce) according to the manufacturers' instructions. Proteins were diluted and denatured by boiling in SDS sample buffer, and separated by electrophoresis on SDS polyacrylamide gels.

For immunoblotting for signal transduction proteins, e.g. AKT, ERK1/2, Dlg-1 and mTOR, sciatic nerves from mice of various ages were dissected and transferred to ice cold PBS containing phosphatase inhibitors: 5 mM NaF, 1 mM Na_3VO_4, 2 mM $Na_4P_2O_7$. The epineurium and perineurium were removed, and nerves were homogenized in RIPA buffer (50 mM Tris pH 7.5, 150 mM NaCl, 1% NP-40, 0.1% SDS, 0.5% sodium deoxycholate, 1 mM EDTA) containing phosphatase and proteinase inhibitors on ice for 25 min. The supernatant was recovered after centrifugation at 13000 rpm at 4^{o}C for 20 min. Protein concentration was determined and proteins were prepared in SDS sample buffer as described. At least 50 μg of protein was loaded for detection of Dlg-1, PTEN and phosphorylated signal transduction proteins by Western blot.

2.9.2 Western Blotting

Following SDS-PAGE, proteins were transferred electrophoretically to nitrocellulose membrane (0.45 μm, Schleicher and Schuell) in transfer buffer containing 25 mM Tris pH 8.3, 192 mM glycine, and 20% methanol for 4 h (or overnight for signal transduction proteins) at 400 mA. Membranes were blocked for 1 h with 5% non-fat milk in Tris-buffered saline, 0.1% Tween 20 (TBST), and then probed with primary antibodies diluted in 1% non-fat milk in TBST for 1.5 h at room temperature. Dilutions of primary and secondary antibodies for Western blotting were specified in Table 2. The membranes were washed several times with TBST before incubation with HRP-conjugated secondary antibodies for 1 h at room temperature. Subsequent

to 4-5 washes of 10 min with TBST, the blots were visualized by electrochemiluminescence (ECL) detection (Santa Cruz).

2.10 INDIRECT IMMUNOFLUORESCENCE

Immunofluorescence was performed on teased fibers, frozen cryosections and cultured cells.

2.10.1 Teased fiber preparation

Mouse quadriceps nerves were removed and immersion fixed for 30 min in 4% paraformaldehyde in 0.1 M sodium phosphate buffer (pH 7.4). Nerves were washed several times with phosphate buffer and transferred into a 35 mm Petri dish containing PBS. The perineurium was removed, and nerve fiber bundles were separated and teased into individual fibers with acupuncture needles in a drop of phosphate buffered saline (PBS, pH 7.4) on 3-aminopropyltriethoxysilane (TESPA, 2%, Sigma)-coated glass slides followed by air-drying. Slides were stored at -20^{o}C until use.

2.10.2 Cryostat sections

Quadriceps and sciatic nerves from mice were dissected, fixed and washed as for teased fiber preparation. Nerves were cryoprotected using a sucrose gradient of 5%, 10% and 25% in 0.1 M sodium phosphate buffer, and subsequently embedded in OCT embedding matrix (CellPath, Ltd) and frozen with isopentane cooled in liquid nitrogen. The blocks were stored at -80^{o}C until use. Longitudinal sections were cut at 7 µm, and transverse sections at 10 µm on a Leica CM 3050 S cryostat. Sections were collected on TESPA-coated glass slides, dried and stored at -20^{o}C until needed. Prior to immunostaining, slides were rinsed twice with PBS to remove OCT.

2.10.3 Immunohistochemistry

Teased fibers or cryosections were blocked with 5% fish skin gelatin, 0.2% Triton X-100 in PBS for 1 h, followed by primary antibody incubation in the same blocking solution in a humidified chamber overnight at room temperature. Primary and secondary antibodies were diluted as shown in Table 2. After washing with at least four changes of 0.1% Triton X-100 in PBS, slides were incubated with fluorescent-conjugated secondary antibodies in blocking solution for 1.5 h in the dark at room

temperature. Slides were washed several times with PBS and mounted in Vectashield (Vector Labs, Burlingame, California) containing DAPI (Sigma).

2.10.4 Fixation and immunostaining of cultured cells

24 h post-transfection, HEK 293 cells grown on poly-D-lysine-coated 13 mm glass coverslips were fixed with 4% paraformaldehyde in 0.1 M phosphate buffer for 20 min, washed three times with PBS, and blocked for 30 min prior to incubation with primary antibodies on parafilm for 1 h at room temperature in a humidified Petri dish. To check for expression of transfection constructs, immunolabeling with anti-FLAG and anti-myc antibodies was performed. Coverslips were washed with four changes of PBS and incubated with secondary antibodies in the dark for 1 h at room temperature. After washing with PBS, cells on coverslips were mounted in Vectashield.

2.10.5 Image acquisition

Bright field and fluorescence imaging for morphometric analysis were performed using an Olympus BX60 microscope equipped with a Hamamatsu ORCA-ER digital camera with assistance of the software OpenLab (version 5.5.2). For confocal laser scanning microscopy, a Leica TCL-SL confocal microscope with a 40× or a 63× objective, 1.4 NA, and Leica proprietary software was used for acquiring fluorescence and phase contrast images of teased fibers and fluorescence images of cryosections. FITC- and TRITC-fluorophores were excited with an Argon (488 nm) and HeNe (543 nm) laser, respectively. Z stacks were assembled using the maximum projection tool of the imaging software. Figures were prepared using Adobe Photoshop CS4 extended version 11 (Adobe Systems).

Table 2. Reagents used for immunfluorescence and Western blot

Primary antibodies, secondary antibodies and fluorophore-conjugated dyes used in the present study are shown in the following tables.

(IF: immunofluorescence; WB: Western blot)

Primary antibodies

Antibody name	**Species**	**Source**	**Dilution (IF)**	**Dilution (WB)**
Anti-γ actin	Rabbit	P.J.Brophy	-	1:10000
Anti-AKT	Rabbit	Cell Signaling	-	1:1000
Anti-c-myc (clone 9E10)	Mouse (Hybridoma)	P.J.Brophy	-	1:10
Anti-c-myc (clone 9E10)	Mouse	Sigma	1:200	-
Anti-Dlg1 (SAP 97)	Mouse	Enzo Lifesciences	1:100	1:1000
Anti-DRP2 2155	Rabbit	P.J.Brophy	-	1:3000
Anti-DRP2 2164	Rabbit	P.J.Brophy	1:300	-
Anti-dystrophin (MANDRA I)	Mouse IgG1	Sigma	1:150	-
Anti-ERK1 (K-23)	Rabbit	Cell Signaling	-	1:1000
Anti-FLAG	Rabbit	Sigma	1:400	-
Anti-FLAG M2	Mouse IgG1	Sigma	-	1:8000
Anti-Gliomedin (720)	Rabbit	E. Peles	1:500	-
Anti-Krox-20	Rabbit	Covance	1:200	1:500
Anti-Kv1.1 channel	Rabbit	Chemicon	1:200	-
Anti-MBP (pep7)	Rabbit	P.J.Brophy	1:400	1:3000
Anti-mTOR (7C10)	Rabbit	Cell Signaling	-	1:1000
Anti-Neurofascin (NF155, NFC2)	Rabbit	P.J.Brophy	1:1000	-
Anti-Neurofascin (NF155 NFC3)	Sheep	P.J.Brophy	1:1000	-
Anti-Neurofilament 200 kDa	Mouse IgG1	Sigma	1:1000	1:10000
Anti-P0	Rabbit	D.Colman	-	1:3000
Anti-P0	Chicken IgY	Aves Labs	1:100	-
Anti-p75 NGFR	Rabbit	Millipore	1:1000	-
Anti-pan Na^+ channel	Mouse IgG1	Sigma	1:200	-
Anti-pan Neurofilament R39	Rabbit	D.Dahl	1:400	-
Anti-Periaxin (Repeat region)	Rabbit	P.J.Brophy	1:8000	1:30000
Anti-Periaxin (C-terminus)	Rabbit	P.J.Brophy	-	1:10000

Anti-Periaxin (N-terminus)	Rabbit	P.J.Brophy	1:2000	1:20000
Anti-phospho AKT (Ser473)	Rabbit	Cell Signaling	-	1:1000
Anti-phospho ERK1/2	Rabbit	Cell Signaling	-	1:1000
Anti-phospho mTOR (Ser2448)	Rabbit	Cell Signaling	-	1:1000
Anti-phospho S6 Ribosomal protein (Ser235/236)	Rabbit	Cell Signaling	-	1:1000
Anti-PTEN (9552)	Rabbit	Cell Signaling	-	1:1000
Anti-Radixin (RAD4)	Rabbit	P.J.Brophy	1:400	-
Anti-s100	Rabbit	DAKO	1:200	-
Anti-S6 Ribosomal protein (5G10)	Rabbit	Cell Signaling	-	1:1000
Anti-Sox10	Guinea pig	M.Wegner	1:1000	-
Anti-Tubulin (ICN)	Rabbit	P.J.Brophy	-	1:1000

Secondary Antibodies

Antibody name	**Species**	**Source**	**Dilution**
FITC-conjugated anti-rabbit IgG	Donkey	Jackson	1:100
FITC-conjugated anti-rabbit IgG	Goat	Cappel	1:200
FITC-conjugated anti-mouse IgG1	Goat	Southern Biotec	1:200
TRITC-conjugated anti-mouse IgG1	Goat	Southern Biotec	1:200
TRITC-conjugated anti-chicken IgY	Donkey	Jackson	1:75
TRITC-conjugated anti-guinea pig IgG	Donkey	Jackson	1:200
Cy3-conjugated anti-rabbit	Donkey	Jackson	1:500
HRP-conjugated anti-rabbit IgG	Goat	Jackson	1:50000
HRP-conjugated anti-mouse IgG	Goat	Jackson	1:20000

Fluorescent-conjugated dyes

Antibody name	**Source**	**Dilution**
Alexa 568-conjugated phalloidin	Invitrogen	1:50
DAPI, 4',6-diamidino-2-phenylindole	Sigma	4 μg/ml

2.11 ELECTRON MICROSCOPY

Mice were terminally anesthetized with intraperitoneal injection (i.p.) of pentobarbital (0.2 mg/g body weight) and perfused transcardially with freshly prepared fixative containing 4% paraformaldehyde, 2.5% glutaraldehyde in 80 mM sodium cacodylate buffer, pH 7.4. Quadriceps nerves were dissected and immersion fixed in the same fixative for 4 h at room temperature then overnight at 4^{o}C. Next day, nerves were washed twice with 0.1 M sodium cacodylate buffer, pH 7.4, followed by post-fixation in 1% osmium tetroxide (OsO_4) in 0.1 M sodium cacodylate buffer for 1 h at room temperature. Subsequently, nerves were washed 3 times with 0.1 M cacodylate buffer prior to dehydration through an ascending series of ethanol (50%, 70%, 90%) for 5 min each, three 10-min changes of absolute ethanol and finally two changes of propylene oxide for 15 min each. The tissue was infiltrated with a 1:1 (v/v) mixture of araldite (araldite CY212 and DDSA, Agar Scientific) and propylene oxide for 1 h followed by araldite overnight at room temperature. After incubating in fresh araldite containing polymerizer (dibutyl phthalate (DBT) and benzyldimethylamine (BDMA), Agar Scientific) for 2 h, nerves were embedded in araldite in transverse orientation in flat silicone moulds. Resin was polymerized at 60^{o}C for 48 h.

400 nm thick semithin cross sections were cut on a Leica Ultracut UCT ultramicrotome, stained with 1% Toluidine in 1% borate buffer, mounted in Cytoseal mounting medium (VWR) and examined by bright field microscopy. Images were captured at 20×, 40× and 100× magnifications using a digital camera with Openlab software. Ultrathin sections of 70 nm were stained with uranyl acetate and lead acetate and examined on a Philips/FEI CM120 BioTwin electron microscope. EM images were acquired using an Orius TEM SC1000 camera (Gatan). Ultrathin sectioning and staining were performed by Stephen Mitchell at the EM facility.

For osmicated teased fiber preparation, following transcardial perfusion quadriceps nerves were excised and fixed as described. Nerves were post-fixed in 1% OsO_4 in 0.1 M sodium cacodylate buffer for 1 h at room temperature and subsequently washed with 0.1 M sodium cacodylate buffer. Nerve fibers were teased into single fibers in a drop of PBS on TESPA-coated slides, mounted in glycerol and examined by bright field microscopy.

2.12 MORPHOMETRY

2.12.1 Internodal length measurements

Teased single fibers isolated from quadriceps nerves of 3-week-old WT, Δ*PDZ-Prx*, *Prx* KO, and *Cnp-Cre*$^{+/-}$ were immunostained with monoclonal mouse anti-dystrophin (Mandra I, Sigma) 1:150, Alexa 568 conjugated-phalloidin and DAPI, and imaged at 10× magnification in a camera-equipped fluorescence microscope with OpenLab acquisition software. The distance between two nodes of Ranvier was measured using the same software. At least 100 Schwann cell internodes were measured per animal ($n \geq 3$ for each group). For internodal length measurements of 4-month-old tamoxifen-treated *Prx*$^{fl/fl}$ and *Prx*$^{fl/fl}$*/P0CreERT* Schwann cells, teased fibers were immunolabeled with anti-dystrophin and anti-Periaxin N-terminus or anti-DRP2. Internodal lengths of recombined *Prx*$^{fl/fl}$*/P0CreERT* fibers lacking Periaxin N-terminus immunoreactivity or DRP2 patches were determined.

For refined internodal length measurements to select for large diameter axons, teased fibers from 3-week-, 6-week- and 4-month-old WT and Δ*PDZ-Prx* quadriceps nerves were immunolabeled with anti-dystrophin (Mandra I), anti-pan neurofilament R39 and DAPI, and imaged using a 10× objective using a digital camera. Axon diameter was estimated as the mean width of each neurofilament-labeled axon at two positions along the measured internode. To determine the cut-off diameter for large caliber axons, 50% of total number of WT fibers at each age representing the percentage of large diameter axons, were taken into account. Average internodal length for large caliber fibers was computed from internodal lengths of myelinated fibers with axon diameter larger than or equal to the cut-off diameter. At least 100 Schwann cell internodes were measured per animal (n=3 for each group).

2.12.2 Schmidt-Lanterman incisure analysis

Quadriceps nerves from 2-month-old WT and Δ*PDZ-Prx* mice were dissected, fixed and teased as described. Teased fibers were stained with rabbit anti-RAD4 1:400 Alexa 568 conjugated-phalloidin and DAPI. Images were captured using a digital camera at 10× magnification with Openlab software. Internodal distance was measured as the distance between two RAD4-labeled Schwann cell microvilli. The

number of SLIs was counted along each internode in randomly chosen individual fibers. At least 100 internodes per animal (*n*=3 per group) were analyzed. The number of SLIs per 100 µm fiber length was presented.

2.12.3 Ratios of myelinating to non-myelinating Schwann cells

Cryostat cross sections of sciatic nerves of 3 weeks and quadriceps nerves from WT, Δ*PDZ-Prx* and *Prx* KO mice of 4 months were prepared as described. Sections were immunolabeled with rabbit anti-Krox20 for Schwann cells committed to myelination, and guinea pig anti-Sox10 for both myelinating and non-myelinating Schwann cells. Images were acquired with a 20× objective in a fluorescence microscope using a digital camera with Openlab software. The numbers of Krox20- and sox10-immunopositive cells were counted per cross section of each genotype (*n*=3 for each group).

2.12.4 Apposition and *g*-ratio analysis

Quadriceps nerves from 3-week-old WT and Δ*PDZ-Prx* mice were prepared for electron microscopy as described. Digitized electron micrographs of ultrathin cross sections of quadriceps nerves were analyzed for apposition numbers and *g*-ratios. Axon area, fiber area and the number of appositions per nerve fiber were measured using NIH Image (Image J) software. For apposition counts, at least 100 randomly selected nerve fibers were analyzed, excluding those surrounded by a Schwann cell nucleus or a Schmidt-Lanterman incisure. For *g*-ratio analysis, images were calibrated based on the scale bar corresponding to the magnification used for each micrograph. The axon (without myelin) and fiber areas (including myelin) of randomly chosen fibers were measured, except for those surrounded by a Schmidt-Lanterman incisure. The axon and fiber diameters were estimated as $2 \bullet \sqrt{(\text{area}/\pi)}$ and *g*-ratio was calculated as axon diameter/fiber diameter. At least 100 nerve fibers per animal (*n*=3 for each group) were analyzed.

2.12.5 Analysis of abnormal myelin profiles, myelinated axon numbers and nerve area

Semithin transverse sections (400 nm) from quadriceps nerves of 2-, 4-, 6- and 9-month-old WT, Δ*PDZ-Prx* and *Prx* KO mice were examined by bright field microscopy in a light microscope, and imaged with a 40× oil objective using a digital

camera with Openlab software. A series of 40× images were edited into a continuous complete quadriceps nerve cross section using Photoshop CS. The total number of myelinated axons was counted per cross section. Thinly myelinated or demyelinated axons were also counted. The proportion of fibers with tomacula and folded myelin, as indicated by redundant myelin loops, was calculated as the percentage of abnormal myelin profiles. The proportion of thinly myelinated or demyelinated axons surrounded by processes of supernumerary Schwann cells was determined as the percentage of onion bulbs. For nerve area analysis, semithin transverse sections from quadriceps nerves were imaged at 20× magnification using a digital camera. Nerve area was measured by NIH Image software. The area of the nerve cross section was measured three times by outlining its outer border and averaged. At least 3 animals per genotype for each time point were analyzed.

2.12.6 Analysis of paranodal myelin tomacula

Osmicated teased fibers of quadriceps nerves from 6-week-old WT and Δ*PDZ-Prx* mice were examined by bright field microscopy. Images were captured with a 20× objective using a digital camera with Openlab. The proportion of paranodes with myelin tomacula was computed as the percentage of paranodal myelin thickenings. At least 430 paranodes were examined per animal (*n*=3) for each genotype.

2.13 PHYSIOLOGY AND BEHAVIORAL ANALYSIS

2.13.1 Nerve Conduction Velocity

Femoral nerves+quadriceps branch were dissected from WT, Δ*PDZ-Prx* and Periaxin-null mice of various ages (3 weeks, 6 weeks, 4 months and 10 months of age; *n*=5-10), and maintained in oxygenated mammalian HEPES physiological solution containing 137 mM NaCl, 5 mM KCl, 2 mM $CaCl_2$, 1 mM $MgCl_2$, 5.5 mM D-glucose and 5 mM HEPES, pH 7.2-7.4. For periods of no longer than 10 min, nerves were transferred and placed on an array of Ag/AgCl electrodes with 1 mm intervals in an isolated chamber and surrounded by liquid paraffin kept at 37^{o}C. Compound action potentials (CAP) were recorded from the distal end of the quadriceps branch by stimulating the proximal end of the femoral nerve with a square wave (0.15 ms, 0.1-1.5 V). Depending on the length of the nerves, the conduction distance was altered from 3 mm to max. 11 mm by adjusting the position

of the stimulating electrode, except for 3-week-old nerves, in which conduction distance varied from 2 to 7 mm. The voltage of stimulus was adjusted to ensure excitation of the exact active population of nerve fibers. Signals of CAP were converted to digitized signals using Scope software (PowerLab data acquisition system). Latencies of the onset of CAP were measured from the stimulus artefact to the peak of the CAP for all conduction distances. The conduction velocity was calculated from the slope of the regression line by plotting conduction distances against the corresponding latencies. Recordings were repeated 2-3 times for each nerve. The conduction velocity per animal was determined by averaging the mean conduction velocities of both nerves.

2.13.2 RotaRod

3 week- and 4-month-old WT, Δ*PDZ-Prx* and *Prx* KO mice (10-16 per group) were trained on a 5-lane mouse RotaRod (Ugo Basile) for two consecutive days before the test on day 3. Animals were placed on a rotating RotaRod (3-cm diameter) sequentially at 24 rpm and 32 rpm for a maximum of 60s, four times at each speed. Each trial run was separated by a 10 min rest period. Mice were removed from the RotaRod either when they fell off the rod or at 60s. The mean latency to fall of each mouse, which measures the length of time each animal was able to stay on the rod, was determined by the mean latency from the four trials for each rotating speed obtained on day 3.

2.13.3 Sensory tests

WT and Δ*PDZ-Prx* mice (4-5 months of age; *n*=9-11) were tested for hindpaw withdrawal response to mechanical and noxious thermal stimulation. These tests were performed by Dr. Ada Delaney. In brief, conscious animals were tested for the threshold of hindpaw withdrawal in response to graded mechanical stimulation with von Frey filaments, which provide a calibrated indentation pressure against the hairless skin of the hindpaws. The threshold response was defined as the nominal bending force of the filament that evoked hindpaw withdrawal 5 times in a 10-time application (Chaplan et al., 1994). The withdrawal response to noxious thermal stimulation was determined by the time for hindpaw withdrawal in response to quantified noxious thermal stimulus by an infrared beam (Hargreaves et al., 1988).

2.14 TAMOXIFEN INDUCTION OF RECOMBINATION

Tamoxifen free base (Sigma, T5648) was dissolved in sunflower seed oil (Sigma)/ethanol (10:1) at 10 mg/ml. Sunflower seed oil was pre-warmed at 70^{o}C for 15 min. Tamoxifen was dissolved in the warm oil/ethanol mixture in a sonicating water bath for 30 min. 4-week-old mice were administered with tamoxifen via intraperitoneal injection (i.p.) at a dose of 1 mg/10g body weight, once per day for 10 consecutive days. Mice were treated again for 5 days after a 7-day rest period. Animals were sacrificed 18 weeks after the last treatment for protein expression and morphological analysis.

2.15 STATISTICS

All statistical analysis was performed and graphs were produced using GraphPad Prism (version 5.0c). All values are expressed as mean ± SEM. Unpaired, two-tailed Student's t- test was used to determine statistical significance between 2 groups of samples. One-way analysis of variance (ANOVA) followed by Tukey HSD multi-comparison post-test was used to assess *p* values between multiple samples (3 or more unpaired groups). For non-parametric statistical analysis, Mann-Whitney *U* test was used to determine statistical significance between 2 groups of samples, and Kruskal-Wallis test followed by Dunn's post-test was used for comparing 3 or more unpaired groups of samples. For hindpaw withdrawal response to mechanical stimulation, statistical significance was evaluated by Mann-Whitney Rank Sum test.

3- RESULTS

3.1 STUDY OF THE FUNCTION OF THE PERIAXIN PDZ DOMAIN IN PERIPHERAL NERVES

Periaxin forms a transmembrane complex with DRP2 and dystroglycan at distinct Schwann cell domains, termed appositions, between the abaxonal surface of the myelin sheath and the cytoplasmic face of the Schwann cell membrane (Sherman and Brophy, 2005; Sherman et al., 2001). This complex is essential for myelin sheath maintenance and stability in the mature PNS.

Charcot-Marie-Tooth (CMT) disease type 4F is caused by nonsense or frameshift mutations in the *Periaxin* gene (*PRX*) mapped on chromosome 19q13 (Delague et al., 2000; Guilbot et al., 2001). Our laboratory had previously generated a Periaxin-null mutant as a mouse model for CMT 4F. Mice deficient for Periaxin initially produce compact myelin, but later develop a peripheral nerve demyelinating neuropathy (Gillespie et al., 2000). In the absence of Periaxin, the Periaxin-DRP2-dystroglycan (PDG) complex is disrupted leading to the disruption of Cajal bands, which are longitudinal and transverse bands of cytoplasm along Schwann cell internodes formed between appositions. *Prx* KO Schwann cells have reduced internodal lengths, resulting in decreased nerve conduction velocities (Court et al., 2004). In the mature PNS, peripheral nerves display extensive demyelination, followed by remyelination, causing severe sensory and motor deficits (Gillespie et al., 2000).

Although the consequences of complete ablation of Periaxin in peripheral nerves have been well characterized, the functions of the different domain regions of Periaxin remain elusive. One of the most important mutations in the human *PRX* gene R1070X introduces a stop codon 28 amino acids upstream of the acidic domain of Periaxin, leading to the production of a large truncated protein lacking the acidic domain and the rest of the C-terminus. Periaxin without the C-terminal acidic domain causes severe demyelination, onion bulb formation and axonal loss in human patients. Patients diagnosed with this type of early onset demyelinating neuropathy display severe clinical symptoms such as unsteady gait contributed by distal muscle weakness and impaired sensory modalities (Guilbot et al., 2001; Kabzinska et al., 2006; Kijima et al., 2004; Otagiri et al., 2006; Parman et al., 2004; Takashima et al.,

2002). This highly implicates the importance of the specific domains within Periaxin for its various regulatory roles.

At the N-terminus of Periaxin is a PDZ domain, which has been speculated to play a chief role in recruiting proteins to a cortical scaffold for transmembrane signaling (Dytrych et al., 1998). Indeed, Periaxin homodimerizes at the PDZ domain in the PDG complex. However, the functional importance of the Periaxin PDZ domain, particularly its dimerization, has not been addressed. The study presented here examines the functions of the PDZ domain of Periaxin in the regulation of apposition formation and maintenance, Schwann cell elongation and stability of the myelin sheath, in a conditional mouse mutant expressing a version of Periaxin lacking the first 116 amino acids at the N-terminus, i.e. the PDZ domain in peripheral nerves.

PART A. GENERATION OF A CONDITIONAL MUTANT MOUSE LACKING THE PERIAXIN PDZ DOMAIN IN PERIPHERAL NERVES

Mice in which exon 5 of the *Prx* gene was floxed had originally been generated in order to ablate Periaxin protein expression in the adult. However, as will be described here, these mice produced after Cre-mediated recombination a form of Periaxin lacking the N-terminal PDZ domain. Therefore, these mice proved to be extremely useful. In order to study the mutant Periaxin lacking the N-terminal PDZ domain, mice carrying the '*floxed*' *Prx* gene, which contain normal amounts of wild-type Periaxin (Fig. 13A), were crossed with a *Cnp-Cre* line (Lappe-Siefke et al., 2003). This system provides a robust and complete recombination of the *loxP* sites in the early embryonic PNS. In this study, $Prx^{fl/fl}$ mice are defined as wild-type (WT).

3.1.1 Expression of a mutant Periaxin protein in $Prx^{fl/fl}$/*Cnp-Cre* mice

Periaxin expression was examined in 3-week-old $Prx^{fl/fl}$ and $Prx^{fl/fl}$/*Cnp-Cre* mice by Western blotting. The absence of wild-type Periaxin in $Prx^{fl/fl}$/*Cnp-Cre* mice analyzed by immunoblotting for the Periaxin N-terminus indicated complete deletion of the wild-type form upon Cre excision of the *'floxed'* gene. A mutant form of Periaxin lower in molecular weight than the WT form was detectable in sciatic nerve homogenate using specific Periaxin antibodies against the repeat region or the C-terminus. This mutant version was not recognized by the anti-Periaxin N-terminus antibody (Fig. 13B). In most $Prx^{fl/fl}$/*Cnp-Cre* mice examined, the mutant Periaxin expression generally appeared to be lower than that of the WT form in control nerves. These data suggested the generation of a Periaxin form containing a large part of the protein without the N-terminus.

Immunostaining of transverse sections of sciatic nerves from mutant animals at 3 weeks old revealed a lack of immunoreactivity for the N-terminus of Periaxin, indicating the absence of the wild-type Periaxin and that no fibers escaped recombination (Fig. 13C). The mutant protein was localized at the abaxonal Schwann cell membrane, as identified by the Periaxin antibody against the repeat region, though perhaps slightly reduced in levels, compared with the wild-type form in the control. These findings were in concurrence with the immunoblotting results.

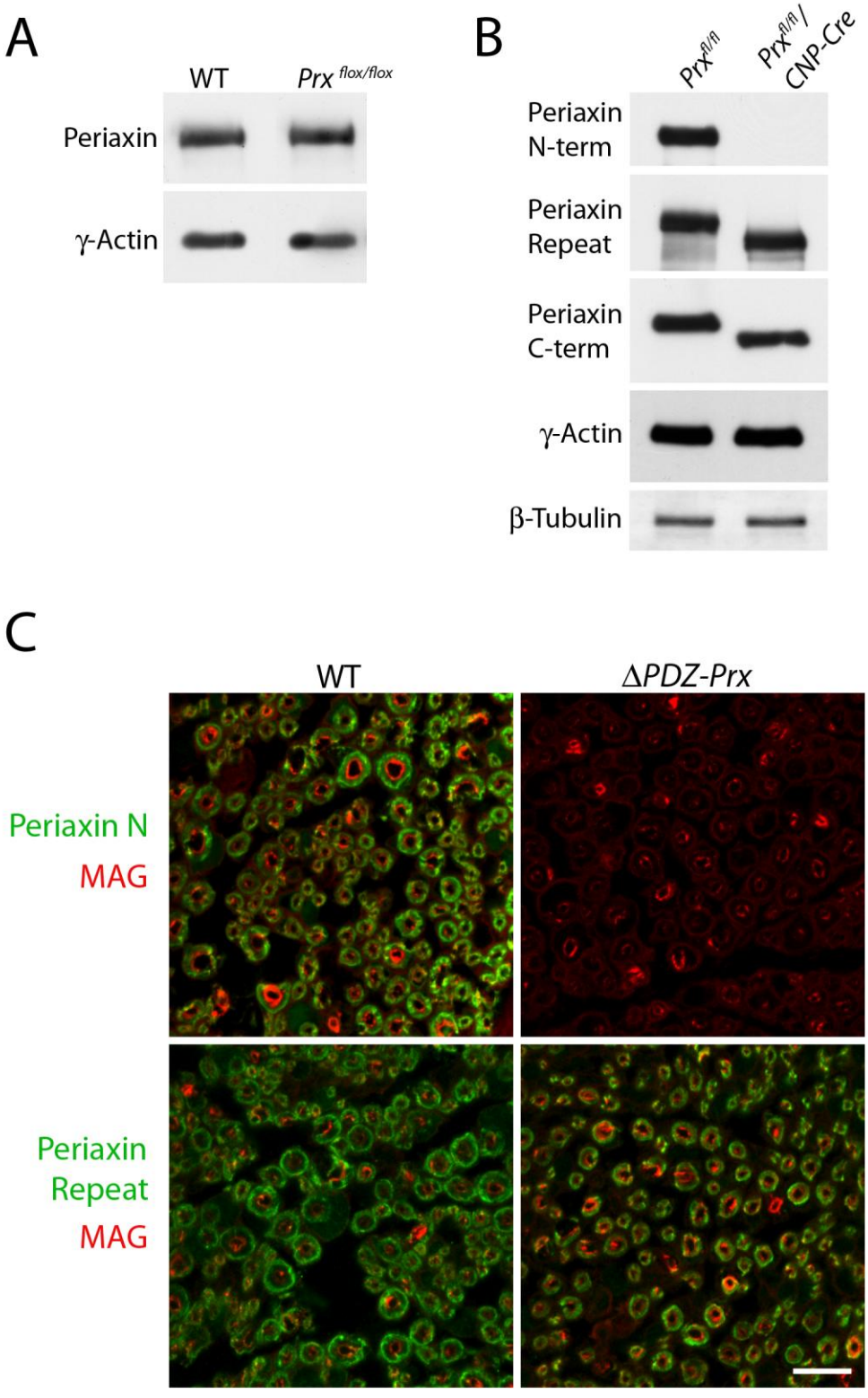
A
WT
Prx flox/flox
Periaxin
γ-Actin
B
Prx fl/fl
Prx fl/fl / CNP-Cre
Periaxin N-term
Periaxin Repeat
Periaxin C-term
γ-Actin
β-Tubulin
C
WT
ΔPDZ-Prx
Periaxin N
MAG
Periaxin Repeat
MAG

Figure 13. A mutant Periaxin protein is expressed in *Prx$^{fl/fl}$/Cnp-Cre* peripheral nerves.

A. By Western blot analysis, sciatic nerve homogenates from homozygous *Prx$^{fl/fl}$* and WT mice showed comparable amounts of Periaxin detected by anti-Periaxin N-terminus antibody.
B. Wild-type Periaxin was not detected in nerve homogenates from 3-week-old *Prx$^{fl/fl}$/Cnp-Cre* mice by the N-terminus antibody. However, a mutant Periaxin form, lower in molecular weight than the wild-type form, was identified by both the repeat region and C-terminus antibodies in the mutant animals. γ-Actin and β-tubulin were used as loading controls.
C. Transverse sections of sciatic nerves from 3-week-old *Prx$^{fl/fl}$* and *Prx$^{fl/fl}$/Cnp-Cre* mice immunolabeled with Periaxin antibodies against the repeat region and the N-terminus show an absence of immunoreactivity for the N-terminus but positive staining for the repeat region in the abaxonal Schwann cell membrane *Prx$^{fl/fl}$/Cnp-Cre* mouse. MAG is localized correctly to the periaxonal membrane of the Schwann cell. Scale bar, 15 μm.

3.1.2 mRNA expression of the mutant Periaxin remains unaltered

To determine whether mRNA levels of the mutant Periaxin in *Prx*$^{fl/fl}$*/Cnp-Cre* mice were comparable to WT, Periaxin transcript levels were compared between 3-week-old WT and Δ*PDZ-Prx* mice using semi-quantitative RT-PCR with a set of primers hybridizing to exon 7 of the *Prx* gene and are specific for both the wild-type and mutant Periaxin. The transcript level of mutant Periaxin was similar to that of the wild-type control (Fig. 14).

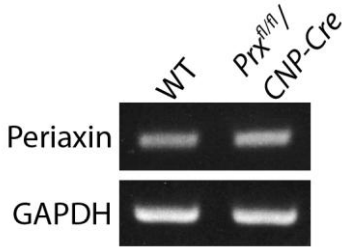

Figure 14. The mRNA expression of mutant Periaxin is unaltered.

Semi-quantitative RT-PCR using primers encoding exon 7 of the *Prx* gene shows that the mRNA expression of the mutant Periaxin in Δ*PDZ-Prx* trigeminal nerves at 3 weeks old is similar to that of wild-type Periaxin in WT nerves. GAPDH was used as the loading control. Both PCR products were ~400 bp.

3.1.3 The hypotheses of exon skipping and translation reinitiation

The conditional system had been predicted to generate a glial specific knockout of Periaxin. However, analysis of protein expression by region-specific antibodies of Periaxin revealed the generation of a mutant Periaxin form (see section 3.1.1).

In order to account for this surprising result, I came up with two hypotheses. First, there might be an exon skipping event in the mutant mice with Cre-mediated recombination. Exon skipping is the most common alternative splicing mechanism in mammals, contributing to the diversity of mammalian proteins (Miriami et al., 2003). Nonsense and missense mutations can cause skipping of exons (Cooper and Mattox, 1997; D'Souza et al., 1999; Vuillaumier-Barrot et al., 1999). Cre-mediated excision of exon 5 in the *Prx* gene might therefore result in an exon skipping event. In the *Prx* gene, exon 4 is in frame with exon 7, skipping of exon 6 in the recombined *Prx* gene would give rise to a Periaxin mutant form lacking the PDZ domain (~10-14 kDa shorter).

To study this further, I isolated RNA from trigeminal nerves of 4-week-old *Prx*$^{fl/fl}$*/Cnp-Cre* mice since abundant amounts of RNA could be extracted from trigeminal nerves, and performed reverse transcription-PCR (RT-PCR). If exon skipping had taken place, amplifying the N-terminal region between exons 4 and 7 using specific primers would yield a DNA fragment that lacks both exon 5 (due to Cre-mediated excision) and exon 6 due to a skipping event (Fig. 15A). However, the RT-PCR and DNA sequencing results did not reveal a sequence due to exon skipping (expected fragment size ~160 bp), but a PCR product lacking exon 5 alone at ~350 bp, as predicted to result from Cre-mediated recombination of the *'floxed' Prx* gene (Fig. 15B). Based on this and in light of the fact that part of exon 4, which should still be present after exon skipping, was not detectable by the N-terminal Periaxin antibody, it seemed unlikely that exon skipping was the reason for the generation of the mutant Periaxin form.

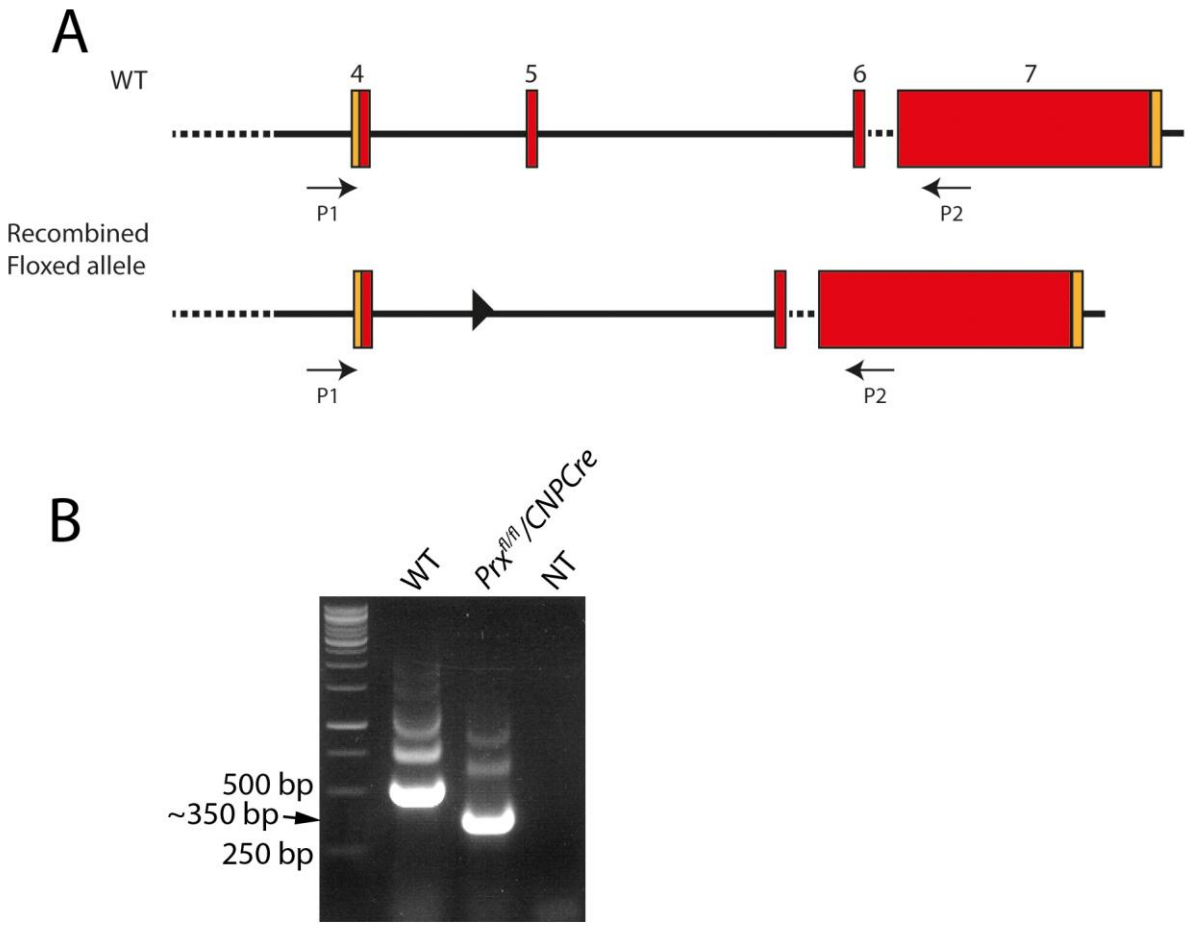

Figure 15. Generation of the mutant Periaxin is not attributed to exon skipping as revealed by RT-PCR analysis in mice with Cre-mediated recombination.

A. Schematic representation of the PCR amplification strategy for identification of an exon skipping event in the *Prx* gene. Exons are numbered. Arrows marked with P1 represent the forward primer in exon 4 of the *Prx* gene, and P2 the reverse primer in exon 7. PCR amplification of wild-type *Prx* cDNA would give rise to a product of 513 bp, and of the recombined *Prx* sequence would yield a 356 bp fragment. Skipping of exon 6 in the recombined gene would generate a 162 bp fragment by PCR.

B. Trigeminal nerve cDNA from reverse transcription was amplified by PCR using primers P1 in exon 4 and P2 in exon 7 of *Prx*, yielding a 500 bp product for WT and a 350 bp product indicative of the predicted recombination in the *'floxed'* allele for $Prx^{fl/fl}$*/Cnp-Cre* mice (Figure 17B shows the actual sequence). No signs of a 160 bp product predicted to be from exon skipping of the recombined gene were found. NT, no template.

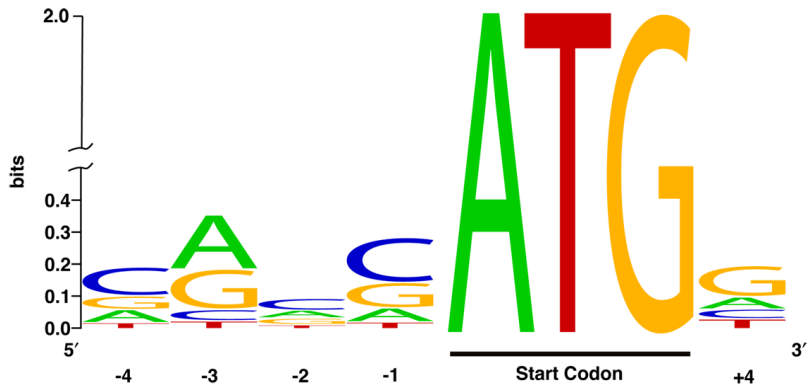

Figure 16. Kozak consensus sequencing surrounding the start codon ATG.

A start codon is in a strong context optimal for translation initiation if a purine (A or G) is in positions -3 and +4 (Harhay et al., 2005).

A second mechanism by which a putative mutant protein lacking the N-terminus might be generated is reinitiation at an internal AUG start codon during protein translation, as proposed in other contexts by Marilyn Kozak. According to the scanning mechanism for initiation of translation in eukaryotes, the 40S ribosomal subunit along with Met-tRNA and various initiation factors, binds to the 5'-end of mRNA and subsequently migrates in a 5' to 3' direction until it encounters the first AUG codon in a favorable context for translation initiation (Kozak, 1978). The 'first AUG rule' applies in more than 90% of vertebrate mRNA sequences studied thus far (Kozak, 1987a). Selection of the initiation site depends on the position and context of the initiation codon. An AUG codon is considered to be in a strong context provided that a purine (A or G) is in positions -3 (3 nucleotides upstream from the AUG) and +4 (preferably G) (Fig. 16) (Kozak, 1989).

Translation initiation is not entirely limited to the first AUG codon closest to the 5'- proximal end. Ribosomes advancing from the 5' end may initiate at downstream AUG codons in certain mRNAs under three specific conditions (Kozak, 1987b; Kozak, 1989). First, when the 5' cap and the first AUG codon are separated by fewer than 10 nucleotides, initiation may take place at the first and second AUG codons (Kelley et al., 1982; Peterson and Piatigorsky, 1986; Strubin et al., 1986). Secondly, ribosomes can reach an internal AUG codon by 'leaky scanning', when the first AUG lies in an unfavorable context for initiation (i.e. when position -3 is a C

or U). In such cases, ribosomes may bypass the first AUG and continue to scan along the mRNA sequence for a downstream AUG in a strong context (Kozak, 1986b). Another mechanism by which access to internal AUG codons is allowed is reinitiation, which operates when the upstream AUG lies in a favorable context, thus ruling out leaky scanning, but is followed shortly by an in-frame stop codon (Kozak, 1984; Kozak, 1986a; Kozak, 1987b). Under such a circumstance, ribosomes may reinitiate translation at the next downstream AUG codon. Interestingly, Marilyn Kozak observed that selection of the reinitiation site is not restricted to the next downstream AUG. She predicted that 40S subunits must attain a certain level of competency for reinitiation to occur. The subunits that are not yet competent when they reach the first AUG codon downstream should continue scanning, skipping over the first AUG and initiating at AUG codons further downstream when they become competent (Kozak, 1987b).

During the generation of *Prx*$^{fl/fl}$*/Cnp-Cre* mice, we predict that exon 5 in the floxed *Prx* gene is excised upon Cre-mediated recombination, thus introducing an in-frame termination codon in exon 6, aborting normal translation of the WT Periaxin protein. By the mechanism of reinitiation, 40S ribosomal subunits may remain bound to mRNA and continue to scan for a downstream AUG codon in a favorable context. As noted in Figure 17B, which illustrates the recombined *Prx* sequence lacking exon 5, there are 4 potential AUG codons (in red and underlined) downstream of the in-frame termination codon. The first three internal AUG codons are either in a weak context (C, a non-purine in +4 position) resulting in 'leaky scanning' or would encounter another termination codon that follows shortly if translation were to reinitiate at them, giving rise to other minicistrons (Kozak, 1987b). Therefore these AUG codons are likely not suitable initiation codons for the translation of the mutant protein.

The fourth AUG codon located in exon 6 downstream of the in-frame stop codon lies within a favorable context, precluding 'leaky scanning'. Considering the fact that it is in-frame with the WT *Prx* sequence (Fig. 17A), I predicted that reinitiation might take place at this AUG codon, resulting in translation starting from the basic domain of Periaxin, omitting the PDZ domain.

The efficiency of reinitiation gradually improves as the distance between the translated sequences initiated at the first AUG and an internal AUG is lengthened. However, the yield of the initiated protein due to reinitiation may decline when the intercistronic distance further increases (Kozak, 1987b). Since the translated sequence initiated at the first AUG in *Prx* gene and that initiated at the fourth AUG codon is 150 nucleotides apart, this might explain the slight reduction in levels of the mutant Periaxin in $Prx^{fl/fl}$*/Cnp-Cre* mice compared to that of the wild-type protein in the wild-type controls.

A

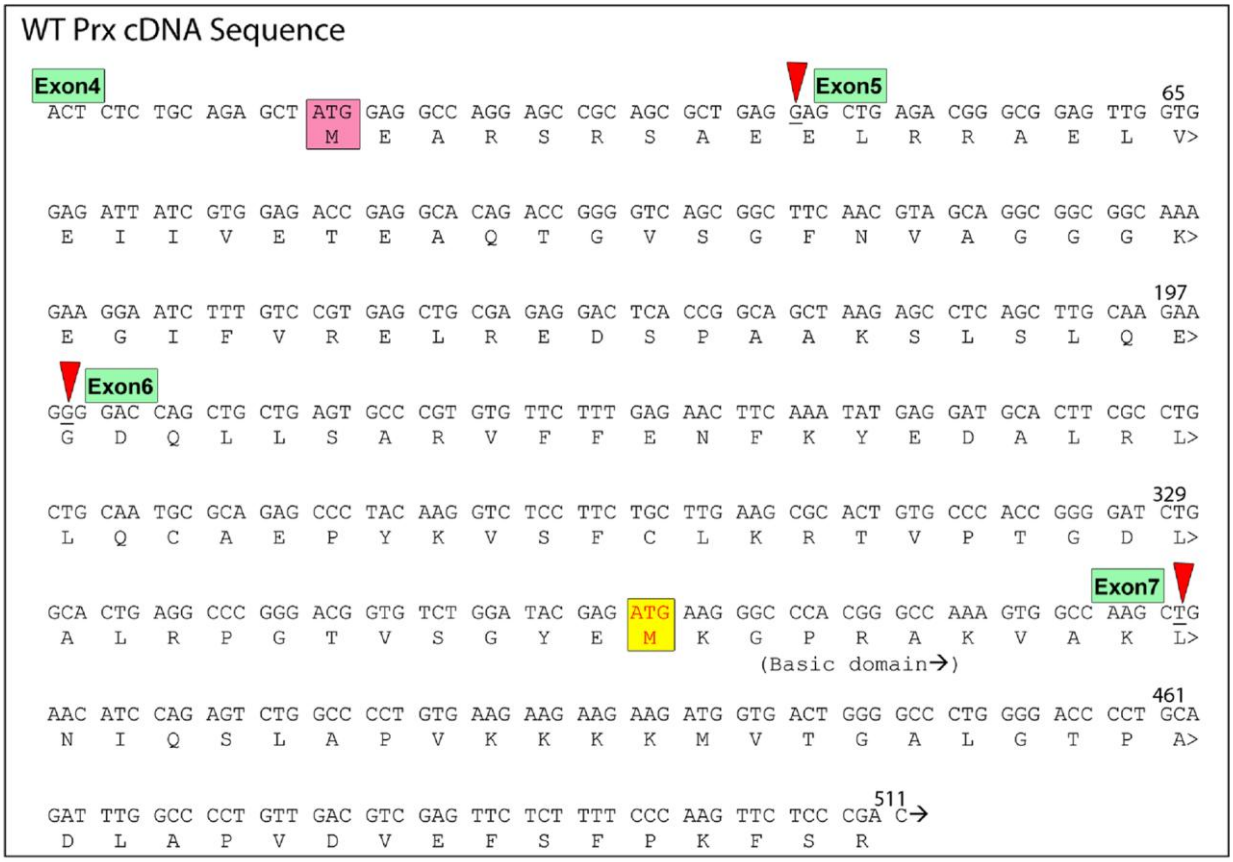
WT Prx cDNA Sequence
Exon4
Exon5
Exon6
Exon7
(Basic domain→)
65
197
329
461
511

B

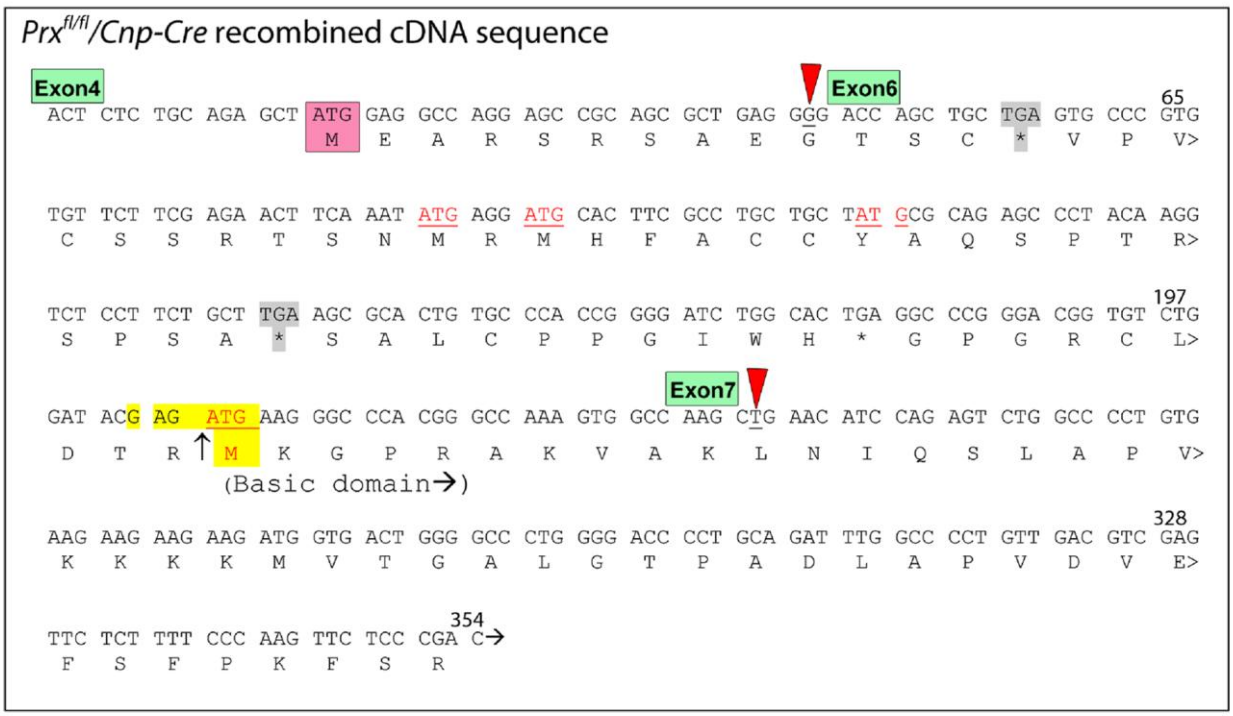
Prx fl/fl /Cnp-Cre recombined cDNA sequence
Exon4
Exon6
Exon7
(Basic domain→)
65
197
328
354

Figure 17. The hypothesis of translation reinitiation for the generation of the mutant Periaxin.

A. The wild-type *Prx* cDNA sequence from exon 4 to the beginning of exon 7. The ATG codon highlighted in pink denotes the start codon closest to the 5' end and is the normal initiator codon for wild-type Periaxin. The ATG (red font and highlighted in yellow), in-frame with the first ATG, is the internal initiator codon suspected to be reinitiated at by 40S ribosomal subunits. The red arrowheads mark the position of the start of an exon.
B. The 350 bp recombined floxed *Prx* sequence obtained from DNA sequencing. Exon 5 was deleted by Cre recombination causing a frameshift and introducing a stop codon in exon 6 (denoted in gray). We hypothesize that 40S subunits remain bound to the mRNA after encountering the first AUG, scan along and reinitiate translation at a downstream AUG codon. From the cDNA sequence, the first 3 ATGs (in red font) downstream of the stop codon are either in a weak context or would generate short cistrons, we believe that reinitiation takes place at the fourth ATG (in red and highlighted in yellow), which will generate a mutant protein lacking the PDZ domain.

3.1.4 N-terminus sequencing supported the reinitiation theory

To further verify the hypothesis, with the help of Dr Diane Sherman, we pulled down the mutant Periaxin protein using a GST-fusion protein containing the third fibronectin III domain of β4-integrin, which strongly interacts with the C-terminus of Periaxin. The N-terminus of the mutant protein was then sequenced by the Edman degradation method (Aberdeen Proteomics, University of Aberdeen). The N-terminus amino acid sequence from proteomics analysis, despite some ambiguity among the first 7 residues, was consistent with the predicted sequence suggested above:

Edman sequencing	M K $\begin{matrix} G \\ P \end{matrix}$ $\begin{matrix} P \\ A \end{matrix}$ $\begin{matrix} R \\ L \end{matrix}$ A $\begin{matrix} K \\ A \end{matrix}$ V A K L N
Predicted sequence	M K G P R A K V A K L N

This showed that the mutant Periaxin lacked the first 116 amino acids of the N-terminus, and strongly confirmed that translation of the mutant Periaxin lacking the PDZ domain, potentially due to reinitiation, started at the predicted downstream AUG in exon 6.

3.1.5 Periaxin does not homodimerize in the absence of the PDZ domain

In the absence of the PDZ domain, homodimerization is predicted to be prevented in the Periaxin-DRP2-dystroglycan complex (Fig. 18). To test whether mutant Periaxin lacking the N-terminal PDZ domain was able to bind full-length Periaxin, FLAG-tagged mutant Periaxin ΔPDZ-Prx lacking the first 116 amino acids and myc-tagged full-length Periaxin were expressed in HEK 293 cells (Fig. 19A). Expression of each construct was confirmed by immunofluorescence staining of the transfected cells using anti-FLAG and anti-myc antibodies (data not shown). By co-immunoprecipitation, mutant FLAG-tagged Periaxin could not bind full-length myc-tagged Periaxin *in vitro*, in contrast to the control full-length FLAG-tagged Periaxin, which was co-immunoprecipitated with myc-tagged Periaxin (Fig. 19C). This suggests that homodimerization does not occur without the PDZ domain in Periaxin. To ensure the specificity of anti-FLAG M2 affinity gel and the antibodies used for co-immunoprecipitation, mutant FLAG-tagged Periaxin and full-length myc-tagged Periaxin were individually expressed in HEK 293 cells. FLAG-tagged mutant

Periaxin was immunoprecipitated using anti-FLAG M2 beads, but was not detected by the anti-myc antibody. Myc-tagged Periaxin alone was not immunoprecipitated (Fig. 19B).

Prx$^{fl/fl}$*/Cnp-Cre* mice harbor a large truncated Periaxin protein lacking 116 amino acids at the N-terminus, i.e. the PDZ domain, which comprises less than 10% of the protein. Hence, I thought it would be of interest to study this mutant mouse as homodimerization of the PDZ domain would not occur. For characterization of the mutant mouse in this work, *Prx*$^{fl/fl}$*/Cnp-Cre* mice are defined as Δ*PDZ-Prx* mice.

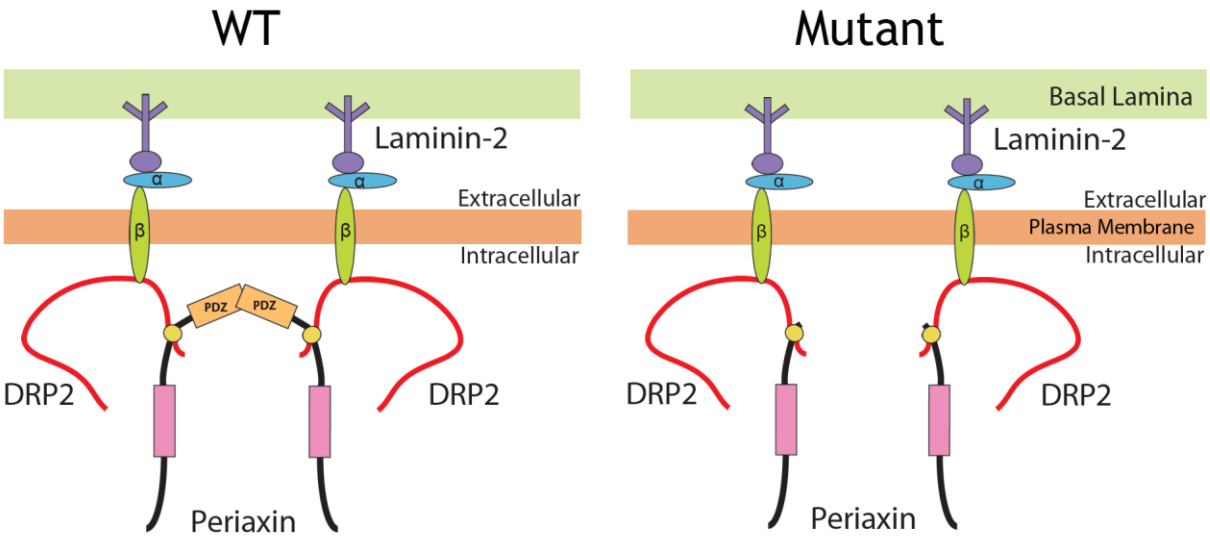

Figure 18. Diagrams show the Periaxin-DRP2-dystroglycan complex in the wild-type (left) and in the Δ*PDZ-Prx* mutant (right).

Periaxin homodimerizes at the N-terminal PDZ domain and interacts via the basic domain with DRP2, which associates with β-dystroglycan, forming a membrane-associated complex in the Schwann cell cortex. Note that dimerization of Periaxin's PDZ domain is predicted to be abrogated in the mutant.

A

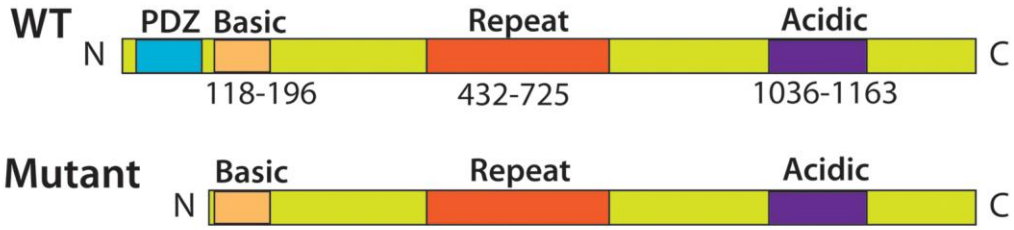
WT
N
PDZ
Basic
Repeat
Acidic
C
118-196
432-725
1036-1163
Mutant
N
Basic
Repeat
Acidic
C

B

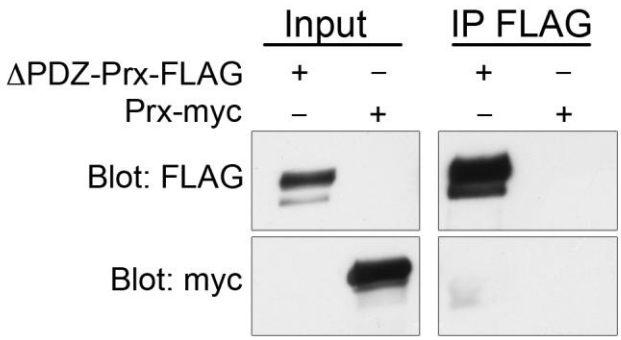
Input
IP FLAG
ΔPDZ-Prx-FLAG + – + –
Prx-myc – + – +
Blot: FLAG
Blot: myc

C

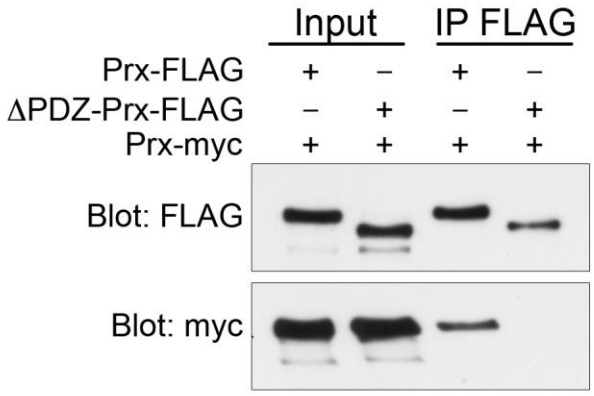
Input
IP FLAG
Prx-FLAG + – + –
ΔPDZ-Prx-FLAG – + – +
Prx-myc + + + +
Blot: FLAG
Blot: myc

Figure 19. Periaxin without the PDZ domain does not homodimerize.

A. Domain structure of full-length wild-type Periaxin (upper panel) and mutant Periaxin (bottom panel) proteins. Periaxin protein from the ΔPDZ-*Prx* mutant lacks 116 amino acids including the PDZ domain at the N-terminus. Amino acid residues are shown.
B. A control experiment showing single expression of FLAG-tagged mutant Periaxin ΔPDZ-Prx or myc-tagged full-length Periaxin confirms the specificity of anti-FLAG M2 affinity gel and antibodies used in co-immunoprecipitation. HEK293 cells transiently expressing FLAG-tagged mutant Periaxin ΔPDZ-Prx alone or myc-tagged full-length Periaxin alone were lysed in a buffer containing 1% Triton X-100, and both were immunoprecipitated using anti-FLAG M2 beads. Immunoprecipitates were analyzed by immunoblotting with anti-FLAG or anti-myc antibodies. The input lanes contain samples of cell lysate.
C. Mutant Periaxin lacking the PDZ domain does not homodimerize with full-length Periaxin in transfected HEK 293 cells. By co-immunoprecipitation, full-length FLAG-tagged Periaxin binds full-length myc-tagged Periaxin. In contrast, mutant FLAG-tagged Periaxin fails to bind full-length myc-tagged Peraxin *in vitro*. The input lanes show comparable expression levels of the respective transfected constructs in the cell line detected by anti-FLAG or anti-myc antibodies.

PART B. CHARACTERIZATION OF Δ*PDZ-Prx* MICE CONTAINING PERIAXIN WITHOUT THE PDZ DOMAIN IN PERIPHERAL NERVES

3.1.6 DRP2 is depleted and DRP2-positive patches are absent in Δ*PDZ-Prx* nerves

In *Prx*-knockout animals, Periaxin/DRP2 rich patches in Schwann cells fail to form and appositions are disrupted. The internodal lengths of Schwann cells in these animals are reduced thus affecting nerve conduction velocity (Court et al., 2004). To investigate whether DRP2-patches were still present in Δ*PDZ-Prx* mice, I analyzed the peripheral nerves of these animals by immunostaining and Western blotting. First, mutant Periaxin was expressed at reduced levels as indicated by a decrease in immunoreactivity detected by the anti-Periaxin repeat region antibody. It remained membrane-associated but was no longer localized in cobblestone-like patches. In the presence of mutant Periaxin (Fig. 20A), DRP2 was diffusely expressed, severely depleted and failed to localize at spheroid domains. This was similar to the DRP2 expression in the *Prx*-null mice (Sherman et al., 2001). DRP2 appears mostly in the phosphorylated form in WT animals, and is non-phosphorylated in the absence of Periaxin in *Prx*-null mutants (Fig. 20B). To study whether DRP2 was phosphorylated in Δ*PDZ-Prx* mice, I analyzed sciatic nerve homogenates for DRP2 expression by Western blotting. In contrast to the wild-type control, DRP2 mainly appeared in the non-phosphorylated form and was reduced in levels in these mice (Fig. 20B).

Since the PDZ domain of Periaxin is not required for association with DRP2 (Sherman et al., 2001), it is interesting that DRP2 was not properly targeted to patches despite the presence of the DRP2-binding basic domain in the mutant Periaxin. In order to test whether the mutant Periaxin interacted with DRP2, a GST-pull down assay was performed. A GST-DRP2 fusion protein (aa 110-390 of DRP2) containing the Periaxin-binding region co-precipitated with mutant Periaxin from Δ*PDZ-Prx* sciatic nerve lysates. However, the degree of binding to the DRP2-fusion protein by mutant Periaxin was reduced compared with the wild-type protein (Fig. 21).

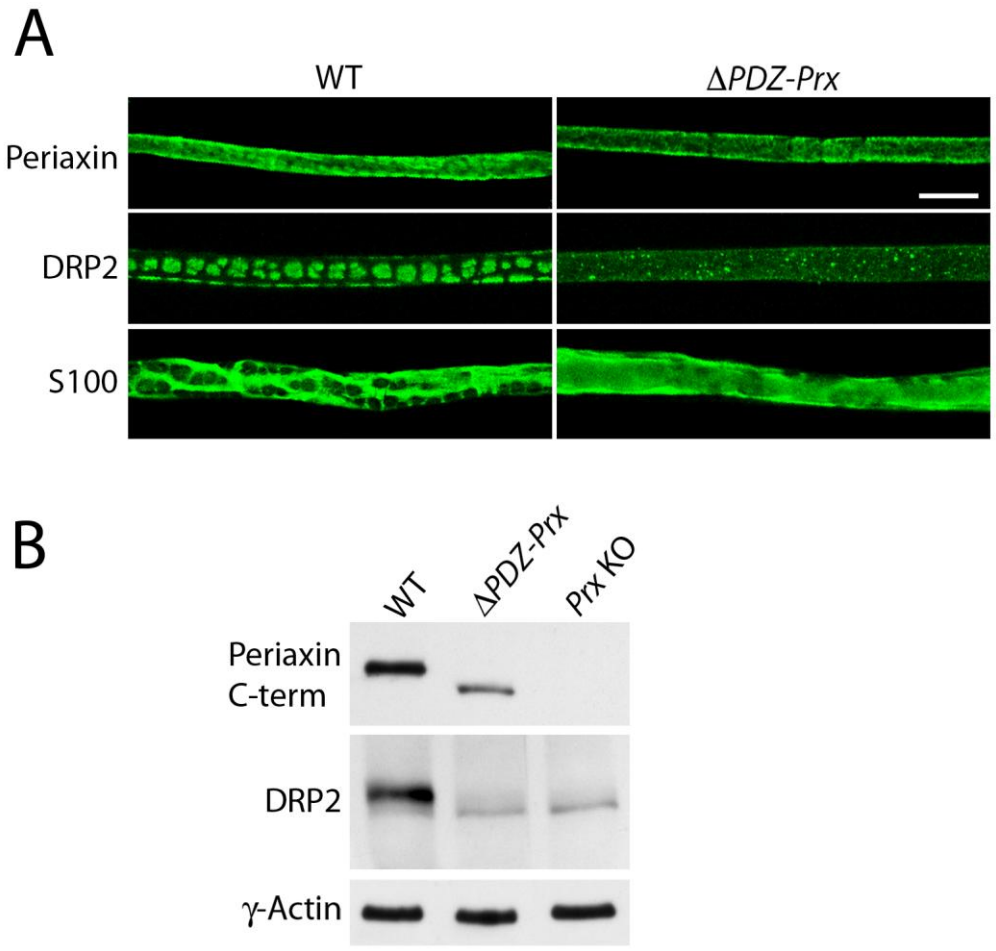

Figure 20. DRP2-patches are absent and Cajal bands disrupted in Δ*PDZ-Prx* Schwann cells.

A. Confocal immunofluorescence analysis of teased fibers of quadriceps nerves from 4-week-old WT and Δ*PDZ-Prx* mice immunolabeled for Periaxin, DRP2 and the Cajal band marker S100. Periaxin detected by the repeat region antibody is present at a reduced level in Δ*PDZ-Prx* mouse (top panels). When stained for DRP2, WT fibers display distinct patches, which are absent in the mutant fibers (middle panels). In addition, Cajal bands are disrupted in the mutant fibers. Unlike WT Schwann cell cytoplasm, which is arranged in longitudinal and transverse bands, the cytoplasm in Δ*PDZ-Prx* Schwann cells appears continuous along the internode (bottom panels). Scale bar, 20 μm.

B. Western blot analysis shows that DRP2 is depleted in the Δ*PDZ-Prx* sciatic nerve homogenates at 3 weeks of age, compared with WT nerves. The DRP2 expression in Δ*PDZ-Prx* nerves is similar to that in *Prx* KO nerves.

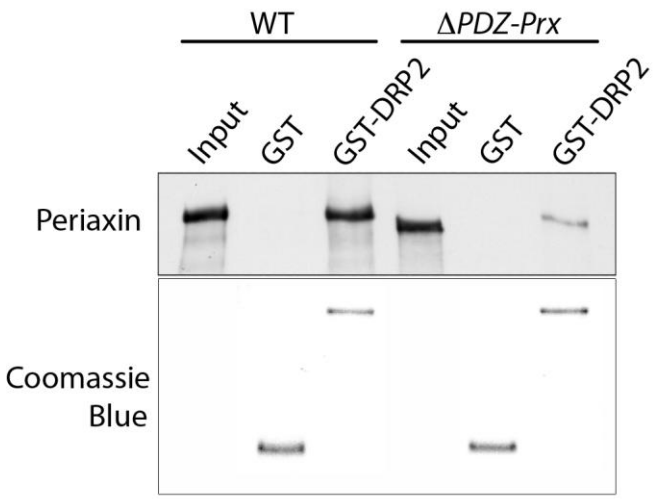

Figure 21. Biochemical evidence showing binding of DRP2 with mutant Periaxin lacking the PDZ domain.

GST or GST-fusion protein of DRP2 (aa 110-390) were incubated with sciatic nerve lysates from 6-week-old WT and Δ*PDZ-Prx* mice. GST-DRP2 fusion protein interacts with mutant Periaxin in Δ*PDZ-Prx* nerves, but at reduced levels. The input lanes confirm the presence of the wild-type Periaxin in WT nerves and the mutant Periaxin in Δ*PDZ-Prx* nerves. The Coomassie-blue-stained gel (bottom panel) shows equal amounts of GST or GST-DRP2 fusion proteins were used for the pulldown assays in the WT and Δ*PDZ-Prx* samples.

3.1.7 Cajal bands are disrupted and appositions absent in Δ*PDZ-Prx* Schwann cells

I further examined whether Cajal bands were present in the mutant Schwann cell by labeling quadriceps nerve teased fibers with an antibody directed against the Schwann cell cytoplasmic protein S100, and found that Cajal bands were disrupted. Instead of arranging in distinct longitudinal and transverse bands as in the WT Schwann cell, cytoplasm of the mutant Schwann cell appeared continuous shown by S100 immunostaining (Fig. 20A).

As mentioned in the 'Introduction' section, the Schwann cell is compartmentalized into discrete domains (Albrecht et al., 2008; Court et al., 2009; Court et al., 2004). Upon the completion of myelin compaction, the cytoplasm of the Schwann cell is restricted to the outer ring of the fiber and is separated by close appositions between the abaxonal membrane of the Schwann cell and the outermost layer of the myelin sheath. To address whether appositions were present in the Δ*PDZ-Prx* Schwann cell, ultrastructural analysis of the Schwann cell-axon unit was performed by electron microscopy. In transverse sections of 3-week-old quadriceps nerves, WT Schwann cells showed distinct regions of cytoplasm restricted by appositions. In sharp contrast, most Δ*PDZ-Prx* Schwann cells contained no appositions and the cytoplasm appeared continuous around the myelin sheath (Fig. 22A). By counting the number of appositions per Schwann cell from randomly selected fields of electron micrographs of WT and Δ*PDZ-Prx* quadriceps nerves, it was obvious that all WT Schwann cells had appositions, with the highest percentage of Schwann cells containing 2-3 appositions. However, the majority of mutant Schwann cells harbored no appositions, with a small proportion of fibers showing only one or two (Fig. 22B). These results suggest that appositions are disrupted when homodimerization of the PDZ domain in Periaxin does not occur.

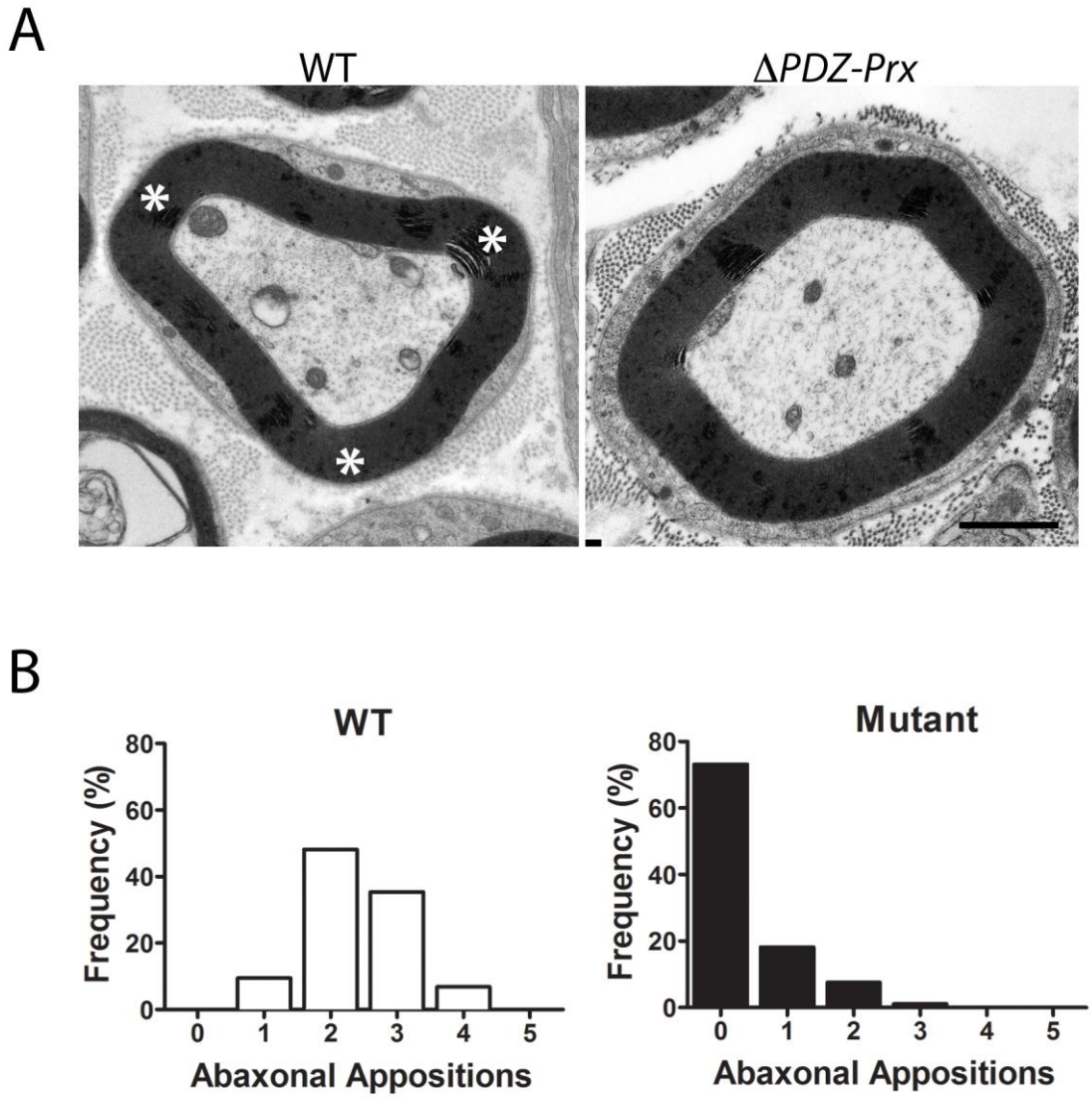

Figure 22. Appositions are absent in Δ*PDZ-Prx* Schwann cells.

A. Electron micrographs of transverse sections of WT and Δ*PDZ-Prx* quadriceps nerves. WT Schwann cell cytoplasm is separated by appositions (asterisks) between the abaxonal Schwann cell membrane and the underlying myelin sheath (left). In Δ*PDZ-Prx* Schwann cells, the absence of appositions results in a concentric ring of cytoplasm around the myelin sheath (right). Scale bar, 1 μm.

B. The quantification of appositions per Schwann cell in 3-week-old quadriceps nerve transverse sections (*n*=3 and 100 fibers for WT and Δ*PDZ-Prx*) shows that most Δ*PDZ-Prx* Schwann cells have no appositions (right), compared with the WT (left).

3.1.8 Axon diameters and myelin sheath thickness are normal in peripheral nerves of Δ*PDZ-Prx* mutant mice

Prior to the development of myelin abnormalities, Periaxin-null peripheral nerves have normal axon diameters and myelin thickness at 3 weeks old (Court et al., 2004). To address whether these parameters were altered in Δ*PDZ-Prx* nerves, axon diameters and myelin sheath thickness were measured in transverse EM micrographs of 3-week-old WT and Δ*PDZ-Prx* quadriceps nerves. The distribution of axon diameters was comparable between WT and Δ*PDZ-Prx* mice (Fig. 23B). Myelin sheath thickness determined by *g*-ratio analysis (axon diameter/ fiber diameter) was also similar between WT and Δ*PDZ-Prx* quadriceps nerves (Figs. 23A and C). The mean *g*-ratio of the mutant nerves at 3 weeks of age was 0.608 ± 0.016, compared with 0.636 ± 0.011 for the WT ($p = 0.2351$), which did not differ significantly (Fig. 23C).

3.1.9 Longitudinal elongation of Δ*PDZ-Prx* Schwann cells is impaired

Periaxin is important for the regulation of Schwann cell elongation. In the absence of Periaxin, *Prx* KO Schwann cells have shorter internodal lengths because the rate of Schwann cell internodal growth fails to match up with that of nerve length (Court et al., 2004). Despite the seemingly normal capacity of myelin assembly in Δ*PDZ-Prx* peripheral nerves, I asked whether abrogation of Periaxin dimerization might influence Schwann cell elongation. To address this question, Δ*PDZ-Prx* Schwann cell internodal lengths were compared with those of the WT and *Prx* KO at 3 weeks and 6 weeks of age. Teased fibers from quadriceps nerves were immunolabeled with anti-dystrophin, a microvillus marker, for identification of the locations of nodes of Ranvier. At 3 weeks old, the average internodal length of Δ*PDZ-Prx* Schwann cells was significantly shorter than that of the WT (WT, 455.3 ± 6.7 μm, $n=8$; Δ*PDZ-Prx*, 328.7 ± 2.4 μm, $n=8$; $p < 0.001$), but was comparable with that of the Periaxin-null Schwann cells (302.7 ± 3.9 μm, $n=5$; Fig. 24A). Schwann cells displayed a heterogeneous distribution of internodal distances in each genotype analyzed. The distributions of internodal lengths at 3 weeks showed that the majority of WT internodes were in the range of 400-599 μm, with only a small proportion of internodes shorter than 400 μm. On the contrary, most Schwann

cells of Δ*PDZ-Prx* and *Prx* KO mice were only 200-399 μm in length (Fig. 24B). Consistently, at 6 weeks old, Δ*PDZ-Prx* Schwann cells remained shorter than that of the WT (WT, 559.3 ± 18.1 μm, n=3; Δ*PDZ-Prx*, 415.6 ± 3.7 μm, n=6; $p < 0.001$; Fig. 24C).

To test whether the internodal lengths of Δ*PDZ-Prx* Schwann cells would eventually catch up with that of the WT control as nerve growth continues with age, I measured WT and Δ*PDZ-Prx* Schwann cell internodal lengths in adult quadriceps nerves at 4 months of age. The mean internodal length of Δ*PDZ-Prx* Schwann cells was 479.4 ± 11.9 μm (n=4), compared with that of the WT controls at 713.9 ± 6.8 μm (n=5), and was statistically different from the WT values ($p < 0.001$; Fig. 24D), suggesting that Schwann cells elongated as nerve length increased with age, but the rate of longitudinal growth of mutant Schwann cells remained slower than that of WT Schwann cells.

Δ*PDZ-Prx* mutants were generated by crossing homozygous $Prx^{fl/fl}$ mice with *Cnp-Cre* animals, in which *Cre* was inserted into the *Cnp* locus (Lappe-Siefke et al., 2003). Δ*PDZ-Prx* mice were heterozygous for CNPase expression. To ensure that the reduction in the mean Schwann cell internodal distance of Δ*PDZ-Prx* mice was specific for the mutation resulting in the absence of Periaxin's PDZ domain but not due to reduced levels of CNPase, the average internodal lengths were compared between 3-week-old WT and mice heterozygous for both the *'floxed'* Periaxin and *Cnp-Cre*, referred to here as $CNP^{+/-}$ mice. $CNP^{+/-}$ Schwann cells had normal internodal lengths, ruling out the possibility of decreased CNPase levels leading to defective Schwann cell elongation in Δ*PDZ-Prx* mutants (Fig. 24E). In addition, the decrease in internodal lengths of Δ*PDZ-Prx* Schwann cells was not due to a reduction in the mutant Periaxin amounts reported in this work. By immunoblotting, the levels of mutant Periaxin in Δ*PDZ-Prx* sciatic nerves were similar to the amounts of wild-type Periaxin in $Prx^{+/-}$ nerves, which had no obvious phenotype shown by Dr Diane Sherman (unpublished data; Fig. 24F).

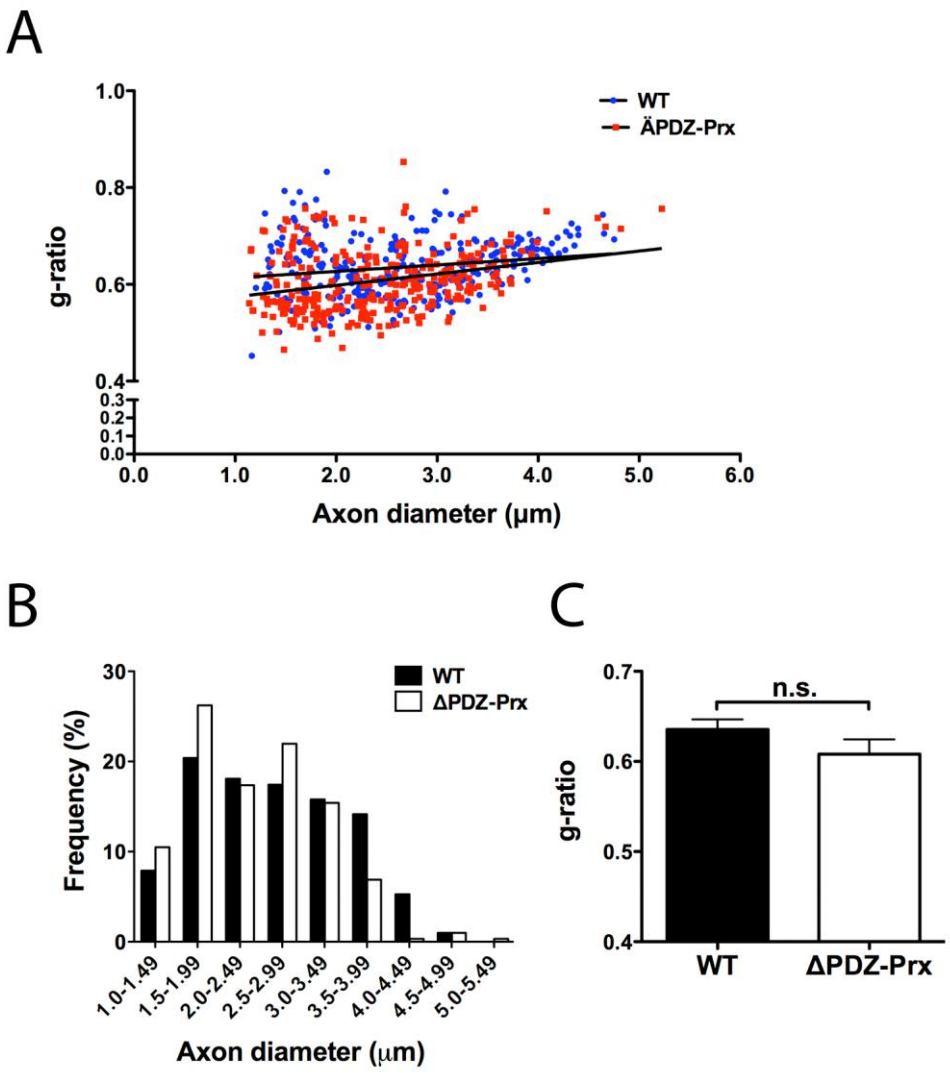

Figure 23. Axon diameters and myelin sheath thickness are normal in quadriceps nerves from 3-week-old Δ*PDZ-Prx* mice.

A. Scatter plot depicts *g*-ratios of myelinated nerve fibers from WT (blue circles) and Δ*PDZ-Prx* quadriceps nerves (red squares) at 3 weeks old, in relation to the axon diameter based on electron micrographs of ultrathin cross sections (*n*=3; 100 fibers per group).

B. In 3-week-old Δ*PDZ-Prx* quadriceps nerves, axons displayed a normal size distribution compared with that of WT axons (*n*=3; 100 fibers per genotype).

C. The mean *g*-ratio of nerve fibers from Δ*PDZ-Prx* quadriceps nerves is not significantly different from that of WT fibers at 3 weeks of age (p = 0.2351; Student's *t*-test).

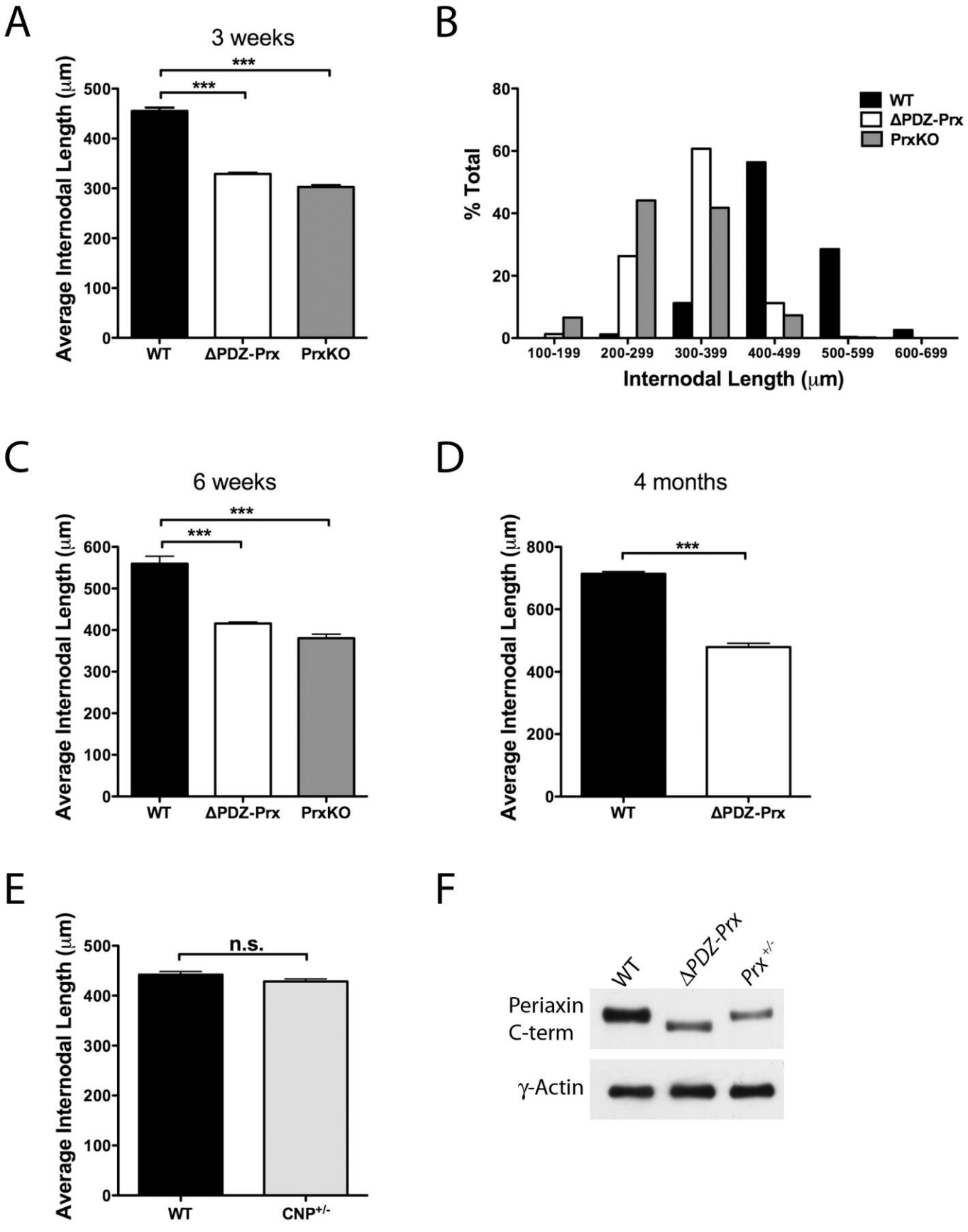
A
3 weeks
***
***
Average Internodal Length (μm)
500
400
300
200
100
0
WT
ΔPDZ-Prx
PrxKO
B
80
60
40
20
0
% Total
WT
ΔPDZ-Prx
PrxKO
100-199
200-299
300-399
400-499
500-599
600-699
Internodal Length (μm)
C
6 weeks
***
***
Average Internodal Length (μm)
600
500
400
300
200
100
0
WT
ΔPDZ-Prx
PrxKO
D
4 months
***
Average Internodal Length (μm)
800
600
400
200
0
WT
ΔPDZ-Prx
E
n.s.
Average Internodal Length (μm)
500
400
300
200
100
0
WT
CNP+/-
F
WT
ΔPDZ-Prx
Prx+/-
Periaxin
C-term
γ-Actin

Figure 24. Δ*PDZ-Prx* Schwann cells lacking the Periaxin PDZ domain have reduced internodal lengths.

A. Internodal length measurements of teased quadriceps nerve fibers from WT (*n*=8), Δ*PDZ-Prx* (*n*=8), and *Prx* KO mice (*n*=5) at 3 weeks. The average Schwann cell internodal lengths of Δ*PDZ-Prx* and *Prx* KO fibers are significantly shorter than WT values ($p < 0.0001$; one-way ANOVA with Tukey's HSD post-test).
B. Distributions of Schwann cell internodal lengths from WT, ΔPDZ-*Prx* and *Prx* KO mice at 3 weeks. The majority of ΔPDZ-*Prx* and *Prx* KO Schwann cells are shorter in length, compared with WT Schwann cells.
C. The mean internodal length of ΔPDZ-*Prx* Schwann cells remains shorter than that of WT Schwann cells at 6 weeks old (*n*=3-6 per genotype; $p < 0.0001$; one-way ANOVA with Tukey's HSD post-test), and at 4 months old (*n*=4-5 per genotype; $p < 0.0001$; Student's *t*-test) in D.
E. The average internodal lengths are similar between 3-week-old WT and mice heterozygous for both the *'floxed'* Periaxin and *Cnp-Cre*, defined as $CNP^{+/-}$ (*n*=3 per group; $p = 0.1596$; Student's *t*-test), suggesting that the reduction in the mean Schwann cell internodal distance of Δ*PDZ-Prx* mice is due to the absence of PDZ domain homodimerization but not the reduced levels of CNPase.
F. Western blot analysis reveals that the amounts of mutant Periaxin in Δ*PDZ-Prx* sciatic nerves are similar to the amounts of wild-type Periaxin in $Prx^{+/-}$ nerves, which have normal internodal lengths, indicating that the reduction of Δ*PDZ-Prx* Schwann cell internodal lengths is not because of a decreased amount of the mutant Periaxin. γ-actin was the loading control.

Shorter internodal lengths in Δ*PDZ-Prx* Schwann cells would suggest an increase in the number of myelinating Schwann cells forming a 1:1 relationship with axons per unit length of nerve fiber. To determine whether Schwann cell number in Δ*PDZ-Prx* nerves differed from that in the WT, I quantified the number of myelinating Schwann cells and Schwann cells in general, immunostained for the transcription factors Krox-20 and Sox10, respectively, in WT and Δ*PDZ-Prx* sciatic nerve transverse sections at 3 weeks of age. In agreement with a one-third reduction in Δ*PDZ-Prx* internodal lengths compared with the WT controls, the number of myelinating Schwann cells in Δ*PDZ-Prx* sciatic nerves was proportionately augmented by 42.2 ± 6.7% (Fig. 25A). Additionally, there was also an increase of 38.8 ± 5.7% in total Schwann cells, labeled as Sox10-immunopositive cells, in the mutant nerves. However, in comparison with the WT nerves, the proportion of myelinating Schwann cells, determined by the ratio of Krox-20+ to Sox10+ cells, remained unchanged, suggesting that myelination was not affected at this age (Fig. 25B). The expression level of Krox-20 was also elevated in 3-week-old Δ*PDZ-Prx* sciatic nerves as demonstrated by immunoblotting, further confirming the increase in quantity of myelinating Schwann cells in the mutant nerves, as a result of a reduction in internodal lengths (Fig. 25C).

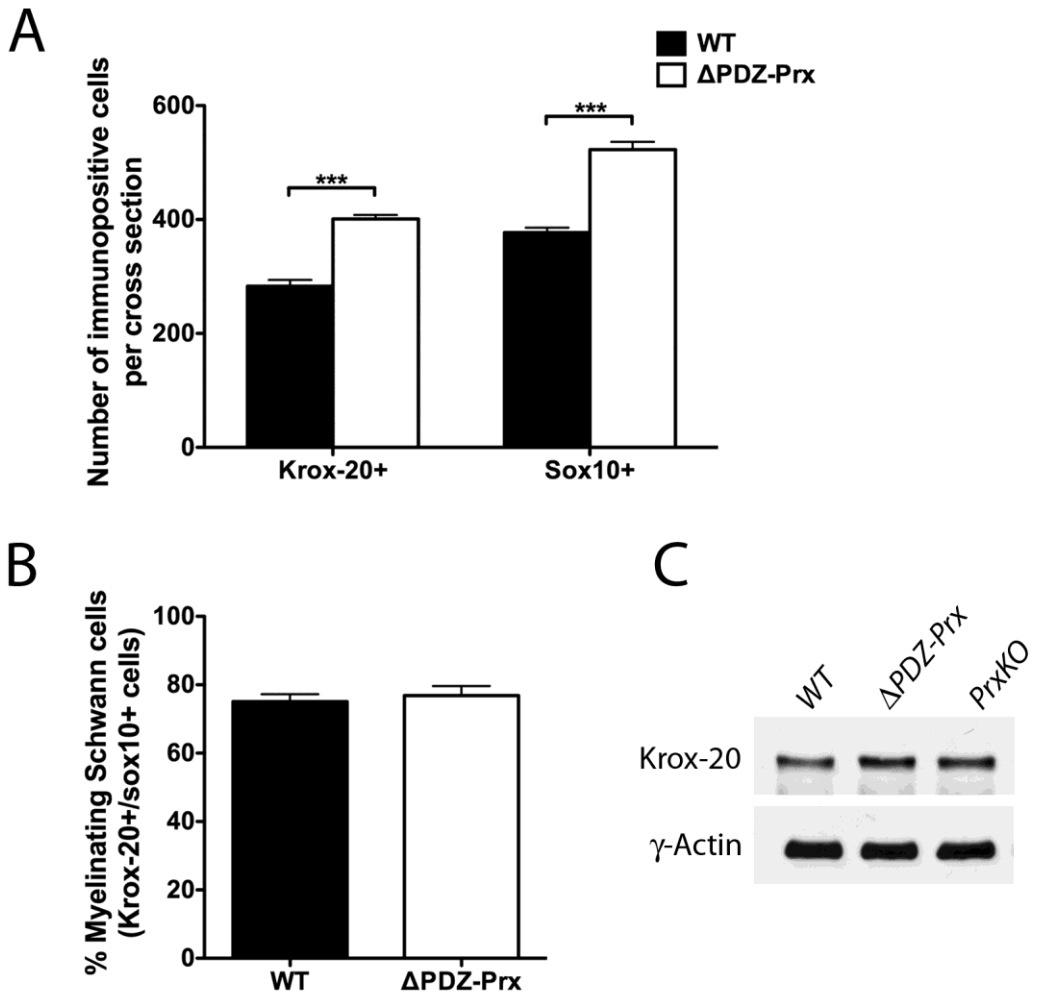

Figure 25. An increase in Schwann cell number is consistent with a decrease in internodal lengths in Δ*PDZ-Prx* peripheral nerves.

A. Sciatic nerve transverse sections from 3-week-old WT and Δ*PDZ-Prx* mice were immunolabeled with anti-Krox-20 antibody for myelinating Schwann cells, and anti-Sox10 antibody for all Schwann cells. Δ*PDZ-Prx* sciatic nerves have significantly more Schwann cells than WT nerves. The numbers of Krox-20+ cells per cross section of WT and Δ*PDZ-Prx* sciatic nerves are 283.0 ± 11.0 and 401.0 ± 7.0, respectively (n=3 per genotype; p = 0.0009), and the numbers of Sox10+ cells are 377.0 ± 8.7 and 522.7 ± 13.9 (p = 0.0008; Student's t-test).
B. The proportion of myelinating Schwann cells (ratio of Krox-20+ to Sox10+ cells) is similar between WT and Δ*PDZ-Prx* sciatic nerves (75.1 ± 2.2 vs 76.9 ± 2.3%; p = 1.000; Mann-Whitney test).
C. Western blot analysis shows that the levels of Krox-20 in Δ*PDZ-Prx* sciatic nerves at 3 weeks old are increased corresponding to an increase in myelinating Schwann cells. γ-actin was used to normalize loading.

3.1.10 Myelin abnormalities in Δ*PDZ-Prx* mice

The structure of the myelin sheath has been well studied in the Periaxin-null mice, which displayed focal thickenings, termed tomacula, and onion bulb pathology indicative of supernumerary Schwann cells attempting to remyelinate following demyelination (Gillespie et al., 2000). I asked whether the myelin sheath was also affected in Δ*PDZ-Prx* nerves at later stages.

The quadriceps nerves of Δ*PDZ-Prx* mice were examined by light microscopy and electron microscopy at various ages. One of the prominent features of the mutant nerves was the enlargement of the endoneurial space resulting in an increase in the nerve cross-sectional area (Fig. 26A). In contrast to the closely arranged axons in the WT nerves, myelinated axons in both the Δ*PDZ-Prx* and *Prx* KO quadriceps nerves were less densely packed due to an accumulation of extracellular matrix (ECM) in the endoneurial and perineurial space. At 2 months of age, the cross-sectional area of Δ*PDZ-Prx* quadriceps nerves was slightly larger than that of the WT. However, by 4 months of age, the area of the mutant nerves remarkably increased by more than two fold, compared with that of the WT nerves (WT, $32.5 \times 10^3 \pm 1078$ μm^2; Δ*PDZ-Prx*, $68.1 \times 10^3 \pm 5770$ μm^2; $p < 0.01$). *Prx* KO nerve area was also significantly enlarged at this age ($57.7 \times 10^3 \pm 4985$ μm^2; $p < 0.05$). Whereas the WT nerve area remained constant at older ages, there was a tendency of a progressive increase in the size of both Δ*PDZ-Prx* and Periaxin-null nerves with age (Fig. 26B).

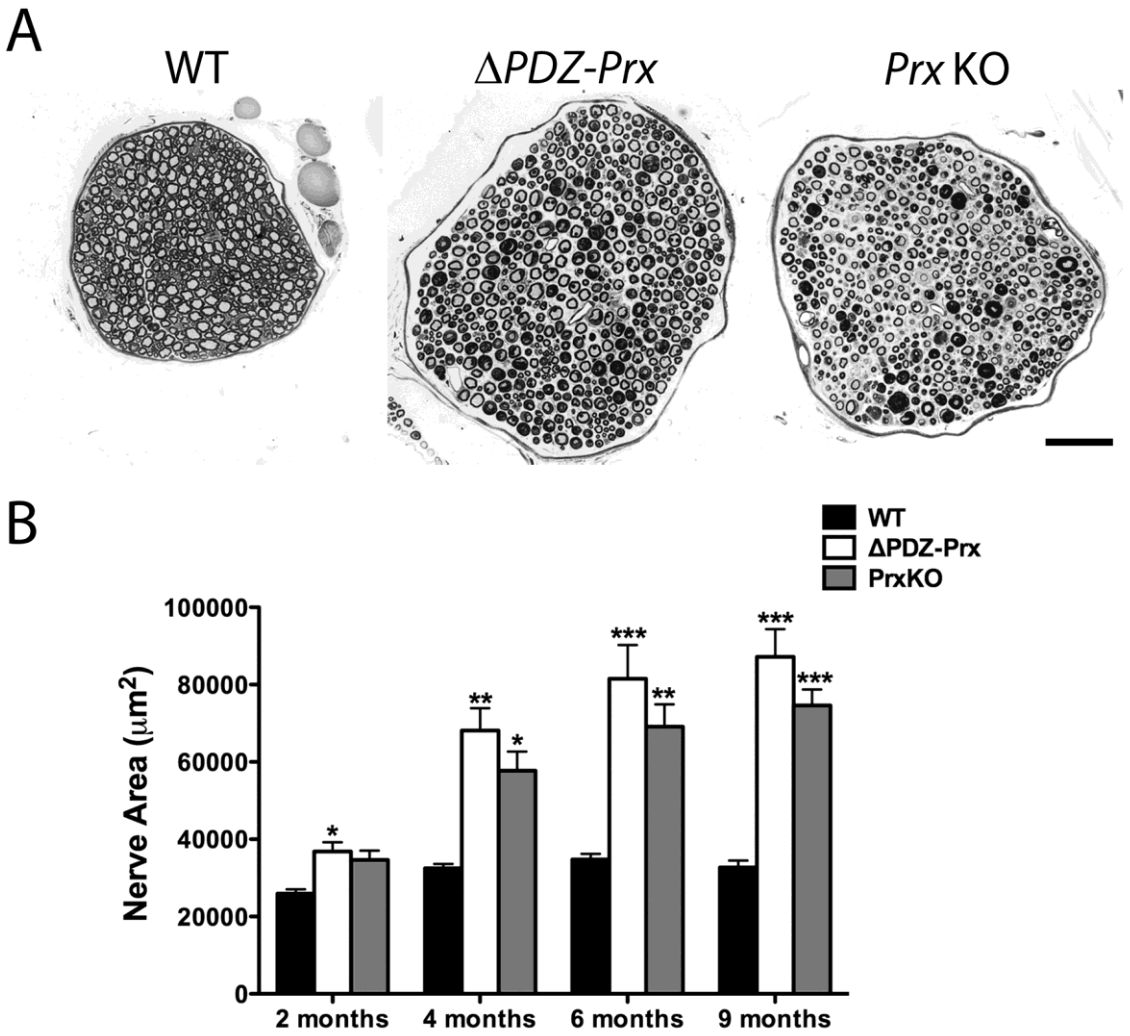

Figure 26. Δ*PDZ-Prx* mice have enlarged quadriceps nerves due to an increase in endoneurial and perineurial space.

A. Semithin transverse sections of WT, Δ*PDZ-Prx* and *Prx* KO quadriceps nerves at 4 months of age were examined by light microscopy at 20× magnification. The cross-sectional areas of both the Δ*PDZ-Prx* and *Prx* KO nerves are increased, compared with that of control nerves. Myelinated axons are less densely arranged because of an increase level of ECM in the endoneurium of Δ*PDZ-Prx* and *Prx* KO nerves. Scale bar, 30 μm.

B. Cross-sectional area measurements of WT, Δ*PDZ-Prx* and *Prx* KO sciatic nerve semithin sections at 2, 4, 6 and 9 months show an enlargement of nerve area in both the Δ*PDZ-Prx* and *Prx*KO nerves, compared with the WT (n=3-4 per genotype per age; *$p < 0.05$, **$p < 0.01$ and ***$p < 0.001$; one-way ANOVA with Tukey's HSD post-test for each age).

At 3 weeks, the myelin sheath in Δ*PDZ-Prx* nerves appeared morphologically indistinguishable from that of WT littermates (Fig. 22A, section 3.1.8). However, in the adult, mutant peripheral nerves displayed hypermyelination with focally folded myelin and tomacula, as revealed by light microscopy of transverse semi-thin Δ*PDZ-Prx* sections (Fig. 27A). In affected Schwann cell-axon units, aberrant loops of myelin arranged around myelinated, usually large diameter axons. Such infolds and outfolds of myelin often drastically altered the axon profile by causing axon compression. Quantitation of abnormal myelin profiles (Fig. 27B) showed that the proportion of fibers containing myelin foldings and tomacula increased progressively in the mutant quadriceps nerves examined at 2 months (15.5 ± 1.4%), 4 months (32.5 ± 2.0%), 6 months (44.2 ± 3.2%) and 9 months (51.3 ± 0.6%). The shape of myelin foldings became more complex with age as demonstrated by transverse EM micrographs of 8-month-old mutant nerves. Focal redundant myelin loops inside a myelinated axon leading to severe constriction of axon cytoplasm were frequently observed (Figs. 28A-C). Within these infolds, axonal material was found in the gap between the inner and outer myelin infolding. Some outfolds consisted of single or multiple recurrent myelin loops that appeared as satellite myelinated axons around a larger myelinated axon ensheathed by the Schwann cell plasma membrane (Figs. 28D-E). Focally folded myelin was also visible in small caliber axons (Fig. 28B).

In Δ*PDZ-Prx* quadriceps nerves at older ages (6-9 months), a small proportion of Schwann cell-axon units were thinly myelinated and associated with supernumerary Schwann cells and processes loosely in contact with axons, surrounded by a basal lamina, forming onion bulbs (Figs. 27A and 28F). This provided another line of evidence for progressive myelin morphological abnormalities in the mutant nerves with age. Nevertheless, in comparison with the quadriceps nerves from Periaxin-deficient mice, Δ*PDZ-Prx* nerves showed a less severe demyelinating phenotype. Additional to myelin tomacula and foldings, *Prx* KO nerves also displayed severe demyelination as revealed by extensive onion bulb pathology at 4 months and 6 months (Fig. 27A). *Prx* KO fibers had a significantly higher percentage of onion bulbs than Δ*PDZ-Prx* nerves at

all ages analyzed (Fig. 27B). The observation that the proportions of myelin foldings and tomacula in *Prx* KO fibers were lower than Δ*PDZ-Prx* values at all ages may suggest that aberrant folding of the myelin sheath occurs prior to demyelination.

Apart from myelin sheath abnormalities, in some *Prx* KO fibers, degeneration of the entire Schwann cell-axon unit was detectable and was characterized by vacuolation of the axoplasm with disruption of the myelin sheath (Fig. 29A). Naked axons surrounded by processes of supernumerary Schwann cells were also evident. While the number of myelinated axons in Δ*PDZ-Prx* quadriceps nerves (~530-550) did not differ significantly from that of the WT at all ages examined, *Prx* KO nerves showed a gradual reduction in myelinated axon number with age. At 9 months, *Prx* KO quadriceps nerves had 411 ± 20 myelinated axons, compared with 554 ± 9 and 550 ± 4 in WT and Δ*PDZ-Prx* nerves, respectively. These results further confirm that Δ*PDZ-Prx* mice develop a less severe demyelinating neuropathy than Periaxin-null animals.

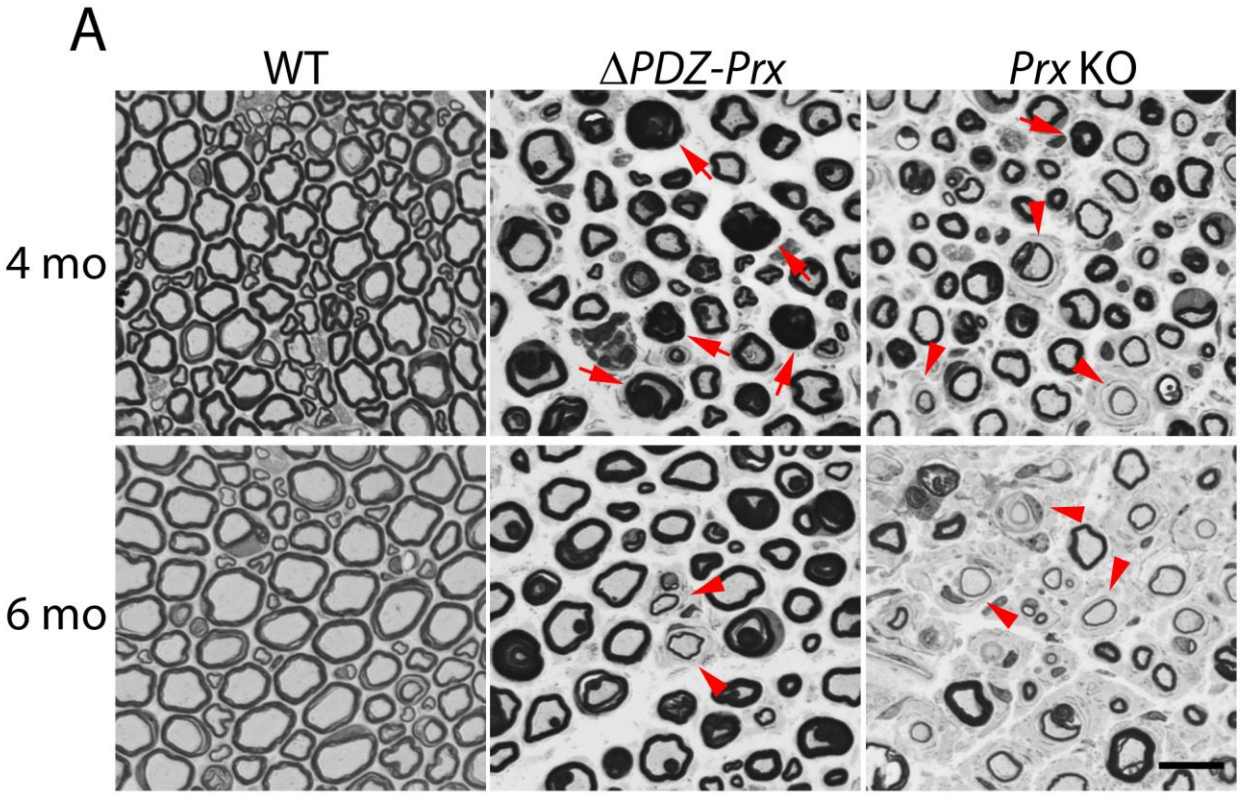
A
WT
ΔPDZ-Prx
Prx KO
4 mo
6 mo

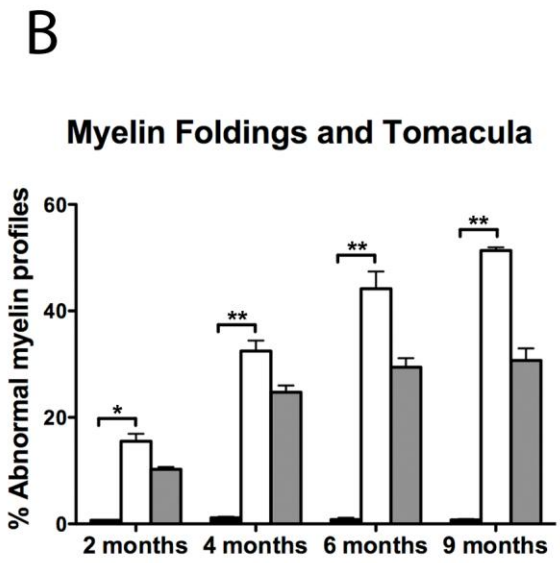
B
Myelin Foldings and Tomacula
% Abnormal myelin profiles
60
40
20
0
*
**
**
**
2 months
4 months
6 months
9 months

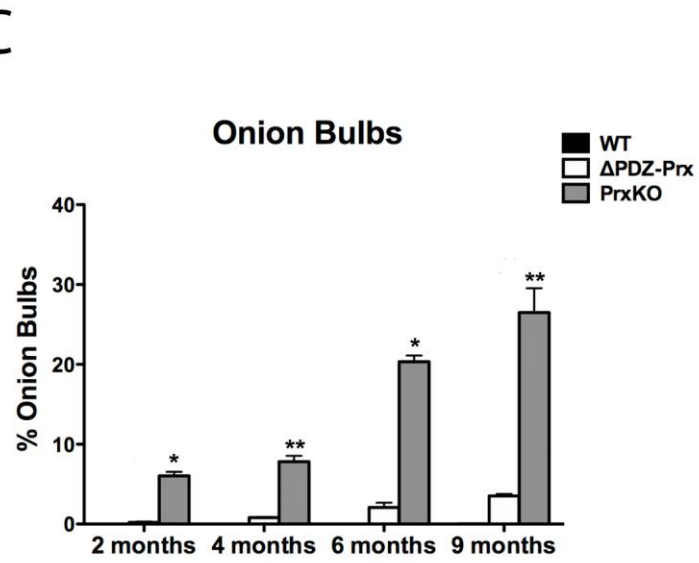
C
Onion Bulbs
WT
ΔPDZ-Prx
PrxKO
% Onion Bulbs
40
30
20
10
0
*
**
*
**
2 months
4 months
6 months
9 months

Figure 27. Myelin foldings in Δ*PDZ-Prx* peripheral nerves.

A. Semithin cross sections of quadriceps nerves from WT, *ΔPDZ-Prx* and *Prx* KO mice at 4 months (top panels) and 6 months (bottom panels) were compared. At 4 months of age, Δ*PDZ-Prx* nerves contain numerous nerve fibers with myelin foldings and redundant myelin loops (red arrows) leading to axon compression. In addition to myelin foldings and thickenings, *Prx* KO nerves show features of onion bulb pathology (red arrowheads) indicative of demyelination followed by attempts of remyelination by supernumerary Schwann cells. At 6 months, thinly myelinated onion bulbs (red arrowheads) are noted in Δ*PDZ-Prx* nerves, indicating a progressive increase in abnormal myelin profiles with age. Δ*PDZ-Prx* nerves display a less severe demyelinating neuropathy than *Prx* KO nerves as revealed by fewer onion bulb formations in Δ*PDZ-Prx* mice. Scale bar, 15 μm.
B. Quantification of the proportion of hypermyelinated nerve fibers containing focally folded myelin or myelin thickenings (tomacula) in WT, Δ*PDZ-Prx* and *Prx* KO quadriceps nerves at 2, 4, 6 and 9 months. At all ages examined, Δ*PDZ-Prx* nerves contain a significantly higher percentage of myelin foldings and thickenings than WT nerves (n=3-5 per genotype for each age; *$p < 0.05$, **$p < 0.01$; Kruskal-Wallis test with Dunn's post-test).
C. The proportions of onion bulb formations are substantially higher in *Prx* KO nerves than in Δ*PDZ-Prx* or WT nerves at all ages examined (n=3-5 per genotype; *$p < 0.05$, **$p < 0.01$; Kruskal-Wallis test with Dunn's post-test).

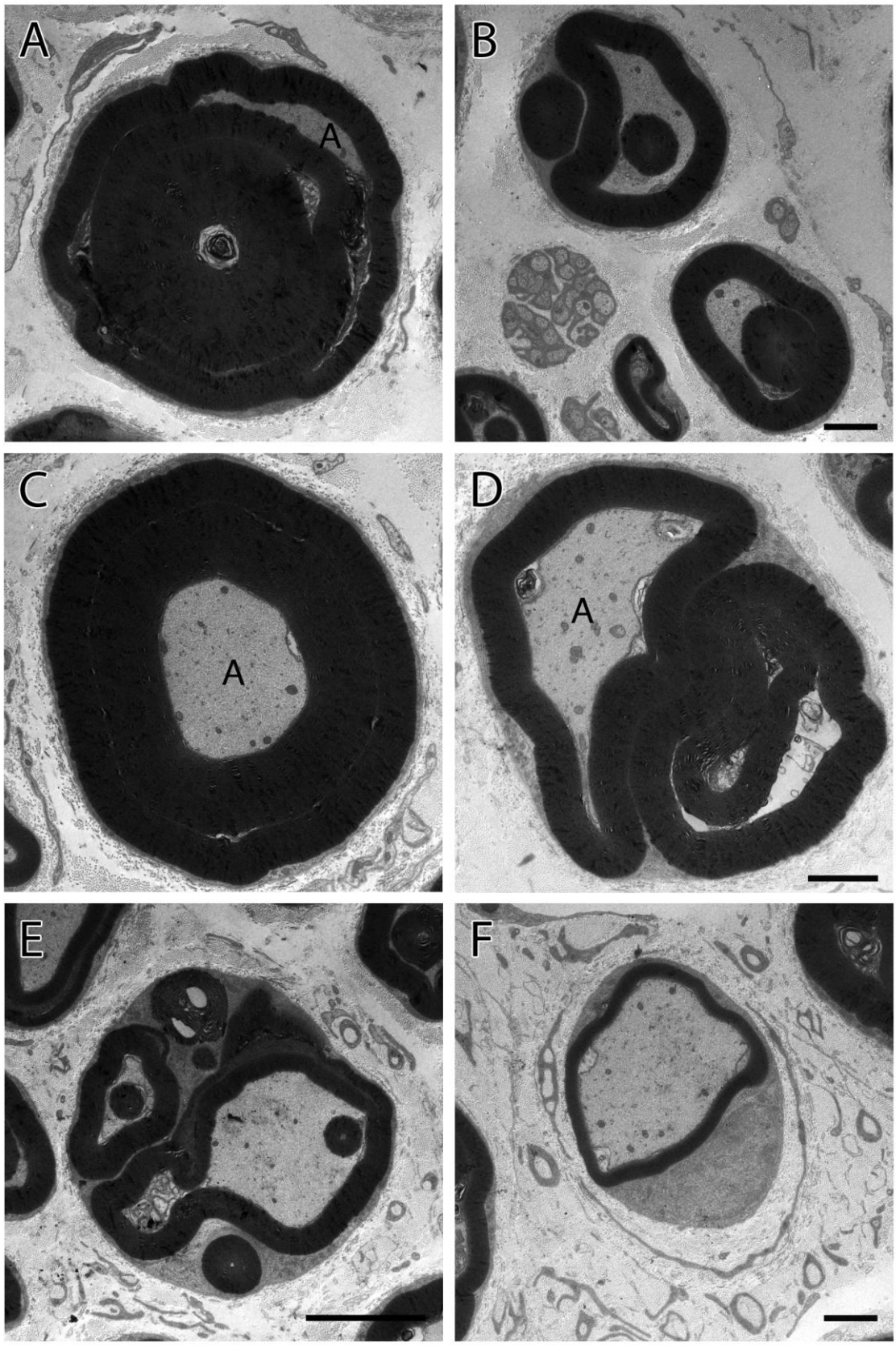
A
A
B
C
A
D
A
E
F

Figure 28. Ultrastructural analysis of Schwann cell-axon units in 8-month-old Δ*PDZ-Prx* quadriceps nerves.

A, C. Electron micrographs show excessive and aberrant myelin loops inside a myelinated axon severely affecting the axonal shape, leading to axon compression. Axonal material is found in the gap between the inner and outer myelin infolding. B. Small caliber fibers also contain myelin infoldings and outfoldings. Single (D) and multiple (E) redundant myelin loops appear as satellite myelinated axons around a larger myelinated axon surrounded by the Schwann cell membrane. F. A thinly myelinated Schwann cell-axon unit is surrounded by processes of Schwann cells forming an onion bulb. Scale bars, 2 μm (A-D, F) and 5 μm (E).

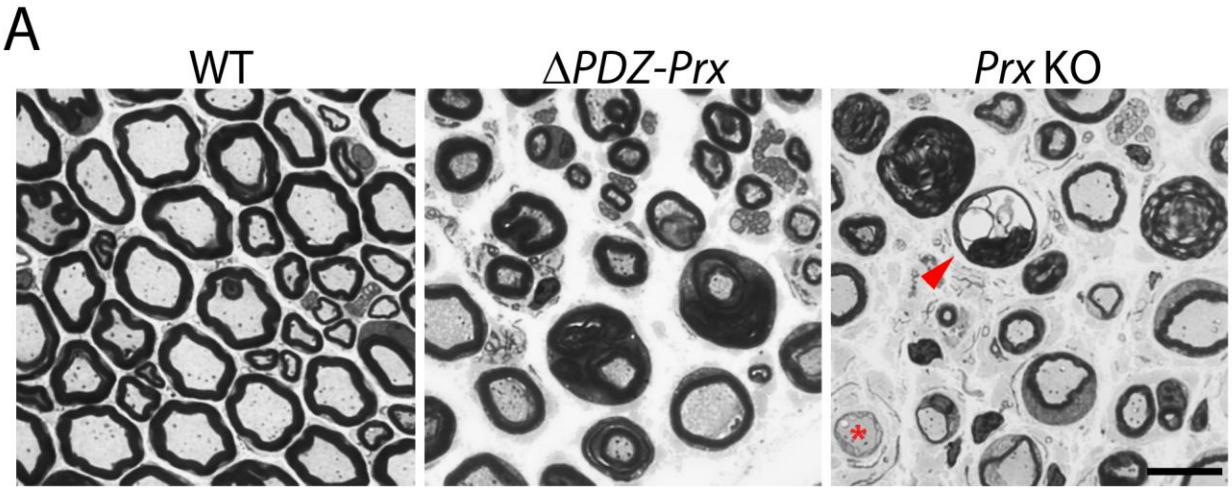
A
WT
ΔPDZ-Prx
Prx KO

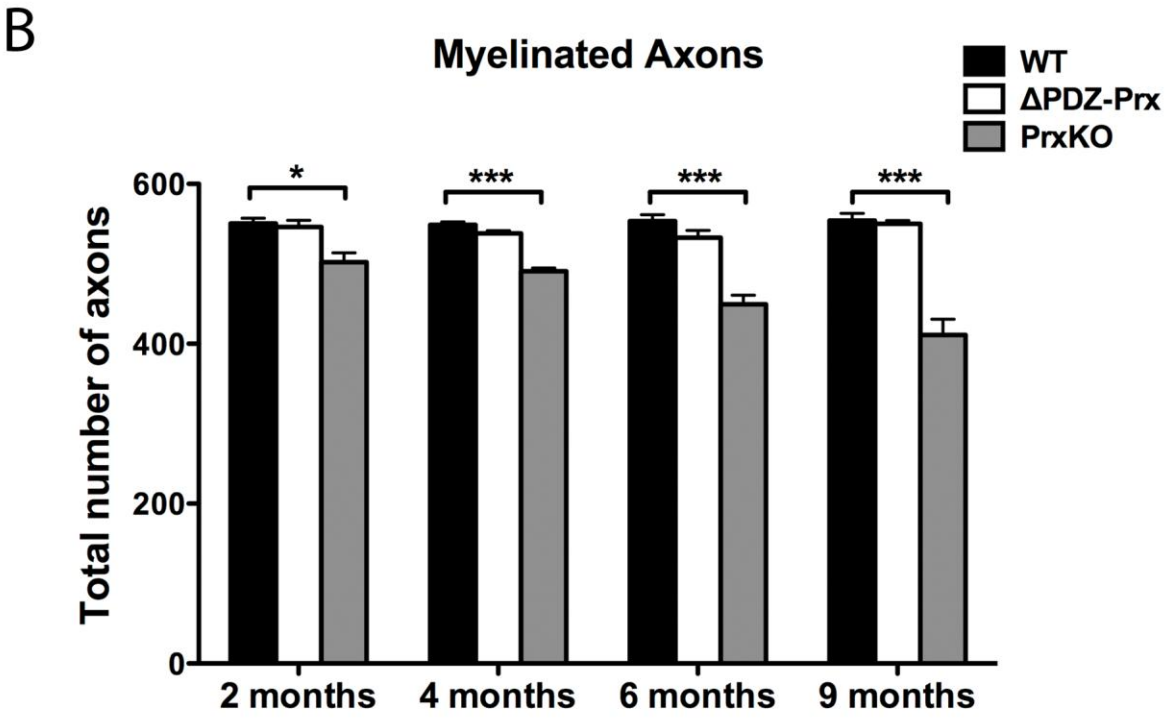
B
Myelinated Axons
WT
ΔPDZ-Prx
PrxKO
Total number of axons
600
400
200
0
*
***
***
***
2 months
4 months
6 months
9 months

Figure 29. Myelinated axon number is normal in Δ*PDZ-Prx* quadriceps nerves.

A. In 4-month-old semithin quadriceps nerve cross sections, Δ*PDZ-Prx* nerves display myelin foldings and redundant loops of myelin, but do not show signs of axon degeneration indicated by vacuolation of the axoplasm as in *Prx* KO nerves (red arrowheads). A naked axon surrounded by processes of supernumerary Schwann cells is seen (asterisk) and complex abnormal myelin morphologies are detectable in *Prx* KO quadriceps nerves. Scale bar, 10 μm.
B. Quantitation of myelinated axon numbers in WT, Δ*PDZ-Prx* and *Prx* KO quadriceps nerves at 2, 4, 6 and 9 months. The number of myelinated axons in Δ*PDZ-Prx* nerves is comparable with that in control nerves at all ages, indicating no axonal loss. However, myelinated axon number progressively decreases with age in *Prx* KO nerves, compared with the WT values (n=3-5 per group for each age; *$p < 0.05$ and ***$p < 0.0001$; one-way ANOVA with Tukey's HSD post-test for each age)

Tomacula are a pathological hallmark of hereditary demyelinating neuropathies and are predominantly located in the nodal and paranodal regions (Amici et al., 2006; Amici et al., 2007; Bolino et al., 2004). By examining single teased fiber preparations from osmicated quadriceps nerves of the Δ*PDZ-Prx* mice, it became evident (earliest age examined was at 6 weeks) that myelin foldings or thickenings were preferentially formed at the paranodes of mutant nerve fibers. Whereas the WT fibers showed regularly shaped myelin with nodes of Ranvier spaced between adjacent Schwann cells, most Δ*PDZ-Prx* myelinated fibers contained redundant loops of myelin at the paranode (Fig. 30A). 71.1 ± 1.2% of paranodal regions in mutant nerve fibers examined showed focal axonal constrictions encased by tomacular swellings (Fig. 30D). Occasionally, focal myelin thickenings were detected near the nuclei of mutant Schwann cells at 6 weeks (Fig. 30B). Consistently, focal overproduction of myelin progressed with age, as revealed by multiple myelin tomacula along the internodal or at paranodal regions in most teased fibers from 4-month-old Δ*PDZ-Prx* quadriceps nerves (Fig. 30C). Interestingly, despite pronounced focal hypermyelination, levels of compact myelin proteins, MBP and myelin protein zero (P_0), were not altered in Δ*PDZ-Prx* sciatic nerves both at 2 months and 6 months, suggesting normal myelin compaction (Fig. 30E).

To test whether the localizations of voltage-gated ion channels were altered because of paranodal myelin thickenings, voltage-gated potassium channels and sodium channels in Δ*PDZ-Prx* teased fibers at 4 months old were immunolabeled with anti-Kv1.1 and anti-pan Na^+ channel antibodies. Kv1.1 was localized in the juxtaparanodal regions of the axon between the paranodes and internodes, and at the inner mesaxon in WT fibers, as described in (Peles and Salzer, 2000). Although Kv1.1 was present in Δ*PDZ-Prx* fibers, it was not properly localized in some mutant fibers and often appeared diffuse, intruding into the internode due to a paranodal tomaculum. However, normal appearance and correct localization of Kv1.1 was also found in fibers with myelin thickenings at the paranodes. Sodium channels were correctly localized to the nodes of Ranvier in both WT and Δ*PDZ-Prx* nerves (Fig. 31).

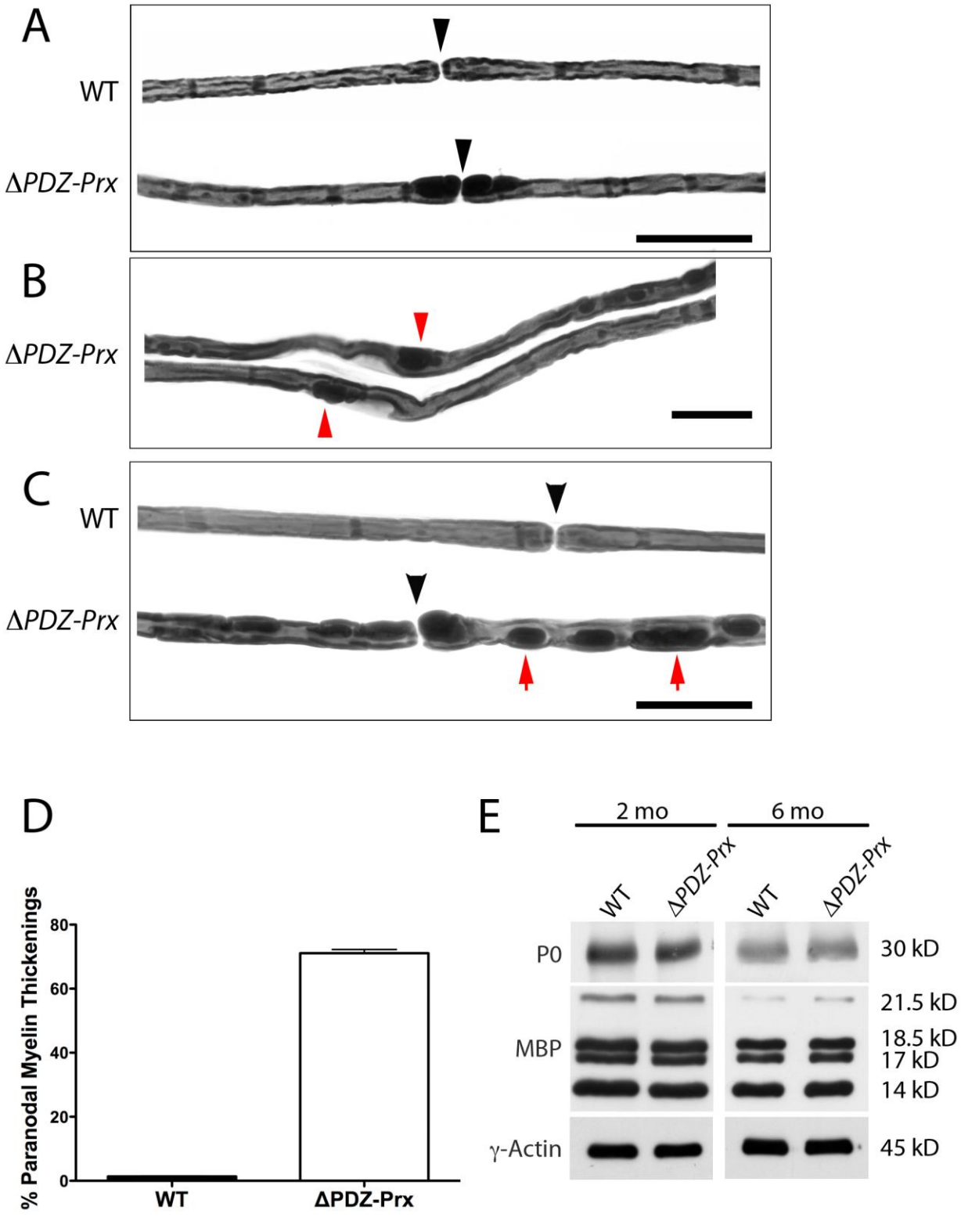
A
WT
ΔPDZ-Prx
B
ΔPDZ-Prx
C
WT
ΔPDZ-Prx
D
% Paranodal Myelin Thickenings
80
60
40
20
0
WT
ΔPDZ-Prx
E
2 mo
6 mo
WT
ΔPDZ-Prx
WT
ΔPDZ-Prx
P0
30 kD
21.5 kD
MBP
18.5 kD
17 kD
14 kD
γ-Actin
45 kD

Figure 30. Paranodal myelin thickenings are evident in teased fibers of Δ*PDZ-Prx* quadriceps nerves at 6 weeks of age.

A. Myelin tomacula are predominantly formed at the paranodal regions in osmicated teased fibers of Δ*PDZ-Prx* quadriceps nerves at 6 weeks old. Black arrowheads denote the nodes of Ranvier. Scale bar, 50 μm.
B. Occasionally, myelin thickenings are detected around the nuclei of Δ*PDZ-Prx* Schwann cells (red arrowheads) at 6 weeks of age. Scale bar, 30 μm.
C. In 4-month-old Δ*PDZ-Prx* quadriceps nerves, multiple myelin depositions are visible along the internodes (red arrows), in addition to paranodal tomacula. Black arrowheads: nodes of Ranvier. Scale bar, 50 μm.
D. Quantitation of the proportion of paranodal myelin thickenings in 6-week-old WT and Δ*PDZ-Prx* fibers reveals that over 70% of paranodes in Δ*PDZ-Prx* fibers contain a tomaculum (*n*=3 per genotype).
E. Western blot analysis of P_0 and MBP on sciatic nerve homogenates from WT and Δ*PDZ-Prx* mice at 2 and 6 months old. At both ages, P_0 and MBP levels in WT and Δ*PDZ-Prx* nerves are similar. γ-actin was used to normalize loading. Molecular weights of proteins in kilodaltons (kD) are indicated on the right.

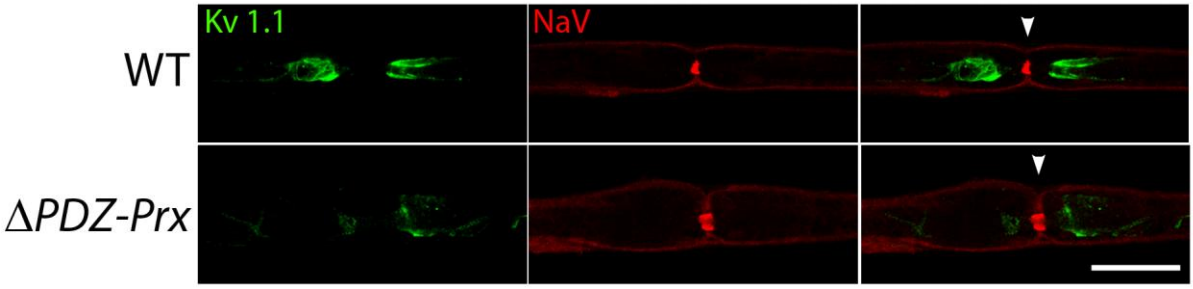

Figure 31. Voltage-gated potassium channels Kv1.1 are abnormally localized in a proportion of Δ*PDZ-Prx* quadriceps nerves fibers.

Teased fibers from quadriceps nerves of 4-month-old WT and Δ*PDZ-Prx* mice were co-labeled with anti-Kv1.1 and anti-NaV antibodies. Sodium channels are correctly localized to the node of Ranvier in both WT and Δ*PDZ-Prx* fibers. Kv1.1 channels are localized to the juxtaparanodes in WT teased fibers. In contrast, it appears diffuse and mislocalized in some mutant fibers due to the presence of paranodal tomacula. Arrowheads denote nodes of Ranvier. Scale bar, 20 μm.

3.1.11 Abnormally myelinated Δ*PDZ-Prx* nerve fibers are prone to mechanical stress leading to shifted localization of nodal proteins

In teased fiber preparations of adult Δ*PDZ-Prx* nerves, displacement of the nodes of Ranvier was occasionally detectable. Figure 32A shows the paranodal region, labeled for glial Neurofascin (Nfasc155), together with the node of Ranvier, of the left fiber invaginating into the paranode on the right. Similarly, in the mutant fiber in Figure 32B, despite normal expression of Neurofascin, the paranode, alongside the gliomedin-stained microvilli, in one Schwann cell-axon unit shifted into the paranodal region of the apposing hypermyelinated Δ*PDZ-Prx* fiber that was surrounded by an abnormal and apparently multi-layered basal lamina. This phenomenon was rarely seen in WT teased fibers.

To determine whether this observation was due to an artifact caused by mechanical stretching during fiber teasing, I examined the localizations of the nodes and paranodes in longitudinal cryostat sections of the quadriceps nerves. Unlike in single teased fibers, nodal displacement was not noted in Δ*PDZ-Prx* nerve fibers on longitudinal sections (data not shown), suggesting that this phenomenon did not occur normally *in vivo*, but was a teasing artifact, likely attributed to unstable anchorage of the paranodal myelin loops to the axolemma because of abnormal focal hypermyelination.

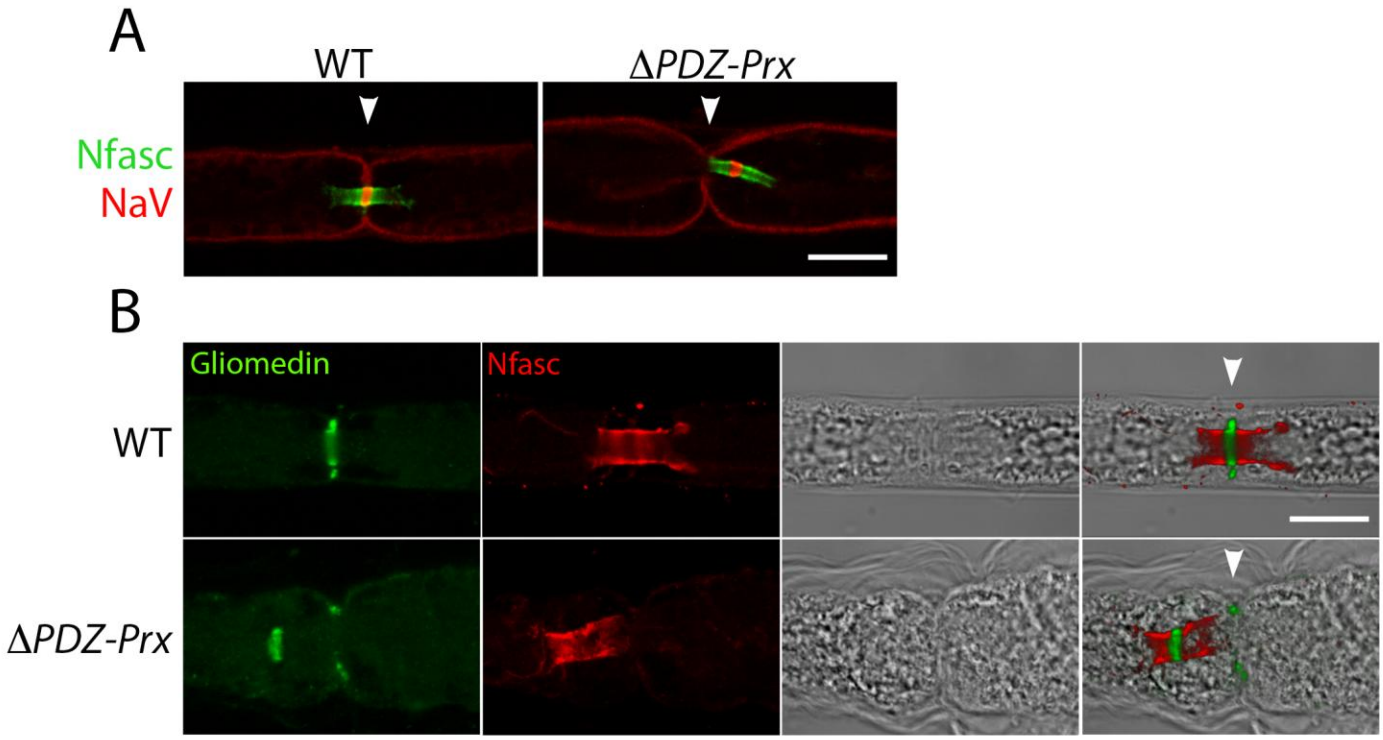

Figure 32. Abnormally folded myelin in Δ*PDZ-Prx* fibers is unstable leading to shifted localization of nodal proteins during fiber teasing.

A. Immunostaining of quadriceps nerve teased fibers from 4-month-old WT and Δ*PDZ-Prx* mice for voltage-gated sodium channels and paranodal marker Neurofascin. In the Δ*PDZ-Prx* teased fiber, the node of Ranvier appears displaced, with the paranode on the left fiber shifted into the apposing Schwann cell-axon unit on the right. Background staining shows myelin thickenings at the paranodal regions in mutant fibers. Arrowheads denote nodes of Ranvier. Scale bar, 10 μm.

B. Immunofluorescence labeling of WT and Δ*PDZ-Prx* quadriceps nerve teased fibers at 4 months for gliomedin in Schwann cell microvilli and paranodal Neurofascin are overlayed with transmitted light images of teased fibers, revealing shifted localization of nodal and paranodal proteins in mutant nerve fibers. Phase contrast images show a thin sheet of regularly shaped basal lamina surrounding the Schwann cell membrane in normal fibers. However, in mutant fibers, basal lamina appears irregular in shape and in multiple layers. Arrowheads denote nodes of Ranvier. Scale bar, 10 μm.

3.1.12 Non-myelinating Schwann cell number is increased in adult Δ*PDZ-Prx* quadriceps nerves

Mature Δ*PDZ-Prx* peripheral nerves characterized by extensive myelin folding are enlarged in size due to ECM accumulation in the endoneurium. Indeed, upregulation of ECM molecules such as collagens, fibronectin and laminin has been reported in the nerve biopsies of Charcot-Marie-Tooth disease type 1 patients (Palumbo et al., 2002). In the twitcher mouse, the activation and proliferation of supernumerary Schwann cells in response to demyelination is associated with excessive ECM in the endoneurial space (Kagitani-Shimono et al., 2008). To assess whether there was an elevation in Schwann cell number, which might be responsible for the increase in endoneurial space in adult Δ*PDZ-Prx* peripheral nerves, despite limited demyelination, I immunostained 4-month-old Δ*PDZ-Prx* quadriceps nerve transverse sections with anti-$p75^{NGFR}$ antibody for non-myelinating Schwann cells. In normal nerves, $p75^{NGFR}$-immunopositive non-myelinating Schwann cells predominantly associated in clusters, presumably with Remak bundles, found between myelinated axons with compact myelin uniformly labeled with anti-P0 antibody. However, in enlarged Δ*PDZ-Prx* and *Prx* KO nerves, $p75^{NGFR}$ immunoreactivity was detected ubiquitously in the endoneurium throughout the entire quadriceps nerve cross sections (Fig. 33A). At higher magnification, numerous $p75^{NGFR}$-immunopositive Schwann cells and processes enveloped thinly myelinated axons or even hypermyelinated axons indicated by irregular P0 staining (Fig. 33B), suggesting an increase in non-myelinating Schwann cells in the Δ*PDZ-Prx* and Periaxin-null nerves.

The augmentation of Schwann cell number was further confirmed by quantification of the number of myelinating Schwann cells and total Schwann cells by Krox-20 and Sox10 immunolabeling per cross section of the quadriceps nerves from WT, Δ*PDZ-Prx* and *Prx* KO mice at 4 months old (Fig. 34A). Δ*PDZ-Prx* and *Prx* KO nerves had two and three times higher the number of Krox-20-positive cells per cross section than WT nerves, respectively. Remarkably, the total number of Schwann cells labeled for Sox10 was significantly elevated by three-fold in Δ*PDZ-Prx* nerves and five-fold in *Prx* KO nerves (n=3; $p < 0.0001$; Fig. 34B), compared with the normal nerves.

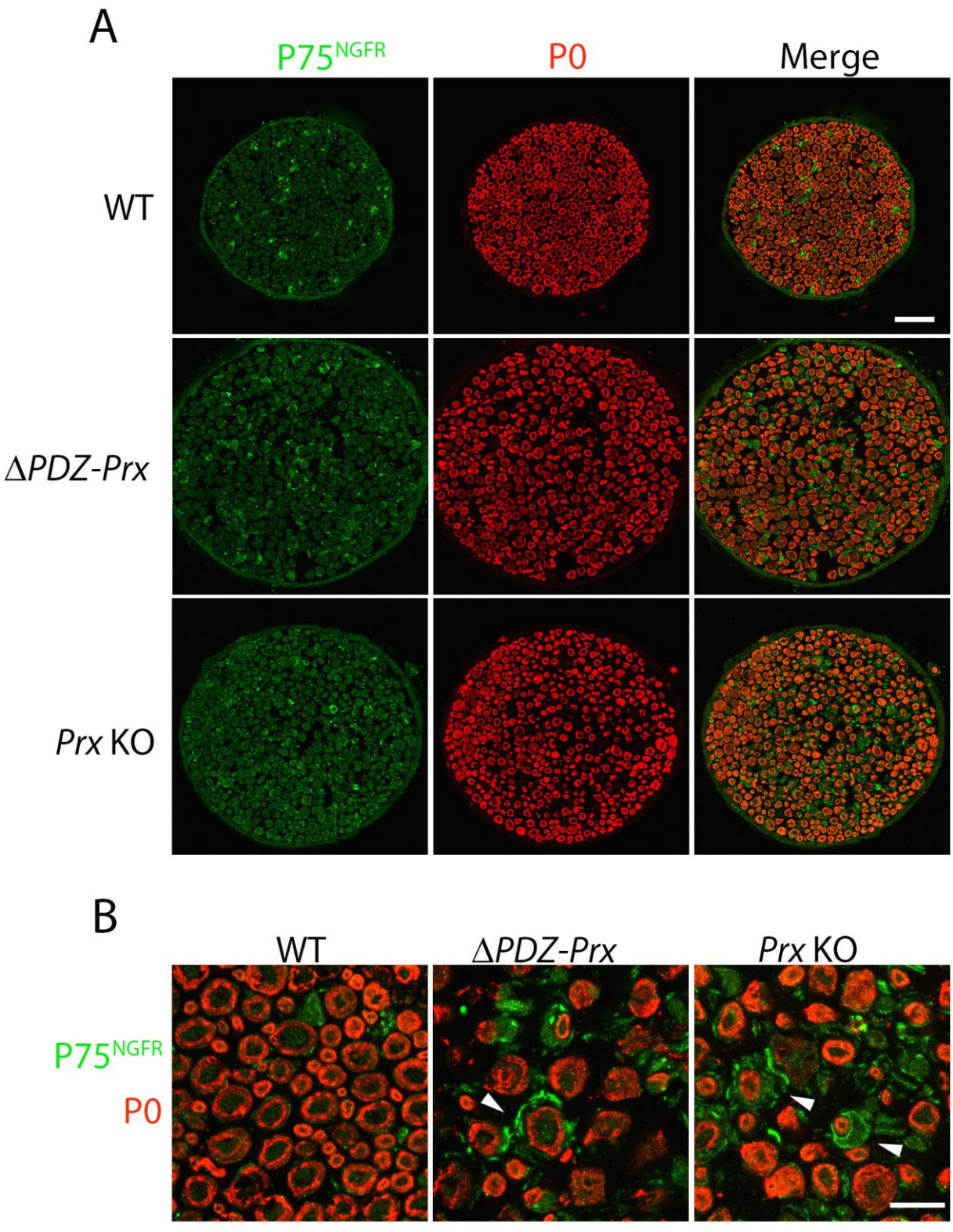
A
P75NGFR
P0
Merge
WT
ΔPDZ-Prx
Prx KO
B
WT
ΔPDZ-Prx
Prx KO
P75NGFR
P0

Figure 33. An increase in non-myelinating Schwann cells in mature Δ*PDZ-Prx* quadriceps nerves

A. Confocal immunofluorescence analysis of quadriceps nerve cross sections from 4-month-old WT, Δ*PDZ-Prx* and *Prx* KO mice doubled-labeled with anti-$P75^{NGFR}$ and anti-P0 antibodies. In WT nerves, $P75^{NGFR}$ immunoreactivity is detected in distinct clusters representing Remak bundles located between myelinated axons. However, in Δ*PDZ-Prx* and *Prx* KO nerve sections, $P75^{NGFR}$-positive non-myelinating Schwann cells are ubiquitously localized between myelinated axons. Scale bar, 50 μm.
B. At higher magnification, thinly myelinated and also hypermyelinated axons are surrounded by non-myelinating Schwann cells labeled for $P75^{NGFR}$ in both Δ*PDZ-Prx* and *Prx* KO quadriceps nerves (arrowheads). Scale bar, 15 μm.

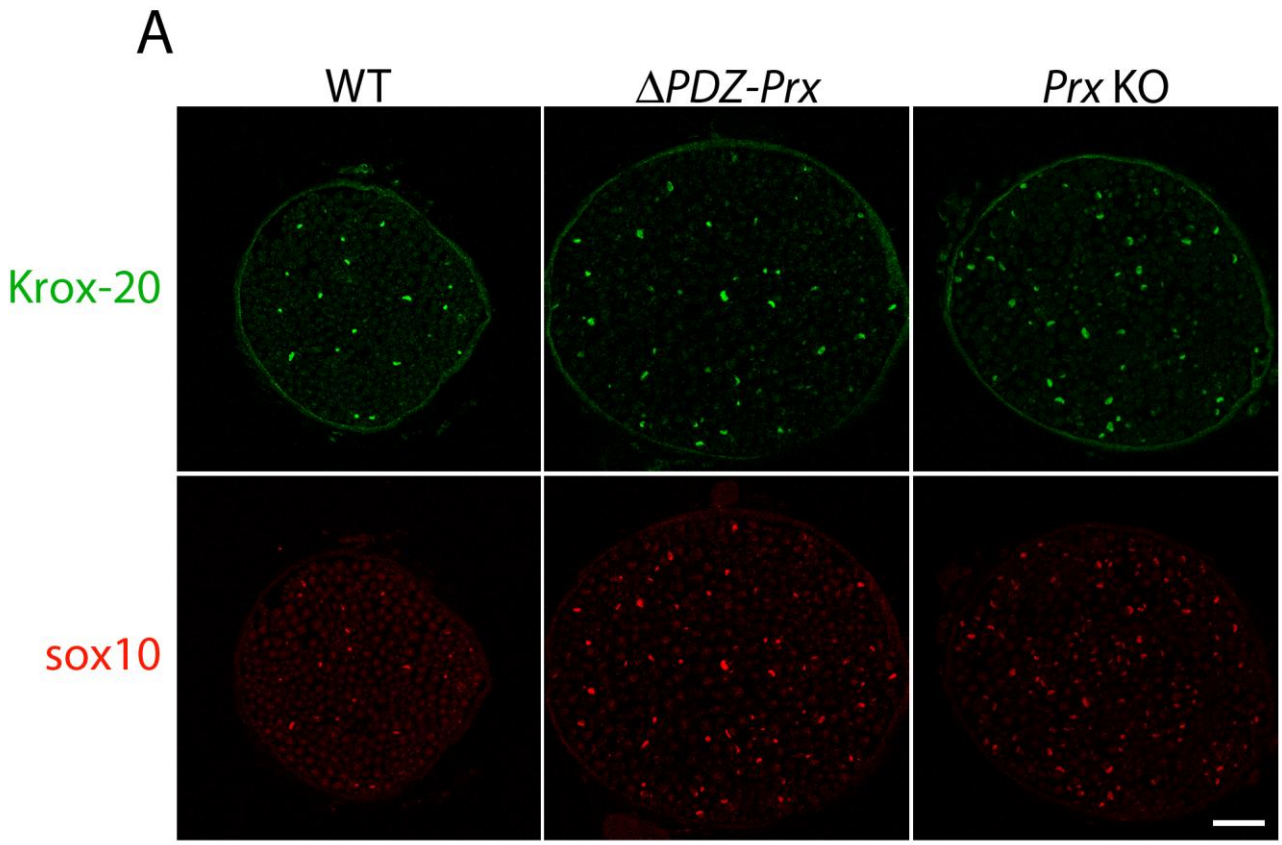
A
WT
ΔPDZ-Prx
Prx KO
Krox-20
sox10

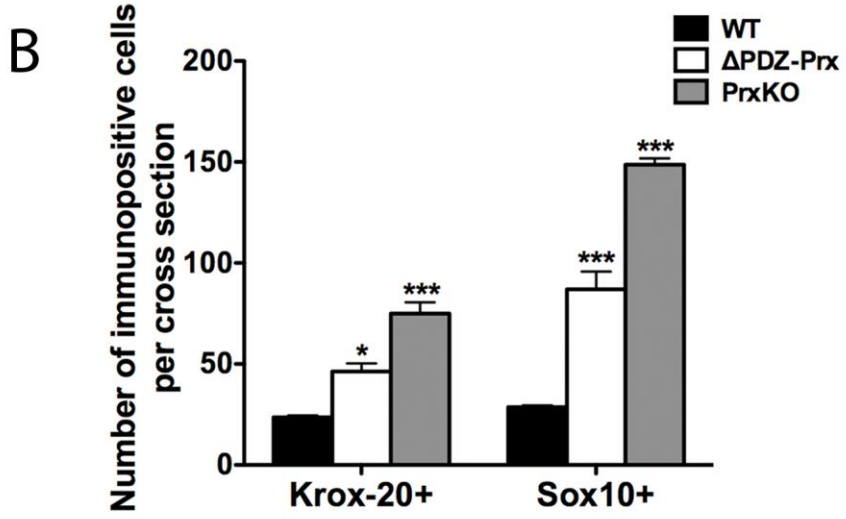
B
WT
ΔPDZ-Prx
PrxKO
Number of immunopositive cells per cross section
200
150
100
50
0
*
***
***
***
Krox-20+
Sox10+

Figure 34. Quantification of Schwann cell numbers shows a significant elevation in non-myelinating Schwann cells in adult Δ*PDZ-Prx* quadriceps nerves.

A. Double labeling of quadriceps nerve cross sections from 4-month-old WT, Δ*PDZ-Prx* and *Prx* KO with anti-Krox-20 and anti-Sox10 antibodies shows an increase in the number of myelinating Schwann cell nuclei labeled for Krox-20 and Schwann cell nuclei for Sox10. Scale bar, 50 μm.
B. Quantitation of the numbers of Krox-20- and Sox10-positive cells per cross section of WT, Δ*PDZ-Prx* and *Prx* KO quadriceps nerves at 4 months old reveals that there is a two- and three-fold increase in the number of Krox-20-positive myelinating Schwann cells in Δ*PDZ-Prx* and *Prx* KO nerves, respectively, compared with WT nerves (n=3; *$p < 0.05$ and ***$p < 0.001$; one-way ANOVA with Tukey's HSD post-test). The number of Sox10-positive Schwann cells is considerably increased by three times in Δ*PDZ-Prx* nerves and five times in *Prx* KO nerves (n=3; $p < 0.0001$; one-way ANOVA with Tukey's HSD post-test).

3.1.13 Schmidt-Lanterman incisures are morphologically normal in myelinated Δ*PDZ-Prx* fibers

Schmidt-Lanterman incisures (SLIs) are cytoplasmic channels within compact myelin that connect the Schwann cell abaxonal cytoplasm to the adaxonal cytoplasm. They have been implicated in facilitating transport of metabolic substances across the myelin sheath via gap junctions (Ghabriel and Allt, 1981; Gould et al., 1995). SLIs become fully mature at 2 months of age in mice (Tricaud et al., 2005). To determine whether SLIs were affected in Δ*PDZ-Prx* nerves, teased fiber preparations from quadriceps nerves at 2 months were labeled with phalloidin, and the number of SLIs was counted. Similar to the WT teased fibers, the morphology of SLIs in Δ*PDZ-Prx* fibers appeared grossly normal (Fig. 35A). In agreement with our published data (Gillespie et al., 2000), SLIs in *Prx* KO nerve fibers were deranged. Δ*PDZ-Prx* fibers contained slightly fewer SLIs per internode than WT fibers (WT, 13.72 ± 0.33; Δ*PDZ-Prx*, 11.95 ± 0.27; $p < 0.05$; Fig. 35C). However, due to a reduction in Schwann cell internodal lengths, SLIs in Δ*PDZ-Prx* nerves appeared more densely arranged along the internode than the WT controls. The number of SLIs per 100 μm fiber was slightly elevated in Δ*PDZ-Prx* fibers compared with that of WT fibers (WT, 2.20 ± 0.04 vs Δ*PDZ-Prx*, 2.63 ± 0.09; $p < 0.05$; Fig. 35B).

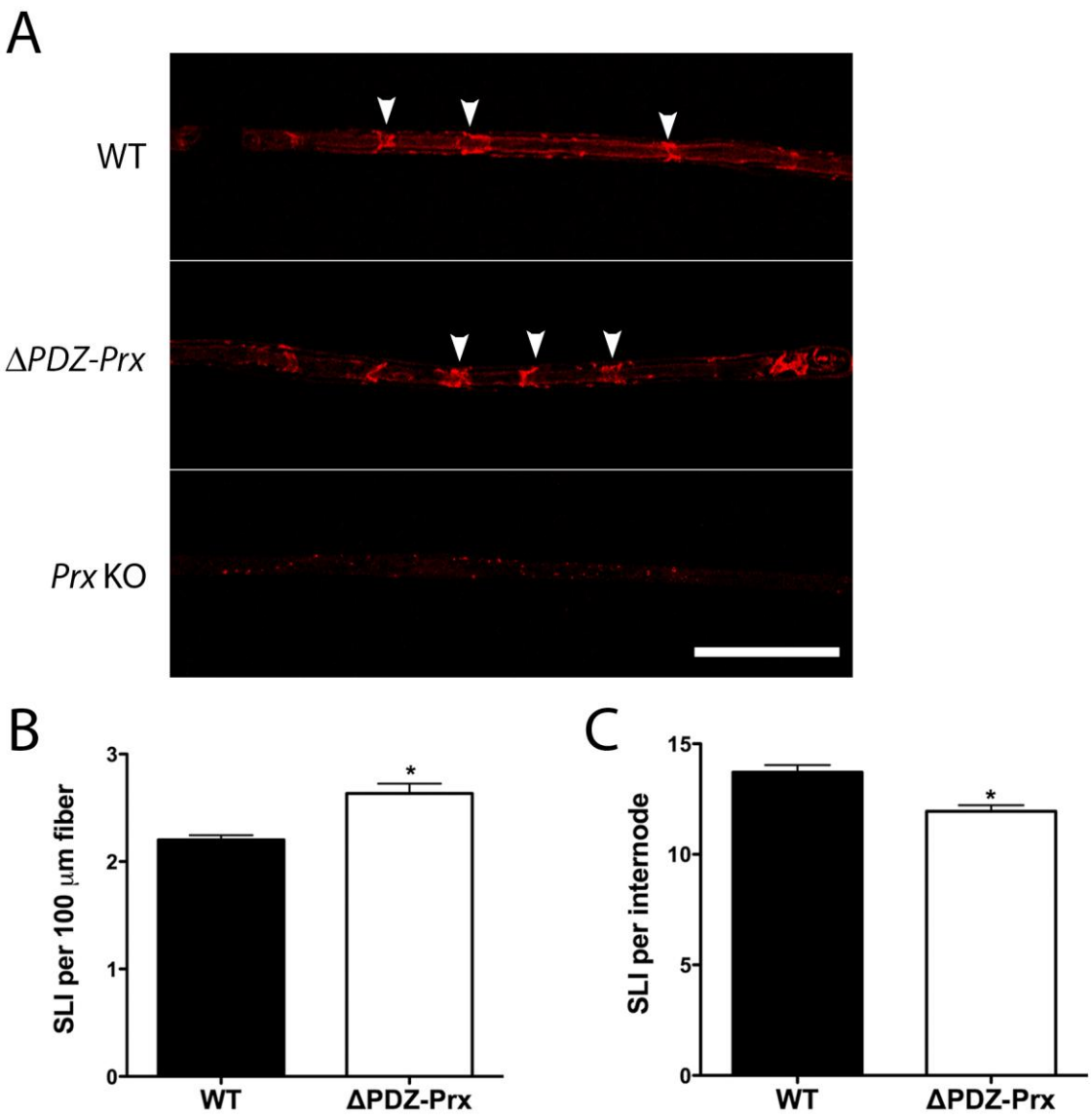

Figure 35. SLIs are morphologically normal in Δ*PDZ-Prx* peripheral nerve fibers.

A. Quadriceps nerve teased fibers were stained with phalloidin for SLIs in 2-month-old mice. Δ*PDZ-Prx* fibers harbored SLIs, which were morphologically similar to those in the WT control (arrowheads). In contrast, the incisures were completely deranged in *Prx* KO nerves. Scale bar, 50 μm.

B. SLIs appeared more densely arranged in Δ*PDZ-Prx* teased fibers due to reduced Schwann cell internodal lengths. Hence, the number of incisures per 100 μm internode is modestly higher in Δ*PDZ-Prx* fibers than in the WT (n=4 per genotype; $p < 0.05$; Mann-Whitney *U*-test).

C. The number of SLIs per internode in Δ*PDZ-Prx* fibers is decreased (n=4 per genotype; $p < 0.05$; Mann-Whitney *U*-test).

3.1.14 Electrophysiological investigations of peripheral nerves in Δ*PDZ-Prx* mice

Our laboratory has previously demonstrated experimentally that nerve conduction velocity is sensitive to changes in internodal lengths in 3-week-old Periaxin-null mice, at which age parameters known to influence nerve conduction velocity, including myelin sheath thickness, axon diameter and localization of sodium channels are normal (Court et al., 2004). In Δ*PDZ-Prx* mice, Schwann cell elongation was impaired leading to a decrease in internodal lengths both in young ages and in the adult (section 3.1.9). It was of particular interest to address whether nerve conduction velocity was reduced with respect to a shortening of Schwann cell internodal distance in Δ*PDZ-Prx* nerves, given that other parameters mentioned above are not affected (section 3.1.8).

3.1.14a- Conduction velocity of Δ*PDZ-Prx* nerves is reduced at 3 weeks, but normal at 4 months

I measured nerve conduction velocity from acutely isolated femoral nerves with the quadriceps branch from 3-week- and 4-month-old WT, Δ*PDZ-Prx* and *Prx* KO (n=5-10 per group for each age). From isolated nerve preparations, latencies of the onset of compound action potentials at varying conduction distances were measured from an active population of the fastest conducting and largest caliber Group A fibers, namely the Aα and Aβ fibers. Nerve conduction velocities were determined as described in methods (section 2.12.1). At 3 weeks, the conduction velocity of Δ*PDZ-Prx* nerves was dramatically reduced compared with the WT (Fig. 36). This was in agreement with the *Prx* KO values, which also showed a significant reduction in nerve conduction velocity (WT, 20.9 ± 1.7 m/s; Δ*PDZ-Prx*, 8.5 ± 0.5 m/s; *Prx* KO, 12.6 ± 1.1 m/s; $p < 0.001$). Intriguingly, despite shorter Schwann cell internodal lengths and myelin abnormalities (sections 3.1.9 and 3.1.10), 4-month-old Δ*PDZ-Prx* nerves had normal conduction velocity, similar to the control values. Due to severe demyelination, the conduction velocity of adult *Prx* KO nerves was considerably reduced compared with both the WT and mutant nerves (WT, 39.4 ± 1.7 m/s; Δ*PDZ-Prx*, 41.6 ± 1.5 m/s; *Prx* KO, 17.9 ± 1.9 m/s).

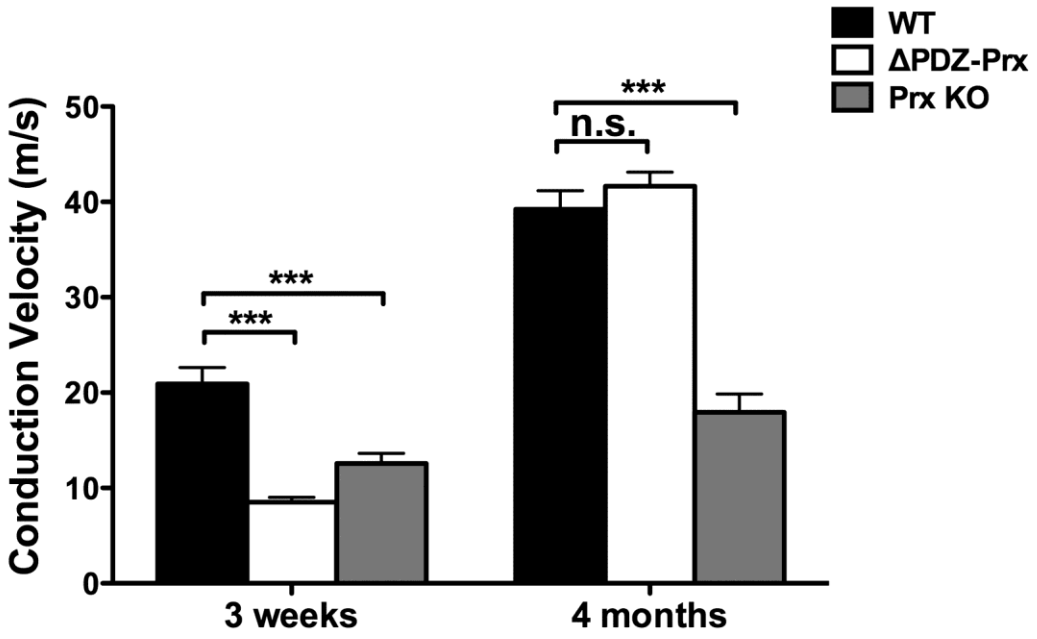

Figure 36. Nerve conduction velocity is reduced at 3 weeks but normal at 4 months in Δ*PDZ-Prx* mice.

Nerve conduction velocities were measured from WT, Δ*PDZ-Prx* and *Prx* KO quadriceps nerves at 3 weeks and 4 months. At 3 weeks old, nerve conduction velocity is reduced, in concurrence with a decrease in internodal length in both Δ*PDZ-Prx* and *Prx* KO mice. Interestingly, the conduction velocity of 4-month-old Δ*PDZ-Prx* nerves is similar to the WT values. Adult *Prx* KO nerves have considerably reduced conduction velocity (n=5-10 per genotype for each age; ***$p < 0.0001$; one-way ANOVA with Tukey's HSD post-test).

3.1.14b- By 4 months old, Δ*PDZ-Prx* Schwann cells are sufficiently long to support normal nerve conduction

Δ*PDZ-Prx* peripheral nerves contained focally folded myelin and tomacula, but limited onion bulb formation suggestive of a low degree of demyelination (section 3.1.10). The observation that Δ*PDZ-Prx* peripheral nerves were able to conduct normally prompted me to hypothesize that in mature mutant peripheral nerves, Schwann cells have elongated sufficiently to support normal conduction of axons when mild demyelination only minimally affects nerve conduction. To test this, the conduction velocities of WT and Δ*PDZ-Prx* nerves at 6 weeks, an age intermediary of 3 weeks and 4 months, were measured. The conduction velocity of WT quadriceps nerves at 6 weeks was 38.3 ± 1.5 m/s, which was not significantly different from that in normal adult nerves. Δ*PDZ-Prx* nerves at 6 weeks had a conduction velocity of 29.4 ± 1.1 m/s, which was between those of Δ*PDZ-Prx* nerves at 3 weeks and 4 months (Fig. 38B).

Whereas the conduction velocity of Δ*PDZ-Prx* nerves at 3 weeks was reduced to half the WT values, Δ*PDZ-Prx* nerve conduction velocity at 6 weeks of age was only slower than that of WT nerves by about 25%. A tendency towards an increase in nerve conduction velocity was evident with Schwann cell longitudinal growth over time in Δ*PDZ-Prx* nerves, highly supportive of the notion that mutant Schwann cells had reached a threshold length to support normal nerve conduction in the adult, alongside an increase in axon diameters with nerve growth.

Next, I decided to estimate the threshold internodal lengths in mutant Schwann cells. Since nerve conduction velocity was measured from the largest caliber Group A fibers using the current set-up, internodal lengths of the largest diameter fibers were selectively determined from quadriceps nerve teased fibers of WT and Δ*PDZ-Prx* mice at 3 weeks, 6 weeks and 4 months of age. Teased fibers were double labeled with an anti-neurofilament antibody for the estimation of axon diameters, and an anti-dystrophin antibody for internodal length measurements. The distributions of axon diameters of WT and mutant fibers were comparable at all ages examined (Fig. 37). The scatter plots in

Figure 37 depicted that, with the same axon diameter, the majority of Δ*PDZ-Prx* internodal lengths were shorter than those of the WT.

Although there have been few quantitative studies of peripheral nerves of the mouse reported in the literature, the composition of peripheral nerves has been extensively studied in cats, from which the general classification and proportion of nerve fibers should apply to other mammals (Boyd, 1968). In cats, the largest caliber Aα and Aβ fibers comprise approximately 60% of all myelinated afferent and efferent nerve fibers, thus excluding non-myelinated C-fibers, in nerves to skeletal muscle (Boyd, 1968). In light of these findings and in order to impose stricter criteria on selection of large diameter fibers, I decided to take into account ~50% of all myelinated fibers for the estimation of the cut-off diameters for large caliber axons in the quadriceps nerve at each age. The cut-off axon diameters at the age of 3 weeks, 6 weeks and 4 months were 4.2 μm, 4.875 μm and 6.0 μm, respectively (Figs. 37B, D and F).

The mean internodal lengths of large diameter fibers from WT and Δ*PDZ-Prx* nerves were calculated from the internodal lengths of myelinated fibers with axon diameter larger than or equal to the cut-off diameter (Table 3 and Fig. 38A). The average internodal length of large diameter fibers at 6 weeks in WT was 575.4 ± 15.5 μm, at which length and axon diameter nerve fibers were conducting as fast as adult nerves. The threshold Schwann cell internodal length for normal nerve conduction in Δ*PDZ-Prx* nerves was in the range of 422.1 ± 15.5 μm and 540.4 ± 8.5 μm, likely close to the higher end, together with an increase in the mean axon diameter with age.

3.1.14C-Δ*PDZ-Prx* mice have reduced nerve conduction velocity at 10 months old

Consistent with a gradual increase in myelin abnormalities and pathological onion bulb formations, the nerve conduction velocity of Δ*PDZ-Prx* mice at 10 months of age, was reduced compared with WT values (WT, 43.1 ± 1.2 m/s vs Δ*PDZ-Prx*, 31.8 ± 1.3 m/s; $p < 0.001$; Fig. 38C).

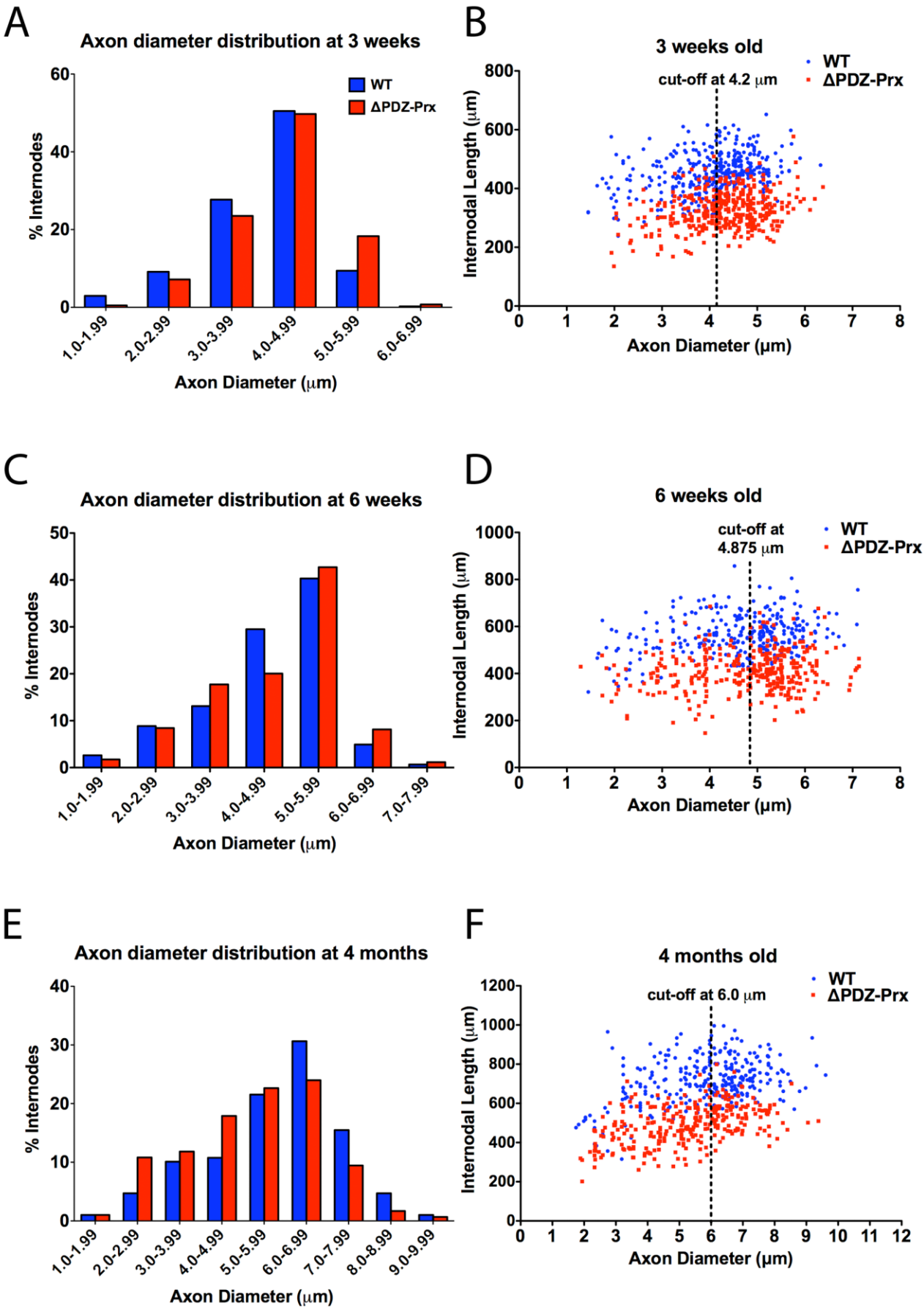
A
Axon diameter distribution at 3 weeks
% Internodes
WT
ΔPDZ-Prx
1.0-1.99
2.0-2.99
3.0-3.99
4.0-4.99
5.0-5.99
6.0-6.99
Axon Diameter (μm)
B
3 weeks old
cut-off at 4.2 μm
WT
ΔPDZ-Prx
Internodal Length (μm)
Axon Diameter (μm)
C
Axon diameter distribution at 6 weeks
% Internodes
1.0-1.99
2.0-2.99
3.0-3.99
4.0-4.99
5.0-5.99
6.0-6.99
7.0-7.99
Axon Diameter (μm)
D
6 weeks old
cut-off at
4.875 μm
WT
ΔPDZ-Prx
Internodal Length (μm)
Axon Diameter (μm)
E
Axon diameter distribution at 4 months
% Internodes
1.0-1.99
2.0-2.99
3.0-3.99
4.0-4.99
5.0-5.99
6.0-6.99
7.0-7.99
8.0-8.99
9.0-9.99
Axon Diameter (μm)
F
4 months old
cut-off at 6.0 μm
WT
ΔPDZ-Prx
Internodal Length (μm)
Axon Diameter (μm)

Figure 37. Determination of the average internodal lengths of large caliber fibers.

Quadriceps nerve teased fibers from WT and Δ*PDZ-Prx* mice at 3 weeks, 6 weeks and 4 months were co-stained with an anti-neurofilament antibody for axon diameter measurements, and an anti-dystrophin antibody for internodal length measurements. The distributions of axon diameters are similar between WT and Δ*PDZ-Prx* myelinated axons at all ages examined shown in A, C and F. The scatter plots in B, D and F show internodal lengths of individual fibers in relation to axon diameter. For determination of the mean internodal lengths of large caliber fibers, fibers with large axon diameters, which comprise 50% all myelinated fibers examined, were taken into account for the estimation of the cut-off axon diameters. The cut-off diameters for 3 weeks, 6 weeks and 4 months are 4.2 μm, 4.875 μm and 6.0 μm, respectively.

	WT		*ΔPDZ-Prx*	
	IL (μm)	NCV (m/s)	IL (μm)	NCV (m/s)
3 weeks	471.9 ± 18.0	20.9 ± 1.7	339.6 ± 6.4	8.5 ± 0.5
6 weeks	575.4 ± 15.5	38.3 ± 1.5	422.1 ± 8.9	29.4 ± 1.1
4 months	737.4 ± 18.5	39.4 ± 1.7	540.4 ± 8.5	41.6 ± 1.5

Table 3. The mean internodal lengths (IL) of large caliber fibers and nerve conduction velocities (NCV) of WT and Δ*PDZ-Prx* at various ages.

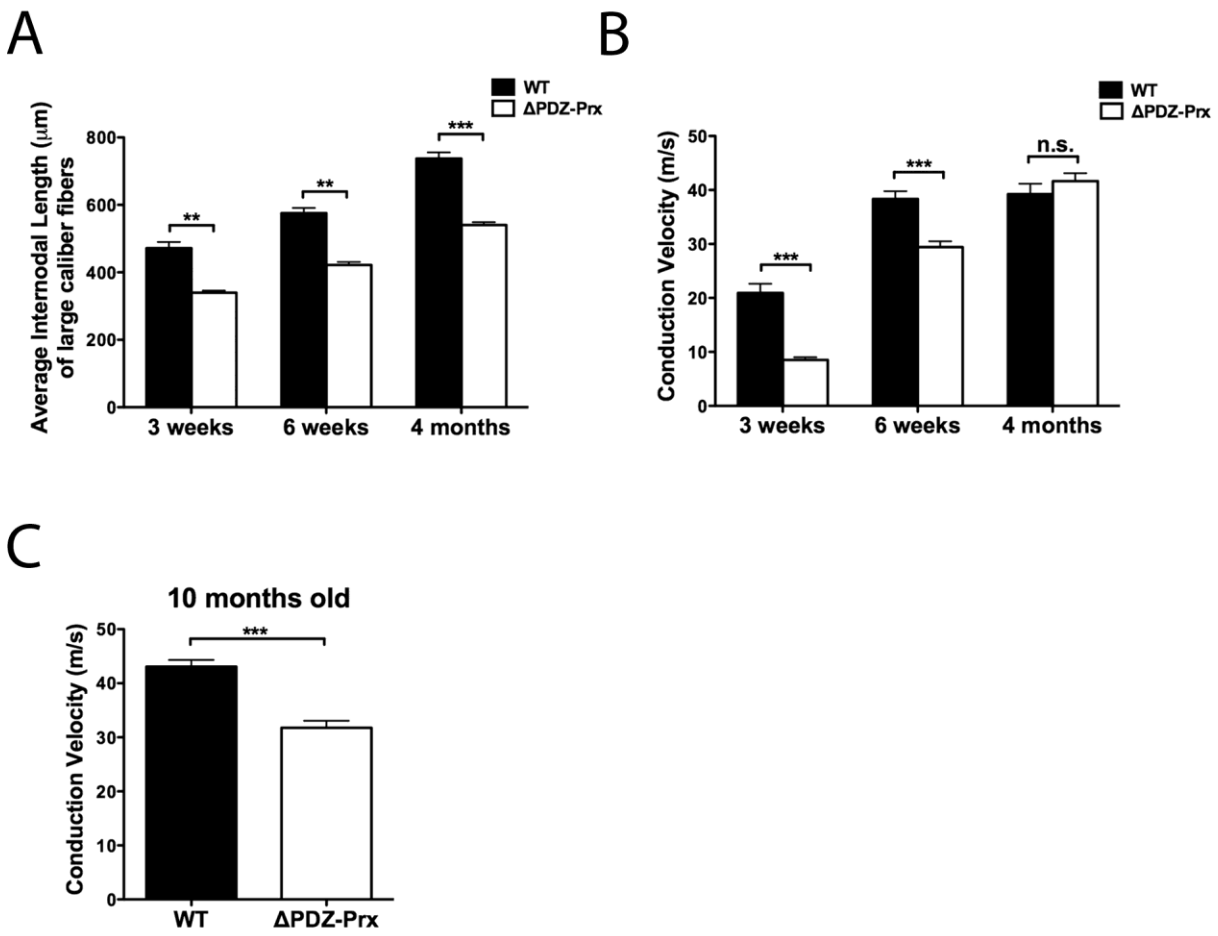

Figure 38. Adult Δ*PDZ-Prx* Schwann cells are sufficiently long to support normal conduction of axons.

A. The average internodal lengths of large caliber fibers from WT and Δ*PDZ-Prx* nerves at 3 weeks, 6 weeks and 4 months were calculated from the internodal lengths of myelinated fibers with axon diameter larger than or equal to the cut-off diameter (n=5-10 per genotype per age; $^{**}p < 0.01$ and $^{***}p < 0.001$; Student's t-test).

B. Nerve conduction velocities were measured in WT and Δ*PDZ-Prx* quadriceps nerves at an intermediate age, 6 weeks. The conduction velocity of WT quadriceps nerves at this age is similar to that of 4-month-old WT nerves. Δ*PDZ-Prx* conduction velocity at 6 weeks is catching up with that of normal nerves and is between values at 3 weeks and 4 months of mutant nerves, showing a tendency to an increase in conduction velocity with age (n=5-10 per genotype per age; $^{***}p < 0.0001$; one-way ANOVA with Tukey's HSD post-test).

C. In agreement with a progressive increase in abnormal profiles and onion bulb formation, 10-month-old Δ*PDZ-Prx* nerves have reduced nerve conduction velocities (n=5-7 per genotype per age; $p = 0.0001$; Student's t-test).

3.1.15 Motor coordination is impaired in 3-week-old but not in 4-month-old Δ*PDZ-Prx* mice

Motor coordination was tested in 3-week- and 4-month-old WT, Δ*PDZ-Prx* and *Prx* KO animals using a RotaRod. Mice were trained on a rotating RotaRod at two rotating speeds, 24 rpm and 32 rpm, for two consecutive days before the test trial. The test was terminated when the mice fell from the rod or at 60 s. RotaRod performance was evaluated by the mean latency to fall at the two rotating speeds tested. At 3 weeks, Δ*PDZ-Prx* and *Prx* KO mice performed equally well as WT mice at 24 rpm (n=12-16 per group). However at 32 rpm, the performance of Δ*PDZ-Prx* and *Prx* KO mice was substantially poorer than WT controls (Fig. 39), confirming impairment in motor coordination consequent to a reduction in nerve conduction velocity at this age.

In concurrence with the normal conduction velocity in adult mutant mice, RotaRod performance of 4-month-old Δ*PDZ-Prx* mice did not differ significantly from that of their WT littermates at 32 rpm (n=10-16 per group). Conversely, Periaxin-null mice, which display a more severe demyelinating phenotype performed considerably poorly on the RotaRod at the same speed (Fig. 39).

3.1.16 Δ*PDZ-Prx* mice display normal sensory reflex behaviors

I compared sensory behaviors in WT and Δ*PDZ-Prx* mice by testing mechanoreception and thermal nociception that are primarily driven by myelinated Aδ and unmyelinated C afferent fibers, respectively (Gillespie et al., 2000). Sensory reflex behavioural tests for mechanical withdrawal threshold with von Frey filaments and withdrawal latency from noxious heat were performed by Dr. Ada Delaney in WT and Δ*PDZ-Prx* mice at 4-5 months old. In both tests, Δ*PDZ-Prx* mice showed normal mechanical response threshold to light tactile stimuli and thermal nociceptive response latency, suggesting that mutant animals did not display mechanical allodynia or thermal hyperalgesia (Table 4 and Fig. 40). These data indicated that in Δ*PDZ-Prx* nerves, small caliber myelinated axons and unmyelinated axons were not affected.

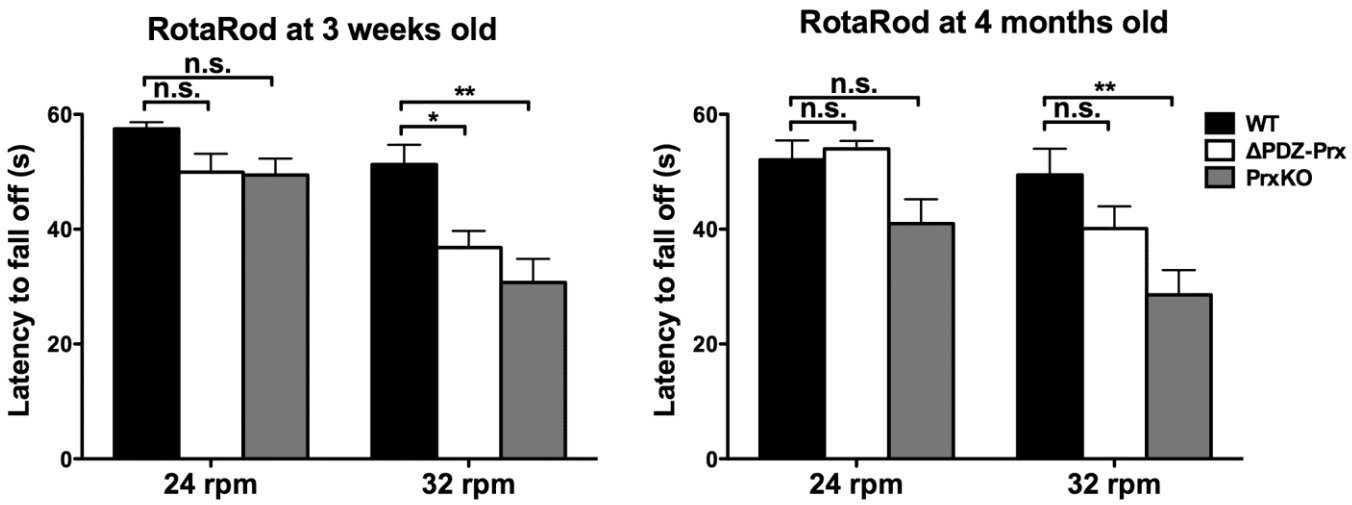

Figure 39. Motor coordination assessed by RotaRod performance is impaired at 3 weeks but normal at 4 months in Δ*PDZ-Prx* mice.

Motor coordination was evaluated in WT, Δ*PDZ-Prx*, and *Prx* KO mice at 3 weeks old (left) and 4 months old (right) using the RotaRod test. At 24 rpm, there is no difference in RotaRod performance in WT, Δ*PDZ-Prx*, and *Prx* KO mice at both ages. However, at 32 rpm, Δ*PDZ-Prx*, and *Prx* KO mice performed significantly poorly, compared with WT mice at 3 weeks old (n=12-16 per group; *$p < 0.05$ and ** $p < 0.01$). Motor coordination of 4-month-old Δ*PDZ-Prx* mice does not differ significantly from WT values at 32 rpm. In contrast, *Prx* KO mice's motor coordination is substantially impaired (n=10-16 per group; ** $p < 0.01$; one-way ANOVA with Tukey's HSD post-test).

	WT	Δ*PDZ-Prx*
Mechanical Withdrawal Threshold (mN/mm^2)	162.8 ± 4.2	178.3 ± 9.6
Withdrawal latency from noxious heat (s)	7.1 ± 0.5	7.2 ± 0.6

Table 4. Hindpaw withdrawal response of mechanical and noxious thermal stimulation at 4-5 months of age.

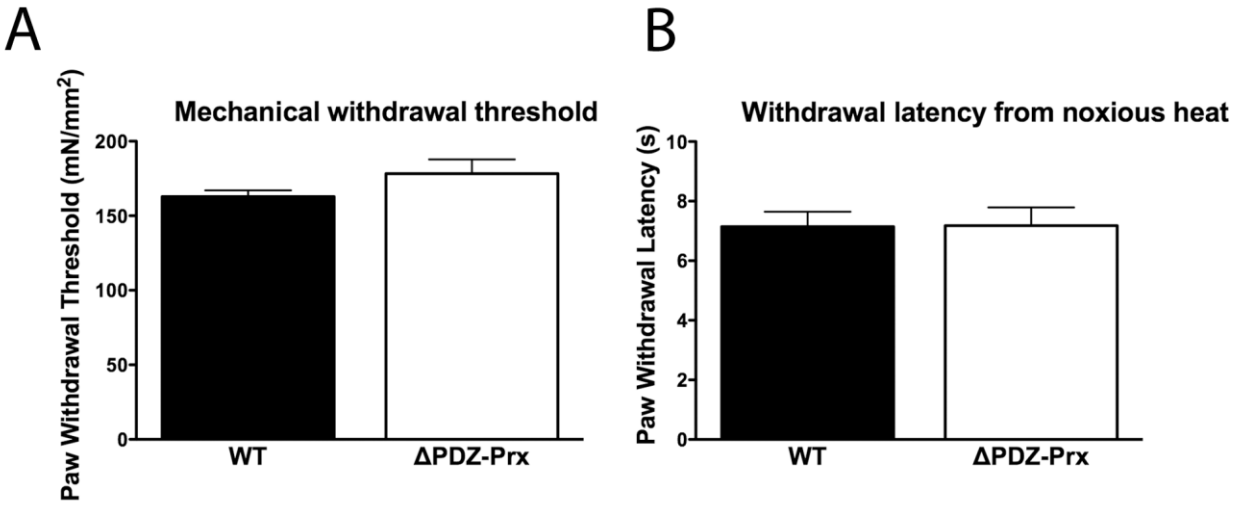

Figure 40. Δ*PDZ-Prx* mice display normal sensory reflex behaviors.

A. Minimum filament indentaton pressure thresholds for repeat paw withdrawal responses to mechanical stimulation with von Frey filaments were measured in 4-5-month-old WT and Δ*PDZ-Prx* mice. Δ*PDZ-Prx* animals have normal mechanical withdrawal threshold (*n*=9-11 per group; $p = 0.2233$; Mann-Whitney Rank Sum test).

B. The thermal nociceptive response latency from an infrared beam was determined in WT and Δ*PDZ-Prx* mice at 4-5 months of age. Δ*PDZ-Prx* mice have normal withdrawal latency from noxious heat, compared with WT littermates ((*n*=9-11 per group; $p = 0.9648$; Student's *t*-test).

3.1.17 Dlg1 levels are increased in Δ*PDZ-Prx* quadriceps nerves

Schwann cell hypermyelination with focally folded myelin and paranodal tomacula, often indicative of defective regulation of myelin production, is a common pathological feature for peripheral demyelinating neuropathies (Suter and Scherer, 2003). Mice deficient for myotubularin-related protein 2 (MTMR2), in which mutations in humans cause autosomal recessive Charcot-Marie-Tooth type 4B1, show a dysmyelinating phenotype characterized by aberrant myelin outfoldings (Bolino et al., 2004; Bonneick et al., 2005). The interaction of MTMR2 with mammalian discs large 1 (Dlg1)/ synapse-associated protein 97 (SAP-97) has been implicated for the regulation of myelin membrane homeostasis in the Schwann cell (Bolino et al., 2004; Bolis et al., 2005; Bolis et al., 2009). Disruption of this interaction results in myelin outfoldings and redundant myelin loops (Bolis et al., 2009). In a recent study, Cotter et al provided evidence that Dlg1 prevents overproduction of peripheral myelin via the interaction with phosphatase and tensin homolog (PTEN), which acts by inhibition of AKT activation (Cotter et al., 2010).

In the absence of the PDZ domain of Periaxin, Δ*PDZ-Prx* mice develop a progressive neuropathy with excessive myelin deposition as myelin foldings and thickenings. To better understand the potential mechanism for myelin foldings, I investigated whether Dlg1/PTEN might be involved in the dysregulation of myelin production in Δ*PDZ-Prx* mutants. The expression of Dlg1 in mature Δ*PDZ-Prx* peripheral nerves was examined by immunostaining and Western blotting. In WT quadriceps nerve teased fibers, Dlg1 was enriched in Schwann cell microvilli at the nodal region (Bolino et al., 2004) and co-localized with a microvillus marker, radixin recognized by anti-RAD4 antibody. Interestingly, enhanced Dlg1 immunoreactivity was detected in the microvilli of Δ*PDZ-Prx* Schwann cells (Fig. 41A). An increased level of Dlg1 expression in Δ*PDZ-Prx* nerves was further confirmed by Western blot analysis of sciatic nerve homogenates from mice at 5 weeks and 6 months of age. However, prior to the development of myelin abnormalities at 3 weeks old, levels of Dlg1 in Δ*PDZ-Prx* sciatic nerves, when normalized against actin, did not differ from those of WT mice.

Sciatic nerves of Periaxin-deficient mice, which develop a more severe phenotype later on, contained elevated amounts of Dlg1 at 3 weeks (Fig. 41B).

The pattern of PTEN expression studied by Western blot analysis of sciatic nerve lysates of 3-week- and 5-week-old Δ*PDZ-Prx* and *Prx* KO coincided with that of Dlg1, with increased levels of PTEN in *Prx* KO nerves at both ages, and in Δ*PDZ-Prx* at 5 weeks. At 6 months old, however, PTEN levels in Δ*PDZ-Prx* peripheral nerves appeared slightly reduced.

Growth factors such as neuregulin and insulin-like growth factor-I (IGF-I) play key roles in the regulation of Schwann cell differentiation (Nave and Trapp, 2008; Ogata et al., 2004). Effects of these growth factors are mediated through intracellular signaling cascades including phosphatidylinositol-3-OH kinase (PI3K) pathways and mitogen-activated protein kinase (MAPK) pathways (Ogata et al., 2004). Signaling molecules including phosphatidylinositol-3-OH kinase (PI3K) and the serine/threonine kinase AKT are important for positively regulating myelination (Ogata et al., 2004). Since disinhibition of AKT activation due to downregulation of Dlg1/PTEN is associated with excessive myelin production (Cotter et al., 2010), I quantified phosphorylated AKT levels to investigate the possibility of its involvement in the overproduction of myelin in the Periaxin mutants. By immunoblotting, amounts of activated AKT that is phosphorylated at serine residue 473 were not altered in Δ*PDZ-Prx* sciatic nerves at 3 weeks or 6 months, or in *Prx* KO sciatic nerves at 3 weeks (Fig. 41C).

Activation of extracellular signal-regulated kinase 1/2 (ERK1/2), a constituent of the MAPK signaling pathways drives the dedifferentiation of Schwann cells *in vitro* (Harrisingh et al., 2004). In addition, studies in mouse models of the demyelinating form of CMT type 1 have demonstrated that ERK1/2 activation leads to an upregulation of Schwann cell-derived chemokine MCP-1 (CCL2), which mediates macrophage activation, promoting myelin degeneration (Fischer et al., 2008; Groh et al., 2010; Kohl et al.). To address whether ERK phosphorylation was altered in the Periaxin mutants, I examined the levels of phosphorylated ERK1/2. At 5 weeks old, levels of phosphorylated ERK1/2 in Δ*PDZ-Prx* sciatic nerves were not changed compared with those in WT nerves. However, in *Prx* KO nerves, phosphorylation of ERK1/2 was

elevated (Fig. 41D). Similar results were obtained at 3 weeks (data not shown). In mature Δ*PDZ-Prx* mice at 6 months old, there was a modest increase in the amounts of activated ERK1/2.

Since there was an increase in the number of Schwann cells in the Periaxin mutants due to reduced internodal lengths, I intended to investigate the Mammalian Target of Rapamycin (mTOR) signaling cascade, which regulates cell growth and proliferation. Activation of mTOR mediated by AKT signaling has also been implicated in the regulation of myelination in the CNS (Narayanan et al., 2009). I evaluated the expression levels of mTOR and its downstream substrate, S6 ribosomal protein in sciatic nerve homogenates of 3-week-old WT, Δ*PDZ-Prx* and *Prx* KO mice. The amounts of phosphorylated mTOR and total mTOR in nerves of both Periaxin mutants were similar to those in normal nerves. Expression of phosphorylated S6 ribosomal protein, however, was markedly augmented in both Δ*PDZ-Prx* and *Prx* KO nerves, with a more notable increase in Periaxin-null mice, in comparison with WT nerves (Fig. 41E). This suggests that S6 ribosomal protein may be a potential signaling molecule downstream of Periaxin.

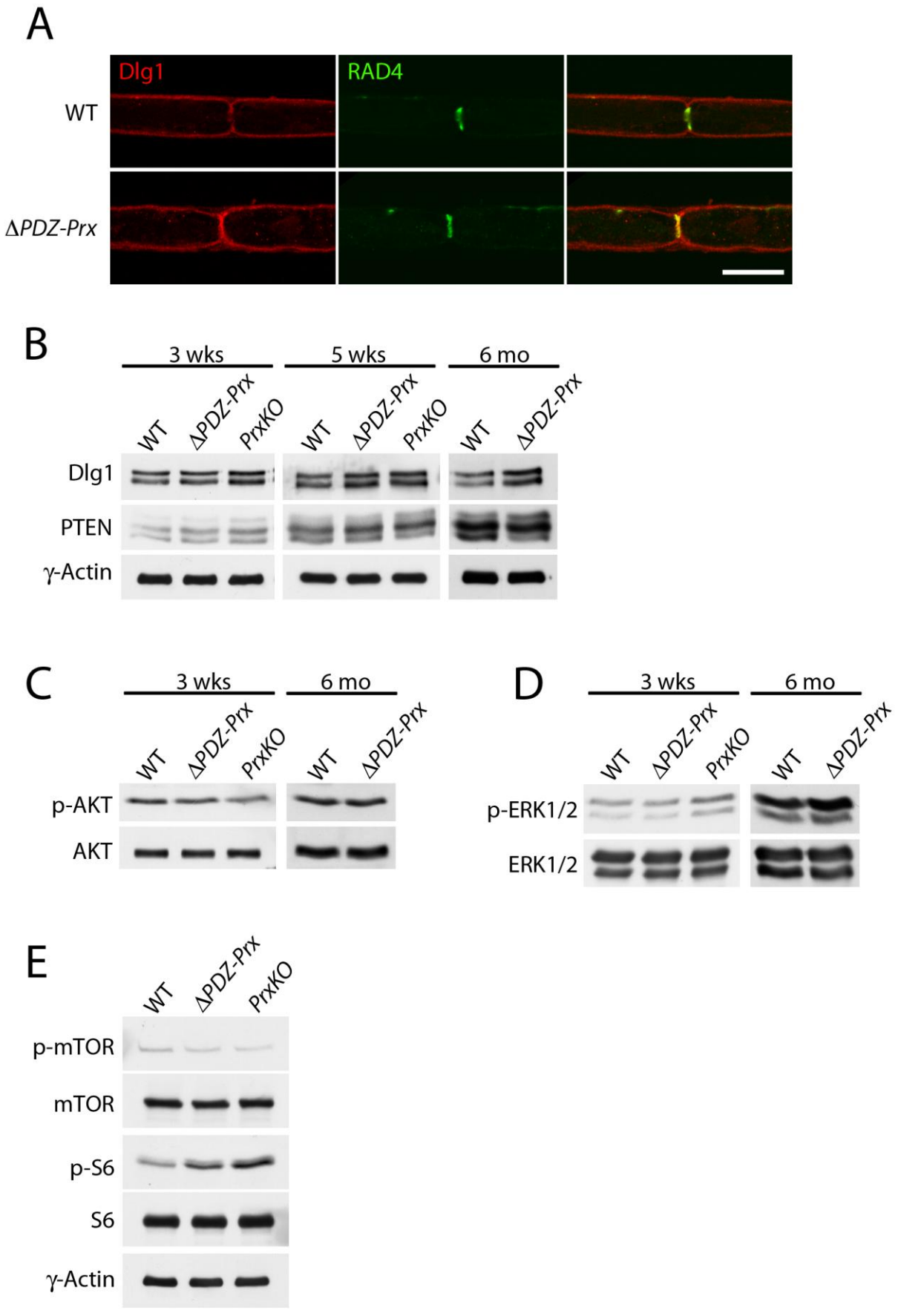
A
Dlg1
RAD4
WT
ΔPDZ-Prx
B
3 wks
5 wks
6 mo
WT
ΔPDZ-Prx
PrxKO
Dlg1
PTEN
γ-Actin
C
p-AKT
AKT
D
p-ERK1/2
ERK1/2
E
p-mTOR
mTOR
p-S6
S6
γ-Actin

Figure 41. Dlg1 levels are increased in Δ*PDZ-Prx* quadriceps nerves.

A. Teased fibers from quadriceps nerves of 2-month-old WT and Δ*PDZ-Prx* mice were co-labeled with anti-Dlg1 and anti-RAD4 antibodies. Dlg1 immunoreactivity enriched at the nodal regions is increased in Δ*PDZ-Prx* nerve fibers. Scale bar, 15 μm.
B. Western blot analysis of Dlg1 and PTEN expression levels in WT, Δ*PDZ-Prx* and *Prx* KO sciatic nerves at 3 weeks, 5 weeks and 6 months. Amounts of Dlg1 are elevated in 5-week- and 6-month-old Δ*PDZ-Prx* nerves. PTEN levels are increased in 5 weeks but not at 6 months in Δ*PDZ-Prx* nerves. γ-actin was used to normalize loading.
C. The amounts of activated AKT phosphorylated at serine 473 in Δ*PDZ-Prx* sciatic nerves are unaltered, compared with those in WT nerves.
D. Δ*PDZ-Prx* sciatic nerves have normal amounts of activated ERK at 5 weeks old. Nevertheless, in mature Δ*PDZ-Prx* peripheral nerves, activated ERK is elevated in levels. *Prx* KO sciatic nerves at 5 weeks contain increased amounts of activated ERK, compared with WT nerves.
E. Phosphorylated mTOR levels in sciatic nerves of 3-week-old Δ*PDZ-Prx* and *Prx* KO mice are not significantly different from those in WT nerves. Amounts of phosphorylated S6, a downstream substrate of mTOR, however, are notably increased in Δ*PDZ-Prx* and *Prx* KO nerves. γ-actin was used as a loading control.

3.1.18 Summary

In this chapter, I have demonstrated that the PDZ domain of Periaxin is required for homodimerization, which is essential for the stabilization of the PDG complex and regulation of the formation of discrete Schwann cell domains, termed appositions.

I have described the generation of a conditional mutant mouse, Δ*PDZ-Prx*, expressing a Periaxin form lacking the N-terminal PDZ domain in peripheral nerves, based on the mechanism of translation reinitiation. Dimerization of Periaxin does not occur in the absence of the PDZ domain. In Δ*PDZ-Prx* Schwann cells, DRP2 fails to form appositions and Cajal bands are disrupted. Schwann cell internodal distances are reduced. This is consistent with an increase in the number of myelinating Schwann cells in Δ*PDZ-Prx* nerves.

In the mature PNS, Δ*PDZ-Prx* mice develop a progressive neuropathy marked with extensive hypermyelination with focally folded myelin and paranodal tomacula. Nevertheless, the *ΔPDZ-Prx* mice show a less severe demyelinating phenotype, compared with the Periaxin-null mice.

Consequent to a decrease in Schwann cell internodal lengths, nerve conduction velocity of quadriceps nerves from 3-week-old Δ*PDZ-Prx* mice is reduced, and motor coordination impaired. Interestingly, adult Δ*PDZ-Prx* nerves, with limited demyelination, have normal conduction velocity, indicating that mutant Schwann cells, albeit defects in longitudinal growth have elongated enough to support normal nerve conduction. These findings suggest that the Δ*PDZ-Prx* mouse serves as a good model for studying the sensitivity of nerve conduction velocity to changes in internodal lengths. In addition, Δ*PDZ-Prx* mice show normal nociceptive sensory function.

Collectively, these data suggest that the PDZ domain of Periaxin is important for regulating apposition stability, Schwann cell internodal lengths, and myelin maintenance, through homodimerization or by binding with potential interactors in the submembranous cortex of the Schwann cell. In order to study this further, it will be necessary to study the downstream signaling mechanisms involved in the regulation of Schwann cell growth and myelin production in the Periaxin mutants.

3.2 THE ROLES OF THE PERIAXIN PDZ DOMAIN IN ESTABLISHED SCHWANN CELL COMPARTMENTS

Abrogation of PDZ domain homodimerization in Periaxin destabilizes the Periaxin-DRP2-dystroglycan (PDG) complex, leading to the absence of DRP2-patches and disruption of appositions and Cajal bands. The absence of the Periaxin PDZ domain in Schwann cells also results in a reduction of Schwann cell internodal lengths and an excessively folded myelin sheath in peripheral nerves. Whether stabilization of the PDG complex, and thus proper maintenance of close appositions in the Schwann cell, is responsible for the regulation of internodal growth remains elusive. In addition, Periaxin is localized in the Schwann cell plasma membrane before the onset of myelination and its association of DRP2 (Sherman and Brophy, 2000). Before homodimerization during formation of the PDG complex, it is still unknown whether the PDZ domain has other functions such as targeting proteins to the cortical cytoskeleton.

When myelination is complete, the cytoplasm of the Schwann cell is restricted to regions segregated by appositions between the Schwann cell membrane and the outermost layer of the myelin sheath, forming distinct compartments. I wished to ask what would happen if the PDG complex was disrupted after compartmentalization of the Schwann cell is accomplished. I investigated the consequences of disrupting Periaxin PDZ domain homodimerization, thus the PDG complex, after the establishment of specific Schwann cell compartments, namely appositions and Cajal bands, in tamoxifen-inducible *Prx*$^{fl/fl}$*/P0CreERT* mice. Mutant Periaxin without the N-terminal PDZ domain was predicted to be generated by Cre-recombination upon tamoxifen induction. In this study, apposition maintenance, Schwann cell internodal lengths and myelin morphology were examined in the peripheral nerves of adult *Prx*$^{fl/fl}$*/P0CreERT* mice.

3.2.1 Mutant Periaxin without the N-terminus is generated by tamoxifen-inducible Cre-recombination in *Prx$^{fl/fl}$/P0CreERT* mice

Tamoxifen was administered to weaned *Prx$^{fl/fl}$/P0CreERT* mice, 3-4 weeks of age, as well as to control littermates *Prx$^{fl/fl}$* for 10 consecutive days. After a rest-period of 7 days, mice were treated again for 5 days. Animals were analyzed for the degree of the *'floxed' Prx* gene recombination at various time points (Fig. 42A). The findings presented here are from the analysis of mice 12 weeks and 18 weeks after the last tamoxifen treatment. Experiments studying non-treated *Prx$^{fl/fl}$/P0CreERT* mice indicated that recombination did not occur without tamoxifen induction (data not shown). Hence, tamoxifen-treated *Prx$^{fl/fl}$* mice were used as the control in the study.

Mice treated with tamoxifen were analyzed for Periaxin expression 12 and 18 weeks following the last treatment. By immunoblotting using a Periaxin antibody against the C-terminus, two Periaxin bands were identified from the sciatic nerve homogenates of *Prx$^{fl/fl}$/P0CreERT* mice 12 weeks post-treatment (Fig. 42B). The mutant form of Periaxin was expressed as a lower molecular weight protein at reduced levels, compared with the wild-type Periaxin in control nerves. This was consistent with the mutant version of Periaxin in *Prx$^{fl/fl}$/Cnp-Cre* mice (known as Δ*PDZ-Prx* mice in the study). Little wild-type Periaxin was expressed in *Prx$^{fl/fl}$/P0CreERT* nerves at this time point (Fig. 42B). At 18 weeks after tamoxifen induction, the amount of wild-type Periaxin was negligible in the *Prx$^{fl/fl}$/P0CreERT* lysates as shown by Western blot analysis, indicating that maximum ablation of wild-type Periaxin was achieved by Cre-mediated recombination (Fig. 42B). What remained was the mutant form of Periaxin in *Prx$^{fl/fl}$/P0CreERT* nerves.

Nevertheless, the deletion efficiency of the wild-type Periaxin was variable among tamoxifen-treated animals. The extent of wild-type protein deletion in the peripheral nerves from *Prx$^{fl/fl}$/P0CreERT* mice was analyzed in different animals 18 weeks after treatment by Western blotting and immunofluorescence staining. Peripheral nerves of some tamoxifen-treated mice contained both the wild-type and mutant forms of Periaxin detected by the Periaxin C-terminus antibody in sciatic nerve homogenates by Western blot analysis (data not shown). By immunofluorescence labeling, in contrast

to myelinated fibers from treated *Prx*$^{fl/fl}$ nerves, which were immunopositive for both the N- and C-terminal regions of Periaxin, approximately 50% of fibers from the quadriceps nerves of *Prx*$^{fl/fl}$*/P0CreERT* mice did not harbor the wild-type Periaxin, but the mutant Periaxin alone, recognized by the Periaxin C-terminus antibody (Fig. 42C). Although residual amounts of the wild-type Periaxin were present in the mutant nerves of some animals even after 18 weeks post-treatment, these data suggest that mutant Periaxin lacking the N-terminus was generated in this tamoxifen-inducible conditional system. Despite only partial ablation of the wild-type Periaxin, the *Prx*$^{fl/fl}$*/P0CreERT* quadriceps nerves containing the mutant Periaxin appeared enlarged in nerve area (Fig. 42C).

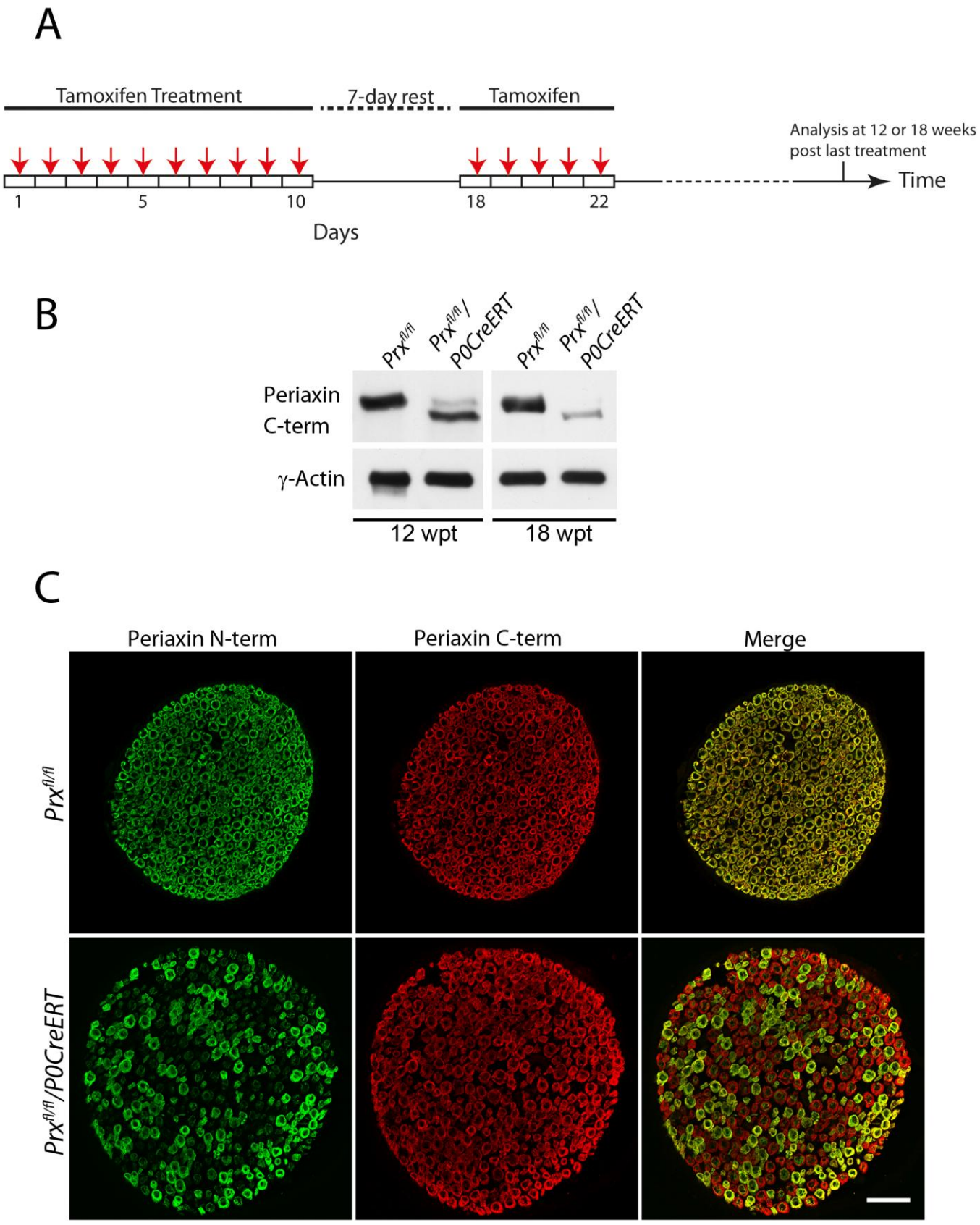
A
Tamoxifen Treatment
7-day rest
Tamoxifen
Analysis at 12 or 18 weeks post last treatment
Time
1
5
10
18
22
Days
B
Prx fl/fl
Prx fl/fl / P0CreERT
Prx fl/fl
Prx fl/fl / P0CreERT
Periaxin C-term
γ-Actin
12 wpt
18 wpt
C
Periaxin N-term
Periaxin C-term
Merge
Prx fl/fl
Prx fl/fl/P0CreERT

Figure 42. Generation of mutant Periaxin ΔPDZ-Prx lacking the N-terminus by tamoxifen-inducible Cre-recombination in *Prx$^{fl/fl}$/P0CreERT* mice.

A. The scheme of the tamoxifen administration protocol. 3-4 weeks old *Prx$^{fl/fl}$* and *Prx$^{fl/fl}$/P0CreERT* littermates were treated with tamoxifen at a dose of 1 mg/10 g body weight once per day for 10 consecutive days. Mice were treated again for 5 days following a 7-day rest period and were analyzed 12 or 18 weeks after the last treatment.
B. Immunoblots probed with a Periaxin antibody against the C-terminus show that the mutant Periaxin was generated in tamoxifen-treated *Prx$^{fl/fl}$/P0CreERT* mice 12 weeks and 18 weeks post-treatment (wpt). Residual amounts of the wild-type Periaxin were still present in *Prx$^{fl/fl}$/P0CreERT* sciatic nerve lysates 12 weeks after treatment. Complete ablation of the wild-type Periaxin was achieved 18 weeks after treatment in this case. When normalized against γ-actin, the mutant Periaxin was expressed at reduced levels, compared with the wild-type Periaxin.
C. Recombination efficiency was variable among tamoxifen-treated *Prx$^{fl/fl}$/P0CreERT* mice 18 weeks post-treatment. Immunofluorescence images show quadriceps nerve cross sections immunolabeled with specific Periaxin antibodies against the N-terminus or C-terminus. Nearly 50% of myelinated fibers lack wild-type Periaxin identified by the Periaxin N-terminus antibody. Deletion of the wild-type Periaxin in this animal was incomplete at this time point. Scale bar, 50 μm.

3.2.2 DRP2 patches are absent and Cajal bands disrupted in Schwann cells of *Prx$^{fl/fl}$/P0CreERT* mice

In the absence of the PDZ domain of Periaxin, DRP2 patches are absent and longitudinal and transverse bands of cytoplasm, the Cajal bands, are disrupted, as analyzed in Δ*PDZ-Prx* peripheral nerves (see sections 3.1.6 and 3.1.7). I asked whether DRP2 patches and Cajal bands were affected when Periaxin's PDZ domain was removed by the generation of the mutant Periaxin after the establishment of appositions. Immunolabeling of teased fibers from quadriceps nerves of tamoxifen-treated animals with the Periaxin repeat region antibody displayed immunoreactivity for Periaxin in the Schwann cell membrane 18 weeks after tamoxifen treatment, albeit reduced in levels, compared with the treated littermate controls. Mutant Periaxin in *Prx$^{fl/fl}$/P0CreERT* fibers was membrane-associated but was not localized to patches. DRP2 levels were reduced and DRP2 patches were absent in the quadriceps nerves of *Prx$^{fl/fl}$/P0CreERT* mice, in contrast to the distinct patch pattern observed in control teased fibers. Cajal bands immunolabeled for S100 were also disrupted and appeared continuous along the internodes, suggesting the disruption of appositions (Fig. 43). Due to the variable degree of recombination in myelination fibers, DRP2 was not equally depleted in all fibers analyzed per animal. By 12 weeks post-treatment, at least 50% of total fibers lacked DRP2 patches in all animals examined (n=3).

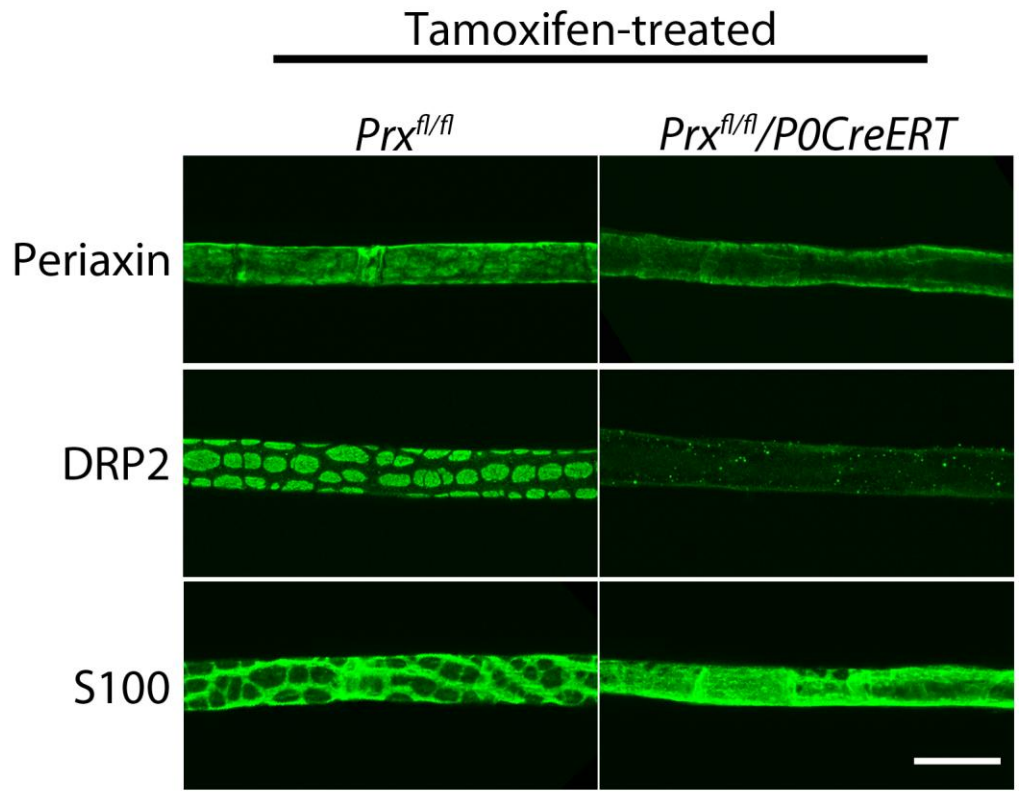

Figure 43. DRP2 patches are absent and Cajal bands disrupted in tamoxifen-inducible *Prx$^{fl/fl}$/P0CreERT* mice 18 weeks post-treatment.

Immunolabeling of teased fibers from quadriceps nerves of *Prx$^{fl/fl}$* and *Prx$^{fl/fl}$/P0CreERT* mice with the Periaxin repeat region antibody shows reduced amounts of Periaxin, presumably the mutant form in *Prx$^{fl/fl}$/P0CreERT* fibers. Note that Periaxin is no longer localized in patches. Analysis of DRP2 immunoreactivity demonstrates that DRP2 appears in patches in control fibers. In contrast, *Prx$^{fl/fl}$/P0CreERT* teased fibers do not display DRP2-patches. Cajal bands immunolabeled for S100 are also disrupted. Scale bar, 20 μm.

3.2.3 Schwann cell internodal lengths are unaltered in *Prx$^{fl/fl}$/P0CreERT* mice

Characterization of Δ*PDZ-Prx* mice indicated that the mutant Periaxin without the PDZ domain failed to homodimerize, resulting in the disruption of the PDG complex and Cajal bands. Δ*PDZ-Prx* mutants also have shorter Schwann cell internodal lengths (see section 3.1.9). By postnatal day 21, myelination is essentially complete, and Schwann cell compartments were well established. Prior to tamoxifen induction in 3-4-week-old *Prx$^{fl/fl}$/P0CreERT* mice, longitudinal growth of *Prx$^{fl/fl}$/P0CreERT* Schwann cells was predicted to be normal. To address whether disruption of the PDG complex and cytoplasmic bands in recombined Schwann cells influenced Schwann cell internodal growth, I measured Schwann cell internodal distances of teased quadriceps fibers from *Prx$^{fl/fl}$/P0CreERT* mice 12 weeks following tamoxifen induction.

Due to the heterogeneity of recombination efficiency in individual fibers, teased fibers were co-immunolabeled for dystrophin for internodal length measurements, and DRP2 or Periaxin N-terminus to select for fibers with a high degree of recombination. Internodal lengths of Schwann cells lacking the Periaxin N-terminus or DRP2 were measured. In contrast to Δ*PDZ-Prx* Schwann cells, which had shorter internodal lengths, *Prx$^{fl/fl}$/P0CreERT* Schwann cells showed normal average internodal length compared with the control value at 12 weeks after tamoxifen treatment (*Prx$^{fl/fl}$*, 753.1 ± 27.4 μm vs *Prx$^{fl/fl}$/P0CreERT*, 730.7 ± 20.7 μm; Fig. 44A). Mutant Schwann cells also displayed a normal internodal length distribution, similar to control Schwann cells (Fig. 44B), indicating that Schwann cell internodal distance was not altered despite the disruption of the PDG complex and Cajal bands. This suggested that disrupting the PDG complex after the establishment of Schwann cell compartments no longer influences Schwann cell elongation.

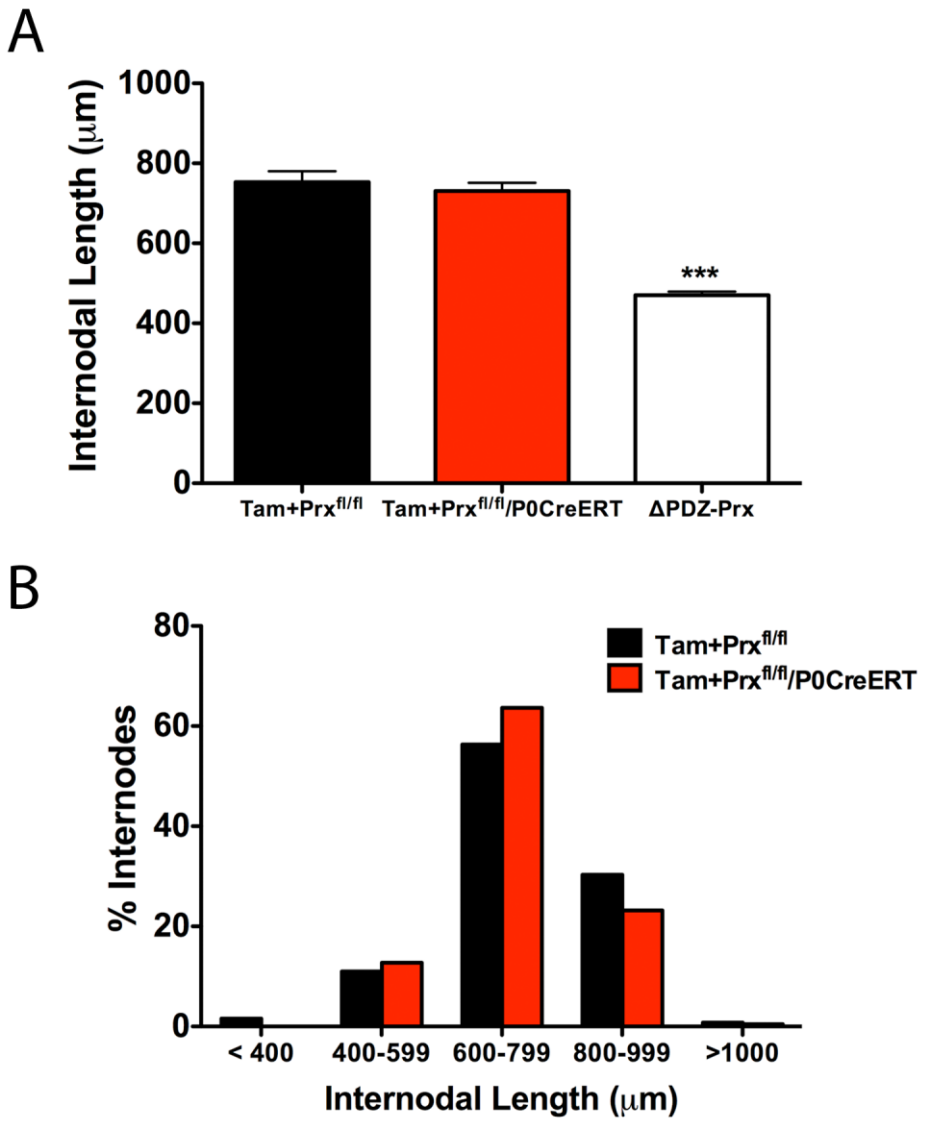

Figure 44. Schwann cell internodal lengths of *Prx$^{fl/fl}$/P0CreERT* mice are normal.

A. Teased fibers were immunolabeled with antibodies directed against dystrophin and DRP2 or the Periaxin N-terminus. Internodal lengths of Schwann cells with depleted DRP2 or without the N-terminus of Periaxin were measured. Unlike Δ*PDZ-Prx* Schwann cells with reduced internodal lengths ($p < 0.0001$), the average internodal distance of recombined *Prx$^{fl/fl}$/P0CreERT* Schwann cells does not differ significantly with the control value (n=3; at least 70 internodes per genotype; one-way ANOVA with Tukey's HSD post-test).

B. Distributions of Schwann cell internodal lengths from teased fibers of 4.5-month-old tamoxifen-treated mice analyzed 12 weeks post-treatment shows that *Prx$^{fl/fl}$/P0CreERT* Schwann cells have normal internodal lengths compared with the control.

3.2.4 Tamoxifen-treated *Prx$^{fl/fl}$/P0CreERT* nerves display abnormal myelin profiles

I next examined the peripheral nerves of *Prx$^{fl/fl}$/P0CreERT* mice by light microscopy to determine if the myelin sheath was affected. Due to the variable degree of recombination in myelinated fibers by tamoxifen induction, quantitation of abnormal myelin profiles was not performed. At 18 weeks after tamoxifen injection, the cross sectional area of the *Prx$^{fl/fl}$/P0CreERT* quadriceps nerves was increased. The endoneurial and perineurial space was strikingly enlarged, compared with control nerves (Figs. 45A and B). Mutant nerves contained numerous focal thickenings and foldings of the myelin sheath, consistent with what was observed in Δ*PDZ-Prx* nerves. Redundant myelin loops inside a myelinated axon appeared as 'U-shaped' infolds, and often causing axon compression. Aberrant myelin invaginations in axons and myelin outfoldings were evident in the mutant nerves (Figs. 45D and F). Additionally, *Prx$^{fl/fl}$/P0CreERT* nerves also harbored thinly myelinated axons enveloped by processes of supernumerary Schwann cells forming onion bulbs (Fig. 45D). These data confirm that Periaxin's PDZ domain is essential for maintenance and stability of the myelin sheath.

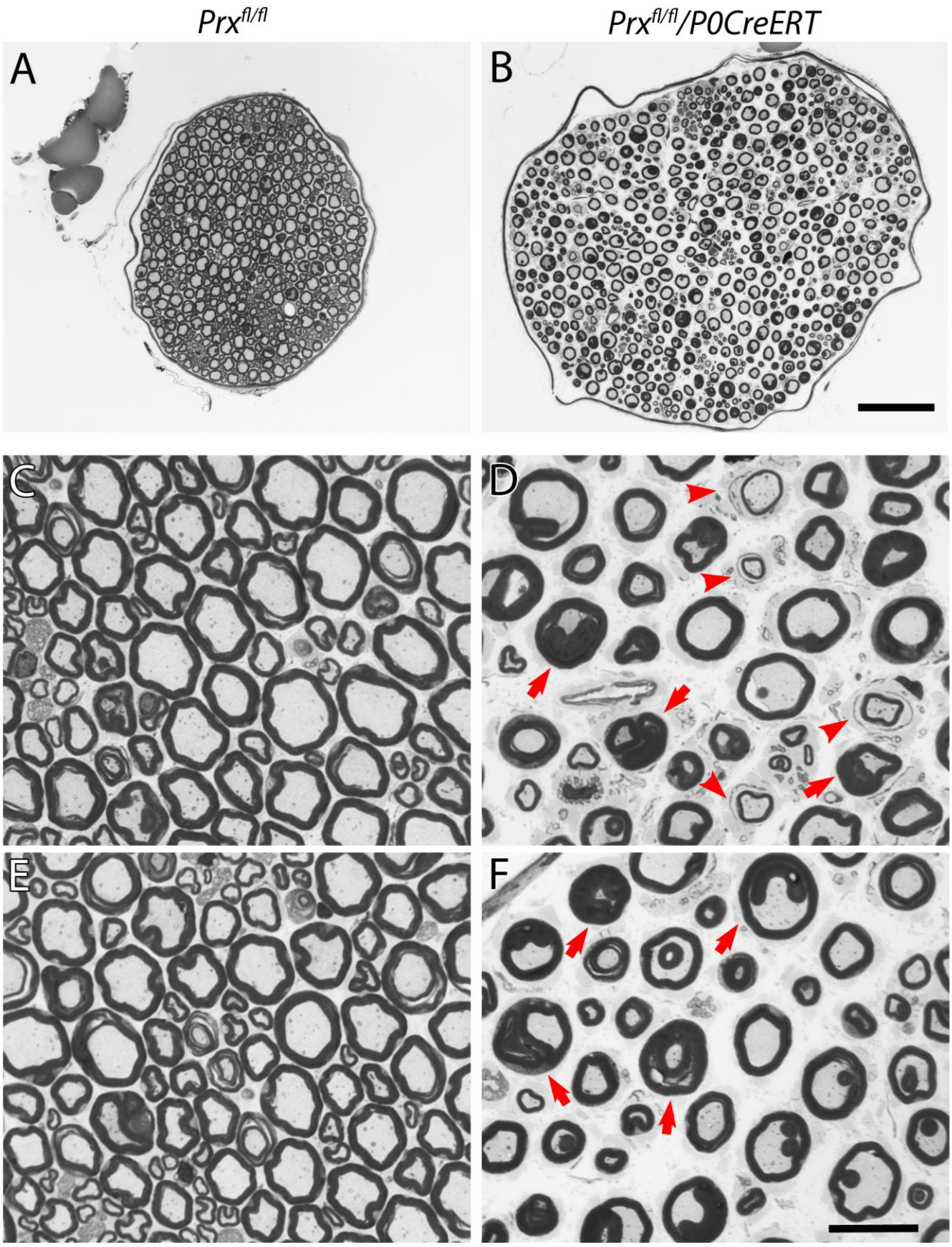
Prx^fl/fl
Prx^fl/fl/P0CreERT
A
B
C
D
E
F

Figure 45. Tamoxifen-treated *Prx$^{fl/fl}$/P0CreERT* nerves show abnormal myelin profiles.

Semithin transverse sections of quadriceps nerves from 6-month-old *Prx$^{fl/fl}$* (A, C and E) and *Prx$^{fl/fl}$/P0CreERT* mice (B, D and F) 18 weeks after tamoxifen injection. A-B. Quadriceps nerve area of *Prx$^{fl/fl}$/P0CreERT* mice is increased due to an increase in endoneurial space, compared with the treated control littermates. Scale bar, 65 μm. D, F. Foldings and focal thickenings of the myelin sheath (red arrows), as well as onion bulbs (red arrowheads) are evident in *Prx$^{fl/fl}$/P0CreERT* nerves after tamoxifen treatment. Scale bar, 15 μm.

3.2.5 Summary

In this chapter, I have shown that the mutant Periaxin lacking the N-terminal PDZ domain was generated by tamoxifen inducible Cre-recombination of the '*floxed*' *Prx* allele in $Prx^{fl/fl}$*/P0CreERT* mice. The wild-type Periaxin was replaced by the mutant Periaxin in Schwann cells with successful recombination. However, residual amounts of wild-type Periaxin were present in some myelinated fibers of mutant nerves analyzed. This might be due to incomplete Cre-recombination of the *'floxed' Prx* allele.

Although the proportions of Schwann cells containing the mutant Periaxin varied among treated animals, recombined myelinated fibers displayed decreased amounts of DRP2 and absence of DRP2-positive patches. Schwann cell cytoplasm was no longer arranged in longitudinal and transverse bands along the internodes, indicating disruption of Cajal bands. Disrupting the PDG complex after the establishment of specific Schwann cell compartments does not affect longitudinal elongation of Schwann cells. The absence of the PDZ domain of Periaxin leads to hypermyelination in peripheral nerves, revealed by extensive myelin foldings indicating dysregulation of myelin production.

Taken together, these results confirm that the PDZ domain of Periaxin is required for the maintenance of appositions and the myelin sheath.

3.3 MUTATIONS IN PERIAXIN PDZ DOMAIN ABROGATES HOMODIMERIZATION

Periaxin contains a PDZ domain at the N-terminus (Dytrych et al., 1998). PDZ domains are peptide-binding domains that are usually 80-100 amino acid residues long. They are specialized protein interaction domains known for binding to short peptide motifs at the carboxy-termini of ligand proteins, and may be important for interactions with the cytoplasmic tail of plasma membrane proteins and with the cortical cytoskeleton (Sheng, 1996). Canonical PDZ domains contain six β-strands (β1-β6 or βA-βF) and two α-helices (α1 and α2 or αA and αB), with a short α1-helix formed in the region between β3 and β4 strands, and a long α2-helix between β5 and β6 (Fig. 46) (Lee and Zheng, 2010).

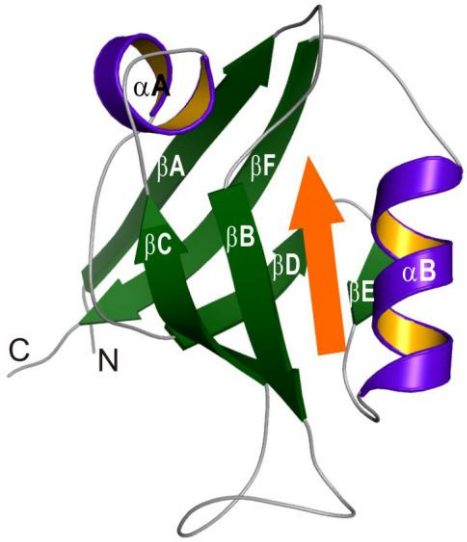

Figure 46. Three-dimensional structure of a canonical PDZ domain.

Ribbon diagram of the structure of the second PDZ (PDZ2) domain of PSD-95 (α-helices in purple, β-strands in green). PSD-95 PDZ2 contains six β-strands and two α-helices (labeled), and adopts the canonical PDZ fold that displays a binding groove for its target C-terminal peptide (orange). N- and C-termini are indicated. Figure adapted from (Wang et al., 2010).

Periaxin is known to homodimerize in the Periaxin-DRP2-dystroglycan (PDG) complex localized to the submembranous cortex of the Schwann cell (Sherman et al., 2001). Like Periaxin, a number of PDZ domain proteins also form dimers with themselves as homodimers, or with other PDZ domain proteins as heterodimers (Kim and Sheng, 2004; Lee and Zheng, 2010). Several scaffolding proteins localized in the postsynaptic terminal have been reported to self-associate to form homodimers such as GRIP-1, Shank1, Tamalin and ZO proteins (Chen et al., 2008; Fanning et al., 2007; Im et al., 2003a; Im et al., 2003b; Sugi et al., 2007; Utepbergenov et al., 2006; Wu et al., 2007); and heterodimers such as nNOS/PSD-95 and nNOS/syntrophin (Hillier et al., 1999; Tochio et al., 2000). Dimerization mechanisms of these PDZ dimers have been extensively described as detailed below.

Structural evidence of PDZ domain homodimerization was first described in the PDZ domain of the glutamate receptor-interacting protein (GRIP). GRIP contains 7 PDZ domains, in which the sixth PDZ domain PDZ6 homodimerizes through an anti-parallel orientation of the N-terminal β1 strands. The dimeric interaction was maintained by hydrogen bonds between polar residues and hydrophobic forces between non-polar residues in the β1 strands. The α1-β4 loop also contributed to mediating dimerization of PDZ6 (Im et al., 2003b). Similarly, Shank1, which is important for organization of synaptic multiprotein complexes, dimerizes via a conserved β2-β3 loop and anti-parallel β1-β1 interactions, supported by hydrogen bonds and van der Waals forces (Im et al., 2003a). Although the N-terminal β1 strands differ in configuration in the two PDZ dimers, the similarity in their dimerization mechanisms through forming anti-parallel β1 strand may imply that the N-terminal β1 strand anti-parallel dimerization could be a common configuration among PDZ dimers.

The second PDZ domain, PDZ2, of tight junction-associated ZO proteins (ZO-1 and ZO-2) employs a unique dimeric conformation, stabilized by extensive symmetrical domain swapping of β-strands (Chen et al., 2008; Fanning et al., 2007; Utepbergenov et al., 2006; Wu et al., 2007). Due to domain swapping of β1 and β2 strands, instead of orienting in an anti-parallel fashion with β3 strand in each PDZ domain, the β2 strand

continues in the same direction connecting to the short β3 strand, allowing β-strands to cross and pack against each PDZ monomer for dimerization (Fanning et al., 2007).

PDZ domain dimerization of Tamalin, a regulator of mGluR trafficking, is mediated by hydrophobic interactions between β2 and β3 strands from each monomer. It is also capable of assembling into a tetramer in crystallized conditions (Sugi et al., 2007). As mentioned, PDZ domains can form heterodimers. A well-known example is the complex formed between neuronal nitric oxide synthase (nNOS) and syntrophin or PSD-95 (Hillier et al., 1999; Tochio et al., 2000). The PDZ domain of nNOS has been shown to dimerize in a head-to-tail arrangement with that of syntrophin and PSD-95 via the insertion of a two-stranded β-sheet structure termed 'β-hairpin finger' into the peptide-binding groove of the PDZ domain of syntrophin or PSD-95. A buried salt bridge, contributed by hydrogen bonding and electrostatic interactions, between the β-finger and the main body of the nNOS PDZ domain is required for stabilizing the β-hairpin structure, which is required for dimeric interactions. The salt bridge is essentially formed between an arginine residue in the β finger and an aspartate in the β4 strand of the PDZ domain (Hillier et al., 1999; Tochio et al., 2000).

Dimerization of PDZ domain proteins does not hinder the access of target proteins to the carboxylate binding site, and thus does not influence binding of their partners (Fanning et al., 2007; Im et al., 2003a; Im et al., 2003b). Although little is understood about the role of PDZ-PDZ interactions, it has been speculated that dimerization might increase the scaffolding capacity of PDZ domain proteins, which would facilitate clustering of binding partners at specific sites, such as the postsynaptic membrane (Fanning et al., 2007; Kim and Sheng, 2004).

As for Periaxin, I have provided biochemical evidence in section 3.1 that homodimerization fails to occur in the absence of the PDZ domain, confirming that PDZ domain self-association is essential for stabilization of the PDG complex and apposition formation in the Schwann cell. Nevertheless, since elimination of 116 amino acids from the N-terminus of Periaxin might induce drastic changes in the protein folding mechanism, the inability of the Periaxin PDZ domain to homodimerize may not be

solely attributed to the lack of the PDZ domain in mutant Periaxin, but could also be due to misfolding of the truncated protein. Completely ruling out the possibility of protein misfolding leading to abrogation of PDZ domain dimerization would be difficult within the time frame of this study. However, it would be possible to examine whether changes in the PDZ domain alone could result in disruption of dimerization when protein structure was largely preserved. In order to minimize drastic perturbations in the protein structure of Periaxin, I generated single amino acid mutations in the PDZ domain of Periaxin.

3.3.1 Predicted three-dimensional structure of Periaxin PDZ domain

To decide which amino acids in the PDZ domain to mutate, the predicted three-dimensional structure of Periaxin PDZ domain was modelled using automated beta SWISS-MODEL based on the template of PDZ3 domain of PSD-95 (Arnold et al., 2006; Guex and Peitsch, 1997; Schwede et al., 2003). PSD-95 PDZ3 was selected as the modeling template because it displayed 32.6% sequence identity to the Periaxin PDZ sequence, the highest among all PDZ templates by template analysis using the SWISS-MODEL repository (Kiefer et al., 2009; Kopp and Schwede, 2004). The PDZ domain of Periaxin was predicted to follow the canonical PDZ domain fold, adopting the βββαββαβ topology with six β-strands and two α-helices (one short and one long). Within the PDZ domain, strands β1 and β6 arrange in an anti-parallel orientation; strand β2 is followed by a loop that turns ~180^{o}, enabling the following sequence to form the anti-parallel strand β3. A short α1-helix is formed between strands β3 and β4, and a long α2-helix between β5 and β6 (Fig. 47A). The conventional structure of Periaxin PDZ domain may allow it to self-associate by employing one or a combination of the known dimerization mechanisms.

A

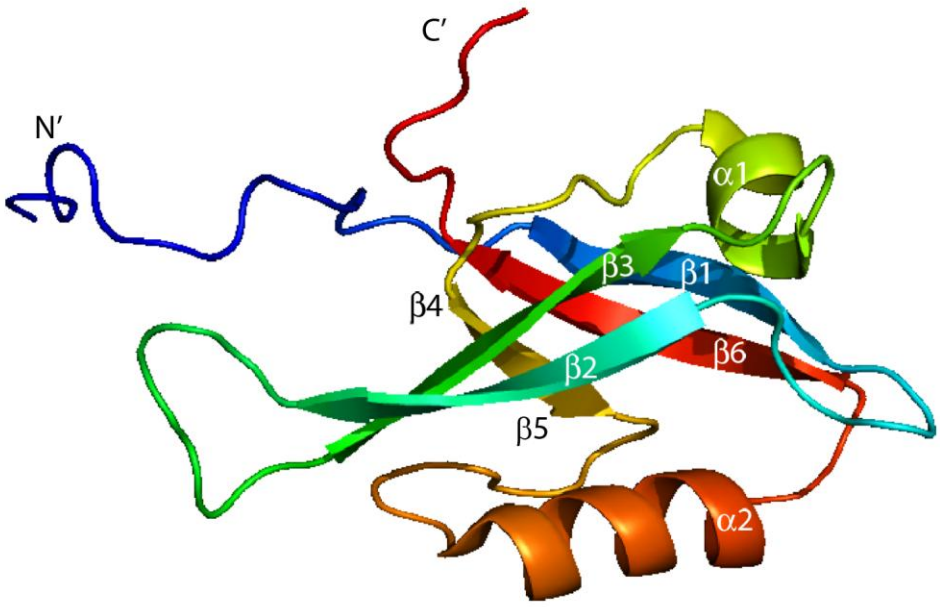
C′
N′
α1
β3
β1
β4
β6
β2
β5
α2

B

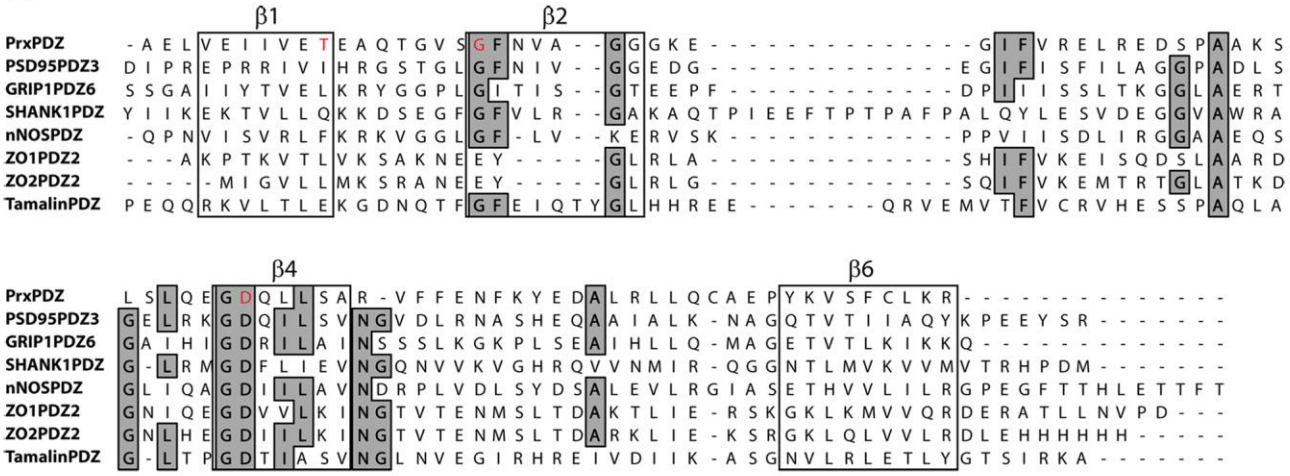
β1
β2
PrxPDZ -AELVEIIVETEAQTGVSGFNVA--GGGKE----------GIFVRELREDSPAAKS
PSD95PDZ3 DIPREPRRIVIHRGSTGLGFNIV--GGEDG----------EGIFISFILAGGPADLS
GRIP1PDZ6 SSGAIIYTVELKRYGGPLGITIS--GTEEPF----------DPIIISSLTKGGLAERT
SHANK1PDZ YIIKEKTVLLQKKDSEGFGFVLR--GAKAQTPIEEFTPTPAFPALQYLESVDEGGVAWRA
nNOSPDZ -QPNVISVRLFKRKVGGLGF-LV--KERVSK----------PPVIISDLIRGGAAEQS
ZO1PDZ2 ---AKPTKVTLVKSAKNEEY-----GLRLA----------SHIFVKEISQDSLAARD
ZO2PDZ2 ----MIGVLLMKSRANEEY-----GLRLG----------SQIFVKEMTRTGLATKD
TamalinPDZ PEQQRKVLTLEKGDNQTFGFEIQTYGLHHREE-------QRVEMVTFVCRVHESSPAQLA
β4
β6
PrxPDZ LSLQEGDQLLSAR-VFFENFKYEDALRLLQCAEPYKVSFCLKR----------
PSD95PDZ3 GELRKGDQILSVNGVDLRNASHEQAAIALK-NAGQTVTIIAQYKPEEYSR-------
GRIP1PDZ6 GAIHIGDRILAINSSSLKGKPLSEAIHLLQ-MAGETVTLKIKKQ----------
SHANK1PDZ G-LRMGDFLIEVNGQNVVKVGHRQVVNMIR-QGGNTLMVKVVMVTRHPDM-------
nNOSPDZ GLIQAGDIILAVNDRPLVDLSYDSALEVLRGIASETHVVLILRGPEGFTTHLETTFT
ZO1PDZ2 GNIQEGDVVLKINGTVTENMSLTDAKTLIE-RSKGKLKMVVQRDERATLLNVPD---
ZO2PDZ2 GNLHEGDIILKINGTVTENMSLTDARKLIE-KSRGKLQLVVLRDLEHHHHHH-----
TamalinPDZ G-LTPGDTIASVNGLNVEGIRHREIVDIIK-ASGNVLRLETLYGTSIRKA-------

Figure 47. Periaxin maintains the canonical PDZ-fold.

A. The predicted 3D structure of the PDZ domain of Periaxin (residues 14-98) was modeled using SWISS-MODEL based on the template of the third PDZ domain of PSD-95. A ribbon diagram shows the monomeric structure of the Periaxin PDZ domain, which follows the canonical PDZ-fold. The β-strands are labeled β1-β6, and the α-helices are labeled α1 and α2.
B. Amino acid sequence alignment of the PDZ domains of proteins that dimerize. The sequences were aligned using ClustalX in MacVector software. The sequence of Periaxin PDZ domain (PrxPDZ; residues 14-98) was compared with amino acid sequences of PSD-95 PDZ3 (residues 306-399), GRIP1 PDZ6 (residues 665-753), Shank1 PDZ (residues 585-690), nNOS PDZ (residues 12-112), ZO-1 PDZ2 (residues 182-273), ZO-2 PDZ2 (residues 305-392) and tamalin PDZ (residues 94-192). Residues conserved or identical in all sequences are shaded in gray. Secondary structure elements involved in this mutation study are labeled and shown in rectangles. The residues in Periaxin colored in red: the threonine residue (T23) in the β1 strand, glycine 31 in β2 strand or the highly conserved aspartate D63 in the β4 strand were mutated in this study (See section 3.3.3).

3.3.2 Truncation of β1 strand in Periaxin PDZ domain abrogates PDZ-PDZ interactions

In light of the speculation by Im et al. that the anti-parallel N-terminal β1 strand dimerization might be a common mechanism among PDZ dimers (Im et al., 2003a; Im et al., 2003b), as well as their finding that a single amino acid mutation Y671D in the β1 strand of GRIP-1 PDZ6 has been demonstrated to completely abolish dimerization of the protein (Im et al., 2003b), I explored the possibility of abrogating PDZ domain self-association of Periaxin by truncation of the N-terminus of Periaxin including the β1 strand of the PDZ domain (Fig. 47B).

Deletion mutants were generated for yeast two-hybrid interaction assays. The N-terminal β1 strand truncated Periaxin PDZ, namely PDZΔβ1 (aa 25-103) and the β6 strand deletion mutant PDZΔβ6 (aa 2-88) in GAL4 binding domain vector pGBKT7 containing a myc-epitope tag were expressed in yeast as shown by Western blot (Fig. 48A). In contrast to the non-mutated PDZ domain control, binding of PDZΔβ1 to the N-terminal PDZ domain of Periaxin (aa 2-164) was abolished as demonstrated by the lack of β-galactosidase (β-gal) activity, indicating that the β1 strand of the Periaxin PDZ domain was required for activating GAL4 transcription, and thus crucial for homodimerization. Interaction of the N-terminal region of Periaxin with PDZΔβ6 lacking the β6 strand, which is normally anti-parallel to the β1 strand, was considerably attenuated, suggesting that the β6 strand was also involved but likely not essential for dimerization. Similar results obtained using the deletion mutants subcloned into another GAL4 binding domain vector pAS2-1, further confirmed the importance of the β1 strand in PDZ-PDZ binding of Periaxin (Fig. 48B).

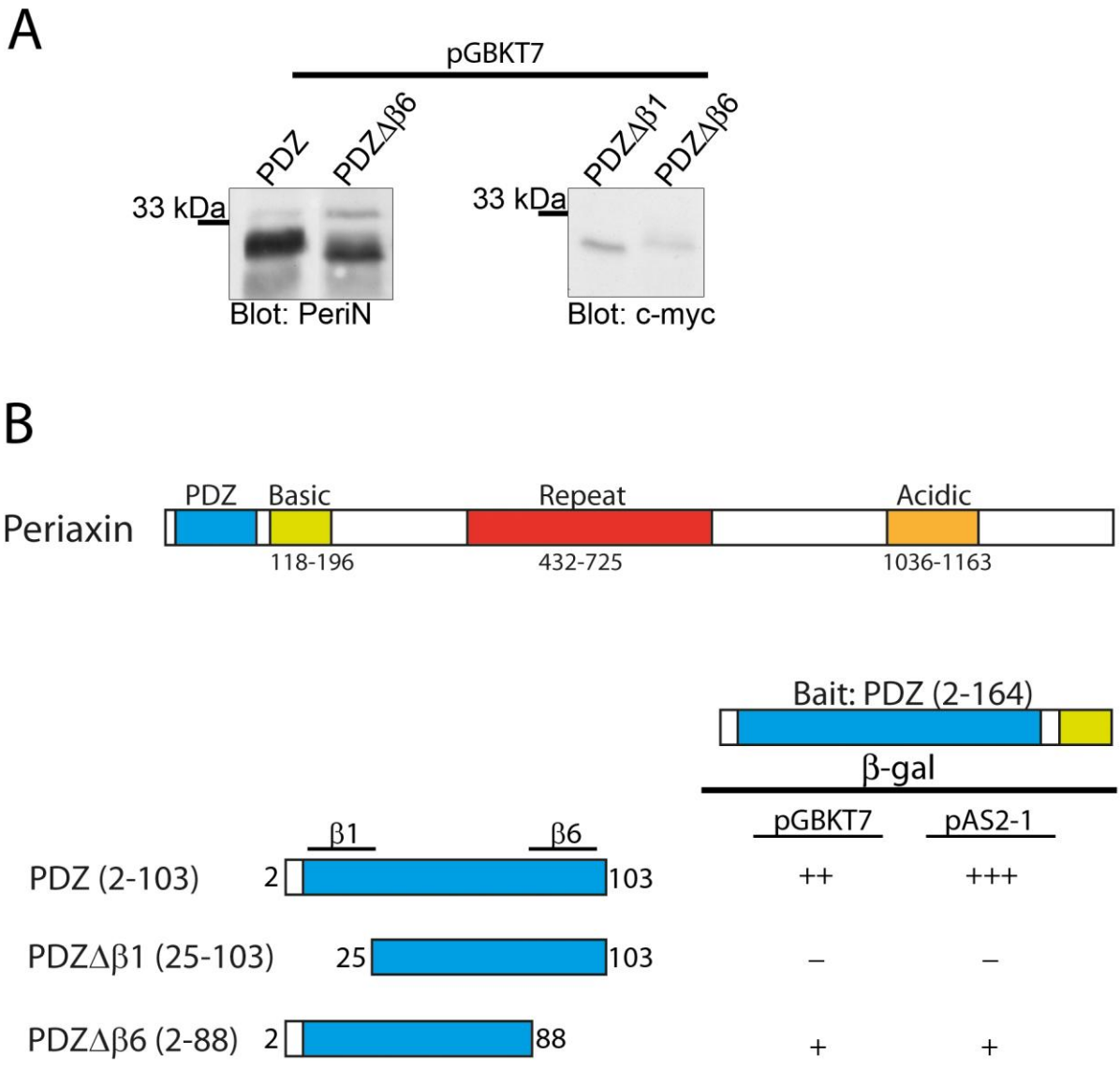
A
pGBKT7
PDZ
PDZΔβ6
33 kDa
Blot: PeriN
PDZΔβ1
PDZΔβ6
33 kDa
Blot: c-myc
B
Periaxin
PDZ
Basic
Repeat
Acidic
118-196
432-725
1036-1163
Bait: PDZ (2-164)
β-gal
pGBKT7
pAS2-1
β1
β6
PDZ (2-103)
2
103
++
+++
PDZΔβ1 (25-103)
25
103
–
–
PDZΔβ6 (2-88)
2
88
+
+

Figure 48. The PDZ domain β1 strand in Periaxin is crucial for PDZ-PDZ interactions.

A. The PDZ domain deletion constructs PDZΔβ1 (aa 25-103) and PDZΔβ6 (aa 2-88), alongside unmutated PDZ domain (aa 2-103) control construct in GAL4 binding domain vector pGBKT7, which contains a c-myc epitope tag, were transformed and expressed in yeast strain Y190. Protein expression was analyzed by Western blot using anti-Periaxin N-terminus (PeriN) antibody for PDZ control and PDZΔβ6 mutant, and anti-myc antibody for PDZΔβ1 because it lacks the extreme N-terminus of Periaxin recognized by the Periaxin antibody used here. The mobility of molecular weight marker (in kilodaltons) is shown on the left of the blots. The molecular weights of PDZ, PDZΔβ1 and PDZΔβ6 fusion proteins are 31 kDa, 29 kDa and 30 kDa.
B. Interaction of the intact N-terminus of Periaxin (aa 2-164) with PDZΔβ1 was disrupted, and with PDZΔβ6 was diminished. The strength of the interaction between the Periaxin N-terminal GAL4 activation domain fusion protein and the PDZ domain deletion fusion proteins, PDZΔβ1 and PDZΔβ6 in pGBKT7 and pAS2-1 in a yeast two-hybrid β-galactosidase assay was semi-quantitatively evaluated by the time taken for the development of blue colonies (+++, <30 min; ++, 30-60 min; +, 60-180 min). A schematic representation of the full length Periaxin is shown for comparison. Amino acid residues are indicated in brackets. The first and last amino acids for the control and mutants, as well as the β-strands involved were specified on the diagram.

3.3.3 Single amino acid changes in Periaxin PDZ domain are sufficient to disrupt homodimerization

In trying to minimize disruption of the tertiary structure of the protein and to identify specific amino acid residues that are important for homodimerization, single amino acid changes were introduced in the PDZ domain of Periaxin. Interactions were tested by a yeast two-hybrid assay.

Since β1-β1 strand anti-parallel interactions in PDZ dimers are primarily maintained by hydrogen bonding and weak electrostatic forces (Im et al., 2003a; Im et al., 2003b), sequence comparison of the β1 strand in Periaxin's PDZ domain with that of GRIP-1 PDZ6 and Shank1 PDZ domains provided clues as to the possible polar residues that might participate in hydrogen bonding in the dimeric conformation, such as threonine 23 (Fig. 49B). Substitution of T23 by an alanine (T23A) was predicted to disrupt hydrogen bonding in the dimeric interface of the Periaxin PDZ domain.

Sequence alignment of PDZ domains from proteins that are known to dimerize showed that the aspartate residue in the β4 strand was highly conserved. This aspartate is crucial for stabilization of the β-finger in the nNOS PDZ (Fig. 49B). Although there is no evidence that the Periaxin PDZ domain forms a β-hairpin finger as in the nNOS PDZ domain (Hillier et al., 1999; Tochio et al., 2000), the highly conserved aspartate (D63) in the β4 strand may be critical for maintaining the canonical structure of the PDZ dimer. The aspartate was therefore selected for mutation in this study.

The third mutant, which was used as a control, was a single amino acid substitution of the glycine in the carboxylate binding site to alanine (G31A). Despite the fact that substituting both the adjacent glycine (G31) and phenylalanine (F32) residues by alanines in the carboxylate binding loop of the Periaxin PDZ domain diminishes homodimerization (Sherman et al., 2001), previous work in our laboratory had suggested that mutating only one of these two amino acids, namely the conserved glycine residue did not alter PDZ-PDZ binding (unpublished data). Hence, the G31A mutation was used as an internal control.

Single amino acid mutant constructs (T23A, D63A and G31A) alongside the intact PDZ domain control construct in pGBKT7 were transformed into yeast and fusion proteins were expressed (Fig. 49A). Interaction of the Periaxin N-terminal region fusion protein with the G31A mutant fusion protein was positive for β-gal activity, and the strength of interaction was comparable to that of the non-mutated PDZ domain control. On the contrary, neither the T23A nor D63A mutated fusion protein interacted with the bait PDZ domain fusion protein as shown by the absence of GAL4 transcription activation, suggesting the importance of these amino acids in PDZ domain homodimerization (Fig. 49B).

A

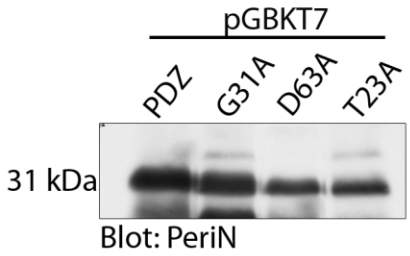

B Interaction with Periaxin PDZ (aa 2-164)

(aa 2-103)	21 31 41 51 61	β-gal pGBKT7	β-gal pAS2-1
PDZ	.... ELVEII VETEAQTGVS GFNVAGGGKE GIFVRELRED SPAAKSLSLQ EGDQL.....	+	+++
PDZ-G31A	.... ELVEII VETEAQTGVS AFNVAGGGKE GIFVRELRED SPAAKSLSLQ EGDQL.....	+	+++
PDZ-T23A	.... ELVEII VEAEAQTGVS GFNVAGGGKE GIFVRELRED SPAAKSLSLQ EGDQL.....	−	−
PDZ-D63A	.... ELVEII VETEAQTGVS GFNVAGGGKE GIFVRELRED SPAAKSLSLQ EGAQL.....	−	−

Figure 49. Single amino acid mutations in Periaxin PDZ domain disrupt PDZ-PDZ binding.

A. An immunoblot shows the yeast protein expression of single amino acid mutants (G31A, D63A and T23A) in pGBKT7 detected by the PeriN antibody. The molecular weights of the control and mutant PDZ constructs are 31 kDa.
B. Substitution of threonine 23 in the β1 strand or aspartate 63 in the β4 strand of Periaxin PDZ domain by an alanine abrogates self-association of the PDZ domain. Interactions of the N-terminal PDZ domain of Periaxin (residues 2-164) with the PDZ-G31A, T23A and D63A (residues 2-103) mutations in vector pGBKT7 were assessed for β-galactosidase activity in a yeast two-hybrid assay. Interaction results were confirmed using mutant constructs in pAS2-1. The G31A mutation was used as a control showing a positive interaction with the intact Periaxin N-terminus. The strength of the interaction was unaltered compared to the unmutated PDZ control. The amino acid sequence of the Periaxin PDZ domain (residues 15-65) is displayed. The positions of the amino acids mutated to alanine are denoted in red.

To determine whether these single amino acid mutations would interrupt homodimerization in a cellular environment, full-length Periaxin was co-expressed with the full-length PDZ mutants in HEK 293 cells and interactions were tested by co-immunoprecipitation. Expression of the constructs was confirmed by immunofluorescence analysis of transfected cells with anti-FLAG and anti-myc antibodies (data not shown). Similar to the non-mutated PDZ domain control, the myc-tagged Periaxin G31A mutant was co-immunoprecipitated with FLAG-tagged Periaxin, confirming that glycine 31 in the carboxylate binding loop was not essential for homodimerization. In agreement with the yeast two-hybrid results (section 3.3.2), the myc-tagged Periaxin D63A mutant failed to bind FLAG-tagged Periaxin, indicating that the highly conserved aspartate (D63A) in the β4 strand was essential for homodimerization (Fig. 50). Mutation of the threonine residue in the β1 strand (T23A) of Periaxin also substantially reduced binding with full-length Periaxin (Fig. 50). These results indicate that single amino acid substitutions in the PDZ domain are sufficient to disrupt homodimerization,

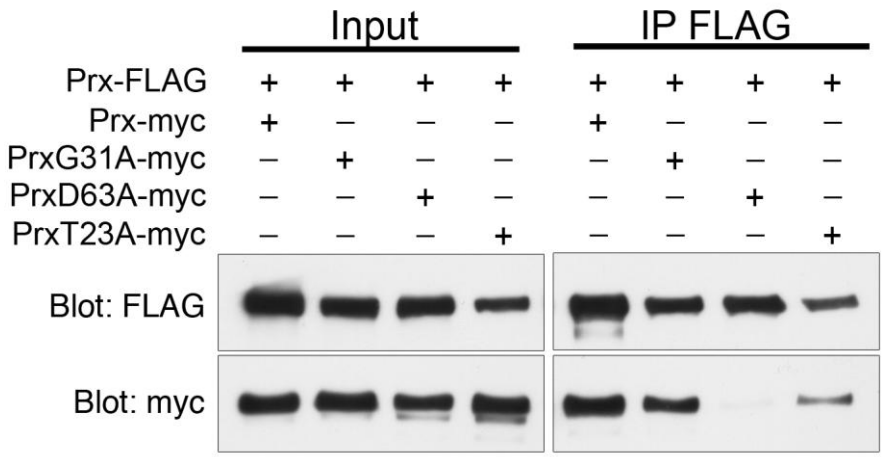

Figure 50. Full-length single amino acid Periaxin mutants D63A and T23A show reduction in homodimerization with full-length Periaxin in transfected HEK 293 cells by co-immunoprecipitation.

HEK293 cells transiently expressing myc-tagged single amino acid mutants and FLAG-tagged full-length Periaxin were lysed. FLAG-tagged-Periaxin was immunoprecipitated using anti-FLAG M2 beads. Immunoprecipitates were analyzed by Western blot with anti-FLAG or anti-myc antibodies. In contrast to the G31A mutation control, the D63A mutant could not bind full-length Periaxin. Binding of the T23A mutant to Periaxin was significantly decreased. The relative protein expression levels of the transfected constructs are shown in the input lanes.

3.3.4 Summary

In this chapter, I have shown by deletion mutant study in a yeast two-hybrid system that the β1 strand of Periaxin PDZ domain is important for dimerization. I have also identified specific amino acids critical for stabilizing the dimeric form of Periaxin PDZ domain, both by yeast two-hybrid interaction assays and co-immunoprecipitation. Homodimerization was considerably reduced by mutations of two amino acid residues, aspartate 63 and threonine 23. The highly conserved aspartate 63 in the β4 strand may contribute to homodimerization of the PDZ domain by virtue of formation of a salt bridge to maintain the structure of the dimer. Disruption of PDZ domain dimerization by mutation of the polar residue threonine 23 may suggest that the dimeric structure of the Periaxin PDZ domain is partly supported by hydrogen bonds formed by polar residues in the β1 strand.

Although it cannot be excluded that inappropriate folding of mutant Periaxin lacking 116 amino acids is responsible for disrupting PDZ domain dimerization *in vivo*, these biochemical data point to the fact that introducing minimal changes in the protein structure of Periaxin by single amino acid mutations in the PDZ domain, thus bypassing protein misfolding, is sufficient to abolish homodimerization, further confirming the requirement of an intact PDZ domain for dimerization.

4- DISCUSSION

OVERVIEW

Diverse biological activities are regulated through protein-protein interactions in signaling cascades. These proteins often contain modular protein interaction domains, such as WW domains, Src homology (SH2 and SH3) domains, pleckstrin-homology (PH) domains and PDZ domains. PDZ domains are found in many proteins that localize to the plasma membrane and interact with the cytoplasmic tails of membrane proteins (Lee and Zheng, 2010). It has been suggested that PDZ domains have two major functions. First, PDZ proteins may serve as a scaffold that allows organization and assembly of multiprotein signaling complexes at specific sites of cytoplasmic surfaces (Kim and Sheng, 2004). Secondly, they may link transmembrane proteins with cytoskeletal elements, such as the actin cytoskeleton as has been proposed for human disc-large (Dlg) (Lue et al., 1994).

Periaxin has an N-terminal PDZ domain that is known to homodimerize in the Periaxin-DRP2 dystroglycan complex in Schwann cell appositions (Sherman et al., 2001). In this work, the function of the Periaxin PDZ domain and the role of dimerization were studied in the PNS of a mouse mutant lacking the N-terminus of Periaxin. The offspring of mice carrying the *Prx* gene in which exon 5 was floxed, crossed with a glial specific *Cnp-Cre* line (Lappe-Siefke et al., 2003) had originally been generated in order to eliminate Periaxin protein expression in Schwann cells. However, these mice synthesized a truncated form of Periaxin lacking the N-terminal PDZ domain after Cre-mediated recombination. This fortuitous outcome allowed me to specifically study the function of the PDZ domain of Periaxin in peripheral nerves. In the absence of the PDZ domain, Periaxin does not homodimerize. Schwann cells lack appositions and have reduced internodal lengths. $Prx^{fl/fl}$*/Cnp-Cre* mice (known as Δ*PDZ-Prx* mice in this study) develop a progressive peripheral neuropathy with prominent myelin folding and redundant myelin loops. In this section, I will discuss the importance of the dimerization of the Periaxin PDZ domain in the clustering of DRP2 and apposition maintenance. I will also speculate how the loss of Periaxin's PDZ domain may contribute to a reduction of internodal length and dysregulation of myelin production.

4.1 GENERATION OF A CONDITIONAL MUTANT MOUSE LACKING THE PDZ DOMAIN OF PERIAXIN IN PERIPHERAL NERVES

4.1.1 An N-terminal truncation of Periaxin through translation reinitiation at a downstream methionine

The inability of the Periaxin specific N-terminus antibody to recognize immunoreactive Periaxin that was, nevertheless, detected by both the repeat region and C-terminus antibodies prompted me to investigate the possibility that protein synthesis is initiated at an internal methionine to generate an N-terminally truncated Periaxin in Δ*PDZ-Prx* Schwann cells. Here I have shown that Δ*PDZ-Prx* mice generated a partially functional truncated Periaxin lacking 116 amino acids at the N-terminus as a result of translation reinitiation. Following Cre-mediated recombination of the *loxP* sites in exon 5 of the *Prx* gene, an in-frame termination codon is introduced in exon 6, which was predicted to lead to a large frameshift gene deletion. However, by the mechanism of translation reinitiation, when a premature termination codon (PTC) follows shortly after the first initiation AUG codon, ribosomes may continue to scan along to reinitiate at downstream AUG codons in an optimal context (Kozak, 1984; Kozak, 1986a; Kozak, 1987b). In the recombined *'floxed' Prx* mRNA, reinitiation was most favorable at the fourth AUG in exon 6 downstream of the in-frame stop codon. Translation reinitiated at this AUG produced a form of Periaxin lacking the N-terminal PDZ domain. This was verified by N-terminal Edman degradation sequencing.

Transcripts with PTCs are prone to degradation by nonsense-mediated mRNA decay, resulting in low transcript levels (Maquat, 1995). Intriguingly, the abundance of the Periaxin transcript from Δ*PDZ-Prx* peripheral nerves was not altered, indicating that the transcript yielded after recombination, albeit in the presence of a PTC, is resistant to nonsense-mediated mRNA decay (NMD) (section 3.1.2). Previous studies of the human triosephosphate isomerase, *BRCA1*, and β-globin mRNA have shown that reinitiation downstream of a PTC will, at least partly, protect the transcript from NMD (Inacio et al., 2004; Perrin-Vidoz et al., 2002; Zhang and Maquat, 1997). Translation reinitiation is likely to explain the failure of the frameshift stop codon in exon 6 of the *Prx* gene to trigger NMD, and thus does not undermine the stability of the recombined transcript.

This results in the generation of an N-terminally truncated protein of Periaxin in Δ*PDZ-Prx* nerves.

The mutant Periaxin was, however, expressed at slightly reduced levels. The similarity of Periaxin transcript levels between WT and Δ*PDZ-Prx* peripheral nerves excludes the possibility of changes in mRNA expression leading to the reduction in protein expression observed. One explanation for the reduced yield of mutant Periaxin may be the decline in the efficiency of reinitiation as the intercistronic distance between the minicistron (short translated sequence) upstream of the premature stop codon and the downstream translated sequence is exceedingly far apart, as proposed by Marilyn Kozak (Kozak, 1987b).

4.1.2 Translation reinitiation of protein and hereditary disorders

Several studies have demonstrated translation reinitiation in patients with inherited disorders, such as in Menkes disease, peroxisome-biogenesis disorder, methylmalonic acidemia and androgen resistance (Chang and Gould, 1998; Ledley, 1990; Paulsen et al., 2006; Zoppi et al., 1993). A report on mutations in *ATP7A* gene, which cause Menkes disease, an X-linked recessive disorder of copper metabolism, has provided evidence that the generation of a partly functional Menkes protein from the NMD-resistant *ATP7A* transcript by translation reinitiation may modulate the disease phenotype. The patient carrying the N-terminally truncated protein displayed milder clinical symptoms and survived through adulthood (Paulsen et al., 2006). In addition, reinitiation of protein translation has been shown in individual patients suffering from peroxisome-biogenesis disorder or androgen resistance (Chang and Gould, 1998; Zoppi et al., 1993), which may or may not modulate the clinical phenotype. In this study, Δ*PDZ-Prx* mice showed a less severe demyelinating neuropathy both morphologically and electrophysiologically than Periaxin-null mice. The moderation of the phenotypic symptoms in these mice may be attributed to the production of the partially functional Periaxin form by downstream reinitiation.

Of the 16 *Periaxin* mutations reported in human patients up until now, most of the mutations occur in exon 7, with the exception of R82fsX96, which occurred in exon

6 resulting in a frameshift termination codon replacing a leucine residue at position 96 (Marchesi et al., 2010; Takashima et al., 2002). The patient with the R82fsX96 mutation showed severe neuropathy with features not distinct from those observed in other patients carrying exon 7 mutations, such as proximal and distal muscle weakness and sensory ataxia, but surprisingly displayed normal sensory conduction velocities. The authors predicted that this mutation would abrogate protein translation due to NMD, resulting in a complete loss of Periaxin expression (Takashima et al., 2002). Although translation reinitiation has not been demonstrated in patients carrying human *PRX* mutations, the R82fsX96 mutation could, in principle, lead to the generation of an N-terminally truncated protein by virtue of reinitiation at a downstream start codon. If this were the case, protein translation would initiate at the first AUG (M140) in exon 7 of the human *Prx* gene, which is in a favorable context, producing a form of Periaxin lacking the PDZ domain and a portion of the basic domain. PDZ dimerization of Periaxin should not occur. The predicted effect on the clinical phenotype may be similar to the less severe demyelinating neuropathy observed in Δ*PDZ-Prx* mice.

4.2 CHARACTERIZATION OF Δ*PDZ-PRX* MICE CONTAINING PERIAXIN LACKING THE PDZ DOMAIN IN PERIPHERAL NERVES

4.2.1 DRP2 is depleted in the absence of the PDZ domain of Periaxin

Dystrophin-related protein 2 (DRP2) is the only molecule that has been shown thus far to interact with Periaxin in the dystroglycan complex (DGC) found in the appositions between the abaxonal Schwann cell membrane and the outer layer of the myelin sheath (Sherman et al., 2001). Clustering of DRP2 to appositions requires Periaxin since DRP2 is depleted and appears non-phosphorylated in Periaxin-null Schwann cells deficient of Periaxin (D. Sherman, personal communication). DRP2+ patches fail to form and appositions are disrupted (Sherman et al., 2001). In Δ*PDZ-Prx* mice, mislocalization and depletion of DRP2 suggests that homodimerization of the Periaxin PDZ domain is essential for proper localization of DRP2 and stabilization of the PDG complex. Although the mutant Periaxin without the PDZ domain contains an intact basic domain, which interacts with DRP2 albeit at reduced levels, abrogation of PDZ domain homodimerization destabilizes its association with DRP2.

Similar to Periaxin-null nerves, DRP2 is reduced in expression and exists primarily in the non-phosphorylated form in Δ*PDZ-Prx* mice. How phosphorylation of DRP2 is regulated remains obscure. One plausible mechanism is that DRP2 phosphorylation is facilitated by PDZ-PDZ dimerization of Periaxin, which might provide a clustered scaffold for recruitment and targeting of protein kinases to the vicinity of DRP2 for phosphorylation. In this context, when Periaxin homodimerization does not occur in the absence of the PDZ domain, the multimolecular scaffold is not assembled, perhaps due to a reduced ability of the truncated Periaxin protein to localize to patches. Hence, DRP2 is not phosphorylated and stays in the non-phosphorylated state, which renders it unstable and likely destined for proteasome-mediated degradation. Indeed components of dystroglycan complexes are known to be degraded by the proteasome (Bonuccelli et al., 2003; Gazzerro et al., 2010). PDZ domain protein interactions have been demonstrated to recruit protein kinases for phosphorylation of complex components in other signaling complexes, such as the SAP97-AKAP79-cAMP-

dependent protein kinase complex (Gardner et al., 2007). In this complex, the PDZ domain at the carboxyl terminus of β1-adrenergic receptor binds to disc large Dlg/ SAP97, another PDZ domain-containing membrane-associated guanylate kinase (MAGUK) protein, which associates with AKAP79 and cyclic AMP-dependent protein kinase (PKA). The interaction brings PKA in close proximity with β1-AR for phosphorylation of the β1-AR at Ser312 that is required for efficient recycling of the β1-AR.

It is also likely that DRP2 is phosphorylated prior to association with Periaxin. Interaction with dimeric Periaxin stabilizes and maintains the phosphorylated form of DRP2 for proper targeting of DRP2 to patches and protecting it from dephosphorylation or subsequent proteasome-dependent degradation. In a similar fashion, the PDZ domain protein α-syntrophin in the dystrophin protein complex plays a crucial role in stabilization of acetylcholine receptor clusters and localization of utrophin and nNOS at the neuromuscular junction (NMJ) (Adams et al., 2010; Adams et al., 2001). Specifically the PDZ domain of syntrophin is required for targeting of nNOS to the sarcolemma and postsynaptic NMJ (Adams et al., 2010; Adams et al., 2001). In *Drosophila*, Fasciclin II and Shaker potassium channels are localized to the NMJ and stabilized via PDZ domain interactions with Dlg, which selectively protects them from degradation (Zito et al., 1997).

Whether dimerization of Periaxin actively enhances DRP2 phosphorylation is unclear, it is, however, evident that the Periaxin PDZ domain dimer is important for stabilizing phosphorylated DRP2, since DRP2 no longer existed in the phosphorylated form when the PDZ domain of Periaxin was eliminated after the formation of Schwann cell compartments in adult Schwann cells by tamoxifen inducible recombination. In addition, it is worth noting that the interaction between Periaxin and DRP2 does not depend on the phosphorylated state of DRP2 because I have shown that a GST-DRP2 fusion protein devoid of the potential phosphorylation sites was able to pull down Periaxin from normal nerves.

4.2.2 Stabilization of the PDG complex by Periaxin dimerization maintains appositions in the Schwann cell

Myelinating Schwann cells are polarized radially and longitudinally for action potential propagation (Salzer, 2003). The cytoplasm of the Schwann cell is compartmentalized into discrete domains, called Cajal bands, which are formed between appositions. Appositions and Cajal bands harbor different DGCs (Albrecht et al., 2008; Court et al., 2009). The DGC consisting of Periaxin, DRP2 and dystroglycan (PDG complex) found in appositions is required for Schwann cell compartmentalization. In the absence of Periaxin, appositions and Cajal bands are disrupted (Court et al., 2004; Sherman et al., 2001). Here I have demonstrated that the self-association of the Periaxin PDZ domain in the PDG complex is required for apposition maintenance. In mutant mice lacking the Periaxin PDZ domain, most Schwann cells had no appositions and Cajal bands were disrupted. Therefore the PDZ domain protein Periaxin may be essential for maintaining cell polarity, as has been suggested to be a central role played by PDZ domain proteins. In *Drosophila*, ablation of the function of PDZ protein Scribble, an interactor of Dlg, leads to loss of cell polarity and tissue architecture (Bilder et al., 2000).

A recent report has suggested that the DGC composed of dystroglycan, utrophin in Cajal bands, together with laminin-2, is important for the regulation of cytoplasmic compartmentalization in the Schwann cell. Specific single deletion of dystroglycan, dystroglyan glycosylation, laminin-2 and utrophin in the Schwann cell results in a reduction in the size of DRP2+ patches and appositions (Court et al., 2009). However, a significant limitation of that study was that no information was provided about the strain backgrounds of the various mutants used. In a different study, the same group has also postulated that the size of Schwann cell domains is partly regulated by the degree of dystroglycan cleavage mediated by metalloproteases MMP2-9 in Schwann cells lacking laminin-2 (Court et al., 2011).

Appositions are likely formed independently of the PDG complex, since it has been suggested that Schwann cell cytoplasm is separated into specific domains by actin cytoskeleton patterning thus restricting actin to Cajal bands prior to the appearance of DRP2+ patches. (Court et al., 2009). Hence, the PDG complex is assembled to maintain

Schwann cell compartments. The stability of DRP2+ patches and their structural correlate, appositions, appears to be exclusively regulated by Periaxin and is independent of the presence of dystroglycan in the plasma membrane. In Schwann cells lacking dystroglycan, DRP2 is present though reduced in expression (Saito et al., 2003), and appositions are formed despite being smaller in size (Court et al., 2009). Furthermore, expression of dystroglycan and other dystrophins (utrophin and Dp116) is normal in Periaxin-null mice (Sherman et al., 2001).

The mechanism by which Periaxin maintains appositions remains to be determined. A possibility is that the Periaxin PDZ homodimer helps stabilize the phosphorylated form of DRP2, which in turn stabilizes the PDG for proper maintenance of appositions. Interestingly, even after the Schwann cell compartments become established during myelination, these defined domains can be disrupted once PDZ domain homodimerization is abrogated in adult Schwann cells, as shown by the disruption of DRP+ patches and Cajal bands in tamoxifen-treated *Prx*$^{fl/fl}$*/P0CreERT* mice. This further confirms the crucial role of Periaxin self-association in maintaining the PDG complex, and hence appositions.

The PDZ scaffold of Periaxin may serve as a platform to target important signaling molecules that mediate compartmentalization of the Schwann cell cytoskeleton. Identifying other interactors of Periaxin would facilitate understanding of the role of Periaxin's PDZ dimerization in apposition maintenance. In addition, in order to confirm that Periaxin regulates apposition stability through its PDZ domain, it would be important to examine whether appositions are present in Periaxin mutants lacking other domains, such as the C-terminal acidic domain.

4.2.3 Regulation of Schwann cell internodal lengths by Periaxin

4.2.3.1 Schwann cell compartmentalization and internodal length

Similar to Periaxin-deficient Schwann cells, mutant Schwann cells lacking the PDZ domain of Periaxin in Δ*PDZ-Prx* nerves display defects in elongation, resulting in a reduction in internodal lengths by one-third at 3 weeks of age. The decrease in Schwann cell longitudinal length is independent of changes in axon caliber or myelin thickness

since both parameters were unaltered in the mutant nerves. The longitudinal growth rate of Δ*PDZ-Prx* Schwann cells remains lower than that of WT Schwann cells as axons extend with age, resulting in shorter internodal lengths also in the adult. How Schwann cell growth capacity is regulated remains unclear. A recent study has postulated that the degree of Schwann cell compartmentalization influences Schwann cell elongation (Court et al., 2009; Court et al., 2011). In Schwann cells with disrupted DGC in Cajal bands (Schwann cell-specific dystroglycan-null, laminin-2-null and utrophin-null mice), appositions are smaller, which has been associated with a reduction in Schwann cell internodal lengths.

Whether proper cytoplasmic compartmentalization regulates Schwann cell elongation capacity is controversial. Work in our laboratory has demonstrated that Schwann cell elongation is normal in DRP2-null mice that lack appositions (D. Sherman, personal communication). It appears that Periaxin influences Schwann cell extension through other yet unknown mechanisms. Proteomics analysis of PNS myelin content indicates that Periaxin is the second most abundant protein in peripheral myelin, comprising 16% of all myelin protein components. DRP2 constitutes about 0.18% of all PNS myelin proteins (Patzig et al., 2011). The abundance of Periaxin protein in peripheral nerves implies that Periaxin expression is not solely restricted to the PDG complex in appositions. It is possible that Periaxin localized elsewhere than appositions may regulate Schwann cell longitudinal extension by interacting with potential membrane proteins such as receptors, ion channels, or kinase and associated proteins via the PDZ domain. Certainly, Periaxin is not restricted to appositions, as DRP2 appears to be. Receptor and ion channel interactions have been reported in many PDZ domain proteins, such as PSD-95, α-syntrophin, GRIP and Dlg (Adams et al., 2010; Gardner et al., 2007; Kornau et al., 1997; Luo et al., 2005).

Interestingly, the effect of Periaxin on internodal growth is developmentally regulated. By replacing wild-type Periaxin with mutant Periaxin lacking the PDZ domain in adult Schwann cells of tamoxifen-inducible $Prx^{fl/fl}$*/P0CreERT* mice, recombined Schwann cells had normal internodal lengths. This indicates that the influence of Periaxin (PDZ) on Schwann cell internodal growth is critical at early stages

of myelination. Once myelination is complete and Schwann cell compartments are well established, elimination of the Periaxin PDZ domain has no apparent effect on internodal length.

4.2.3.2 Increase in the number of Schwann cells is proportionate with shortening of internodal lengths in Δ*PDZ-Prx* nerves

With a one-third reduction in Schwann cell internodal lengths, there should have been an increase in the number of Schwann cells and Δ*PDZ-Prx* peripheral nerves harbor a proportionate excess of Schwann cell nuclei associated with myelinated axons, compared with normal nerves. Shortening of Schwann cell length has been described in PMP22-null mice at 3 weeks old, alongside abnormal myelin morphology (Neuberg et al., 1999). The authors proposed that PMP22 is implicated in early control of Schwann cell proliferation during development. It is unknown whether Periaxin plays a role in regulating Schwann cell proliferation in PNS development. As Periaxin mutant nerve fibers studied at all ages were completely populated by Schwann cells, this would suggest that Schwann cell proliferation prior to myelination before birth is not compromised.

Since Schwann cell internodal lengths are comparable between WT and Periaxin-null mice at the onset of myelination (postnatal day 2) (Court et al., 2004), abnormally short internodes formed by Periaxin mutant Schwann cells during myelination implies that additional myelin-forming Schwann cells may be acquired from an existing pool of Schwann cells to associate with the growing axon. It is possible that non-myelinating Schwann cells, which have the potential to myelinate (Griffin and Thompson, 2008), proliferate to supply the additional cells needed to populate and myelinate axons in the Periaxin mutants. It has been shown that in the presence of exogenously administered GDNF, non-myelinating Schwann cells proliferate and are able to sort and myelinate normally unmyelinated small axons (Hoke et al., 2003). Expression of neuronal signal Neuregulin-1 type III in normally unmyelinated sympathetic neurons *in vitro* is also sufficient to instruct non-myelin forming Schwann cells to produce myelin (Taveggia et al., 2005). Proliferation assays using BrdU incorporation or other proliferation markers, alongside cell type specific markers, may

provide insights into the identity of the cell population that contributes to the surplus of myelinating Schwann cells in the Periaxin mutant nerves.

4.2.3.3 Regulation of internodal length and cytoskeletal dynamics

Control of Schwann cell longitudinal growth likely involves regulation of cytoskeletal dynamics. The microtubule network is disrupted in Cajal band-lacking *Prx* KO Schwann cells affecting mRNA transport to the paranodal regions (Court et al., 2004). It would be of interest to investigate whether Periaxin regulates Schwann cell elongation through Rho/Rho kinase (ROCK) signaling, which regulates myosin light chain phosphorylation, leading to the stimulation of myosin II activity and actin polymerization for forming stress fibers (Tapon and Hall, 1997). By inhibiting ROCK in Schwann cells *in vitro*, myelin segments are shorter (Melendez-Vasquez et al., 2004). The authors proposed that Rho/ROCK is important for organizing the movement of Schwann cell membrane around the axon during myelination. Another central regulator of the actin cytoskeleton is the Rho GTPase Rac1, which is activated by β1-integrin signaling and is essential for Schwann cell shape, process extension and stabilization during axonal sorting and myelination (Benninger et al., 2007; Nodari et al., 2007).

4.2.4 Myelin abnormalities

4.2.4.1 Hypermyelination with aberrantly folded myelin is a major morphological feature of Δ*PDZ-Prx* peripheral nerves

The mature myelin sheath of Δ*PDZ-Prx* peripheral nerves is characterized by extensive infoldings and outfoldings, as well as focal paranodal thickenings. Paranodal tomacula were observed in over 70% quadriceps nerve teased fibers at 6 weeks old. Myelin foldings increased gradually in number and complexity with time. Redundant myelin loops invading the axon leading to axonal constrictions were frequently noted. However, Δ*PDZ-Prx* mice develop a milder form of demyelinating neuropathy than that seen in Periaxin-null mice since major onion bulb formations in Δ*PDZ-Prx* nerves were not pronounced. No secondary axonal loss was found in Δ*PDZ-Prx* nerves up to the age of 9 months (oldest age examined). Since abnormal overproduction of myelin renders the myelin sheath unstable, the appearance of myelin foldings and tomacula often precedes

demyelination and remyelination (Adlkofer et al., 1997; Maycox et al., 1997). Hence, the increased severity of the progressive neuropathy developed in Δ*PDZ-Prx* mice may likely allow manifestation of the full development of the demyelinating neuropathy at ages older than 9 months.

The presence of other structural domains in the truncated Periaxin, such as the C-terminal acidic domain may account for the modulation of the morphological phenotype. Indeed, the C-terminus of Periaxin is crucial for myelin maintenance since severe demyelination and axonal loss has been described in the peripheral nerves of CMT 4F patients with the R1070X mutation in the *PRX* gene expressing a form of Periaxin protein without the acidic domain at the C-terminus (Kijima et al., 2004; Otagiri et al., 2006; Parman et al., 2004). Analysis of Periaxin mouse mutants lacking the C-terminus may provide insights into the regulation of peripheral myelin production and stability, as well as whether demyelination is regulated differently from apposition formation and internodal lengths. In this light, the Periaxin PDZ domain may act as a modulator of the C-terminus function in maintaining myelin integrity.

4.2.4.2 Schwann cell compartments and myelin stabilization

It is unclear whether intact Schwann cell compartments such as Cajal bands contribute to maintaining myelin integrity. A speculation is that destabilization of the PDG complex, and thus disruption of appositions leads to myelin abnormalities. Nevertheless, Δ*PDZ-Prx* and *Prx* KO mutants, both with disruption of appositions and Cajal bands, exhibit different degrees of demyelination. Other mutants with disrupted DGC, and thus abnormal Schwann cell compartments including Schwann cell dystroglycan-knockout mice, and human patients with laminin-2 mutations display a rather mild dysmyelinating neuropathy with focally folded myelin (Di Muzio et al., 2003; Nodari et al., 2008; Saito et al., 2003). It seems unlikely that the lack of appositions is the cause of myelin instability and eventually destruction. This may suggest that apposition maintenance and myelin stability are likely regulated via independent mechanisms.

Interestingly in the inducible conditional system, disruption of the Periaxin PDZ domain postnatally in Schwann cells after myelination is complete and Schwann cell

appositions and Cajal bands are established also leads to excessive folding of the myelin sheath and mild demyelinating and remyelinating phenotype, suggesting that the regulation of myelin maintenance by Periaxin is a late event and further confirming the requirement of Periaxin for a stable myelin sheath. Importantly, the finding that Schwann cell internodal length is normal in recombined Schwann cells of tamoxifen-treated mice suggests that the regulatory role of Periaxin on Schwann cell longitudinal growth is independent of its function in myelin stability control.

4.2.4.3 Increase in supernumerary Schwann cells in mature Δ*PDZ-Prx* nerves

A notable feature of Δ*PDZ-Prx* nerves is the enlargement of nerve area as a result of an increase in endoneurial and perineurial space, as has been commonly described in human patients with the demyelinating form of CMT neuropathies (Donaghy, 2003) and dystroglycan-deficient mouse nerves (Saito et al., 2003). This phenomenon is associated with the activation and proliferation of supernumerary Schwann cells, leading to the generation of extracellular matrix in the endoneurium (Kagitani-Shimono et al., 2008). Indeed, an increase in Schwann cell number was noted in both Δ*PDZ-Prx* and *Prx* KO mutants, which could not be solely accounted for by the addition of Schwann cells due a shortening of internodal lengths. There was a striking increase in supernumerary Schwann cells lying in the endoneurial space outside the basal lamina of neighboring nerve fibers. Non-myelinating supernumerary Schwann cells were frequently seen enveloping abnormally or thinly myelinated axons in Periaxin mutant nerves.

Demyelination results in active proliferation of Schwann cells. One source of dividing Schwann cells that give rise to supernumerary Schwann cells is the Schwann cells that have lost the myelin sheath (Hall and Gregson, 1974). Consistent with severe demyelination and the increase in ERK activation, which is sufficient to drive dedifferentiation of Schwann cells (Harrisingh et al., 2004), the total number of Schwann cells indicated by Sox10+ nuclei was elevated by fivefold in *Prx* KO nerves, alongside a threefold increase in Krox20+ cells representing myelin-forming Schwann cells, or those that are committed to myelination (Zorick et al., 1996a). In addition, the recruitment of Schwann cells of unmyelinated Remak fibers to proliferate may

contribute to the remarkable increase in non-myelinating Schwann cells in mature *Prx* KO nerves (Griffin et al., 1987; Griffin et al., 1990).

Nevertheless, in Δ*PDZ-Prx* nerves, the limited degree of demyelination would not be sufficient to explain the significant increase in Schwann cell number since dedifferentiation of Schwann cells would not be a major source of proliferating Schwann cells. In the case where demyelination is rare, supernumerary Schwann cells in the endoneurial space may be derived from proliferation of Schwann cells of unmyelinated fibers, as shown previously in an induced model of axonal swellings and paranodal demyelination (Griffin et al., 1987).

4.2.4.4 Periaxin and a potential mechanism for regulation of myelin stabilization

The pathological hallmark of extensively folded myelin sheaths, but relatively mild demyelination observed in Δ*PDZ-Prx* mice is similar to the myelin alterations described in mouse models of other subtypes of CMT4, including MTMR2-null (CMT 4B1) mice and MTMR13-null (CMT 4B2) (Bolino et al., 2004; Bolis et al., 2005; Bonneick et al., 2005; Robinson et al., 2008; Tersar et al., 2007). These mutant mice develop a progressive neuropathy exhibiting excessive myelin depositions as focally folded myelin; however, primary demyelination and remyelination are not evident. In MTMR2-deficient mice, the disruption of the interaction between MTMR2 and PDZ domain protein mammalian discs large 1 (Dlg1), also known as synapse associated protein 97 (SAP 97) has been attributed to the dysregulation of myelin membrane homeostasis, leading to aberrant myelin outfoldings (Bolino et al., 2004; Bolis et al., 2009). Dlg1, a multidomain scaffolding protein in the abaxonal domain, negatively controls myelin production by interacting with the adaxonal apical domain-protein phosphatase and tensin homolog (PTEN), which acts by inhibition of AKT activation (Cotter et al., 2010). However, how these two components that are localized in distinct Schwann cell compartments interact *in vivo* is currently not understood. Loss of PTEN in Schwann cells results in hypermyelination in the PNS (Goebbels et al., 2010).

The high frequency of myelin tomacula at the paranodes after postnatal week 3 in teased fibers of Δ*PDZ-Prx* quadriceps nerves prompted me to analyze levels of Dlg1,

which is preferentially enriched at the nodal/ paranodal regions (Bolino et al., 2004; Bolis et al., 2005). Unexpectedly, I observed an increased level of Dlg1 by immunofluorescence and Western blot analysis, in contrast to that described in MTMR2-deficient mutants (Bolino et al., 2004). In a recent report, the same group proposed a mechanism for coordination of myelin membrane homeostatic control by Dlg1, Sec8 and MTMR2. Dlg1 interacts with Sec8 exocyst component to promote membrane formation in Schwann cells *in vitro*, and with MTMR2 to oppose membrane addition (Bolis et al., 2009). Periaxin that is membrane-associated in the abaxonal domain of the myelinating Schwann cell may signal through the Dlg1/Sec8 complex localized in the same region, to regulate myelin membrane homeostasis. It may be possible that in Δ*PDZ-Prx* mice, formation of redundant myelin folds is mediated by an upregulation of Dlg1/Sec8 complex that results in excessive membrane transport to the paranodes.

Evidence from previous studies might support this model. In *Drosophila*, Dlg has been shown to promote membrane formation by interaction with t-SNARE Gtaxin at the postsynaptic junction during larvae development (Gorczyca et al., 2007). In another study, Dlg forms a complex with the integral membrane protein Stbm to promote membrane formation in *Drosophila* epithelial cells. More importantly, overexpression of the Dlg/Stbm complex in cells stimulates excessive formation of the plasma membrane, likely by increasing vesicle transport to these sites (Lee et al., 2003). In addition, Sec8 has been shown to regulate oligodendrocyte morphology and membrane formation through targeting transport vesicles to sites of rapid membrane growth (Anitei et al., 2006). Indeed, the balance between exocytosis and endocytosis of myelin proteins has been implicated in oligodendroglial membrane remodeling (Trajkovic et al., 2006; Winterstein et al., 2008).

The abundant expression of Periaxin in the Schwann cell may suggest other yet unknown functions of the protein, one of which may be regulation of Dlg1 function. Further study of Dlg1 or the Dlg1/Sec8 complex in the Periaxin mutant mice is required. Moreover, identification of additional interactors of the Periaxin PDZ domain will facilitate understanding of its regulatory role in myelin sheath homeostasis in the PNS.

4.2.5 Electrophysiological analysis in Δ*PDZ-Prx* mice

4.2.5.1 Nerve conduction velocity is not altered in the presence of myelin foldings in adult Δ*PDZ-Prx* nerves

Axon caliber, myelin thickness, internodal length and nodal architecture are important determinants of conduction velocity in myelinated nerve fibers (Waxman, 1980). In classes of fibers showing geometric similarity, myelin thickness and internodal length vary linearly to axon diameter, which is proportional to conduction velocity (Hursh, 1939; Rushton, 1951). How conduction velocity varies in response to changes in these parameters has been tested mathematically and experimentally. The reduction in nerve conduction velocity in Periaxin-deficient nerve fibers with shorter internodes is the first experimental evidence of the direct influence of internodal lengths in nerve conduction velocity, when all other parameters known to affect nerve conduction remain normal (Court et al., 2004). In the absence of the Periaxin N-terminal PDZ domain, mutant Schwann cell internodal lengths are shorter, resulting in decreased nerve conduction velocities at 3 weeks old. This result confirms the role of internodal lengths in nerve conduction regulation. Poorer motor coordination in Δ*PDZ-Prx* mice determined by RotaRod performance further validates the electrophysiological abnormalities in mutant nerves at 3 weeks old.

Intriguingly, I found that in the mature PNS, Δ*PDZ-Prx* nerves with an aberrantly folded myelin sheath were able to conduct normally, despite the impairment of Schwann cell elongation. Normal conduction velocities in adult Δ*PDZ-Prx* mice resulted in normal motor coordination. In Δ*PDZ-Prx* mice, the presence of a functional truncated Periaxin, albeit lacking an important PDZ domain in Schwann cells seems to slow down the progression of myelin sheath destruction. Unlike in mature *Prx* KO nerves where severe demyelination leads to a reduced safety factor for normal transmission of action potentials and hence conduction delay or failure (Sircar, 2008), limited demyelination and absence of secondary axonal loss in Δ*PDZ-Prx* nerves resulted in no effect on nerve conduction. Similarly, mouse mutants that display focally folded myelin and a mild demyelinating phenotype, such as connexin 32-, MTMR13/Sbf2- or MTMR2-mutant mice also exhibit minor electrophysiological

abnormalities and normal conduction velocities in mature nerves even up to advanced ages (Anzini et al., 1997; Bonneick et al., 2005; Tersar et al., 2007), suggesting that low level of demyelination is not sufficient to affect nerve conduction.

However, it was perhaps surprising that the presence of myelin foldings and tomacula did not alter nerve conduction in adult Δ*PDZ-Prx* mice. Theoretical and mathematical analysis of the effects of fiber size on conduction velocity in myelinated fibers suggested that myelin thickness measured in terms of *g*-ratio (axon diameter/ fiber diameter) should have an optimal value of 0.6-0.7 for maximum conduction velocity (Rushton, 1951; Smith and Koles, 1970). Changes in the *g*-ratio between 0.47 (for hypermyelinated fibers) and 0.74 (for hypomyelinated fibers) would lead to a reduction in nerve conduction velocity of not more than 5% (Rushton, 1951). Moreover, mathematical models have shown that for a fixed axon diameter, conduction velocity increases with myelin thickness (Smith and Koles, 1970). Experimentally the proximal stump fibers of crushed nerves during the early stage of regeneration have smaller axon diameters but thicker myelin sheaths than normal nerves. These regenerating fibers conduct considerably faster than normal fibers (Sanders and Whitteridge, 1946). Therefore, in Δ*PDZ-Prx* mice the heterogeneity of myelin thickness along an internode due to focally folded myelin may not negatively affect nerve conduction. Nevertheless, axon compression by major myelin infoldings, as shown in MTMR13/Sbf2-null mice, influences compound muscle action potential (CMAP) amplitudes (not determined in this work) but not the conduction velocity per se (Tersar et al., 2007).

4.2.5.2 Sensitivity of nerve conduction velocity to internodal length change

Computer simulations of conduction through myelinated nerve fibers have shown that nerve conduction velocity is sensitive to internodal lengths in the shorter range, but becomes less sensitive at longer Schwann cell lengths (Brill et al., 1977; Moore et al., 1978). The development of a mild demyelinating phenotype in Δ*PDZ-Prx* mice has proved to be extremely useful because it has allowed me to study experimentally the sensitivity of nerve conduction velocity to internodal length changes with age in detail.

The normal nerve conduction of adult Δ*PDZ-Prx* nerves, albeit with shorter internodes, is a result of Schwann cells having elongated sufficiently to allow for optimal conduction, alongside an increase in axon diameter and myelin thickness as the axon extends. I showed this by determining the conduction velocity of Δ*PDZ-Prx* quadriceps nerves at an age between 3 weeks and 4 months. Schwann cells of 6-week-old Δ*PDZ-Prx* nerves had internodal lengths intermediary of those in 3-week and 4-month-old mutant mice, corresponding to the conduction velocity at a value between those at 3 weeks and 4 months. A tendency towards increasing nerve conduction velocity was demonstrated with Schwann cell internodal growth over time in Δ*PDZ-Prx* nerves, indicating that mutant Schwann cells had reached a threshold length for normal conduction of action potentials in the adult. Therefore, the internodal lengths of adult Δ*PDZ-Prx* Schwann cells probably lie in the range in which mathematical models have been shown not to affect nerve conduction velocity. It is interesting to compare this with the results from a study of nerve conduction velocity in regenerated fibers by Sanders and Whitteridge. After regeneration, axon diameters and myelin sheath thickness regain their normal sizes, but internodal lengths are reduced and nerve conduction velocity is normal (Sanders and Whitteridge, 1946). The internodal lengths of regenerated fibers are in the range where conduction velocity is no longer sensitive to internodal length.

As the phenotype of Δ*PDZ-Prx* mice increases in severity with age, with more myelin foldings that contribute to severe axonal constrictions, as well as progressive myelin degeneration, Δ*PDZ-Prx* mice at older ages (10 months old) showed a slowing of nerve conduction.

4.2.6 Periaxin and other signaling pathways

I have also examined the expression of activated mTOR and a downstream signal S6 ribosomal protein in the PI3K/AKT/mTOR signaling cascade in Δ*PDZ-Prx* and *Prx* KO nerves. mTOR, best known for regulating cell growth and protein synthesis via the phosphorylation of downstream substrates p70 S6 kinase 1 (p70S6K1) and 4E-BP1 (Guertin and Sabatini, 2009), is required for oligodendrocyte differentiation (Narayanan et al., 2009; Tyler et al., 2009). Activation of rapamycin-sensitive mTOR (mTORC1) mediated by AKT signaling has been implicated in the regulation of CNS myelination (Narayanan et al., 2009). Maximal activation of AKT is brought about by phosphorylation at Thr308 by the constitutively active phosphate-dependent kinase (PDK1), and at Ser473 by mTOR (rapamycin-insensitive mTORC2) (Calleja et al., 2009; Iwanami et al., 2009). At postnatal week 3, activated mTOR levels were not altered in these nerves. Consistently, AKT phosphorylation at Ser473 was normal in both Δ*PDZ-Prx* and *Prx* KO nerves. It remains to be determined whether levels of AKT phosphorylated at Thr308 are altered.

Unexpectedly, phosphorylated S6 ribosomal protein, a substrate of mTOR's downstream target p70S6K1 was upregulated in Δ*PDZ-Prx* and *Prx* KO nerves at 3 weeks old, with a more substantial increase in nerves from *Prx* KO mice. Since mTOR, the key regulator of p70S6K1, was not affected in the Periaxin mutants, the upregulation of activated S6 ribosomal protein may be mediated directly by PDK-1, and independently of the PI3K/AKT signaling. PDK1 regulates several other enzymes such as p70S6K1, PKC kinases and SGK that are involved in cancer growth, proliferation and survival (Bayascas, 2008; Iwanami et al., 2009; Mora et al., 2004). The elevated levels of activated S6 ribosomal protein in Δ*PDZ-Prx* and *Prx* KO nerves may reflect an increase in proliferation, perhaps of unmyelinating and myelinating Schwann cells. It would be necessary to perform immunofluorescence analysis of these signaling molecules in Schwann cells to confirm the observations from Western blotting. Further investigation of these important signaling pathways is needed to define the mechanisms for regulation of internodal growth, cell proliferation and myelination in the Periaxin mutants.

4.2.7 A possible dimerization mechanism for the Periaxin PDZ domain

Deletion of 116 amino acids (less than 10% of the protein) at the N-terminal PDZ domain of Periaxin may cause changes in the structure of the protein as well as removing the PDZ domain. Without the PDZ domain, Periaxin does not dimerize *in vitro*. In Δ*PDZ-Prx* nerves, it would be difficult to rule out the possibility of protein misfolding leading to the loss of Schwann cell compartments. I have demonstrated by biochemical methods that introducing minimal changes in the structure of Periaxin protein using single amino acid substitutions in the PDZ domain is sufficient to abrogate Periaxin dimerization. Two amino acids in the Periaxin PDZ domain were identified to play essential roles in maintaining the dimeric structure of Periaxin. This supported the view that even subtle changes to the PDZ domain could undermine its function.

Formation of a dimeric conformation requires the β1 strand of Periaxin's PDZ domain. Specific disruption of the β1 strand affects Periaxin dimerization. Self-association of the Periaxin PDZ domain is partly dependent on hydrogen bonding contributed by polar residues in the β1 strand, since substitution of polar threonine 23 by an alanine in the same strand results in attenuation of PDZ-PDZ binding. It remains to be determined whether the PDZ domain dimerizes via anti-parallel β1-β1 strand interactions as described in GRIP PDZ6 and Shank1 PDZ (Im et al., 2003a; Im et al., 2003b), or through β1 strand interaction with other secondary elements of the PDZ domain. In order to identify the structural basis for PDZ-domain mediated dimerization in Periaxin, it would be necessary to determine the crystal structure of the PDZ dimer.

The highly conserved aspartate 63 in β4 strand is also required for establishment of the dimeric structure of Periaxin. The mechanism by which this residue contributes to PDZ-PDZ dimerization in Periaxin is not known. One possibility is that aspartate 63 forms a salt bridge with another residue in the main body of the PDZ domain for stabilization of the Periaxin PDZ dimeric configuration, similar to that formed in nNOS PDZ of the nNOS/syntrophin and nNOS/PSD-95 heterodimers (Hillier et al., 1999; Tochio et al., 2000). To confirm the function of the PDZ domain *in vivo*, it would be necessary to generate a Periaxin mutant mouse that carries a single amino acid change, such as D63A in the PDZ domain.

4.3 CONCLUSIONS

The function of homodimerization of PDZ domain proteins has not been well defined. Homodimerization of GRIP PDZ 6 has been suggested to facilitate the PDZ domains to simultaneously interact with multiple ligands to form a network (Im et al., 2003b). In this thesis, I have studied the role of the Periaxin N-terminal PDZ domain and its dimerization in myelinating Schwann cells of the PNS.

By characterizing a conditional mouse mutant expressing a version of Periaxin lacking the N-terminal PDZ domain in peripheral nerves, I have shown that homodimerization of the Periaxin PDZ domain is required for maintaining cytoplasmic compartments, namely Cajal bands and appositions. The PDZ domain of Periaxin is also required for Schwann cell elongation and establishment of extensive myelinated segments around the axon, which in turn regulates the speed of action potential propagation. In mature peripheral nerves, myelin production is dysregulated in the absence of the Periaxin PDZ domain in Schwann cells, indicating its importance in myelin sheath maintenance. Disrupting Periaxin homodimerization in Schwann cells after myelination is accomplished and Schwann cell compartments established also destabilizes the complex Periaxin associates with, and causes myelin abnormalities. This work suggests that the regulation of Schwann cell elongation and myelin stability may be through independent mechanisms.

Finally, I have shown by biochemical means that introducing subtle changes in the Periaxin PDZ domain structure could attenuate its dimerization capacity. I have also suggested a possible mechanism for the homodimerization of the Periaxin PDZ domain.

Collectively, these findings highlight the crucial role of the protein interacting PDZ domain of Periaxin in regulating Schwann cell function. Future studies in identifying other interacting partners of the Periaxin PDZ domain, perhaps elsewhere than at appositions, will facilitate understanding of the underlying mechanisms by which Periaxin control Schwann cell longitudinal growth and myelin stability.

4.4 FUTURE WORK

Specific deletion of the N-terminal PDZ domain of Periaxin in Schwann cells phenocopies the defects in Schwann cell compartmentalization as well as longitudinal growth described in complete Periaxin-null mutants (Court et al., 2004). In the absence of the Periaxin PDZ domain, the myelin sheath becomes unstable and mutant mice develop a peripheral neuropathy characterized by abnormal myelin folding and redundant myelin loops. Nevertheless, the myelin abnormalities in Δ*PDZ-Prx* mice are less severe than the demyelinating phenotype in *Prx* KO mice. How does Periaxin regulate Schwann cell elongation and myelin stability? Indeed, this work has revealed the requirement of Periaxin's PDZ domain dimerization for these functions. As mentioned, it would be essential to identify other protein binding partners of the Periaxin PDZ domain. Perhaps one possible way is to search for binding partners of the dimeric PDZ domain of Periaxin in a yeast two-hybrid screen.

Determining the downstream signaling cascades of Periaxin would also facilitate the understanding of the mechanisms of internodal length regulation and control of myelin production. For this, I examined various signaling pathways that have been implicated in regulating cell growth and myelin production. Further investigation into the role of Dlg1 in myelin membrane homeostasis in the Periaxin mutants will be required. In addition, detailed examination of the AKT/mTOR pathway, as well as downstream targets such as S6 kinase, in cell growth control in the Periaxin mutants would be necessary. Furthermore, it would be important to understand how the normal Periaxin-DRP2 complex may interact with extracellular ligands in the basal lamina in maintaining Schwann cell-axon integrity.

Besides the PDZ domain, other domains of Periaxin such as the basic domain that binds DRP2, and the C-terminal acidic domain may play distinct roles in the regulatory function of Periaxin, such as control of myelin stability and targeting of DRP2. Studying Periaxin mutants lacking these individual domains would help to understand Periaxin's function in myelinating Schwann cells.

Finally, since minimal disruption of the PDZ domain structure has been proven to effectively abrogate PDZ-PDZ dimerization of Periaxin, it would be interesting to generate and analyze a mouse mutant containing a full-length Periaxin with a mutated PDZ domain in order to confirm the current findings in the role of Periaxin's PDZ domain. One possible single amino acid mutation would be substituting aspartate 63 with an alanine.

5- REFERENCES

Adams, M.E., K.N. Anderson, and S.C. Froehner. 2010. The alpha-syntrophin PH and PDZ domains scaffold acetylcholine receptors, utrophin, and neuronal nitric oxide synthase at the neuromuscular junction. *J Neurosci*. 30:11004-11010.

Adams, M.E., H.A. Mueller, and S.C. Froehner. 2001. In vivo requirement of the alpha-syntrophin PDZ domain for the sarcolemmal localization of nNOS and aquaporin-4. *The Journal of cell biology*. 155:113-122.

Adlkofer, K., R. Frei, D.H. Neuberg, J. Zielasek, K.V. Toyka, and U. Suter. 1997. Heterozygous peripheral myelin protein 22-deficient mice are affected by a progressive demyelinating tomaculous neuropathy. *J Neurosci*. 17:4662-4671.

Ahn, A.H., and L.M. Kunkel. 1993. The structural and functional diversity of dystrophin. *Nat Genet*. 3:283-291.

Albrecht, D.E., D.L. Sherman, P.J. Brophy, and S.C. Froehner. 2008. The ABCA1 cholesterol transporter associates with one of two distinct dystrophin-based scaffolds in Schwann cells. *Glia*. 56:611-618.

Amici, S.A., W.A. Dunn, Jr., A.J. Murphy, N.C. Adams, N.W. Gale, D.M. Valenzuela, G.D. Yancopoulos, and L. Notterpek. 2006. Peripheral myelin protein 22 is in complex with alpha6beta4 integrin, and its absence alters the Schwann cell basal lamina. *J Neurosci*. 26:1179-1189.

Amici, S.A., W.A. Dunn, Jr., and L. Notterpek. 2007. Developmental abnormalities in the nerves of peripheral myelin protein 22-deficient mice. *J Neurosci Res*. 85:238-249.

Anitei, M., M. Ifrim, M.A. Ewart, A.E. Cowan, J.H. Carson, R. Bansal, and S.E. Pfeiffer. 2006. A role for Sec8 in oligodendrocyte morphological differentiation. *J Cell Sci*. 119:807-818.

Anzini, P., D.H. Neuberg, M. Schachner, E. Nelles, K. Willecke, J. Zielasek, K.V. Toyka, U. Suter, and R. Martini. 1997. Structural abnormalities and deficient maintenance of peripheral nerve myelin in mice lacking the gap junction protein connexin 32. *J Neurosci*. 17:4545-4551.

Arnold, K., L. Bordoli, J. Kopp, and T. Schwede. 2006. The SWISS-MODEL workspace: a web-based environment for protein structure homology modelling. *Bioinformatics*. 22:195-201.

Arthur-Farraj, P., K. Wanek, J. Hantke, C.M. Davis, A. Jayakar, D.B. Parkinson, R. Mirsky, and K.R. Jessen. 2011. Mouse schwann cells need both NRG1 and cyclic AMP to myelinate. *Glia*. 59:720-733.

Atanasoski, S., S.S. Scherer, E. Sirkowski, D. Leone, A.N. Garratt, C. Birchmeier, and U. Suter. 2006. ErbB2 signaling in Schwann cells is mostly dispensable for maintenance of myelinated peripheral nerves and proliferation of adult Schwann cells after injury. *J Neurosci*. 26:2124-2131.

Barankova, L., D. Siskova, K. Huhne, E. Vyhnalkova, I. Sakmaryova, M. Bojar, B. Rautenstrauss, and P. Seeman. 2008. A 71-nucleotide deletion in the periaxin

gene in a Romani patient with early-onset slowly progressive demyelinating CMT. *Eur J Neurol*. 15:548-551.

Bayascas, J.R. 2008. Dissecting the role of the 3-phosphoinositide-dependent protein kinase-1 (PDK1) signalling pathways. *Cell Cycle*. 7:2978-2982.

Beirowski, B., J. Gustin, S.M. Armour, H. Yamamoto, A. Viader, B.J. North, S. Michan, R.H. Baloh, J.P. Golden, R.E. Schmidt, D.A. Sinclair, J. Auwerx, and J. Milbrandt. 2011. Sir-two-homolog 2 (Sirt2) modulates peripheral myelination through polarity protein Par-3/atypical protein kinase C (aPKC) signaling. *Proc Natl Acad Sci U S A*. 108:E952-961.

Benninger, Y., T. Thurnherr, J.A. Pereira, S. Krause, X. Wu, A. Chrostek-Grashoff, D. Herzog, K.A. Nave, R.J. Franklin, D. Meijer, C. Brakebusch, U. Suter, and J.B. Relvas. 2007. Essential and distinct roles for cdc42 and rac1 in the regulation of Schwann cell biology during peripheral nervous system development. *The Journal of cell biology*. 177:1051-1061.

Berger, P., A. Niemann, and U. Suter. 2006. Schwann cells and the pathogenesis of inherited motor and sensory neuropathies (Charcot-Marie-Tooth disease). *Glia*. 54:243-257.

Bermingham, J.R., Jr., S.S. Scherer, S. O'Connell, E. Arroyo, K.A. Kalla, F.L. Powell, and M.G. Rosenfeld. 1996. Tst-1/Oct-6/SCIP regulates a unique step in peripheral myelination and is required for normal respiration. *Genes Dev*. 10:1751-1762.

Bermingham, J.R., Jr., H. Shearin, J. Pennington, J. O'Moore, M. Jaegle, S. Driegen, A. van Zon, A. Darbas, E. Ozkaynak, E.J. Ryu, J. Milbrandt, and D. Meijer. 2006. The claw paw mutation reveals a role for Lgi4 in peripheral nerve development. *Nat Neurosci*. 9:76-84.

Berti, C., L. Bartesaghi, M. Ghidinelli, D. Zambroni, G. Figlia, Z.L. Chen, A. Quattrini, L. Wrabetz, and M.L. Feltri. 2011. Non-redundant function of dystroglycan and beta1 integrins in radial sorting of axons. *Development*. 138:4025-4037.

Berti, C., A. Nodari, L. Wrabetz, and M.L. Feltri. 2006. Role of integrins in peripheral nerves and hereditary neuropathies. *Neuromolecular Med*. 8:191-204.

Bilder, D., M. Li, and N. Perrimon. 2000. Cooperative regulation of cell polarity and growth by Drosophila tumor suppressors. *Science*. 289:113-116.

Birchmeier, C., and K.A. Nave. 2008. Neuregulin-1, a key axonal signal that drives Schwann cell growth and differentiation. *Glia*. 56:1491-1497.

Blanchard, A.D., A. Sinanan, E. Parmantier, R. Zwart, L. Broos, D. Meijer, C. Meier, K.R. Jessen, and R. Mirsky. 1996. Oct-6 (SCIP/Tst-1) is expressed in Schwann cell precursors, embryonic Schwann cells, and postnatal myelinating Schwann cells: comparison with Oct-1, Krox-20, and Pax-3. *J Neurosci Res*. 46:630-640.

Blobel, C.P. 2005. ADAMs: key components in EGFR signalling and development. *Nat Rev Mol Cell Biol*. 6:32-43.

Boerkoel, C.F., H. Takashima, P. Stankiewicz, C.A. Garcia, S.M. Leber, L. Rhee-Morris, and J.R. Lupski. 2001. Periaxin mutations cause recessive Dejerine-Sottas neuropathy. *Am J Hum Genet*. 68:325-333.

Bolino, A., A. Bolis, S.C. Previtali, G. Dina, S. Bussini, G. Dati, S. Amadio, U. Del Carro, D.D. Mruk, M.L. Feltri, C.Y. Cheng, A. Quattrini, and L. Wrabetz. 2004.

Disruption of Mtmr2 produces CMT4B1-like neuropathy with myelin outfolding and impaired spermatogenesis. *The Journal of cell biology*. 167:711-721.

Bolis, A., S. Coviello, S. Bussini, G. Dina, C. Pardini, S.C. Previtali, M. Malaguti, P. Morana, U. Del Carro, M.L. Feltri, A. Quattrini, L. Wrabetz, and A. Bolino. 2005. Loss of Mtmr2 phosphatase in Schwann cells but not in motor neurons causes Charcot-Marie-Tooth type 4B1 neuropathy with myelin outfoldings. *J Neurosci*. 25:8567-8577.

Bolis, A., S. Coviello, I. Visigalli, C. Taveggia, A. Bachi, A.H. Chishti, T. Hanada, A. Quattrini, S.C. Previtali, A. Biffi, and A. Bolino. 2009. Dlg1, Sec8, and Mtmr2 regulate membrane homeostasis in Schwann cell myelination. *J Neurosci*. 29:8858-8870.

Bonneick, S., M. Boentert, P. Berger, S. Atanasoski, N. Mantei, C. Wessig, K.V. Toyka, P. Young, and U. Suter. 2005. An animal model for Charcot-Marie-Tooth disease type 4B1. *Hum Mol Genet*. 14:3685-3695.

Bonuccelli, G., F. Sotgia, W. Schubert, D.S. Park, P.G. Frank, S.E. Woodman, L. Insabato, M. Cammer, C. Minetti, and M.P. Lisanti. 2003. Proteasome inhibitor (MG-132) treatment of mdx mice rescues the expression and membrane localization of dystrophin and dystrophin-associated proteins. *Am J Pathol*. 163:1663-1675.

Boyd, I.A., Davey M. R. 1968. Composition of Peripheral Nerves. E & S Livingstone Ltd, Edinburgh and London.

Bradley, W.G., and M. Jenkison. 1973. Abnormalities of peripheral nerves in murine muscular dystrophy. *J Neurol Sci*. 18:227-247.

Bremer, M., F. Frob, T. Kichko, P. Reeh, E.R. Tamm, U. Suter, and M. Wegner. 2011. Sox10 is required for Schwann-cell homeostasis and myelin maintenance in the adult peripheral nerve. *Glia*. 59:1022-1032.

Brennan, A., C.H. Dean, A.L. Zhang, D.T. Cass, R. Mirsky, and K.R. Jessen. 2000. Endothelins control the timing of Schwann cell generation in vitro and in vivo. *Dev Biol*. 227:545-557.

Brill, M.H., S.G. Waxman, J.W. Moore, and R.W. Joyner. 1977. Conduction velocity and spike configuration in myelinated fibres: computed dependence on internode distance. *J Neurol Neurosurg Psychiatry*. 40:769-774.

Britsch, S., D.E. Goerich, D. Riethmacher, R.I. Peirano, M. Rossner, K.A. Nave, C. Birchmeier, and M. Wegner. 2001. The transcription factor Sox10 is a key regulator of peripheral glial development. *Genes Dev*. 15:66-78.

Bunge, R.P. 1993. Expanding roles for the Schwann cell: ensheathment, myelination, trophism and regeneration. *Curr Opin Neurobiol*. 3:805-809.

Bunge, R.P., and M.B. Bunge. 1983. Interrelationship between Schwann cell function and extracellular matrix production. *Trends in Neurosciences*. 6:499-505.

Bunge, R.P., M.B. Bunge, and C.F. Eldridge. 1986. Linkage between axonal ensheathment and basal lamina production by Schwann cells. *Annu Rev Neurosci*. 9:305-328.

Calleja, V., M. Laguerre, P.J. Parker, and B. Larijani. 2009. Role of a novel PH-kinase domain interface in PKB/Akt regulation: structural mechanism for allosteric inhibition. *PLoS Biol*. 7:e17.

Chan, J.R., C. Jolicoeur, J. Yamauchi, J. Elliott, J.P. Fawcett, B.K. Ng, and M. Cayouette. 2006. The polarity protein Par-3 directly interacts with p75NTR to regulate myelination. *Science*. 314:832-836.

Chang, C.C., and S.J. Gould. 1998. Phenotype-genotype relationships in complementation group 3 of the peroxisome-biogenesis disorders. *Am J Hum Genet*. 63:1294-1306.

Chaplan, S.R., F.W. Bach, J.W. Pogrel, J.M. Chung, and T.L. Yaksh. 1994. Quantitative assessment of tactile allodynia in the rat paw. *J Neurosci Methods*. 53:55-63.

Chen, J., L. Pan, Z. Wei, Y. Zhao, and M. Zhang. 2008. Domain-swapped dimerization of ZO-1 PDZ2 generates specific and regulatory connexin43-binding sites. *Embo J*. 27:2113-2123.

Chen, S., M.O. Velardez, X. Warot, Z.X. Yu, S.J. Miller, D. Cros, and G. Corfas. 2006. Neuregulin 1-erbB signaling is necessary for normal myelination and sensory function. *J Neurosci*. 26:3079-3086.

Chen, Y., H. Wang, S.O. Yoon, X. Xu, M.O. Hottiger, J. Svaren, K.A. Nave, H.A. Kim, E.N. Olson, and Q.R. Lu. 2011. HDAC-mediated deacetylation of NF-kappaB is critical for Schwann cell myelination. *Nat Neurosci*. 14:437-441.

Chen, Z.L., and S. Strickland. 2003. Laminin gamma1 is critical for Schwann cell differentiation, axon myelination, and regeneration in the peripheral nerve. *The Journal of cell biology*. 163:889-899.

Chernousov, M.A., W.M. Yu, Z.L. Chen, D.J. Carey, and S. Strickland. 2008. Regulation of Schwann cell function by the extracellular matrix. *Glia*. 56:1498-1507.

Chomczynski, P., and N. Sacchi. 1987. Single-step method of RNA isolation by acid guanidinium thiocyanate-phenol-chloroform extraction. *Analytical biochemistry*. 162:156-159.

Chomczynski, P., and N. Sacchi. 2006. The single-step method of RNA isolation by acid guanidinium thiocyanate-phenol-chloroform extraction: twenty-something years on. *Nat Protoc*. 1:581-585.

Clark, M.B., and M.B. Bunge. 1989. Cultured Schwann cells assemble normal-appearing basal lamina only when they ensheathe axons. *Dev Biol*. 133:393-404.

Cooper, T.A., and W. Mattox. 1997. The regulation of splice-site selection, and its role in human disease. *Am J Hum Genet*. 61:259-266.

Cotter, L., M. Ozcelik, C. Jacob, J.A. Pereira, V. Locher, R. Baumann, J.B. Relvas, U. Suter, and N. Tricaud. 2010. Dlg1-PTEN interaction regulates myelin thickness to prevent damaging peripheral nerve overmyelination. *Science*. 328:1415-1418.

Court, F.A., P.J. Brophy, and R.R. Ribchester. 2008. Remodeling of motor nerve terminals in demyelinating axons of periaxin-null mice. *Glia*. 56:471-479.

Court, F.A., J.E. Hewitt, K. Davies, B.L. Patton, A. Uncini, L. Wrabetz, and M.L. Feltri. 2009. A laminin-2, dystroglycan, utrophin axis is required for compartmentalization and elongation of myelin segments. *J Neurosci*. 29:3908-3919.

Court, F.A., D.L. Sherman, T. Pratt, E.M. Garry, R.R. Ribchester, D.F. Cottrell, S.M. Fleetwood-Walker, and P.J. Brophy. 2004. Restricted growth of Schwann cells

lacking Cajal bands slows conduction in myelinated nerves. *Nature*. 431:191-195.

Court, F.A., D. Zambroni, E. Pavoni, C. Colombelli, C. Baragli, G. Figlia, L. Sorokin, W. Ching, J.L. Salzer, L. Wrabetz, and M.L. Feltri. 2011. MMP2-9 Cleavage of Dystroglycan Alters the Size and Molecular Composition of Schwann Cell Domains. *J Neurosci*. 31:12208-12217.

D'Antonio, M., A. Droggiti, M.L. Feltri, J. Roes, L. Wrabetz, R. Mirsky, and K.R. Jessen. 2006. TGFbeta type II receptor signaling controls Schwann cell death and proliferation in developing nerves. *J Neurosci*. 26:8417-8427.

D'Souza, B., A. Miyamoto, and G. Weinmaster. 2008. The many facets of Notch ligands. *Oncogene*. 27:5148-5167.

D'Souza, I., P. Poorkaj, M. Hong, D. Nochlin, V.M. Lee, T.D. Bird, and G.D. Schellenberg. 1999. Missense and silent tau gene mutations cause frontotemporal dementia with parkinsonism-chromosome 17 type, by affecting multiple alternative RNA splicing regulatory elements. *Proc Natl Acad Sci U S A*. 96:5598-5603.

de Morree, A., M. Droog, L. Grand Moursel, I.J. Bisschop, A. Impagliazzo, R.R. Frants, R. Klooster, and S.M. van der Maarel. 2011. Self-regulated alternative splicing at the AHNAK locus. *Faseb J*.

Decker, L., C. Desmarquet-Trin-Dinh, E. Taillebourg, J. Ghislain, J.M. Vallat, and P. Charnay. 2006. Peripheral myelin maintenance is a dynamic process requiring constant Krox20 expression. *J Neurosci*. 26:9771-9779.

Delague, V., C. Bareil, S. Tuffery, P. Bouvagnet, E. Chouery, S. Koussa, T. Maisonobe, J. Loiselet, A. Megarbane, and M. Claustres. 2000. Mapping of a new locus for autosomal recessive demyelinating Charcot-Marie-Tooth disease to 19q13.1-13.3 in a large consanguineous Lebanese family: exclusion of MAG as a candidate gene. *Am J Hum Genet*. 67:236-243.

Di Muzio, A., M.V. De Angelis, P. Di Fulvio, A. Ratti, A. Pizzuti, L. Stuppia, D. Gambi, and A. Uncini. 2003. Dysmyelinating sensory-motor neuropathy in merosin-deficient congenital muscular dystrophy. *Muscle Nerve*. 27:500-506.

Donaghy, M. 2003. Enlarged Peripheral Nerves. *Practical Neurology*:40-45.

Dong, Z., A. Brennan, N. Liu, Y. Yarden, G. Lefkowitz, R. Mirsky, and K.R. Jessen. 1995. Neu differentiation factor is a neuron-glia signal and regulates survival, proliferation, and maturation of rat Schwann cell precursors. *Neuron*. 15:585-596.

Dong, Z., A. Sinanan, D. Parkinson, E. Parmantier, R. Mirsky, and K.R. Jessen. 1999. Schwann cell development in embryonic mouse nerves. *J Neurosci Res*. 56:334-348.

Drubin, D.G., and W.J. Nelson. 1996. Origins of cell polarity. *Cell*. 84:335-344.

Dyck, P.J., and E.H. Lambert. 1968. Lower motor and primary sensory neuron diseases with peroneal muscular atrophy. I. Neurologic, genetic, and electrophysiologic findings in hereditary polyneuropathies. *Arch Neurol*. 18:603-618.

Dytrych, L., D.L. Sherman, C.S. Gillespie, and P.J. Brophy. 1998. Two PDZ domain proteins encoded by the murine periaxin gene are the result of alternative intron

retention and are differentially targeted in Schwann cells. *J Biol Chem*. 273:5794-5800.

Ervasti, J.M., and K.P. Campbell. 1993. A role for the dystrophin-glycoprotein complex as a transmembrane linker between laminin and actin. *The Journal of cell biology*. 122:809-823.

Fanning, A.S., M.F. Lye, J.M. Anderson, and A. Lavie. 2007. Domain swapping within PDZ2 is responsible for dimerization of ZO proteins. *J Biol Chem*. 282:37710-37716.

Feltri, M.L., D. Graus Porta, S.C. Previtali, A. Nodari, B. Migliavacca, A. Cassetti, A. Littlewood-Evans, L.F. Reichardt, A. Messing, A. Quattrini, U. Mueller, and L. Wrabetz. 2002. Conditional disruption of beta 1 integrin in Schwann cells impedes interactions with axons. *The Journal of cell biology*. 156:199-209.

Feltri, M.L., S.S. Scherer, R. Nemni, J. Kamholz, H. Vogelbacker, M.O. Scott, N. Canal, V. Quaranta, and L. Wrabetz. 1994. Beta 4 integrin expression in myelinating Schwann cells is polarized, developmentally regulated and axonally dependent. *Development*. 120:1287-1301.

Feltri, M.L., and L. Wrabetz. 2005. Laminins and their receptors in Schwann cells and hereditary neuropathies. *J Peripher Nerv Syst*. 10:128-143.

Finzsch, M., S. Schreiner, T. Kichko, P. Reeh, E.R. Tamm, M.R. Bosl, D. Meijer, and M. Wegner. 2010. Sox10 is required for Schwann cell identity and progression beyond the immature Schwann cell stage. *The Journal of cell biology*. 189:701-712.

Fischer, S., A. Weishaupt, J. Troppmair, and R. Martini. 2008. Increase of MCP-1 (CCL2) in myelin mutant Schwann cells is mediated by MEK-ERK signaling pathway. *Glia*. 56:836-843.

Flores, A.I., S.P. Narayanan, E.N. Morse, H.E. Shick, X. Yin, G. Kidd, R.L. Avila, D.A. Kirschner, and W.B. Macklin. 2008. Constitutively active Akt induces enhanced myelination in the CNS. *J Neurosci*. 28:7174-7183.

Freese, C., A.N. Garratt, F. Fahrenholz, and K. Endres. 2009. The effects of alpha-secretase ADAM10 on the proteolysis of neuregulin-1. *Febs J*. 276:1568-1580.

Fricker, F.R., N. Lago, S. Balarajah, C. Tsantoulas, S. Tanna, N. Zhu, S.K. Fageiry, M. Jenkins, A.N. Garratt, C. Birchmeier, and D.L. Bennett. 2011. Axonally derived neuregulin-1 is required for remyelination and regeneration after nerve injury in adulthood. *J Neurosci*. 31:3225-3233.

Garbay, B., A.M. Heape, F. Sargueil, and C. Cassagne. 2000. Myelin synthesis in the peripheral nervous system. *Prog Neurobiol*. 61:267-304.

Gardner, L.A., A.P. Naren, and S.W. Bahouth. 2007. Assembly of an SAP97-AKAP79-cAMP-dependent protein kinase scaffold at the type 1 PSD-95/DLG/ZO1 motif of the human beta(1)-adrenergic receptor generates a receptosome involved in receptor recycling and networking. *J Biol Chem*. 282:5085-5099.

Garratt, A.N., S. Britsch, and C. Birchmeier. 2000a. Neuregulin, a factor with many functions in the life of a schwann cell. *Bioessays*. 22:987-996.

Garratt, A.N., O. Voiculescu, P. Topilko, P. Charnay, and C. Birchmeier. 2000b. A dual role of erbB2 in myelination and in expansion of the schwann cell precursor pool. *The Journal of cell biology*. 148:1035-1046.

Gazzerro, E., S. Assereto, A. Bonetto, F. Sotgia, S. Scarfi, A. Pistorio, G. Bonuccelli, M. Cilli, C. Bruno, F. Zara, M.P. Lisanti, and C. Minetti. 2010. Therapeutic potential of proteasome inhibition in Duchenne and Becker muscular dystrophies. *Am J Pathol*. 176:1863-1877.

Gee, S.H., R.W. Blacher, P.J. Douville, P.R. Provost, P.D. Yurchenco, and S. Carbonetto. 1993. Laminin-binding protein 120 from brain is closely related to the dystrophin-associated glycoprotein, dystroglycan, and binds with high affinity to the major heparin binding domain of laminin. *J Biol Chem*. 268:14972-14980.

Ghabriel, M.N., and G. Allt. 1981. Incisures of Schmidt-Lanterman. *Prog Neurobiol*. 17:25-58.

Gillespie, C.S., M. Lee, J.F. Fantes, and P.J. Brophy. 1997. The gene encoding the Schwann cell protein periaxin localizes on mouse chromosome 7 (Prx). *Genomics*. 41:297-298.

Gillespie, C.S., D.L. Sherman, G.E. Blair, and P.J. Brophy. 1994. Periaxin, a novel protein of myelinating Schwann cells with a possible role in axonal ensheathment. *Neuron*. 12:497-508.

Gillespie, C.S., D.L. Sherman, S.M. Fleetwood-Walker, D.F. Cottrell, S. Tait, E.M. Garry, V.C. Wallace, J. Ure, I.R. Griffiths, A. Smith, and P.J. Brophy. 2000. Peripheral demyelination and neuropathic pain behavior in periaxin-deficient mice. *Neuron*. 26:523-531.

Goebbels, S., J.H. Oltrogge, R. Kemper, I. Heilmann, I. Bormuth, S. Wolfer, S.P. Wichert, W. Mobius, X. Liu, C. Lappe-Siefke, M.J. Rossner, M. Groszer, U. Suter, J. Frahm, S. Boretius, and K.A. Nave. 2010. Elevated phosphatidylinositol 3,4,5-trisphosphate in glia triggers cell-autonomous membrane wrapping and myelination. *J Neurosci*. 30:8953-8964.

Gorczyca, D., J. Ashley, S. Speese, N. Gherbesi, U. Thomas, E. Gundelfinger, L.S. Gramates, and V. Budnik. 2007. Postsynaptic membrane addition depends on the Discs-Large-interacting t-SNARE Gtaxin. *J Neurosci*. 27:1033-1044.

Gould, R.M., A.L. Byrd, and E. Barbarese. 1995. The number of Schmidt-Lanterman incisures is more than doubled in shiverer PNS myelin sheaths. *J Neurocytol*. 24:85-98.

Griffin, J.W., N. Drucker, B.G. Gold, J. Rosenfeld, M. Benzaquen, L.R. Charnas, K.E. Fahnestock, and E.A. Stocks. 1987. Schwann cell proliferation and migration during paranodal demyelination. *J Neurosci*. 7:682-699.

Griffin, J.W., E.A. Stocks, K. Fahnestock, A. Van Praagh, and B.D. Trapp. 1990. Schwann cell proliferation following lysolecithin-induced demyelination. *J Neurocytol*. 19:367-384.

Griffin, J.W., and W.J. Thompson. 2008. Biology and pathology of nonmyelinating Schwann cells. *Glia*. 56:1518-1531.

Groh, J., K. Heinl, B. Kohl, C. Wessig, J. Greeske, S. Fischer, and R. Martini. 2010. Attenuation of MCP-1/CCL2 expression ameliorates neuropathy in a mouse model for Charcot-Marie-Tooth 1X. *Hum Mol Genet*. 19:3530-3543.

Grossmann, K.S., H. Wende, F.E. Paul, C. Cheret, A.N. Garratt, S. Zurborg, K. Feinberg, D. Besser, H. Schulz, E. Peles, M. Selbach, W. Birchmeier, and C.

Birchmeier. 2009. The tyrosine phosphatase Shp2 (PTPN11) directs Neuregulin-1/ErbB signaling throughout Schwann cell development. *Proc Natl Acad Sci U S A*. 106:16704-16709.

Grove, M., N.H. Komiyama, K.A. Nave, S.G. Grant, D.L. Sherman, and P.J. Brophy. 2007. FAK is required for axonal sorting by Schwann cells. *The Journal of cell biology*. 176:277-282.

Guertin, D.A., and D.M. Sabatini. 2009. The pharmacology of mTOR inhibition. *Sci Signal*. 2:pe24.

Guex, N., and M.C. Peitsch. 1997. SWISS-MODEL and the Swiss-PdbViewer: an environment for comparative protein modeling. *Electrophoresis*. 18:2714-2723.

Guilbot, A., A. Williams, N. Ravise, C. Verny, A. Brice, D.L. Sherman, P.J. Brophy, E. LeGuern, V. Delague, C. Bareil, A. Megarbane, and M. Claustres. 2001. A mutation in periaxin is responsible for CMT4F, an autosomal recessive form of Charcot-Marie-Tooth disease. *Hum Mol Genet*. 10:415-421.

Hall, S.M., and N.A. Gregson. 1974. The effects of mitomycin C on remyelination in the peripheral nervous system. *Nature*. 252:303-305.

Hargreaves, K., R. Dubner, F. Brown, C. Flores, and J. Joris. 1988. A new and sensitive method for measuring thermal nociception in cutaneous hyperalgesia. *Pain*. 32:77-88.

Harhay, G.P., T.S. Sonstegard, J.W. Keele, M.P. Heaton, M.L. Clawson, W.M. Snelling, R.T. Wiedmann, C.P. Van Tassell, and T.P. Smith. 2005. Characterization of 954 bovine full-CDS cDNA sequences. *BMC genomics*. 6:166.

Harrisingh, M.C., E. Perez-Nadales, D.B. Parkinson, D.S. Malcolm, A.W. Mudge, and A.C. Lloyd. 2004. The Ras/Raf/ERK signalling pathway drives Schwann cell dedifferentiation. *Embo J*. 23:3061-3071.

Hartline, D.K., and D.R. Colman. 2007. Rapid conduction and the evolution of giant axons and myelinated fibers. *Curr Biol*. 17:R29-35.

He, Y., J.Y. Kim, J. Dupree, A. Tewari, C. Melendez-Vasquez, J. Svaren, and P. Casaccia. 2010. Yy1 as a molecular link between neuregulin and transcriptional modulation of peripheral myelination. *Nat Neurosci*. 13:1472-1480.

Hillier, B.J., K.S. Christopherson, K.E. Prehoda, D.S. Bredt, and W.A. Lim. 1999. Unexpected modes of PDZ domain scaffolding revealed by structure of nNOS-syntrophin complex. *Science*. 284:812-815.

Hoke, A., T. Ho, T.O. Crawford, C. LeBel, D. Hilt, and J.W. Griffin. 2003. Glial cell line-derived neurotrophic factor alters axon schwann cell units and promotes myelination in unmyelinated nerve fibers. *J Neurosci*. 23:561-567.

Hu, X., W. He, C. Diaconu, X. Tang, G.J. Kidd, W.B. Macklin, B.D. Trapp, and R. Yan. 2008. Genetic deletion of BACE1 in mice affects remyelination of sciatic nerves. *Faseb J*. 22:2970-2980.

Hursh, J.B. 1939. Conduction velocity and diameter of nerve fibers. *Am J Physiol*. 127:131-139.

Im, Y.J., J.H. Lee, S.H. Park, S.J. Park, S.H. Rho, G.B. Kang, E. Kim, and S.H. Eom. 2003a. Crystal structure of the Shank PDZ-ligand complex reveals a class I PDZ interaction and a novel PDZ-PDZ dimerization. *J Biol Chem*. 278:48099-48104.

Im, Y.J., S.H. Park, S.H. Rho, J.H. Lee, G.B. Kang, M. Sheng, E. Kim, and S.H. Eom. 2003b. Crystal structure of GRIP1 PDZ6-peptide complex reveals the structural basis for class II PDZ target recognition and PDZ domain-mediated multimerization. *J Biol Chem*. 278:8501-8507.

Imamura, M., K. Araishi, S. Noguchi, and E. Ozawa. 2000. A sarcoglycan-dystroglycan complex anchors Dp116 and utrophin in the peripheral nervous system. *Hum Mol Genet*. 9:3091-3100.

Inacio, A., A.L. Silva, J. Pinto, X. Ji, A. Morgado, F. Almeida, P. Faustino, J. Lavinha, S.A. Liebhaber, and L. Romao. 2004. Nonsense mutations in close proximity to the initiation codon fail to trigger full nonsense-mediated mRNA decay. *J Biol Chem*. 279:32170-32180.

Inoue, K., M. Khajavi, T. Ohyama, S. Hirabayashi, J. Wilson, J.D. Reggin, P. Mancias, I.J. Butler, M.F. Wilkinson, M. Wegner, and J.R. Lupski. 2004. Molecular mechanism for distinct neurological phenotypes conveyed by allelic truncating mutations. *Nat Genet*. 36:361-369.

Iwanami, A., T.F. Cloughesy, and P.S. Mischel. 2009. Striking the balance between PTEN and PDK1: it all depends on the cell context. *Genes Dev*. 23:1699-1704.

Jacob, C., C.N. Christen, J.A. Pereira, C. Somandin, A. Baggiolini, P. Lotscher, M. Ozcelik, N. Tricaud, D. Meijer, T. Yamaguchi, P. Matthias, and U. Suter. 2011. HDAC1 and HDAC2 control the transcriptional program of myelination and the survival of Schwann cells. *Nat Neurosci*. 14:429-436.

Jaegle, M., M. Ghazvini, W. Mandemakers, M. Piirsoo, S. Driegen, F. Levavasseur, S. Raghoenath, F. Grosveld, and D. Meijer. 2003. The POU proteins Brn-2 and Oct-6 share important functions in Schwann cell development. *Genes Dev*. 17:1380-1391.

Jaegle, M., W. Mandemakers, L. Broos, R. Zwart, A. Karis, P. Visser, F. Grosveld, and D. Meijer. 1996. The POU factor Oct-6 and Schwann cell differentiation. *Science*. 273:507-510.

Jaegle, M., and D. Meijer. 1998. Role of Oct-6 in Schwann cell differentiation. *Microsc Res Tech*. 41:372-378.

Jagalur, N.B., M. Ghazvini, W. Mandemakers, S. Driegen, A. Maas, E.A. Jones, M. Jaegle, F. Grosveld, J. Svaren, and D. Meijer. 2011. Functional dissection of the Oct6 Schwann cell enhancer reveals an essential role for dimeric Sox10 binding. *J Neurosci*. 31:8585-8594.

Jangouk, P., T. Dehmel, G. Meyer Zu Horste, A. Ludwig, H.C. Lehmann, and B.C. Kieseier. 2009. Involvement of ADAM10 in axonal outgrowth and myelination of the peripheral nerve. *Glia*. 57:1765-1774.

Jessen, K.R., A. Brennan, L. Morgan, R. Mirsky, A. Kent, Y. Hashimoto, and J. Gavrilovic. 1994. The Schwann cell precursor and its fate: a study of cell death and differentiation during gliogenesis in rat embryonic nerves. *Neuron*. 12:509-527.

Jessen, K.R., and R. Mirsky. 2005. The origin and development of glial cells in peripheral nerves. *Nat Rev Neurosci*. 6:671-682.

Jessen, K.R., and R. Mirsky. 2008. Negative regulation of myelination: relevance for development, injury, and demyelinating disease. *Glia*. 56:1552-1565.

Jones, E.A., S.W. Jang, G.M. Mager, L.W. Chang, R. Srinivasan, N.G. Gokey, R.M. Ward, R. Nagarajan, and J. Svaren. 2007. Interactions of Sox10 and Egr2 in myelin gene regulation. *Neuron Glia Biol*. 3:377-387.

Kabzinska, D., H. Drac, D.L. Sherman, A. Kostera-Pruszczyk, P.J. Brophy, A. Kochanski, and I. Hausmanowa-Petrusewicz. 2006. Charcot-Marie-Tooth type 4F disease caused by S399fsx410 mutation in the PRX gene. *Neurology*. 66:745-747.

Kagitani-Shimono, K., I. Mohri, T. Yagi, M. Taniike, and K. Suzuki. 2008. Peripheral neuropathy in the twitcher mouse: accumulation of extracellular matrix in the endoneurium and aberrant expression of ion channels. *Acta Neuropathol*. 115:577-587.

Kao, S.C., H. Wu, J. Xie, C.P. Chang, J.A. Ranish, I.A. Graef, and G.R. Crabtree. 2009. Calcineurin/NFAT signaling is required for neuregulin-regulated Schwann cell differentiation. *Science*. 323:651-654.

Kelley, D.E., C. Coleclough, and R.P. Perry. 1982. Functional significance and evolutionary development of the 5'-terminal regions of immunoglobulin variable-region genes. *Cell*. 29:681-689.

Kiefer, F., K. Arnold, M. Kunzli, L. Bordoli, and T. Schwede. 2009. The SWISS-MODEL Repository and associated resources. *Nucleic acids research*. 37:D387-392.

Kijima, K., C. Numakura, E. Shirahata, Y. Sawaishi, M. Shimohata, S. Igarashi, T. Tanaka, and K. Hayasaka. 2004. Periaxin mutation causes early-onset but slow-progressive Charcot-Marie-Tooth disease. *J Hum Genet*. 49:376-379.

Kim, D.S., Y.K. Hayashi, H. Matsumoto, M. Ogawa, S. Noguchi, N. Murakami, R. Sakuta, M. Mochizuki, D.E. Michele, K.P. Campbell, I. Nonaka, and I. Nishino. 2004. POMT1 mutation results in defective glycosylation and loss of laminin-binding activity in alpha-DG. *Neurology*. 62:1009-1011.

Kim, E., and M. Sheng. 2004. PDZ domain proteins of synapses. *Nat Rev Neurosci*. 5:771-781.

Kohl, B., S. Fischer, J. Groh, C. Wessig, and R. Martini. MCP-1/CCL2 modifies axon properties in a PMP22-overexpressing mouse model for Charcot-Marie-tooth 1A neuropathy. *Am J Pathol*. 176:1390-1399.

Kopp, J., and T. Schwede. 2004. The SWISS-MODEL Repository of annotated three-dimensional protein structure homology models. *Nucleic acids research*. 32:D230-234.

Kornau, H.C., P.H. Seeburg, and M.B. Kennedy. 1997. Interaction of ion channels and receptors with PDZ domain proteins. *Curr Opin Neurobiol*. 7:368-373.

Kozak, M. 1978. How do eucaryotic ribosomes select initiation regions in messenger RNA? *Cell*. 15:1109-1123.

Kozak, M. 1984. Selection of initiation sites by eucaryotic ribosomes: effect of inserting AUG triplets upstream from the coding sequence for preproinsulin. *Nucleic acids research*. 12:3873-3893.

Kozak, M. 1986a. Bifunctional messenger RNAs in eukaryotes. *Cell*. 47:481-483.

Kozak, M. 1986b. Regulation of protein synthesis in virus-infected animal cells. *Advances in virus research*. 31:229-292.

Kozak, M. 1987a. An analysis of 5'-noncoding sequences from 699 vertebrate messenger RNAs. *Nucleic acids research*. 15:8125-8148.

Kozak, M. 1987b. Effects of intercistronic length on the efficiency of reinitiation by eucaryotic ribosomes. *Molecular and cellular biology*. 7:3438-3445.

Kozak, M. 1989. The scanning model for translation: an update. *The Journal of cell biology*. 108:229-241.

Kubu, C.J., K. Orimoto, S.J. Morrison, G. Weinmaster, D.J. Anderson, and J.M. Verdi. 2002. Developmental changes in Notch1 and numb expression mediated by local cell-cell interactions underlie progressively increasing delta sensitivity in neural crest stem cells. *Dev Biol*. 244:199-214.

Kuhlbrodt, K., B. Herbarth, E. Sock, I. Hermans-Borgmeyer, and M. Wegner. 1998. Sox10, a novel transcriptional modulator in glial cells. *J Neurosci*. 18:237-250.

La Marca, R., F. Cerri, K. Horiuchi, A. Bachi, M.L. Feltri, L. Wrabetz, C.P. Blobel, A. Quattrini, J.L. Salzer, and C. Taveggia. 2011. TACE (ADAM17) inhibits Schwann cell myelination. *Nat Neurosci*. 14:857-865.

Lappe-Siefke, C., S. Goebbels, M. Gravel, E. Nicksch, J. Lee, P.E. Braun, I.R. Griffiths, and K.A. Nave. 2003. Disruption of Cnp1 uncouples oligodendroglial functions in axonal support and myelination. *Nat Genet*. 33:366-374.

Le Douarin, N.M., and E. Dupin. 2003. Multipotentiality of the neural crest. *Current opinion in genetics & development*. 13:529-536.

Le, N., R. Nagarajan, J.Y. Wang, T. Araki, R.E. Schmidt, and J. Milbrandt. 2005. Analysis of congenital hypomyelinating Egr2Lo/Lo nerves identifies Sox2 as an inhibitor of Schwann cell differentiation and myelination. *Proc Natl Acad Sci U S A*. 102:2596-2601.

LeBlanc, S.E., S.W. Jang, R.M. Ward, L. Wrabetz, and J. Svaren. 2006. Direct regulation of myelin protein zero expression by the Egr2 transactivator. *J Biol Chem*. 281:5453-5460.

LeBlanc, S.E., R.M. Ward, and J. Svaren. 2007. Neuropathy-associated Egr2 mutants disrupt cooperative activation of myelin protein zero by Egr2 and Sox10. *Molecular and cellular biology*. 27:3521-3529.

Ledley, F.D. 1990. Perspectives on methylmalonic acidemia resulting from molecular cloning of methylmalonyl CoA mutase. *Bioessays*. 12:335-340.

Lee, H.J., and J.J. Zheng. 2010. PDZ domains and their binding partners: structure, specificity, and modification. *Cell Commun Signal*. 8:8.

Lee, O.K., K.K. Frese, J.S. James, D. Chadda, Z.H. Chen, R.T. Javier, and K.O. Cho. 2003. Discs-Large and Strabismus are functionally linked to plasma membrane formation. *Nat Cell Biol*. 5:987-993.

Leone, D.P., S. Genoud, S. Atanasoski, R. Grausenburger, P. Berger, D. Metzger, W.B. Macklin, P. Chambon, and U. Suter. 2003. Tamoxifen-inducible glia-specific Cre mice for somatic mutagenesis in oligodendrocytes and Schwann cells. *Mol Cell Neurosci*. 22:430-440.

Levedakou, E.N., X.J. Chen, B. Soliven, and B. Popko. 2005. Disruption of the mouse Large gene in the enr and myd mutants results in nerve, muscle, and neuromuscular junction defects. *Mol Cell Neurosci*. 28:757-769.

Limpert, A.S., and B.D. Carter. 2010. Axonal neuregulin 1 type III activates NF-kappaB in Schwann cells during myelin formation. *J Biol Chem*. 285:16614-16622.

Lue, R.A., S.M. Marfatia, D. Branton, and A.H. Chishti. 1994. Cloning and characterization of hdlg: the human homologue of the Drosophila discs large tumor suppressor binds to protein 4.1. *Proc Natl Acad Sci U S A*. 91:9818-9822.

Luo, S., Y. Chen, K.O. Lai, J.C. Arevalo, S.C. Froehner, M.E. Adams, M.V. Chao, and N.Y. Ip. 2005. {alpha}-Syntrophin regulates ARMS localization at the neuromuscular junction and enhances EphA4 signaling in an ARMS-dependent manner. *The Journal of cell biology*. 169:813-824.

Luo, X., M. Prior, W. He, X. Hu, X. Tang, W. Shen, S. Yadav, S. Kiryu-Seo, R. Miller, B.D. Trapp, and R. Yan. 2011. Cleavage of neuregulin-1 by BACE1 or ADAM10 protein produces differential effects on myelination. *J Biol Chem*. 286:23967-23974.

Ma, Z., J. Wang, F. Song, and J.A. Loeb. 2011. Critical period of axoglial signaling between neuregulin-1 and brain-derived neurotrophic factor required for early Schwann cell survival and differentiation. *J Neurosci*. 31:9630-9640.

Maddala, R., N.P. Skiba, R. Lalane, 3rd, D.L. Sherman, P.J. Brophy, and P.V. Rao. 2011. Periaxin is required for hexagonal geometry and membrane organization of mature lens fibers. *Dev Biol*. 357:179-190.

Madrid, R.E., E. Jaros, M.J. Cullen, and W.G. Bradley. 1975. Genetically determined defect of Schwann cell basement membrane in dystrophic mouse. *Nature*. 257:319-321.

Maier, M., P. Berger, and U. Suter. 2002. Understanding Schwann cell-neurone interactions: the key to Charcot-Marie-Tooth disease? *J Anat*. 200:357-366.

Maquat, L.E. 1995. When cells stop making sense: effects of nonsense codons on RNA metabolism in vertebrate cells. *Rna*. 1:453-465.

Marchesi, C., M. Milani, M. Morbin, M. Cesani, G. Lauria, V. Scaioli, G. Piccolo, G.M. Fabrizi, T. Cavallaro, F. Taroni, and D. Pareyson. 2010. Four novel cases of periaxin-related neuropathy and review of the literature. *Neurology*. 75:1830-1838.

Maro, G.S., M. Vermeren, O. Voiculescu, L. Melton, J. Cohen, P. Charnay, and P. Topilko. 2004. Neural crest boundary cap cells constitute a source of neuronal and glial cells of the PNS. *Nat Neurosci*. 7:930-938.

Martin, J.R., and H.D. Webster. 1973. Mitotic Schwann cells in developing nerve: their changes in shape, fine structure, and axon relationships. *Dev Biol*. 32:417-431.

Masaki, T., and K. Matsumura. 2010. Biological role of dystroglycan in Schwann cell function and its implications in peripheral nervous system diseases. *J Biomed Biotechnol*. 2010:740403.

Maurel, P., S. Einheber, J. Galinska, P. Thaker, I. Lam, M.B. Rubin, S.S. Scherer, Y. Murakami, D.H. Gutmann, and J.L. Salzer. 2007. Nectin-like proteins mediate axon Schwann cell interactions along the internode and are essential for myelination. *The Journal of cell biology*. 178:861-874.

Maurel, P., and J.L. Salzer. 2000. Axonal regulation of Schwann cell proliferation and survival and the initial events of myelination requires PI 3-kinase activity. *J Neurosci*. 20:4635-4645.

Maycox, P.R., D. Ortuno, P. Burrola, R. Kuhn, P.L. Bieri, J.C. Arrezo, and G. Lemke. 1997. A transgenic mouse model for human hereditary neuropathy with liability to pressure palsies. *Mol Cell Neurosci*. 8:405-416.

Mei, L., and W.C. Xiong. 2008. Neuregulin 1 in neural development, synaptic plasticity and schizophrenia. *Nat Rev Neurosci*. 9:437-452.

Melendez-Vasquez, C.V., S. Einheber, and J.L. Salzer. 2004. Rho kinase regulates schwann cell myelination and formation of associated axonal domains. *J Neurosci*. 24:3953-3963.

Meyer, D., T. Yamaai, A. Garratt, E. Riethmacher-Sonnenberg, D. Kane, L.E. Theill, and C. Birchmeier. 1997. Isoform-specific expression and function of neuregulin. *Development*. 124:3575-3586.

Michailov, G.V., M.W. Sereda, B.G. Brinkmann, T.M. Fischer, B. Haug, C. Birchmeier, L. Role, C. Lai, M.H. Schwab, and K.A. Nave. 2004. Axonal neuregulin-1 regulates myelin sheath thickness. *Science*. 304:700-703.

Michele, D.E., R. Barresi, M. Kanagawa, F. Saito, R.D. Cohn, J.S. Satz, J. Dollar, I. Nishino, R.I. Kelley, H. Somer, V. Straub, K.D. Mathews, S.A. Moore, and K.P. Campbell. 2002. Post-translational disruption of dystroglycan-ligand interactions in congenital muscular dystrophies. *Nature*. 418:417-422.

Miriami, E., H. Margalit, and R. Sperling. 2003. Conserved sequence elements associated with exon skipping. *Nucleic acids research*. 31:1974-1983.

Mirsky, R., A. Woodhoo, D.B. Parkinson, P. Arthur-Farraj, A. Bhaskaran, and K.R. Jessen. 2008. Novel signals controlling embryonic Schwann cell development, myelination and dedifferentiation. *J Peripher Nerv Syst*. 13:122-135.

Monk, K.R., S.G. Naylor, T.D. Glenn, S. Mercurio, J.R. Perlin, C. Dominguez, C.B. Moens, and W.S. Talbot. 2009. A G protein-coupled receptor is essential for Schwann cells to initiate myelination. *Science*. 325:1402-1405.

Monk, K.R., K. Oshima, S. Jors, S. Heller, and W.S. Talbot. 2011. Gpr126 is essential for peripheral nerve development and myelination in mammals. *Development*. 138:2673-2680.

Monuki, E.S., G. Weinmaster, R. Kuhn, and G. Lemke. 1989. SCIP: a glial POU domain gene regulated by cyclic AMP. *Neuron*. 3:783-793.

Moore, J.W., R.W. Joyner, M.H. Brill, S.D. Waxman, and M. Najar-Joa. 1978. Simulations of conduction in uniform myelinated fibers. Relative sensitivity to changes in nodal and internodal parameters. *Biophysical journal*. 21:147-160.

Mora, A., D. Komander, D.M. van Aalten, and D.R. Alessi. 2004. PDK1, the master regulator of AGC kinase signal transduction. *Semin Cell Dev Biol*. 15:161-170.

Morgan, L., K.R. Jessen, and R. Mirsky. 1991. The effects of cAMP on differentiation of cultured Schwann cells: progression from an early phenotype (04+) to a myelin phenotype (P0+, GFAP-, N-CAM-, NGF-receptor-) depends on growth inhibition. *The Journal of cell biology*. 112:457-467.

Morris, J.K., W. Lin, C. Hauser, Y. Marchuk, D. Getman, and K.F. Lee. 1999. Rescue of the cardiac defect in ErbB2 mutant mice reveals essential roles of ErbB2 in peripheral nervous system development. *Neuron*. 23:273-283.

Morrison, S.J., S.E. Perez, Z. Qiao, J.M. Verdi, C. Hicks, G. Weinmaster, and D.J. Anderson. 2000. Transient Notch activation initiates an irreversible switch from neurogenesis to gliogenesis by neural crest stem cells. *Cell*. 101:499-510.

Morrissey, T.K., A.D. Levi, A. Nuijens, M.X. Sliwkowski, and R.P. Bunge. 1995. Axon-induced mitogenesis of human Schwann cells involves heregulin and p185erbB2. *Proc Natl Acad Sci U S A*. 92:1431-1435.

Nagarajan, R., J. Svaren, N. Le, T. Araki, M. Watson, and J. Milbrandt. 2001. EGR2 mutations in inherited neuropathies dominant-negatively inhibit myelin gene expression. *Neuron*. 30:355-368.

Narayanan, S.P., A.I. Flores, F. Wang, and W.B. Macklin. 2009. Akt signals through the mammalian target of rapamycin pathway to regulate CNS myelination. *J Neurosci*. 29:6860-6870.

Nave, K.A. 2010. Myelination and support of axonal integrity by glia. *Nature*. 468:244-252.

Nave, K.A., and J.L. Salzer. 2006. Axonal regulation of myelination by neuregulin 1. *Curr Opin Neurobiol*. 16:492-500.

Nave, K.A., and B.D. Trapp. 2008. Axon-glial signaling and the glial support of axon function. *Annu Rev Neurosci*. 31:535-561.

Neuberg, D.H., S. Sancho, and U. Suter. 1999. Altered molecular architecture of peripheral nerves in mice lacking the peripheral myelin protein 22 or connexin32. *J Neurosci Res*. 58:612-623.

Newbern, J., and C. Birchmeier. 2010. Nrg1/ErbB signaling networks in Schwann cell development and myelination. *Semin Cell Dev Biol*. 21:922-928.

Newbern, J.M., X. Li, S.E. Shoemaker, J. Zhou, J. Zhong, Y. Wu, D. Bonder, S. Hollenback, G. Coppola, D.H. Geschwind, G.E. Landreth, and W.D. Snider. 2011. Specific functions for ERK/MAPK signaling during PNS development. *Neuron*. 69:91-105.

Nodari, A., S.C. Previtali, G. Dati, S. Occhi, F.A. Court, C. Colombelli, D. Zambroni, G. Dina, U. Del Carro, K.P. Campbell, A. Quattrini, L. Wrabetz, and M.L. Feltri. 2008. Alpha6beta4 integrin and dystroglycan cooperate to stabilize the myelin sheath. *J Neurosci*. 28:6714-6719.

Nodari, A., D. Zambroni, A. Quattrini, F.A. Court, A. D'Urso, A. Recchia, V.L. Tybulewicz, L. Wrabetz, and M.L. Feltri. 2007. Beta1 integrin activates Rac1 in Schwann cells to generate radial lamellae during axonal sorting and myelination. *The Journal of cell biology*. 177:1063-1075.

Nourry, C., S.G. Grant, and J.P. Borg. 2003. PDZ domain proteins: plug and play! *Sci STKE*. 2003:RE7.

Occhi, S., D. Zambroni, U. Del Carro, S. Amadio, E.E. Sirkowski, S.S. Scherer, K.P. Campbell, S.A. Moore, Z.L. Chen, S. Strickland, A. Di Muzio, A. Uncini, L. Wrabetz, and M.L. Feltri. 2005. Both laminin and Schwann cell dystroglycan are necessary for proper clustering of sodium channels at nodes of Ranvier. *J Neurosci*. 25:9418-9427.

Ogata, T., S. Iijima, S. Hoshikawa, T. Miura, S. Yamamoto, H. Oda, K. Nakamura, and S. Tanaka. 2004. Opposing extracellular signal-regulated kinase and Akt pathways control Schwann cell myelination. *J Neurosci*. 24:6724-6732.

Otagiri, T., K. Sugai, K. Kijima, H. Arai, Y. Sawaishi, M. Shimohata, and K. Hayasaka. 2006. Periaxin mutation in Japanese patients with Charcot-Marie-Tooth disease. *J Hum Genet*. 51:625-628.

Ozcelik, M., L. Cotter, C. Jacob, J.A. Pereira, J.B. Relvas, U. Suter, and N. Tricaud. 2010. Pals1 is a major regulator of the epithelial-like polarization and the extension of the myelin sheath in peripheral nerves. *J Neurosci*. 30:4120-4131.

Ozkaynak, E., G. Abello, M. Jaegle, L. van Berge, D. Hamer, L. Kegel, S. Driegen, K. Sagane, J.R. Bermingham, Jr., and D. Meijer. 2010. Adam22 is a major neuronal receptor for Lgi4-mediated Schwann cell signaling. *J Neurosci*. 30:3857-3864.

Palumbo, C., R. Massa, M.B. Panico, A. Di Muzio, P. Sinibaldi, G. Bernardi, and A. Modesti. 2002. Peripheral nerve extracellular matrix remodeling in Charcot-Marie-Tooth type I disease. *Acta Neuropathol*. 104:287-296.

Parkinson, D.B., A. Bhaskaran, P. Arthur-Farraj, L.A. Noon, A. Woodhoo, A.C. Lloyd, M.L. Feltri, L. Wrabetz, A. Behrens, R. Mirsky, and K.R. Jessen. 2008. c-Jun is a negative regulator of myelination. *The Journal of cell biology*. 181:625-637.

Parkinson, D.B., A. Bhaskaran, A. Droggiti, S. Dickinson, M. D'Antonio, R. Mirsky, and K.R. Jessen. 2004. Krox-20 inhibits Jun-NH2-terminal kinase/c-Jun to control Schwann cell proliferation and death. *The Journal of cell biology*. 164:385-394.

Parkinson, D.B., S. Dickinson, A. Bhaskaran, M.T. Kinsella, P.J. Brophy, D.L. Sherman, S. Sharghi-Namini, M.B. Duran Alonso, R. Mirsky, and K.R. Jessen. 2003. Regulation of the myelin gene periaxin provides evidence for Krox-20-independent myelin-related signalling in Schwann cells. *Mol Cell Neurosci*. 23:13-27.

Parman, Y., E. Battaloglu, I. Baris, B. Bilir, M. Poyraz, N. Bissar-Tadmouri, A. Williams, N. Ammar, E. Nelis, V. Timmerman, P. De Jonghe, A. Najafov, F. Deymeer, P. Serdaroglu, P.J. Brophy, and G. Said. 2004. Clinicopathological and genetic study of early-onset demyelinating neuropathy. *Brain*. 127:2540-2550.

Patzig, J., O. Jahn, S. Tenzer, S.P. Wichert, P. de Monasterio-Schrader, S. Rosfa, J. Kuharev, K. Yan, I. Bormuth, J. Bremer, A. Aguzzi, F. Orfaniotou, D. Hesse, M.H. Schwab, W. Mobius, K.A. Nave, and H.B. Werner. 2011. Quantitative and Integrative Proteome Analysis of Peripheral Nerve Myelin Identifies Novel Myelin Proteins and Candidate Neuropathy Loci. *J Neurosci*. 31:16369-16386.

Paulsen, M., C. Lund, Z. Akram, J.R. Winther, N. Horn, and L.B. Moller. 2006. Evidence that translation reinitiation leads to a partially functional Menkes protein containing two copper-binding sites. *Am J Hum Genet*. 79:214-229.

Peirano, R.I., D.E. Goerich, D. Riethmacher, and M. Wegner. 2000. Protein zero gene expression is regulated by the glial transcription factor Sox10. *Molecular and cellular biology*. 20:3198-3209.

Peles, E., and J.L. Salzer. 2000. Molecular domains of myelinated axons. *Curr Opin Neurobiol*. 10:558-565.

Pereira, J.A., Y. Benninger, R. Baumann, A.F. Goncalves, M. Ozcelik, T. Thurnherr, N. Tricaud, D. Meijer, R. Fassler, U. Suter, and J.B. Relvas. 2009. Integrin-linked kinase is required for radial sorting of axons and Schwann cell remyelination in the peripheral nervous system. *The Journal of cell biology*. 185:147-161.

Perrin-Vidoz, L., O.M. Sinilnikova, D. Stoppa-Lyonnet, G.M. Lenoir, and S. Mazoyer. 2002. The nonsense-mediated mRNA decay pathway triggers degradation of most BRCA1 mRNAs bearing premature termination codons. *Hum Mol Genet*. 11:2805-2814.

Pertusa, M., C. Morenilla-Palao, C. Carteron, F. Viana, and H. Cabedo. 2007. Transcriptional control of cholesterol biosynthesis in Schwann cells by axonal neuregulin 1. *J Biol Chem*. 282:28768-28778.

Peters, A., and A.R. Muir. 1959. The relationship between axons and Schwann cells during development of peripheral nerves in the rat. *Q J Exp Physiol Cogn Med Sci*: 117-130.

Peterson, C.A., and J. Piatigorsky. 1986. Preferential conservation of the globular domains of the beta A3/A1-crystallin polypeptide of the chicken eye lens. *Gene*. 45:139-147.

Podratz, J.L., E. Rodriguez, and A.J. Windebank. 2001. Role of the extracellular matrix in myelination of peripheral nerve. *Glia*. 35:35-40.

Previtali, S.C., G. Dina, A. Nodari, M. Fasolini, L. Wrabetz, U. Mayer, M.L. Feltri, and A. Quattrini. 2003a. Schwann cells synthesize alpha7beta1 integrin which is dispensable for peripheral nerve development and myelination. *Mol Cell Neurosci*. 23:210-218.

Previtali, S.C., A. Nodari, C. Taveggia, C. Pardini, G. Dina, A. Villa, L. Wrabetz, A. Quattrini, and M.L. Feltri. 2003b. Expression of laminin receptors in schwann cell differentiation: evidence for distinct roles. *J Neurosci*. 23:5520-5530.

Ramón y Cajal, S. 1933. Histology. Bailliere, Tindall & Cox, London.

Raphael, A.R., D.A. Lyons, and W.S. Talbot. 2011. ErbB signaling has a role in radial sorting independent of Schwann cell number. *Glia*. 59:1047-1055.

Rasminsky, M., R.E. Kearney, A.J. Aguayo, and G.M. Bray. 1978. Conduction of nervous impulses in spinal roots and peripheral nerves of dystrophic mice. *Brain Res*. 143:71-85.

Richardson, W.D., N. Kessaris, and N. Pringle. 2006. Oligodendrocyte wars. *Nat Rev Neurosci*. 7:11-18.

Riethmacher, D., E. Sonnenberg-Riethmacher, V. Brinkmann, T. Yamaai, G.R. Lewin, and C. Birchmeier. 1997. Severe neuropathies in mice with targeted mutations in the ErbB3 receptor. *Nature*. 389:725-730.

Robertson, W.F. 1899. On a new method of obtaining a black
reaction in certain tissue elements of the central nervous system
(platinum method).
. *Scottish Medical and Surgical Journal*. 4:23-30.

Robinson, F.L., I.R. Niesman, K.K. Beiswenger, and J.E. Dixon. 2008. Loss of the inactive myotubularin-related phosphatase Mtmr13 leads to a Charcot-Marie-Tooth 4B2-like peripheral neuropathy in mice. *Proc Natl Acad Sci U S A*. 105:4916-4921.

Rushton, W.A. 1951. A theory of the effects of fibre size in medullated nerve. *J Physiol*. 115:101-122.

Sagane, K., K. Hayakawa, J. Kai, T. Hirohashi, E. Takahashi, N. Miyamoto, M. Ino, T. Oki, K. Yamazaki, and T. Nagasu. 2005. Ataxia and peripheral nerve hypomyelination in ADAM22-deficient mice. *BMC Neurosci*. 6:33.

Saher, G., S. Quintes, W. Mobius, M.C. Wehr, E.M. Kramer-Albers, B. Brugger, and K.A. Nave. 2009. Cholesterol regulates the endoplasmic reticulum exit of the major membrane protein P0 required for peripheral myelin compaction. *J Neurosci*. 29:6094-6104.

Saito, F., T. Masaki, K. Kamakura, L.V. Anderson, S. Fujita, H. Fukuta-Ohi, Y. Sunada, T. Shimizu, and K. Matsumura. 1999. Characterization of the transmembrane molecular architecture of the dystroglycan complex in schwann cells. *J Biol Chem*. 274:8240-8246.

Saito, F., T. Masaki, Y. Saito, A. Nakamura, S. Takeda, T. Shimizu, T. Toda, and K. Matsumura. 2007. Defective peripheral nerve myelination and neuromuscular junction formation in fukutin-deficient chimeric mice. *J Neurochem*. 101:1712-1722.

Saito, F., S.A. Moore, R. Barresi, M.D. Henry, A. Messing, S.E. Ross-Barta, R.D. Cohn, R.A. Williamson, K.A. Sluka, D.L. Sherman, P.J. Brophy, J.D. Schmelzer, P.A. Low, L. Wrabetz, M.L. Feltri, and K.P. Campbell. 2003. Unique role of dystroglycan in peripheral nerve myelination, nodal structure, and sodium channel stabilization. *Neuron*. 38:747-758.

Salim, C., Y.V. Boxberg, J. Alterio, S. Fereol, and F. Nothias. 2009. The giant protein AHNAK involved in morphogenesis and laminin substrate adhesion of myelinating Schwann cells. *Glia*. 57:535-549.

Salzer, J.L. 2003. Polarized domains of myelinated axons. *Neuron*. 40:297-318.

Salzer, J.L., P.J. Brophy, and E. Peles. 2008. Molecular domains of myelinated axons in the peripheral nervous system. *Glia*. 56:1532-1540.

Sambrook, J., and D. Russell. 2001. Molecular Cloning: A Laboratory Manual. Cold Spring Harbor Laboratory Press.

Sanders, F.K., and D. Whitteridge. 1946. Conduction velocity and myelin thickness in regenerating nerve fibres. *J Physiol*. 105:152-174.

Scherer, S.S., D.Y. Wang, R. Kuhn, G. Lemke, L. Wrabetz, and J. Kamholz. 1994. Axons regulate Schwann cell expression of the POU transcription factor SCIP. *J Neurosci*. 14:1930-1942.

Scherer, S.S., and L. Wrabetz. 2008. Molecular mechanisms of inherited demyelinating neuropathies. *Glia*. 56:1578-1589.

Scherer, S.S., Y.T. Xu, P.G. Bannerman, D.L. Sherman, and P.J. Brophy. 1995. Periaxin expression in myelinating Schwann cells: modulation by axon-glial interactions and polarized localization during development. *Development*. 121:4265-4273.

Schreiner, S., F. Cossais, K. Fischer, S. Scholz, M.R. Bosl, B. Holtmann, M. Sendtner, and M. Wegner. 2007. Hypomorphic Sox10 alleles reveal novel protein functions and unravel developmental differences in glial lineages. *Development*. 134:3271-3281.

Schwann, T. 1839. Mikroskopische Untersuchungen über die Übereinstimmung in der Struktur und dem Wachstume der Tiere und Pflanzen. . G.E. Reimer, Berlin.

Schwede, T., J. Kopp, N. Guex, and M.C. Peitsch. 2003. SWISS-MODEL: An automated protein homology-modeling server. *Nucleic acids research*. 31:3381-3385.

Shah, N.M., M.A. Marchionni, I. Isaacs, P. Stroobant, and D.J. Anderson. 1994. Glial growth factor restricts mammalian neural crest stem cells to a glial fate. *Cell*. 77:349-360.

Sheng, M. 1996. PDZs and receptor/channel clustering: rounding up the latest suspects. *Neuron*. 17:575-578.

Sherman, D.L., and P.J. Brophy. 2000. A tripartite nuclear localization signal in the PDZ-domain protein L-periaxin. *J Biol Chem*. 275:4537-4540.

Sherman, D.L., and P.J. Brophy. 2005. Mechanisms of axon ensheathment and myelin growth. *Nat Rev Neurosci*. 6:683-690.

Sherman, D.L., C. Fabrizi, C.S. Gillespie, and P.J. Brophy. 2001. Specific disruption of a schwann cell dystrophin-related protein complex in a demyelinating neuropathy. *Neuron*. 30:677-687.

Shirakabe, K., S. Wakatsuki, T. Kurisaki, and A. Fujisawa-Sehara. 2001. Roles of Meltrin beta /ADAM19 in the processing of neuregulin. *J Biol Chem*. 276:9352-9358.

Sircar, S. 2008. Principles Of Medical Physiology. Thieme Medical Publishers. 852 pp.

Skre, H. 1974. Genetic and clinical aspects of Charcot-Marie-Tooth's disease. *Clin Genet*. 6:98-118.

Smith, R.S., and Z.J. Koles. 1970. Myelinated nerve fibers: computed effect of myelin thickness on conduction velocity. *Am J Physiol*. 219:1256-1258.

Spiegel, I., K. Adamsky, Y. Eshed, R. Milo, H. Sabanay, O. Sarig-Nadir, I. Horresh, S.S. Scherer, M.N. Rasband, and E. Peles. 2007. A central role for Necl4 (SynCAM4) in Schwann cell-axon interaction and myelination. *Nat Neurosci*. 10:861-869.

Stewart, H.J., A. Brennan, M. Rahman, G. Zoidl, P.J. Mitchell, K.R. Jessen, and R. Mirsky. 2001. Developmental regulation and overexpression of the transcription factor AP-2, a potential regulator of the timing of Schwann cell generation. *Eur J Neurosci*. 14:363-372.

Stewart, H.J., L. Morgan, K.R. Jessen, and R. Mirsky. 1993. Changes in DNA synthesis rate in the Schwann cell lineage in vivo are correlated with the precursor--Schwann cell transition and myelination. *Eur J Neurosci*. 5:1136-1144.

Stirling, C.A. 1975. Abnormalities in Schwann cell sheaths in spinal nerve roots of dystrophic mice. *J Anat*. 119:169-180.

Straub, B.K., J. Boda, C. Kuhn, M. Schnoelzer, U. Korf, T. Kempf, H. Spring, M. Hatzfeld, and W.W. Franke. 2003. A novel cell-cell junction system: the cortex adhaerens mosaic of lens fiber cells. *J Cell Sci*. 116:4985-4995.

Strubin, M., E.O. Long, and B. Mach. 1986. Two forms of the Ia antigen-associated invariant chain result from alternative initiations at two in-phase AUGs. *Cell*. 47:619-625.

Sugi, T., T. Oyama, T. Muto, S. Nakanishi, K. Morikawa, and H. Jingami. 2007. Crystal structures of autoinhibitory PDZ domain of Tamalin: implications for metabotropic glutamate receptor trafficking regulation. *Embo J*. 26:2192-2205.

Susuki, K., A.R. Raphael, Y. Ogawa, M.C. Stankewich, E. Peles, W.S. Talbot, and M.N. Rasband. 2011. Schwann cell spectrins modulate peripheral nerve myelination. *Proc Natl Acad Sci U S A*. 108:8009-8014.

Suter, U., and S.S. Scherer. 2003. Disease mechanisms in inherited neuropathies. *Nat Rev Neurosci*. 4:714-726.

Svaren, J., and D. Meijer. 2008. The molecular machinery of myelin gene transcription in Schwann cells. *Glia*. 56:1541-1551.

Syed, N., K. Reddy, D.P. Yang, C. Taveggia, J.L. Salzer, P. Maurel, and H.A. Kim. 2010. Soluble neuregulin-1 has bifunctional, concentration-dependent effects on Schwann cell myelination. *J Neurosci*. 30:6122-6131.

Takahashi, M., and N. Osumi. 2005. Identification of a novel type II classical cadherin: rat cadherin19 is expressed in the cranial ganglia and Schwann cell precursors during development. *Dev Dyn*. 232:200-208.

Takashima, H., C.F. Boerkoel, P. De Jonghe, C. Ceuterick, J.J. Martin, T. Voit, J.M. Schroder, A. Williams, P.J. Brophy, V. Timmerman, and J.R. Lupski. 2002. Periaxin mutations cause a broad spectrum of demyelinating neuropathies. *Ann Neurol*. 51:709-715.

Tao, Y., P. Dai, Y. Liu, S. Marchetto, W.C. Xiong, J.P. Borg, and L. Mei. 2009. Erbin regulates NRG1 signaling and myelination. *Proc Natl Acad Sci U S A*. 106:9477-9482.

Tapon, N., and A. Hall. 1997. Rho, Rac and Cdc42 GTPases regulate the organization of the actin cytoskeleton. *Curr Opin Cell Biol*. 9:86-92.

Taveggia, C., M.L. Feltri, and L. Wrabetz. 2010. Signals to promote myelin formation and repair. *Nat Rev Neurol*. 6:276-287.

Taveggia, C., G. Zanazzi, A. Petrylak, H. Yano, J. Rosenbluth, S. Einheber, X. Xu, R.M. Esper, J.A. Loeb, P. Shrager, M.V. Chao, D.L. Falls, L. Role, and J.L. Salzer. 2005. Neuregulin-1 type III determines the ensheathment fate of axons. *Neuron*. 47:681-694.

Taylor, M.K., K. Yeager, and S.J. Morrison. 2007. Physiological Notch signaling promotes gliogenesis in the developing peripheral and central nervous systems. *Development*. 134:2435-2447.

Tersar, K., M. Boentert, P. Berger, S. Bonneick, C. Wessig, K.V. Toyka, P. Young, and U. Suter. 2007. Mtmr13/Sbf2-deficient mice: an animal model for CMT4B2. *Hum Mol Genet*. 16:2991-3001.

Thomas, P., and T.G. Smart. 2005. HEK293 cell line: a vehicle for the expression of recombinant proteins. *Journal of pharmacological and toxicological methods*. 51:187-200.

Tochio, H., Y.K. Mok, Q. Zhang, H.M. Kan, D.S. Bredt, and M. Zhang. 2000. Formation of nNOS/PSD-95 PDZ dimer requires a preformed beta-finger structure from the nNOS PDZ domain. *J Mol Biol*. 303:359-370.

Tolwani, R.J., J.M. Cosgaya, S. Varma, R. Jacob, L.E. Kuo, and E.M. Shooter. 2004. BDNF overexpression produces a long-term increase in myelin formation in the peripheral nervous system. *J Neurosci Res*. 77:662-669.

Topilko, P., S. Schneider-Maunoury, G. Levi, A. Baron-Van Evercooren, A.B. Chennoufi, T. Seitanidou, C. Babinet, and P. Charnay. 1994. Krox-20 controls myelination in the peripheral nervous system. *Nature*. 371:796-799.

Trajkovic, K., A.S. Dhaunchak, J.T. Goncalves, D. Wenzel, A. Schneider, G. Bunt, K.A. Nave, and M. Simons. 2006. Neuron to glia signaling triggers myelin membrane exocytosis from endosomal storage sites. *The Journal of cell biology*. 172:937-948.

Tricaud, N., C. Perrin-Tricaud, J.L. Bruses, and U. Rutishauser. 2005. Adherens junctions in myelinating Schwann cells stabilize Schmidt-Lanterman incisures via recruitment of p120 catenin to E-cadherin. *J Neurosci*. 25:3259-3269.

Tyler, W.A., N. Gangoli, P. Gokina, H.A. Kim, M. Covey, S.W. Levison, and T.L. Wood. 2009. Activation of the mammalian target of rapamycin (mTOR) is essential for oligodendrocyte differentiation. *J Neurosci*. 29:6367-6378.

Utepbergenov, D.I., A.S. Fanning, and J.M. Anderson. 2006. Dimerization of the scaffolding protein ZO-1 through the second PDZ domain. *J Biol Chem*. 281:24671-24677.

Vartanian, T., A. Goodearl, S. Lefebvre, S.K. Park, and G. Fischbach. 2000. Neuregulin induces the rapid association of focal adhesion kinase with the erbB2-erbB3 receptor complex in schwann cells. *Biochem Biophys Res Commun*. 271:414-417.

Velanac, V., T. Unterbarnscheidt, W. Hinrichs, M.N. Gummert, T.M. Fischer, M.J. Rossner, A. Trimarco, V. Brivio, C. Taveggia, M. Willem, C. Haass, W. Mobius, K.A. Nave, and M.H. Schwab. 2011. Bace1 processing of NRG1 type III produces a myelin-inducing signal but is not essential for the stimulation of myelination. *Glia*.

Vuillaumier-Barrot, S., A. Barnier, M. Cuer, G. Durand, B. Grandchamp, and N. Seta. 1999. Characterization of the 415G>A (E139K) PMM2 mutation in carbohydrate-deficient glycoprotein syndrome type Ia disrupting a splicing enhancer resulting in exon 5 skipping. *Hum Mutat*. 14:543-544.

Wakatsuki, S., N. Yumoto, K. Komatsu, T. Araki, and A. Sehara-Fujisawa. 2009. Roles of meltrin-beta/ADAM19 in progression of Schwann cell differentiation and myelination during sciatic nerve regeneration. *J Biol Chem*. 284:2957-2966.

Wallquist, W., S. Plantman, S. Thams, J. Thyboll, J. Kortesmaa, J. Lannergren, A. Domogatskaya, S.O. Ogren, M. Risling, H. Hammarberg, K. Tryggvason, and S. Cullheim. 2005. Impeded interaction between Schwann cells and axons in the absence of laminin alpha4. *J Neurosci*. 25:3692-3700.

Wang, C.K., L. Pan, J. Chen, and M. Zhang. 2010. Extensions of PDZ domains as important structural and functional elements. *Protein Cell*. 1:737-751.

Waxman, S.G. 1980. Determinants of conduction velocity in myelinated nerve fibers. *Muscle Nerve*. 3:141-150.

Willem, M., A.N. Garratt, B. Novak, M. Citron, S. Kaufmann, A. Rittger, B. DeStrooper, P. Saftig, C. Birchmeier, and C. Haass. 2006. Control of peripheral nerve myelination by the beta-secretase BACE1. *Science*. 314:664-666.

Williams, A.C., and P.J. Brophy. 2002. The function of the Periaxin gene during nerve repair in a model of CMT4F. *J Anat*. 200:323-330.

Winterstein, C., J. Trotter, and E.M. Kramer-Albers. 2008. Distinct endocytic recycling of myelin proteins promotes oligodendroglial membrane remodeling. *J Cell Sci*. 121:834-842.

Woldeyesus, M.T., S. Britsch, D. Riethmacher, L. Xu, E. Sonnenberg-Riethmacher, F. Abou-Rebyeh, R. Harvey, P. Caroni, and C. Birchmeier. 1999. Peripheral nervous system defects in erbB2 mutants following genetic rescue of heart development. *Genes Dev*. 13:2538-2548.

Wolpowitz, D., T.B. Mason, P. Dietrich, M. Mendelsohn, D.A. Talmage, and L.W. Role. 2000. Cysteine-rich domain isoforms of the neuregulin-1 gene are required for maintenance of peripheral synapses. *Neuron*. 25:79-91.

Woodhoo, A., M.B. Alonso, A. Droggiti, M. Turmaine, M. D'Antonio, D.B. Parkinson, D.K. Wilton, R. Al-Shawi, P. Simons, J. Shen, F. Guillemot, F. Radtke, D. Meijer, M.L. Feltri, L. Wrabetz, R. Mirsky, and K.R. Jessen. 2009. Notch controls embryonic Schwann cell differentiation, postnatal myelination and adult plasticity. *Nat Neurosci*. 12:839-847.

Woodhoo, A., C.H. Dean, A. Droggiti, R. Mirsky, and K.R. Jessen. 2004. The trunk neural crest and its early glial derivatives: a study of survival responses, developmental schedules and autocrine mechanisms. *Mol Cell Neurosci*. 25:30-41.

Woodhoo, A., and L. Sommer. 2008. Development of the Schwann cell lineage: from the neural crest to the myelinated nerve. *Glia*. 56:1481-1490.

Wu, J., Y. Yang, J. Zhang, P. Ji, W. Du, P. Jiang, D. Xie, H. Huang, M. Wu, G. Zhang, J. Wu, and Y. Shi. 2007. Domain-swapped dimerization of the second PDZ domain of ZO2 may provide a structural basis for the polymerization of claudins. *J Biol Chem*. 282:35988-35999.

Yamada, H., A. Chiba, T. Endo, A. Kobata, L.V. Anderson, H. Hori, H. Fukuta-Ohi, I. Kanazawa, K.P. Campbell, T. Shimizu, and K. Matsumura. 1996a. Characterization of dp6troglycan-laminin interaction in peripheral nerve. *J Neurochem*. 66:1518-1524.

Yamada, H., A. Chiba, T. Endo, A. Kobata, L.V. Anderson, H. Hori, H. Fukuta-Ohi, I. Kanazawa, K.P. Campbell, T. Shimizu, and K. Matsumura. 1996b. Characterization of dystroglycan-laminin interaction in peripheral nerve. *J Neurochem*. 66:1518-1524.

Yamada, H., F. Saito, H. Fukuta-Ohi, D. Zhong, A. Hase, K. Arai, A. Okuyama, R. Maekawa, T. Shimizu, and K. Matsumura. 2001. Processing of beta-dystroglycan by matrix metalloproteinase disrupts the link between the extracellular matrix and cell membrane via the dystroglycan complex. *Hum Mol Genet*. 10:1563-1569.

Yang, D., J. Bierman, Y.S. Tarumi, Y.P. Zhong, R. Rangwala, T.M. Proctor, Y. Miyagoe-Suzuki, S. Takeda, J.H. Miner, L.S. Sherman, B.G. Gold, and B.L. Patton. 2005. Coordinate control of axon defasciculation and myelination by laminin-2 and -8. *The Journal of cell biology*. 168:655-666.

Yang, P., K.A. Baker, and T. Hagg. 2006. The ADAMs family: coordinators of nervous system development, plasticity and repair. *Prog Neurobiol*. 79:73-94.

Yoon, C., Z. Korade, and B.D. Carter. 2008. Protein kinase A-induced phosphorylation of the p65 subunit of nuclear factor-kappaB promotes Schwann cell differentiation into a myelinating phenotype. *J Neurosci*. 28:3738-3746.

Young, P., and U. Suter. 2003. The causes of Charcot-Marie-Tooth disease. *Cell Mol Life Sci*. 60:2547-2560.

Yu, W.M., Z.L. Chen, A.J. North, and S. Strickland. 2009a. Laminin is required for Schwann cell morphogenesis. *J Cell Sci*. 122:929-936.

Yu, W.M., M.L. Feltri, L. Wrabetz, S. Strickland, and Z.L. Chen. 2005. Schwann cell-specific ablation of laminin gamma1 causes apoptosis and prevents proliferation. *J Neurosci*. 25:4463-4472.

Yu, W.M., H. Yu, Z.L. Chen, and S. Strickland. 2009b. Disruption of laminin in the peripheral nervous system impedes nonmyelinating Schwann cell development and impairs nociceptive sensory function. *Glia*. 57:850-859.

Zhang, J., and L.E. Maquat. 1997. Evidence that translation reinitiation abrogates nonsense-mediated mRNA decay in mammalian cells. *Embo J*. 16:826-833.

Zhong, D., F. Saito, Y. Saito, A. Nakamura, T. Shimizu, and K. Matsumura. 2006. Characterization of the protease activity that cleaves the extracellular domain of beta-dystroglycan. *Biochem Biophys Res Commun*. 345:867-871.

Zito, K., R.D. Fetter, C.S. Goodman, and E.Y. Isacoff. 1997. Synaptic clustering of Fascilin II and Shaker: essential targeting sequences and role of Dlg. *Neuron*. 19:1007-1016.

Zoppi, S., C.M. Wilson, M.D. Harbison, J.E. Griffin, J.D. Wilson, M.J. McPhaul, and M. Marcelli. 1993. Complete testicular feminization caused by an amino-terminal truncation of the androgen receptor with downstream initiation. *J Clin Invest*. 91:1105-1112.

Zorick, T.S., D.E. Syroid, E. Arroyo, S.S. Scherer, and G. Lemke. 1996a. The Transcription Factors SCIP and Krox-20 Mark Distinct Stages and Cell Fates in Schwann Cell Differentiation. *Mol Cell Neurosci*. 8:129-145.

Zorick, T.S., D.E. Syroid, E. Arroyo, S.S. Scherer, and G. Lemke. 1996b. The transcription factors SCIP and Krox-20 mark distinct stages and cell fates in Schwann cell differentiation. *Mol Cell Neurosci*. 8:129-145.

Zorick, T.S., D.E. Syroid, A. Brown, T. Gridley, and G. Lemke. 1999. Krox-20 controls SCIP expression, cell cycle exit and susceptibility to apoptosis in developing myelinating Schwann cells. *Development*. 126:1397-1406.